University of Sussex

Search for squarks in compressed states and states with jets from charm quarks with the ATLAS detector

Samuel Jones

Submitted for the degree of Doctor of Philosophy
University of Sussex
8th December 2019

UNIVERSITY OF SUSSEX

Samuel Jones, Doctor of Philosophy
Supervisor: Prof. Iacopo Vivarelli

Search for squarks in compressed states and states with jets from charm quarks with the ATLAS detector

Abstract

This thesis presents a search for R-parity conserving Supersymmetry with the ATLAS detector, in final states with missing transverse momentum and jets. A search is designed, targeting pair produced scalar top quarks decaying as $\tilde{t}_1 \rightarrow c\tilde{\chi}_1^0$ and scalar charm quarks decaying as $\tilde{c}_1 \rightarrow c\tilde{\chi}_1^0$, where $\tilde{\chi}_1^0$ is the lightest neutralino. Charm tagging methods are used to identify jets originating from charm quarks. This search is based on LHC proton-proton collision data collected by ATLAS in 2015 and 2016, amounting to 36.1 fb^{-1} of integrated luminosity. No significant excess of data beyond Standard Model expectations was observed and squarks were excluded up to a mass of 850 GeV for a massless neutralino and up to 500 GeV for a mass splitting between the squark and neutralino of less than 100 GeV. All limits assume a 100% branching ratio to the $c\tilde{\chi}_1^0$ final state.

This thesis also presents a novel technique to identify low momentum b-hadrons using tracks from the ATLAS inner detector. This technique is developed to target compressed Supersymmetry models where the mass splitting between the squark and neutralino is small, leading to low momentum b-hadrons in the final state. With this technique b-hadrons with transverse momentum in the range $10 - 20$ GeV can be identified with an efficiency of $\sim 20\%$ with a mis-identification rate corresponding to $\sim 2.5\%$ of simulated events with no b-hadrons.

Acknowledgements

I am extremely grateful to my supervisor Iacopo, who has been a patient mentor, providing invaluable advice and guidance throughout my PhD. I will always admire your experience and insights. I am also grateful to Antonella, my second PhD supervisor and first supervisor for my masters project, who had the faith to allow me to continue with ATLAS at Sussex following this project. I must of course mention Kerim, who has been an extra supervisor throughout my PhD, and shared all my tea!

My entire career in physics has been at Sussex, where I have spent the last 9 years, from my access course to undergraduate studies to the submission of my PhD thesis. It is a wonderful department, although, admittedly, I have a sample size of one... I am grateful to my undergraduate project supervisors, Diego Porras (also my academic advisor) and Veronica Sanz (who help me on my trajectory toward SUSY searches). I am grateful to the entire Sussex EPP team: faculty, post docs and PhD colleagues. They are all wonderful people, to the last person. I give special mention to Suf, who was my mentor at the beginning of my time working on ATLAS for my masters project, and to my CERN drinking buddies: Fabio, Emma, Fab, Nicola, Mark, Olly and the rest. Thanks to Fabio you will never forget: you'll never get a better bit of butter on your knife!

I am grateful to my Dad, who loves physics as much as I do and has always taken so much interest in my physics journey. I am grateful to my Mum, who is always there to catch me out with a surprise question about an obscure topic from the corner of physics. I am grateful to the rest of my family, more accurately described as a horde. It would take too long to thank them all, so I give my thanks the Jones Hive Mind! I thank all my Hastings and Portway friends for their support, without you my thesis would have been completed six months faster, and to a standard twice as high.

I thank my wonderful wife Anne, who has supported me throughout this journey more than anyone else, unjealously humouring my passion for physics, even through my affair with SUSY...

And finally, with a quote, I give a nod to Oliver and Clemens, who helped to kindle my love of physics with discussions about chaos theory, quantum mechanics and special relativity during R.E. classes at secondary school: *"the drummer from Def Leppard only has one arm..."*

Contents

List of Tables

List of Figures

1 Introduction

The Standard Model of particle physics is a theoretical framework for describing fundamental particles and their interactions. It is a remarkably successful theory, compatible with decades of collider data. In the Standard Model, W and Z bosons acquire mass through the Higgs mechanism, which predicts the existence of a scalar boson. The discovery and measurement of a Standard Model Higgs by ATLAS and CMS at the Large Hadron Collider completes the Standard Model. The Standard Model in its current form cannot account for a number of important observations. For example, it provides no candidate for dark matter and no mechanism that can explain electroweak baryogenesis. Another shortcoming of the Standard Model is the apparent instability of the Higgs mass to the large variations of scales associated to the fundamental interactions, which requires fine tuning of parameters to reproduce its measured value, the so-called Hierarchy problem. Many extensions to the Standard Model have been proposed to address these limitations.

Central to the Standard Model is the notion of symmetries. Symmetries have long been associated with aesthetics and can simplify seemingly complex systems. It was Emmy Noether who first demonstrated the deep connection between symmetries and conservation laws in nature, and the relativistic fields described by the Standard Model are representations of the Poincaré symmetry group. The force mediators of the Standard Model, which describe the fundamental interactions, arise from local gauge symmetries. Supersymmetry is an extension to the Standard Model that posits an additional symmetry of nature between fermions and bosons, introducing a bosonic partner for each fermion, and vice versa. Miraculously, the consequences of assuming such a symmetry can address many of the limitations of the Standard Model. Supersymmetry can provide a candidate for dark matter, a mechanism for electroweak baryogenesis and stabilise the Higgs mass. Together with its theoretical appeal, this provides strong motivation for Supersymmetry searches at the Large Hadron Collider.

The ability of Supersymmetry to address the limitations of the Standard Model depends on the masses of Supersymmetric particles. In particular, for Supersymmetry to stabilise the Higgs mass without reintroducing the need for fine tuning, Supersymmetric particles should be below 1 TeV, accessible to the Large Hadron Collider. At the time of writing, Supersymmetry is conspicuous by its absence, with no search to date finding significant evidence for any Supersymmetric model. The ATLAS and CMS Supersymmetry search program comprises dozens of individual searches targeting simplified models, and each null result provides exclusion coverage for part of the Supersymmetry parameter space. This thesis presents a search for Supersymmetry in final states with missing transverse energy and jets from charm quarks using 36.1 fb^{-1} of data collected by ATLAS in 2015 and 2016. This search provides additional coverage in the search for discovery, or eventual exclusion, of Supersymmetry as a solution to the Hierarchy problem.

At the time of writing, Run 2 of the Large Hadron Collider has ended. With data taking on hold for at least two years, it becomes crucial not only to improve the particle identification capabilities of the ATLAS detector in preparation for Run 3, but also to extend the reach of ATLAS searches in existing data. One important

limitation of particle reconstruction at ATLAS is the loss of low momentum b-hadrons, which are present in the experimental signature of many interesting models of Supersymmetry. This thesis presents a new algorithm that allows these low momentum b-hadrons, previously beyond the reach of the ATLAS detector, to be recovered, extending the sensitivity of ATLAS Supersymmetry searches.

The work of this thesis was conducted as part of the ATLAS collaboration. The data collected by the ATLAS detector must be processed, reconstructed and simulated for interpretation. This involves hundreds of auxiliary measurements and studies, a highly collaborative effort involving thousands of physicists. The author of this thesis contributed significantly to the ongoing calibration of the ATLAS electron trigger from 2015-2017, the results of which are used by analyses throughout ATLAS, including those documented in this thesis. This work is reported in a dedicated appendix.

The analyses presented in this thesis build on years of previous work, and were carried out by teams of researchers. In such a collaborative environment it can be difficult to distinguish the contribution of an individual from the organisation as a whole. In some cases the boundaries between contributions may not be easy to define, for example calibration results that are used by hundreds of analyses that use ATLAS data. A list of publications to which the author of this document played a central role, along with the key contributions to each, is given below:

- *Search for supersymmetry in final states with charm jets and missing transverse momentum in 13 TeV pp collisions with the ATLAS detector* [1], the subject of chapter 5.

  - This analysis was conducted by a small research team within the ATLAS SUSY working group. The author of this thesis was one of two PhD students working in the team, contributing to most aspects of the analysis. These contributions include: signal region development, background estimation (particularly relating to the one-lepton and multijet backgrounds), optimisation of charm tagging operating points and the derivation of associated efficiencies and systematic uncertainties and the evaluation of the final results.

- *Soft b-hadron tagging for compressed SUSY scenarios* [2], the subject of chapter 6.

  - The above publication describes three techniques for the identification of soft b-hadrons with the ATLAS detector. Chapter 6 focuses almost entirely on the development of one of these techniques: the reconstruction of b-hadrons by reconstructing their decay vertices in clusters of tracks. This analysis is the author's own work.

- *Electron reconstruction and identification in the ATLAS experiment using the 2015 and 2016 LHC proton-proton collision data at* $\sqrt{s} = 13$ *TeV* [3] and *Performance of electron and photon triggers in ATLAS during LHC Run 2* [4], both using the results of appendix A.

  - These publications document electron trigger efficiency of the ATLAS detector in Run 2 of the LHC. The author of this thesis provided the

official electron trigger efficiency measurements used by ATLAS for all of 2016 and 2017 data taking, and continued to contribute in 2018 in a more supervisory capacity.

This thesis is structured as follows: chapter 2 presents an overview of the Standard Model, highlighting some of its important limitations, and introduces Supersymmetry and its current status. Chapter 3 describes the Large Hadron Collider and the ATLAS detector, with attention given to each of its main subsystems, including the hardware of the trigger system. Chapter 4 gives details for data acquisition, processing and reconstruction, including details of the Monte Carlo simulations that are essential for interpreting the data. Chapter 5 presents a search for Supersymmetry in final states with missing transverse energy and jets from charm quarks, and chapter 6 presents a new algorithm for the identification of low momentum b-hadrons at ATLAS. The electron trigger calibration work and additional analysis details are given in the appendices.

2 | Theoretical Background

The experimental searches detailed in this thesis concern supersymmetry (SUSY) and the Standard Model (SM). This chapter develops the theoretical background necessary to set these searches in context. Section 2.1 describes the SM and section 2.2 its limitations. Section 2.3 introduces SUSY and its phenomenology at the LHC, focusing on the SUSY models considered by the analyses presented in this thesis. Finally, section 2.3.6 expands the scope, discussing more general SUSY models and the wider SUSY search effort, and presents some of the current limits on SUSY parameters.

2.1 The Standard Model

The Standard Model of particle physics is a quantum field theory that successfully accounts for three of the four fundamental forces of nature. The fourth, gravity, is too weak to play a significant role at energies accessible to modern particle physics experiments. Particle physics processes are described in terms of spin $\frac{1}{2}$ fermionic fields interacting through bosonic mediator fields with integer spin. Developed in the 1970s, the SM is the culmination of more than seven decades of experimental and theoretical discovery. This section provides a brief discussion of some the key ingredients in the development of the SM and a summary of the SM itself.

2.1.1 Quantum Field Theories

The SM is a *quantum field theory* [5, 6]. Quantum field theory (QFT) is a theoretical framework that incorporates quantum mechanics and special relativity. This is achieved through a procedure of quantisation of relativistic fields, with particles understood as excitations of these fields.

The language of QFT is the Lagrangian formalism, where the dynamics of a system are summarised by the Lagrangian density $\mathcal{L}(\phi, \partial\phi)$, a function that depends on relativistic fields and their derivatives. The equations of motion of a system are derived by minimising the action $\mathcal{S}$:

$$\mathcal{S} = \int d^4x \mathcal{L}. \tag{2.1}$$

The S-matrix element for a scattering process is computed in the interaction picture, where the Lagrangian density is split into two components:

$$\mathcal{L} = \mathcal{L}_{\text{free}} + \mathcal{L}_{\text{int}}, \tag{2.2}$$

where $\mathcal{L}_{\text{free}}$ describes free fields and $\mathcal{L}_{\text{int}}$ the interactions between these fields. The S-matrix can be represented as a perturbative expansion in powers of $\mathcal{L}_{\text{int}}$. Once the S-matrix has been determined, it can be used to make predictions about observable quantities, for example cross-sections and decay rates.

Terms in the perturbative expansion can be represented diagrammatically using Feynman diagrams, composed of vertices, lines and propagators, each representing a factor in the final expression for the S-matrix . To first order the S-matrix is simply the sum of the first order *tree level* Feynman diagrams. Higher order diagrams contain *loop* corrections which typically contribute divergent integrals to the expression for the S-matrix. A set of prescriptions exists to treat such divergences, collectively known as *renormalisation*.

Renormalisation proceeds by splitting the Lagrangian into infinite and finite pieces:

$$\mathcal{L} = [\mathcal{L} - \delta\mathcal{L}(E)] + \delta\mathcal{L}(E), \tag{2.3}$$

where the energy E is some cutoff scale, and $\delta\mathcal{L}$ is the measurable part of the Lagrangian. $\delta\mathcal{L}$ is constrained such that the measurable quantities, for example the coupling constants and particle masses, do not depend on the cutoff energy. This restriction gives rise to the renormalisation group equations (RGEs), which describe how the coupling constants of the fundamental forces run with energy. For a QFT to be predictive, it must be renormalisable. Any physically descriptive QFT must therefore include only renormalisable terms in the Lagrangian.

2.1.2 Symmetries in Particles Physics

A field theory is said to possess a symmetry if a transformation leaves the action $\mathcal{S}$ of the theory unchanged. Noether's theorem [7] states that for any continuous symmetry of $\mathcal{S}$ a corresponding conserved current can be derived. For example, the Noether current associated to the invariance of the action $\mathcal{S}$ under space and time translations gives rise to momentum and energy conservation, respectively. Noether's theorem demonstrates how the symmetries displayed by the Lagrangian reveal important information about the behaviour of a theory.

Central to QFTs is the Poincaré symmetry group, which describes translations, rotations and boosts in Minkowski space. A causal theory is constructed by requiring that the action S be invariant under Poincaré transformations:

$$x_\mu \to x'_\mu = \Lambda^\nu_\mu x_\nu + a_\mu, \tag{2.4}$$

where the Λ is a general Lorentz transformation and a is an additional translation in spacetime coordinates. Any relativistic field is a representation of the Poincaré group. QFTs are the result of quantisation of these fields.

The SM is a *gauge theory*, constructed by imposing invariance under a set of gauge transformations. A gauge transformation is a continuous set of local transformations, forming a Lie group, which can be represented through a basis of linear transformations. The independence of the chosen gauge in a theory represents redundant degrees of freedom in the Lagrangian. To ensure invariance of the Lagrangian under a gauge transformation, a corresponding gauge covariant derivative is defined, introducing additional gauge fields in the Lagrangian. These gauge fields relate the symmetry transformations at different points in spacetime, and are realised as force mediators. The strong, electromagnetic (EM) and weak interactions can be associated to specific gauge groups.

The basic recipe for constructing the SM is then to assume a set of fermion spinor fields to correspond to the known fundamental particles of matter, assume a set of gauge symmetries that can account for the fundamental interactions, and then write down the most general, renormalisable Lagrangian.

2.1.3 The Electroweak Interaction

The EM and weak interactions are unified in the SM according to the Glashow-Salam-Weinberg mechanism [8, 9]. Below the electroweak scale, $\mathcal{O}(246)$ GeV, they split into the familiar EM and weak interactions through the mechanism of electroweak symmetry breaking (section 2.1.4).

Electroweak theory is described by the gauge group $SU(2)_L \times U(1)_Y$ acting on fermionic spinor fields, which can be represented in terms of left- and right-handed chiral projections:

$$\psi = \psi_L + \psi_R = \frac{1}{2}(1-\gamma^5)\psi + \frac{1}{2}(1+\gamma^5)\psi, \tag{2.5}$$

where γ^5 is the fifth gamma matrix (definitions for the five gamma matrices are given in Refs. [5, 6]) . In the theory, left-handed fermions form doublets under $SU(2)_L$ and right-handed fermions form $SU(2)_L$ singlets. As a result, the weak interaction couples only to left-handed chiral fields; this property is denoted by the subscript L. The chirality of the weak interaction is not an emergent property of the gauge symmetry, but necessary to account for experimental evidence of maximal parity violation in weak interactions [10]. The Y subscript in $U(1)_Y$ denotes the weak hypercharge which relates the unified electroweak interaction to electromagnetism (see equation 2.10, later in this section).

Invariance of the Lagrangian under $SU(2)_L \times U(1)_Y$ can be enforced by introducing the covariant derivative

$$\partial_\mu \rightarrow D_\mu = \partial_\mu + igW_\mu^a t^a + ig'B_\mu Y, \tag{2.6}$$

where a runs over $1, 2, 3$ and g, g' are coupling constants. The three gauge fields W_μ^a are associated to $SU(2)_L$ and B_μ to $U(1)_Y$. Fermion and scalar fields are assigned weak isospin $I = 0, \frac{1}{2}$ and weak hypercharge Y quantum numbers. The t^a are defined

$$t^a = \begin{cases} 0 & \text{for} \quad I = 0, \\ \sigma^a & \text{for} \quad I = \frac{1}{2}, \end{cases} \tag{2.7}$$

where $I = \frac{1}{2}$, 0 for fermions with left- and right-handed chirality, respectively. The gauge fields for charged currents arise as a linear combination of $SU(2)_L$ eigenstates:

$$W_\mu^\pm = \frac{W_\mu^1 \mp iW_\mu^2}{\sqrt{2}}. \tag{2.8}$$

The physical neutral fields are obtained through the mixing of $SU(2)_L$ and $U(1)_Y$:

$$\begin{pmatrix} Z_\mu \\ A_\mu \end{pmatrix} = \begin{pmatrix} \cos\theta_W & -\sin\theta_W \\ \sin\theta_W & \cos\theta_W \end{pmatrix} \begin{pmatrix} W_\mu^3 \\ B_\mu \end{pmatrix}, \tag{2.9}$$

where θ_W is the Weinberg angle. θ_W is an important parameter of the SM, relating neutral and charged currents, and was first measured in 1973 [11]. EM charge is related to the weak isospin and hypercharge quantum numbers through the Gell-Mann-Nishijima relation [12, 13], given by

$$Q = T_3 + \frac{Y}{2}, \tag{2.10}$$

where T_3 is the third component of weak isospin, which can take on the values $-\frac{1}{2}, 0, \frac{1}{2}$.

The particle content of the SM can be organised into three generations of $SU(2)_L$ weak isospin doublets:

$$\begin{pmatrix}\nu_e\\ e\end{pmatrix}_L \begin{pmatrix}\nu_\mu\\ \mu\end{pmatrix}_L \begin{pmatrix}\nu_\tau\\ \tau\end{pmatrix}_L, \begin{pmatrix}u\\ d\end{pmatrix}_L \begin{pmatrix}c\\ s\end{pmatrix}_L \begin{pmatrix}t\\ b\end{pmatrix}_L \tag{2.11}$$

and corresponding right-handed singlets. The components of the doublets correspond to the familiar flavour pairs, assigning a neutrino to each lepton and pairing quarks into "up" and "down" types. In the SM, neutrinos are assumed to be massless. Since neutrinos only interact via the weak interaction, right-handed neutrinos are omitted from the SM. The $W^\pm$ gauge field transforms between isospin doublet states, giving rise to flavour changing charged currents. The Z^0 field does not transform between isospin states and as a result flavour changing neutral currents (FCNCs) are not predicted at tree level in the SM. The fermions and their corresponding electroweak quantum numbers are summarised in table 2.1.

Leptons	T_3	Y	$Q = T_3 + \frac{Y}{2}$	Quarks	T_3	Y	$Q = T_3 + \frac{Y}{2}$
ν_L^e, ν_L^μ, ν_L^τ	$+\frac{1}{2}$	-1	0	u_L, c_L, t_L	$+\frac{1}{2}$	$+\frac{1}{3}$	$+\frac{2}{3}$
e_L, μ_L, τ_L	$-\frac{1}{2}$	-1	-1	d_L, s_L, b_L	$-\frac{1}{2}$	$+\frac{1}{3}$	$-\frac{1}{3}$
e_R, μ_R, τ_R	0	-2	-1	u_R, c_R, t_R	0	$+\frac{4}{3}$	$+\frac{2}{3}$
				d_R, s_R, b_R	0	$-\frac{2}{3}$	$-\frac{1}{3}$

Table 2.1: Summary of the particle content of the electroweak theory.

2.1.4 Electroweak Symmetry Breaking and The Higgs Mechanism

The electroweak theory described so far includes only massless gauge fields for the weak interaction. This is inconsistent with the physical weak interaction, which is known to be short range. Simply adding mass terms to the Lagrangian spoils gauge invariance under $SU(2)_L \times U(1)_Y$, a fundamental assumption of the theory. This difficulty is circumvented through the Higgs mechanism [14–16].

The Higgs mechanism proceeds by introducing the most general scalar potential permitted under the restrictions of $SU(2)_L$ invariance and renormalisability:

$$V(\Phi) = \mu^2 \Phi^\dagger \Phi + \lambda (\Phi^\dagger \Phi)^2, \tag{2.12}$$

where Φ is complex scalar doublet under $SU(2)_L$, given by

$$\Phi = \begin{pmatrix}\phi^+\\ \phi^0\end{pmatrix} = \frac{1}{\sqrt{2}} \begin{pmatrix}\phi_1 + i\phi_2\\ \phi_3 + i\phi_4\end{pmatrix}, \tag{2.13}$$

and where μ and $\lambda > 0$ are additional parameters. The doublet Φ is identified as the Higgs field. For the case $\mu^2 < 0$, $V(\Phi)$ describes a potential with a local maximum at $\Phi = 0$ surrounded by minima in the region defined by $\Phi = \sqrt{\frac{-\mu^2}{\lambda}} \equiv v$

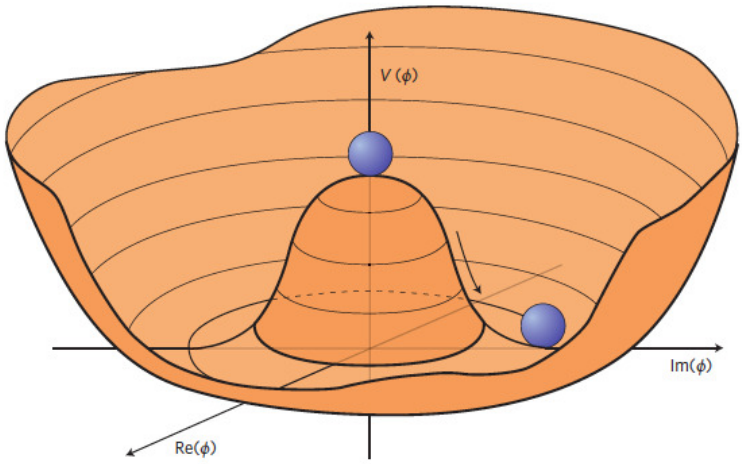

Figure 2.1: Illustration of the Higgs potential for the case $\mu^2 < 0$ [17]. The minima at $|\phi|^2 = \frac{\mu^2}{2\lambda}$ define the vacuum. This potential preserves $SU(2)_L$ symmetry, but it is spontaneously broken when the field ϕ is forced to take on a vacuum state.

(see figure 2.1). The underlying $SU(2)$ symmetry of the Lagrangian is preserved, but the field picks up a vacuum expectation value (VEV) v, *spontaneously* breaking the symmetry. The addition of the scalar doublet contributes the following to the Lagrangian

$$\mathcal{L}_\Phi = (D^\mu \Phi)^\dagger (D_\mu \Phi) - V(\Phi), \tag{2.14}$$

where D_μ is the $SU(2)_L$ covariant derivative (equation 2.6). To spontaneously break $SU(2)_L$, one must choose a minimum around which to develop Φ. It is convenient to choose

$$\Phi = \frac{1}{\sqrt{2}} \begin{pmatrix} 0 \\ v + h \end{pmatrix}, \tag{2.15}$$

where h is a small perturbation to the scalar field. Expanding around the chosen minimum introduces mass terms into the Lagrangian, from which the gauge field masses can be identified as:

$$M_W^2 = \frac{1}{4} g^2 v^2, \quad M_Z^2 = \frac{1}{4}(g^2 + g'^2)v^2, \quad M_A = 0. \tag{2.16}$$

Thus the Higgs mechanism confers mass to the weak gauge bosons whilst maintaining $SU(2)_L$ invariance, through the process of electroweak symmetry breaking (EWSB).

The Higgs field can also be used to generate mass for fermion fields. A fermionic mass term takes the form

$$\mathcal{L}_{mass} = -m\bar{\psi}\psi = -m(\bar{\psi}_L \psi_R + \bar{\psi}_R \psi_L). \tag{2.17}$$

The left- and right-handed spinor fields transform differently under $SU(2)_L$ so that the addition of such a term is not permitted by the theory. Instead one can consider the Yukawa coupling of the Higgs field to a fermion:

$$\mathcal{L}_f = -\lambda_d \bar{Q}_L \Phi d_R + \text{higher terms} \tag{2.18}$$

with the left-handed fermion doublet

$$Q = \begin{pmatrix} f_u \\ f_d \end{pmatrix}_L. \tag{2.19}$$

Mass terms are introduced by once again making use of the expansion from equation 2.15 to yield the effective coupling

$$\lambda_d \frac{1}{\sqrt{2}}(\bar{u}_L, \bar{d}_L) \begin{pmatrix} 0 \\ v+h \end{pmatrix} d_R + \text{higher terms.} \tag{2.20}$$

The factor

$$m_d = \frac{\lambda_d v}{\sqrt{2}} \tag{2.21}$$

can be identified as the mass of the down-type fermion. The mass term for the up-type fermion is generated in a similar way by exploiting the charge-conjugate to the Higgs field $\Phi^c \equiv -i\sigma_2\Phi^*$ to transform the up-flavour component of the fermion doublet.

In the case of quarks, the additional Yukawa couplings introduce mass matrices corresponding to up and down types. These matrices are diagonalised by different transformations, which results in a modification of the charged current interaction that relates the components of the $SU(2)_L$ doublet. The modification of the weak interaction is summarised by the Cabibbo-Kobayashi-Maskawa (CKM) matrix [18, 19] which mixes the weak flavour eigenstates. The CKM mixing introduces a phase shift, which behaves differently for particles and antiparticles, a source of CP violation in the SM.

Inserting the expansion from equation 2.15 into $\mathcal{L}_\Phi$ (equation 2.14), one identifies the pure Higgs Lagrangian

$$\mathcal{L}_h = \frac{1}{2}(\partial^\mu h)^2 - \frac{2\lambda v^2}{2}h^2 - \lambda v h^3 - \frac{\lambda}{4}h^4 + \frac{\lambda v^4}{4}, \tag{2.22}$$

where the expression for the VEV has been used to make the substitution $\mu^2 = -v^2\lambda$. Equation 2.22 contains a kinetic term, resulting from the coupling of the Higgs field to the gauge covariant derivative, cubic and quartic self-interactions and a mass term, from which the Higgs mass

$$M_h = 2\lambda v^2 \tag{2.23}$$

can be identified. Thus the Higgs mechanism is verifiable, predicting a new scalar, the Higgs boson. The λ parameter is a free parameter of the theory, and must be experimentally determined.

The observation of a Higgs-like particle with a mass of 125 GeV at the LHC was announced by ATLAS and CMS in 2012 [20, 21]. A Higgs, with couplings as predicted by the SM, has been observed in many different channels since (see figure 2.2), a major success for the SM.

2.1.5 The Strong Interaction

Quantum Chromodynamics (QCD) is the theory of the strong force, describing the interactions of quarks and gluons. It is derived in analogy with the electroweak interaction, instead requiring gauge invariance under the unbroken $SU(3)_C$ symmetry group. The subscript C indicates *colour* charge, which can take three values labelled as *red*, *green* and *blue*. Quarks can be represented by

$$\begin{pmatrix} \psi_R \\ \psi_B \\ \psi_G \end{pmatrix}, \tag{2.24}$$

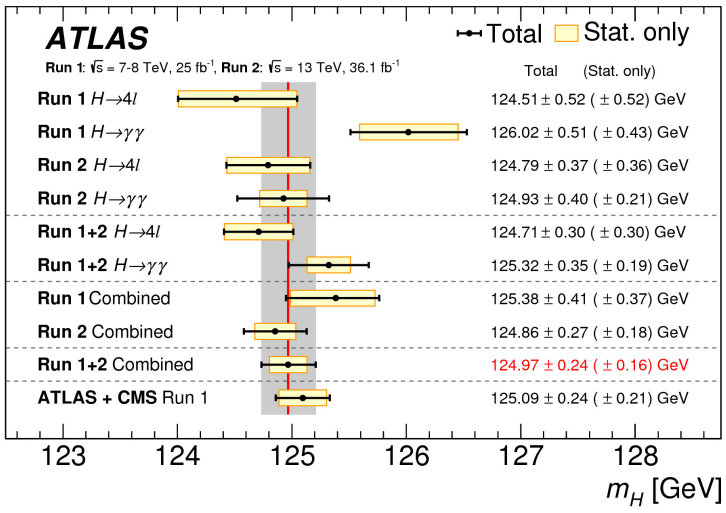

(a)

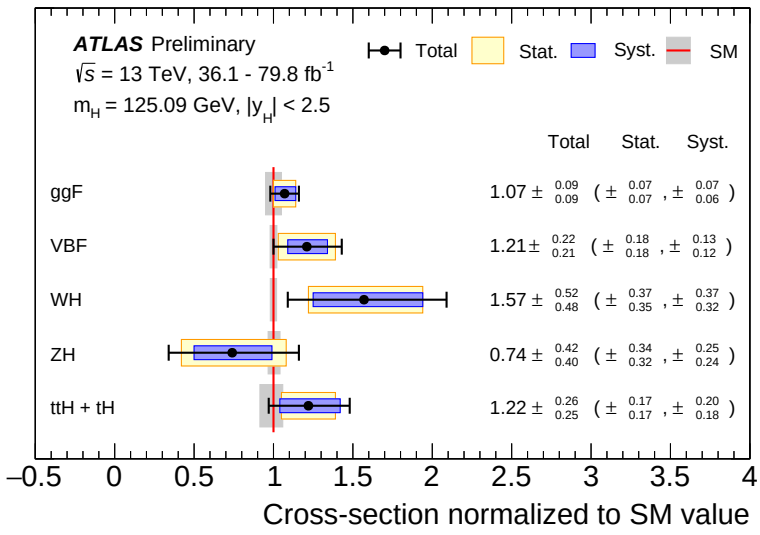

(b)

Figure 2.2: (a) Summary of the Higgs boson mass measurements from the individual and combined analyses [22], compared with the combined Run 1 measurement by ATLAS and CMS [23]. The statistical-only (horizontal yellow-shaded bands) and total (black error bars) uncertainties are indicated. The (red) vertical line and corresponding (grey) shaded column indicate the central value and the total uncertainty of the combined ATLAS Run 1 + 2 measurement, respectively. (b) Higgs cross-sections, normalised to their SM predictions and with SM branching fractions assumed. The black error bars, blue boxes and yellow boxes show the total, systematic, and statistical uncertainties in the measurements, respectively. The grey bands indicate the theory uncertainties in the cross-section predictions. Taken from Ref. [24].

$SU(3)_C$ colour triplets.

The $SU(3)_C$ gauge covariant derivative is given by

$$\partial^\mu \rightarrow D^\mu = \partial^\mu + ig_s G_a^\mu T^a, \tag{2.25}$$

where g_s is the coupling constant. The T^a, $a = 1, 2.., 8$ are the Gell-Mann matrices, an extension of the Pauli matrices to $SU(3)_C$. The G_a^μ are the gauge fields associated to the strong interaction. $SU(3)_C$ is a non-Abelian group, and the G_a^μ are non-commutative. As a result the corresponding field strength tensor takes the form

$$G_{\mu\nu}^a = \partial_\mu G_\nu^a - \partial_\nu G_\mu^a - g_s f_{bc}^a G_\mu^b G_\nu^c \tag{2.26}$$

resembling the $F_{\mu\nu}$ from electromagnetism, with an additional term added to maintain gauge invariance. The f_{abc} are *structure constants* associated with the gauge group. The additional term in the field strength describes self-interacting gluons.

This self-interaction results in a strong dependence of the coupling constant on the energy transfer of the interaction Q^2. Using the parameterisation $\alpha_s = \frac{g_s^2}{4\pi}$, to first-order, this dependence takes the form [5]

$$\alpha_s(Q^2) = \frac{\alpha_s}{1 + [(11 - \frac{2}{3}n_f)\frac{\alpha_s}{2\pi}] \ln(Q^2/M^2)}. \tag{2.27}$$

This expression uses the initial condition $\alpha_s = \alpha_s(M^2)$ where M^2 is some renormalisation scale. n_f is the number of approximately massless quarks at the scale Q^2 such that $m_q \ll Q$.

In the SM case $11 - \frac{2}{3}n_f > 0$. The form of $\alpha_s(Q^2)$ suggests that the coupling increases with distance. The result is colour confinement; only colour neutral singlet states, baryons and mesons, are stable in QCD. At large separations, the potential energy between coloured particles increases to the point that it is energetically favourable to create colour neutral singlet states from the vacuum. This causes the quark to fragment and produce a *jet* of particles, a phenomenon known as hadronisation. At high energies, $\alpha_s(Q^2)$ decreases such that as $Q^2 \rightarrow \infty$, $\alpha_s(Q^2) \rightarrow 0$. This property of QCD is known as asymptotic freedom.

2.1.6 Summary of the Standard Model

Together the strong and electroweak interactions make up the SM. Formally, the SM is the gauge theory formed from the $SU(3)_C \times SU(2)_L \times U(1)_Y$ gauge symmetry. The QCD sector, the electroweak sector and the Higgs mechanism together account for all of the interactions that are relevant in particle physics experiments. With the addition of the lepton and quark fields, the SM provides a complete theoretical apparatus for making phenomenological predictions for collider experiments.

The SM contains 19 parameters that are not predicted by the theory: 9 fermion masses (assuming massless neutrinos), 3 coupling constants, 1 Higgs VEV, 1 Higgs mass, 3 angles and 1 phase from CKM mixing and 1 strong CP parameter, which quantifies the degree to which strong interactions violate CP symmetry. All of these parameters have now been experimentally measured and are summarised in Ref. [25]. Evidence of neutrino oscillations [26] implies that neutrinos are massive, which would require the addition of 3 neutrino masses and 4 mixing parameters to bring the total to 25. An overview of the experimental properties of the particles of the SM is given in table 2.2.

	Name	Mass	Charge (e)		Name	Mass	Charge (e)
Quarks spin $= \frac{1}{2}$	u	2.2 MeV	$+\frac{2}{3}$	Leptons spin $= \frac{1}{2}$	ν_e	< 2 eV	0
	d	4.7 MeV	$-\frac{1}{3}$		e	0.511 MeV	-1
	c	1.28 GeV	$+\frac{2}{3}$		ν_μ	< 0.19 MeV	0
	s	96 MeV	$-\frac{1}{3}$		μ	106 MeV	-1
	t	173.1 GeV	$+\frac{2}{3}$		ν_τ	< 18.2 MeV	0
	b	4.18 MeV	$-\frac{1}{3}$		τ	1.78 GeV	-1

	Name	Mass	Charge (e)
Gauge Bosons spin $= 1$	gluon, g	0	0
	photon, γ	0	0
	W boson	80.385 GeV	± 1
	Z boson	91.1876 GeV	0
Scalar spin $= 0$	Higgs boson, H	125.18	0

Table 2.2: Summary of the particle content of the SM. All values taken from Ref. [25].

2.2 Limitations of the Standard Model

The SM provides a description of the electroweak and QCD sectors and makes verifiable predictions about scattering processes. These predictions have been extensively verified over the years with no significant deviation from the SM observed in decades of particle physics experiments. Despite this success, the SM is known to be incomplete. It fails to account for, and sometimes is in direct tension with, experimental evidence, in particular astronomy and neutrino experiments. There are also unanswered questions about the *naturalness* of the SM, the apparent need to "fine tune" parameters to explain observed phenomena.

This section will discuss of some of the main theoretical limitations of the SM that may potentially be addressed by SUSY [27–32]: the origin of matter/antimatter asymmetry, the Gauge Hierarchy Problem and the origin of dark matter. These open questions are by no means exhaustive, the scope of this section is restricted to the issues most germane to the SUSY searches described in this thesis.

- **Electroweak Baryogenesis:** The problem of electroweak baryogenesis concerns the overwhelming excess of matter over antimatter in the Universe. The Sakharov conditions [33] state the requirements for excess baryogenesis to occur:

  1. At least one baryon number violating process.
  2. CP violation.
  3. Interactions outside of equilibrium.

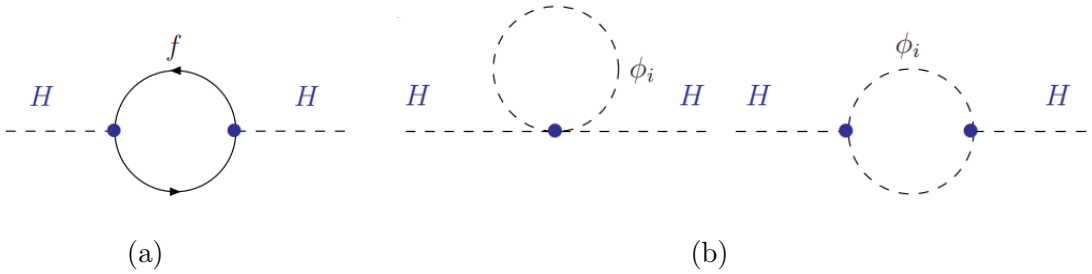

Figure 2.3: (a) Loop corrections to the Higgs mass from fermions and (b) trilinear and quadrilinear scalars [40].

A successful description of baryogenesis must satisfy these conditions sufficiently to reproduce the observed excess baryon to photon ratio [34]:

$$\eta = \frac{n_B - \bar{n}_B}{\gamma} = 6 \times 10^{-10} \frac{\text{excess baryons}}{\text{photons}}. \tag{2.28}$$

All of the above ingredients are present in the SM. Condition (1) is satisfied in the SM through quantum effects associated with the weak interaction [35]. Condition (2) arises from CKM mixing and condition (3) can be satisfied through electroweak phase transitions. However experimental values for CKM mixing and the measured Higgs mass suggest that conditions (2) and (3) are not satisfied to a sufficient degree to account for the observed value of η. This suggests that physics beyond the SM is required to explain baryogenesis. SUSY theories can provide new sources of CP violation and additional Higgs fields to modify electroweak phase transitions in order to explain baryogenesis [36].

- **The Gauge Hierarchy Problem:** Each of the fundamental interactions in the SM possesses a characteristic energy scale: ~ 200 MeV for the QCD sector and ~ 246 GeV for the electroweak sector, corresponding to the Higgs field VEV. The characteristic energy for gravity is believed to be the Planck scale [37], $M_{\text{Planck}} \sim 10^{19}$ GeV. This large variation forms a *hierarchy* of energy scales.

  The Gauge Hierarchy problem [38] concerns the instability of the Higgs mass M_H to this hierarchy of scales. The Higgs mass receives the quadratically divergent one-loop quantum correction [39]

  $$\delta M_H^2 = f(g)\Lambda_{\text{UV}}^2, \tag{2.29}$$

  where $f(g)$ is a known function of coupling constants. The parameter Λ_{UV} is an ultra-violet cutoff representing some scale at which the SM is no longer valid. A natural choice for Λ_{UV} would be M_{Planck}, where the effects of gravity will become important. The quantum corrections of equation 2.29 for such a choice lead to a predicted Higgs mass some 30 orders of magnitude larger than the observed value, unless the parameters of the theory are fine tuned to an accuracy of 10^{-30} in each order of the perturbative expansion. The appearance of the Higgs boson with such an unlikely mass, without some underlying mechanism to explain the cancellations, seems *unnatural*.

One possible mechanism for introducing the cancellations needed to tame the Higgs mass can be illustrated by considering the fermionic and scalar loop corrections shown in figure 2.3. The total fermionic and scalar contributions to M_H are both quadratically divergent, so that if some relationship is assumed relating these fields and their coupling to the Higgs field, the net correction cancels. The degree of cancellation depends on the relative mass of the fermion and the scalar; if the masses are equal, the correction vanishes. Thus by assuming an additional symmetry relating fermions to scalars, the need for fine tuning the Higgs mass to stabilise it against loop corrections from fermions is eliminated. This mechanism is a natural result of SUSY.

- **Dark Matter:** It has long been known [41] that luminous matter alone cannot account for the observed rotation of galaxies. From simple Newtonian dynamics, one would expect the rotational speed $v(r)$ to approximately obey

$$v(r) = \sqrt{\frac{GM(r)}{r}}, \tag{2.30}$$

where G is the gravitational constant, r is the radial distance from the galactic centre, and $M(r)$ satisfies

$$M(r) = 4\pi \int \rho(r) r^2 dr \tag{2.31}$$

with $\rho(r)$ the density profile, which is assumed to depend only on r. Thus one would naively expect to see the rotational speed fall off as $1/\sqrt{r}$ outside the galactic radius. Instead, the speed is observed to fall more slowly, or even remain roughly constant, outside the galactic radius (see the rotation curves shown in figure 2.4). This effect can be explained by the presence of a halo of non-luminous, gravitating *dark matter* surrounding the galaxy.

Additional evidence for the existence of dark matter comes from gravitational lensing [43], where the light from a distant galaxy is distorted by an intervening massive object, due to the spacetime curvature effects of general relativity. As a result the galaxy appears in the form of duplicated "arclets" in close proximity, with similar redshift and spectra. The angular radius of these arclets is given by the Einstein radius θ_E [41]:

$$\theta_E = \sqrt{\frac{4GM}{c^2}\frac{d_{LS}}{d_L d_S}}, \tag{2.32}$$

where the G is the gravitational constant, M is the mass of the gravitational lens, c is the speed of light and d_{LS}, d_L and d_S are the distance between the lens and the source, the distance to the lens, and the distance to the source, respectively. Thus equation 2.32 can be used to determine the mass of the source. The luminosity of such sources is found to be insufficient to explain their masses, another indicator for the presence of dark matter.

There is strong evidence to suggest that dark matter cannot be accounted for in the SM. One source of evidence is the apparent lack of baryonic dark matter candidates, classified as MACHOs (MAssive Compact Halo Objects) [44, 45]. Arguments based on Big Bang Nucleosynthesis (BBN) and the observed ratio

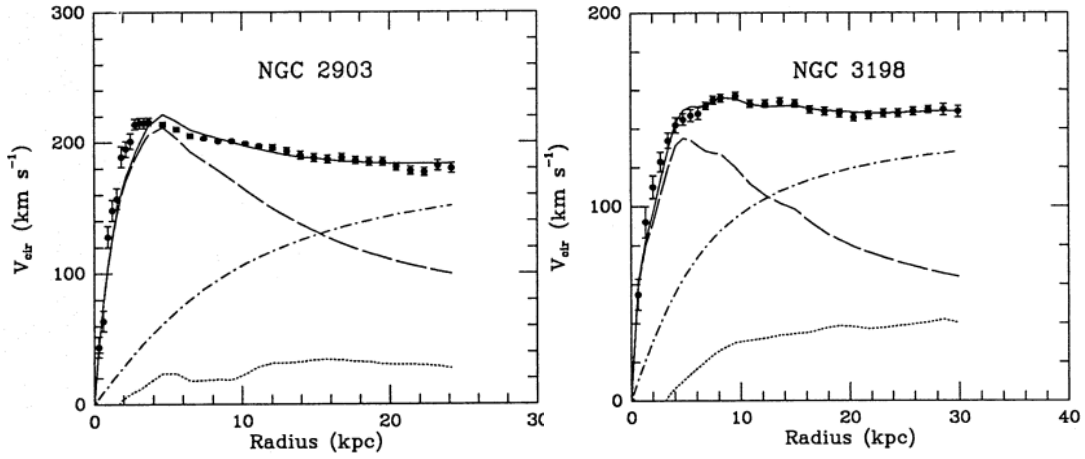

(a) (b)

Figure 2.4: Evidence for dark matter from galactic rotation curves for galaxies (a) NGC2903 and (b) NGC3198. The solid curve shows a three-parameter fit to the data points, with the fitting parameters shown with dashed, dotted and dash-dot curves for the visible, gas and dark-halo components, respectively. Made using observation data of the Doppler shifted 21-cm absorption line of neutral hydrogen. Image taken from Ref. [42].

of deuterium and hydrogen [46] in the Universe suggest that the overall baryon abundance can only account for $\sim 20\%$ of the total matter density of the Universe. This figure is supported by estimates based on anisotropies from the Cosmic Microwave Background (CMB), measured by the Wilkinson Microwave Anisotropy Probe (WMAP) [34].

Dark matter could be explained by the existence of a stable weakly interacting massive particle (WIMP). In the early Universe, WIMPs would have been in a high-energy thermal equilibrium with SM particles. As the Universe expanded and cooled, the WIMPs would eventually "freeze" out of the thermal equilibrium after the temperature fell below the threshold for WIMP pair production. The relic abundance of WIMPs Ω_χ is given by [25]:

$$\Omega_\chi h^2 \simeq \text{const} \cdot \frac{T_0^3}{M_{\text{Planck}}^3 \langle \sigma_A v \rangle} \simeq \frac{0.1\,\text{pb} \cdot c}{\langle \sigma_A v \rangle}, \tag{2.33}$$

where h is Hubble's constant, T_0 is the current CMB temperature, M_{Planck} is the Planck mass, c is the speed of light, σ_A is the annihilation cross-section of the WIMP to SM particles and v is the relative velocity of the WIMPs in their centre-of-mass system. The dark matter relic abundance has been measured by the Planck collaboration [47] to be:

$$\Omega_{\text{DM}}^{\text{obs}} h^2 = 0.1200 \pm 0.0012. \tag{2.34}$$

Based on the above evidence, a WIMP dark matter candidate particle must satisfy the following criteria: it must be stable, sufficiently massive, electrically neutral, weakly interacting and satisfy the relic abundance. SM neutrinos fail to satisfy the second of these criteria. Due to their low mass, neutrinos are relativistic. A Universe rich enough in SM neutrinos to satisfy the entire

dark matter content would have restricted structure formation, in tension with experimental observations [48].

Many generic models of SUSY predict a lightest mass eigenstate which satisfies all of the criteria enumerated above [49, 50].

2.3 Supersymmetry

The SM is a successful theory, built on symmetries (see section 2.1.2). SUSY is an extension to the SM that is aesthetically appealing in the sense that it simply goes *one symmetry further*, by assuming an additional symmetry that relates bosons to fermions, and vice versa. It is striking that by making this assumption, one arrives at a theory that, if observed, could address many of the remaining problems of the SM.

In this section, the basic recipe for obtaining a supersymmetric theory is outlined, along with some of the phenomenological aspects of such a theory in the context of the LHC.

2.3.1 Constructing Supersymmetry

The first step in constructing a supersymmetric theory is to postulate a symmetry operator Q relating fermions and bosons:

$$Q_\alpha \left|\text{boson}\right\rangle = \left|\text{fermion}\right\rangle_\alpha ; \quad Q_\alpha \left|\text{fermion}\right\rangle^\alpha = \left|\text{boson}\right\rangle , \tag{2.35}$$

where α denotes the spinor component of the fermion states. Since the symmetry operator Q transforms between half-integer and integer spin, it must be fermionic. Such operators may be accommodated by extending the coordinate system to include spinor-like coordinates. To construct a relativistic supersymmetric theory the Poincaré algebra is extended to include the new fermionic coordinates. Supersymmetric particle fields, *superfields* emerge as representations under the extended symmetry group.

The supersymmetric particle spectrum is generated by writing down the most general superfield possible and imposing constraints based on the supersymmetric covariant derivative D_α to obtain irreducible representations of the extended Poincaré algebra. Superfields are classified according to their transformation properties under the supersymmetric covariant derivative: *left-handed chiral superfields* (LHχSFs) satisfy the constraint $D_\alpha \phi = 0$ and *vector superfields* (VSFs) satisfy the constraint $D_\alpha V = V^\dagger$. The Hermitian conjugate to a LHχSF is a *right-handed chiral superfield* (RHχSF).

The three fields LHχSF, RHχSF and VSF provide the equipment to describe SUSY particles. Each superfield introduces a set of fields: the LHχSF contains a scalar and fermion fields and the VSF contains a vector boson field and a massless spinor field. Thus each of the particles described by a SUSY model are part of a superdoublet, with each superpartner differing only by spin $\frac{1}{2}$. This is exactly the kind of scheme required to achieve the kind of cancellation needed to solve the hierarchy problem (see section 2.2), which, provided the masses of the superpartners are identical, is exact.

Unfortunately, nature has not deigned to make things so simple. No SUSY particle has yet been observed and therefore equivalent masses for particles and

their superpartners is contradictory to observation. For a supersymmetric model to be physical, SUSY must therefore be a broken symmetry. The contribution to the Higgs mass from a scalar and fermionic supermulitplet can be written [40]:

$$\delta M_H^2 = f(g)[(m_f^2 - m_s^2)\ln\left(\frac{\Lambda_{\mathrm{UV}}}{m_S}\right) + 3m_f^2\ln\left(\frac{m_S}{m_f}\right)] + \mathcal{O}(\frac{1}{\Lambda_{\mathrm{UV}}^2}), \tag{2.36}$$

where $f(g)$ is a function of known coupling constants. Thus the degree to which SUSY is broken determines the degree to which it solves the hierarchy problem, the *naturalness* of the theory.

Broken SUSY requires the addition of SUSY breaking terms to the Lagrangian [51]. To preserve the relationship between SUSY particles and SM particles that brings about the cancellation of quadratic divergences, only *soft* terms (with positive mass dimension) may be added [52]. The Lagrangian is split into soft terms that explicitly violate SUSY and terms that respect SUSY:

$$\mathcal{L} = \mathcal{L}_{\mathrm{SUSY}} + \mathcal{L}_{\mathrm{soft}}. \tag{2.37}$$

The total Lagrangian should be invariant under SUSY transformations, with SUSY broken spontaneously. Since the process by which this occurs is not known, the $\mathcal{L}_{\mathrm{soft}}$ terms must be added. If a SUSY signal were to be observed, the underlying mechanism for spontaneous SUSY breaking could be studied in more detail in context of the specific SUSY model.

2.3.2 The Minimal Supersymmetric Standard Model

The *Minimal Supersymmetric Standard Model* (MSSM) [53–55] is the supersymmetric extension to SM that makes the fewest additional theoretical assumptions possible for a phenomenologically consistent, low-energy, SUSY theory. The MSSM gauge group is $SU(3)_C \times SU(2)_L \times U(1)_Y$ with addition of SUSY transformations. The gauge fields of the SM arise from the VSF associated to this gauge group, each with an associated SUSY partner with spin $\frac{1}{2}$. The vector supermuliplets of the MSSM are summarised in table 2.3.

	spin = 1	spin = $\frac{1}{2}$	$(SU(3)_C, SU(2)_L, U(1)_Y)$
gluons & gluinos	g	$\tilde{g}$	(8,1,0)
W-bosons & winos	$W^{\pm}, W^0$	$\tilde{W}^{\pm}, \tilde{W}^0$	(1,3,0)
B-boson & binos	B	$\tilde{B}$	(1,1,0)

Table 2.3: Summary of the vector supermultiplets of the MSSM, with their quantum numbers. The superpartners of the gauge bosons are denoted with a tilde.

Chiral superfields generate the particle content of the MSSM. The fermions of the SM are part of chiral supermultiplets, each with a scalar superpartner. Three such multiplets are required, with no right-handed neutrinos assumed. The Higgs boson makes up the scalar part of a chiral superfield, with the masses of down-type fermions generated as in the SM. The SM prescription for generating up-type quark

masses (section 2.1.4) cannot be applied in the MSSM since the conjugate Higgs field violates SUSY. Instead, an additional Higgs doublet must be introduced. The chiral supermultiplets of the MSSM is summarised in table 2.4.

	LHχSF	spin $= \frac{1}{2}$	spin $= 0$	$(SU(3)_C, SU(2)_L, U(1)_Y)$
quarks and squarks	Q	(u_L, d_L)	$(\tilde{u}_L, \tilde{d}_L)$	$(3, 2, \frac{1}{6})$
	U	u_R^*	$\tilde{u}_R^*$	$(3, 1, -\frac{2}{3})$
	D	d_R^*	$\tilde{d}_R^*$	$(3, 1, \frac{1}{3})$
leptons and sleptons	L	(ν_L, l_L)	$(\tilde{\nu}_L, \tilde{l}_L)$	$(1, 2, -\frac{1}{2})$
	E	l_R^*	$\tilde{l}_R^*$	$(1, 1, 1)$
Higgs and higgsinos	H_u	$(\tilde{h}_u^+, \tilde{h}_u^0)$	(h_u^+, h_u^0)	$(1, 2, \frac{1}{2})$
	H_d	$(\tilde{h}_d^0, \tilde{h}_d^-)$	(h_d^0, h_d^-)	$(1, 2, -\frac{1}{2})$

Table 2.4: Summary of the chiral supermultiplets of the MSSM, with their quantum numbers. The superpartners of SM particles are denoted with a tilde.

In generic SUSY models, lepton and baryon number are not automatically conserved. This is unsurprising since baryon and lepton number conservation are *accidental* in the SM in the sense that they are not explicitly assumed. Nature appears to respect the conservation of these quantum numbers, in particular, proton decay has never been observed. This motivates the assumption of a discrete symmetry, R-parity, defined as:

$$R \equiv (-1)^{3B+L+2s} \tag{2.38}$$

in the MSSM. The dependence on the baryon number B, the lepton number L and the spin s ensures conservation of baryon and lepton number. R-parity is taken to be an exact symmetry, prohibiting the decay of SUSY to SM particles. An important consequence of this is that the lightest supersymmetric particle (LSP) is stable. If the LSP is also electrically neutral, it may provide a candidate for dark matter.

To break SUSY, soft mass terms are introduced for each of the SUSY particles (*sparticles*). Due to intergenerational mixing, these terms introduce 105 new parameters, on top of the 19 from the SM. The complexity of the MSSM can be reduced by making phenomenologically motivated assumptions to derive simpler models. For example, one may make the following assumptions:

- No additional sources of CP violation are introduced.
- No FCNCs are introduced.
- Mass degeneracy and equal trilinear couplings at low energy for the first- and second-generation SUSY fermions (*sfermions*) to satisfy constraints on flavour violating couplings [56, 57].

Under these assumptions the additional parameters introduced by the MSSM are reduced to 22, listed below:

- $\tan\beta$: The ratio of the VEVs of the Higgs doublets
- μ, m_A: The mass parameters for the Higgs fields
- M_1, M_2, M_3: The mass parameters for the bino, wino and gluino
- $m_{\tilde{q}}, m_{\tilde{u_R}}, m_{\tilde{d_R}}, m_{\tilde{l}}, m_{\tilde{e_R}}$: The first and second generation sfermion mass parameters
- A_u, A_d, A_e: The first and second generation trilinear couplings
- $m_{\tilde{Q}}, m_{\tilde{t_R}}, m_{\tilde{b_R}}, m_{\tilde{L}}, m_{\tilde{\tau_R}}$: The third generation sfermion mass parameters
- A_t, A_b, A_τ: The third generation trilinear couplings

2.3.3 SUSY Phenomenology

Names	Spin	R-parity	Physical Mass Eigenstates
Higgs bosons	0	+1	$h^0\ H^0\ A^0\ H^\pm$
squarks	0	-1	$\tilde{u}_1\ \tilde{u}_2\ \tilde{d}_1\ \tilde{d}_2$ $\tilde{c}_1\ \tilde{c}_2\ \tilde{s}_1\ \tilde{s}_2$ $\tilde{t}_1\ \tilde{t}_2\ \tilde{b}_1\ \tilde{b}_2$
sleptons	0	-1	$\tilde{e}_1\ \tilde{e}_2\ \tilde{\nu}_e$ $\tilde{\mu}_1\ \tilde{\mu}_2\ \tilde{\nu}_\mu$ $\tilde{\tau}_1\ \tilde{\tau}_2\ \tilde{\nu}_\tau$
neutralinos	$\frac{1}{2}$	-1	$\tilde{\chi}_1^0\ \tilde{\chi}_2^0\ \tilde{\chi}_3^0\ \tilde{\chi}_4^0$
charginos	$\frac{1}{2}$	-1	$\tilde{\chi}_1^\pm\ \tilde{\chi}_2^\pm$
gluinos	$\frac{1}{2}$	-1	$\tilde{g}$

Table 2.5: Summary of the physical supersymmetric particle spectrum and Higgs sector of the MSSM. It is customary to denote a lighter mass eigenstate with a lower value subscript.

In the MSSM, physical mass eigenstates are formed from the mixing of terms in the supersymmetric Lagrangian. Two doublets of charged eigenstates, *charginos* are generated through the linear mixing of the charged gauginos ($\tilde{W}^\pm$) and the charged higgsinos ($\tilde{H}^\pm$). In terms of MSSM parameters, the chargino mass matrix is given by [25]

$$\begin{pmatrix} M_2 & \sqrt{2}m_W \sin\beta \\ \sqrt{2}m_W \cos\beta & \mu \end{pmatrix} \tag{2.39}$$

in the $(\tilde{W}^\pm, \tilde{H}^\pm_{u/d})$ basis, where M_2 is the wino mass parameter and μ is a Higgs field mass parameter. The ratio of Higgs vacuum expectation values is parameterised in terms of $\sin\beta$ and $\cos\beta$. The neutral gauginos ($\tilde{B}$ and $\tilde{W}^0$) mix with the neutral

higgsinos ($\tilde{H}_d^0$ and $\tilde{H}_u^0$) to form four *neutralinos*. In the $(\tilde{B}, \tilde{W}^0, \tilde{H}_u^0, \tilde{H}_d^0)$ basis the neutralino mass matrix is given by

$$\begin{pmatrix} M_1 & 0 & -m_Z \cos\beta \sin\theta_W & m_Z \sin\beta \sin\theta_W \\ 0 & M_2 & m_Z \cos\beta \cos\theta_W & -m_Z \sin\beta \cos\theta_W \\ -m_Z \cos\beta \sin\theta_W & m_Z \cos\beta \cos\theta_W & 0 & -\mu \\ m_Z \sin\beta \sin\theta_W & -m_Z \sin\beta \cos\theta_W & -\mu & 0 \end{pmatrix}, \tag{2.40}$$

where M_1 is the bino mass parameter. The neutralinos and charginos are collectively known as *electroweakinos*. Physical squark mass eigenstates arise from the mixing of left- and right-handed fields, according to the mass matrix $\mathcal{M}_{\tilde{q}}^2$. In the case of third generation squarks, $\mathcal{M}_{\tilde{q}}^2$ is given by [58]

$$\mathcal{M}_{\tilde{q}}^2 = \begin{pmatrix} m_{\tilde{q}L}^2 & a_q m_q \\ a_q m_q & m_{\tilde{q}R}^2 \end{pmatrix} \tag{2.41}$$

in the $(\tilde{q}_L, \tilde{q}_R)$ basis. This mass matrix is fully determined by the squark and quark masses, and the term

$$a_q m_q = \begin{cases} (A_t - \mu \cot\beta) m_t & \text{for} \quad \tilde{q} = \tilde{t}, \\ (A_b - \mu \tan\beta) m_b & \text{for} \quad \tilde{q} = \tilde{b}. \end{cases} \tag{2.42}$$

In the above expression A_t and A_b are third generation trilinear couplings. Finally, the MSSM Higgs sector contains five physical scalar Higgs states: a charged Higgs boson pair $H^\pm$, two CP-even states, h^0 and H^0, and one CP-odd neutral Higgs, A^0. The gluinos carry colour charge so do not mix. The physical SUSY particle content of the MSSM and its Higgs sector are summarised in table 2.5.

2.3.4 Second and Third Generation Squarks

Due to its enhanced coupling to the Higgs, the degree to which the limitations of the SM are addressed by SUSY is dependent on the mass of the scalar top quark. Naturalness arguments suggest that the mass of the lightest scalar top quark should be the same order as the mass of the top [59, 60]. Light stops are also required to explain baryogenesis [61]. Furthermore, the unification of the gauge couplings at the GUT scale can be perfect in some SUSY models, provided SUSY particle masses are at the order of 1 TeV [25]. These factors provide strong motivation for stop searches at the LHC.

The stop decay mode depends heavily on the mass splitting between the stop and the LSP: $\Delta m = m_{\tilde{t}_1} - m_{\tilde{\chi}_1^0}$. The different cases are illustrated in figure 2.5, assuming the only SUSY particles taking part in the process are the stop itself and the LSP. A more complete discussion of the stop phenomenology, where this assumption is relaxed, can be found in Ref. [62]. If $\Delta m > m_t$ the stop preferentially decays to a top and a LSP. For the case $m_W + m_b < \Delta m < m_t$ the stop decays to a b, W and a LSP. For $\Delta m < m_b + m_W$, the stop decay can proceed through two competing mechanisms: four-body decay to bff' (figure 2.6a) and a LSP or through decay to a c and a LSP (figure 2.6b). The flavour violating stop to charm decay is loop-suppressed, however scans of MSSM parameters [63] show that in many models the branching fraction of this process is as important as stop four-body decay.

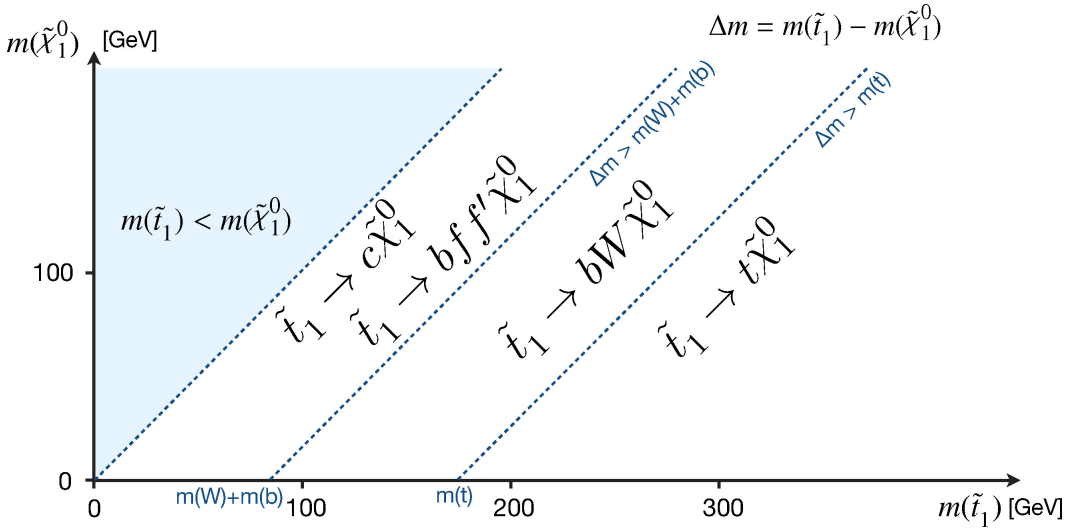

Figure 2.5: Illustration of stop decay modes in the plane spanned by the masses of $\tilde{t}_1$ and $\tilde{\chi}_1^0$, where the latter is assumed to be the LSP. Stop decays to supersymmetric particles other than the LSP are not displayed. Image is taken from Ref. [62].

The scalar top and scalar bottom occupy an $SU(2)_L$ doublet so that the same naturalness arguments for a light stop apply to the sbottom. This suggests that the sbottom should be significantly lighter than the other squarks. In the simplified MSSM model under consideration, the sbottom decay is expected to proceed as $\tilde{b}_1 \to b\tilde{\chi}_1^0$ (figure 2.6c) or as $\tilde{b} \to t\tilde{\chi}_1^\pm$, which is favoured in the case that $\tilde{b}_1 \sim \tilde{b}_L$. This signal is characterised by collimated jets from the fragmentation of the b quarks and missing transverse energy from the LSP.

In compressed models, where the mass splitting between the lightest stop or sbottom and the LSP is in the range 15-30 GeV, the dark matter relic abundance can be satisfied through stop-neutralino co-annihilation [64] making this an interesting region of parameter space. The small mass splitting between the squark and LSP results in *soft* decay products with very low transverse momentum, p_{T}, often below the threshold for reconstruction by the ATLAS detector. This makes compressed signals particularly difficult to measure, prompting the development of novel methods to "tag" the soft b quarks. The soft b-tagging analysis in chapter 6 is presented in the context of compressed sbottom and stop four-body decay. The $\tilde{t}_1 \to bff'\tilde{\chi}_1^0$ process (figure 2.6a) resembles $\tilde{b}_1 \to b\tilde{\chi}_1^0$, with jets from fragmenting b quarks and missing transverse momentum from LSPs, but with a more compressed p_{T} spectrum for the b-quarks due to additional decay products.

First and second generation squarks are disfavoured by ATLAS and CMS up to the TeV level [65, 66]. These limits are derived in the context of simplified models (see section 2.3.5), with mass degenerate LHχSFs: Q, U and D (see table 2.4) for the first and second generations to satisfy flavour violation constraints (see section 2.3.2). Relaxing this condition allows for more generic SUSY models, which do not necessarily violate flavour constraints. For example, in SUSY alignment models [67] FCNCs are suppressed by assuming a horizontal $U(1)$ symmetry to align the quark and squark mass matrices.

Non-degenerate squark masses can reduce the sensitivity of existing limits in two ways [68]: reduced signal efficiency for low masses due to kinematic cuts and

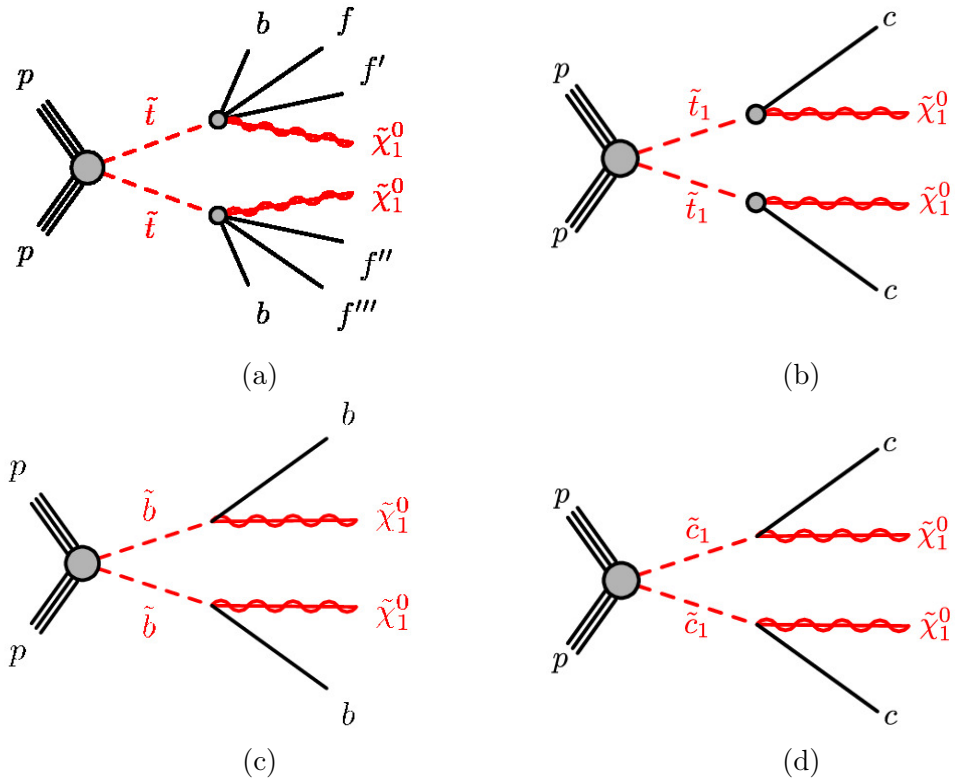

Figure 2.6: Production diagrams for the pair production of scalar tops followed by (a) four-body decay and (b) decay into charm quarks. (c) Pair production of scalar bottoms with subsequent decay into bottom quarks and (d) pair production of scalar charm quarks with subsequent decay into charm quarks. For simplicity, differentiation of particles and anti-particles is omitted but should be implicitly assumed.

lowered cross-sections for second-generation squarks due to modified parton distribution functions (PDFs). Mass splitting also allows for light scalar charm quarks. These considerations motivate dedicated searches for direct scharm pair production at the LHC. If the other phenomenological assumptions are kept, relaxing only the restriction of mass-degeneracy for the squarks, scharms will be pair-produced, decaying as $\tilde{c}_1 \to c\tilde{\chi}_1^0$ (figure 2.6d). The signal topology for such a process is identical the stop decay $\tilde{t}_1 \to c\tilde{\chi}_1^0$ (figure 2.6b), differing only by the mass of the scharm and the mass splitting between the scharm and the LSP. These processes are characterised by jets originating from fragmenting charm quarks and missing transverse energy from the LSP. Searches for such SUSY signals with charm quarks in the final state are the subject of chapter 5.

2.3.5 Simplified Models

The SUSY searches considered in this thesis make use of simplified models [69–71], where squarks are assumed to be pair produced, with no other SUSY particles playing a role in the production or decay, and a 100% branching fraction for the assumed decay mode. These assumptions are based on phenomenological simplicity, and give experimentally measurable signatures. These simplifying assumptions may not be well motivated, and can even limit the ability of the SUSY model to address the limitations of the SM outlined in section 2.2. They do however allow for a broad class of SUSY models to be excluded, and can be considered approximations to more to realistic SUSY models with more complex spectra. If a signal based on a simplified model were to be measured, it would allow much more precise determination of the properties of the physical realisation of SUSY.

The mass hierarchy of the electroweakinos depends on the mixing of the gauginos and higgsinos (see figure 2.7). In the case of a pure bino LSP, with no mixing, all electroweakinos except for the LSP are heavy, and the only sparticles that will participate in LHC processes are the third generation squarks. Thus the simplified models considered in this thesis are realised in some SUSY scenarios. The exclusion limits set by these searches can be extended to any SUSY model that predicts the same experimental signature, with the strength of the limits determined by the degree to which the assumptions hold.

2.3.6 The Bigger Picture

The searches considered in this thesis are inspired by the simplified models described above. They are parochial in scope if considered as standalone searches. These searches should therefore be understood in the context of the wider experimental SUSY search effort. They are part of a rich program of SUSY searches currently being undertaken by the ATLAS and CMS collaborations at the LHC, and the wider particle physics community. The current status of SUSY is outlined below. This summary is *brief* and is not intended to be a review, nor an exhaustive account of the state of SUSY.

SUSY can be constrained indirectly, for example using data from flavour physics experiments. Rare $B_S \to \mu\mu$ decays are strongly suppressed and precisely determined in the SM, with many SUSY models predicting deviations [72–76]. Recent measurements from ATLAS and LHCb [77, 78] observe no such deviations, placing

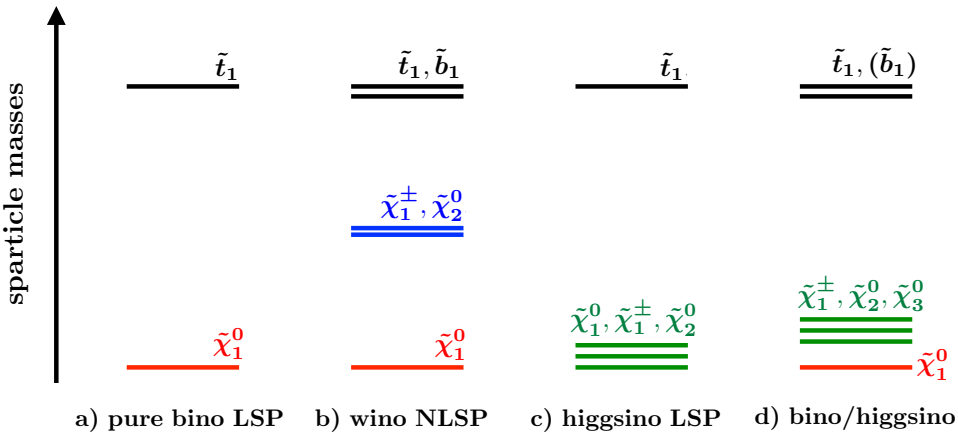

Figure 2.7: Electroweakino mass hierarchy dependence on the gaugino and higgsino mixing.

limits on SUSY. Further constraints can be placed by other precision SM measurements. In many SUSY models, loop induced couplings of the Higgs, for example gluon fusion and photonic decay, are modified [79, 80]. LHC measurements of these couplings can be applied to obtain constraints on sparticle masses [81]. Astrophysical data, for example the determination of the dark matter relic density, place additional limits on many SUSY models [47]. Indirect limits such these can exclude SUSY masses to high energy scales, tending to be strongly model dependent.

For the remainder of this section, the focus will be direct searches by the ATLAS and CMS collaborations. These searches are inspired by a variety of different flavours of SUSY model and employ a diverse range of experimental techniques. Together they form part of a "bottom-up" approach, with searches targeting low mass eigenstates from each of the main categories of sparticle in simplified models that can be produced at the LHC. A brief overview of the current status of these searches and the current limits on SUSY parameters is given below, organised into five main categories:

- **Strong Production:** This category concerns the direct production of gluinos and squarks in R-parity conserving SUSY models. If gluinos and squarks are decoupled, R-parity requires that they are pair produced, otherwise mixed production is possible. Since they are superpartners of gluons and quarks, production proceeds through the strong interaction by virtue of the colour charge they carry. As a result these processes benefit from high cross-sections. Searches often target simple decays, for example gluinos decaying to a quark pair and a LSP or squarks decaying to a single quark and a LSP. Depending on the SUSY particle spectrum below squark and gluino masses, these decays can proceed directly or through additional intermediate particle states, resulting for example in an additional W (1-step) or W and Z (2-step). These signals therefore tend to produce a large number of hadronic jets and missing transverse momentum, $\boldsymbol{p}_{\mathrm{T}}^{\mathrm{miss}}$, due to the LSP leaving the detector unmeasured. In the case of 1-step and 2-step decays, additional jets and leptons can be present in the final state. *Inclusive* searches, targeting high jet multiplicity and $\boldsymbol{p}_{\mathrm{T}}^{\mathrm{miss}}$, are designed to be sensitive to a broad class of models, and place stringent

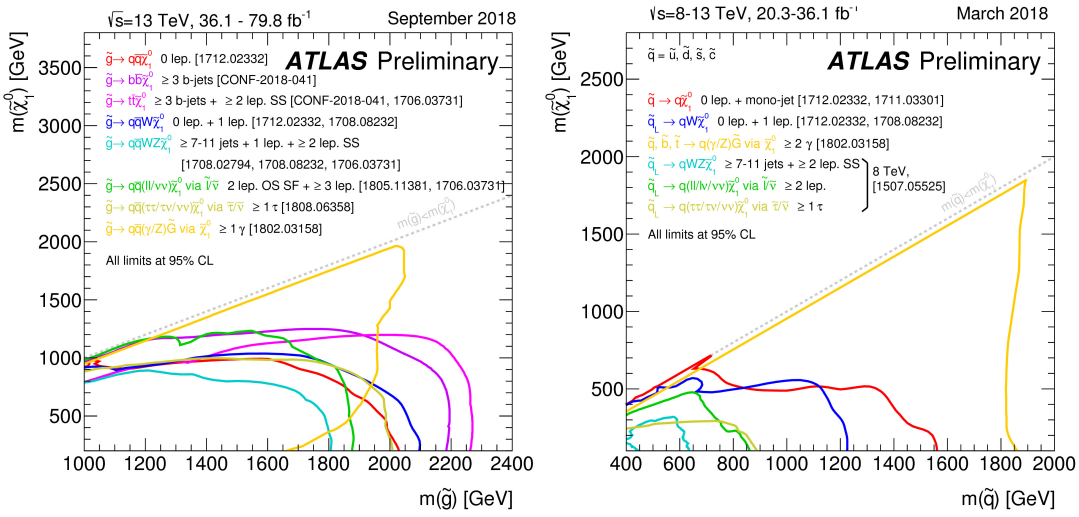

(a) (b)

Figure 2.8: ATLAS exclusion limits at 95% confidence limit based on 13 TeV data in (a) gluino and (b) squark versus LSP mass plane for different simplified models featuring the decay of the gluino to the LSP (lightest neutralino or gravitino) either directly or through a cascade chain featuring other SUSY particles with intermediate masses. For each line, the gluino decay mode is reported in the legend and it is assumed to proceed with 100% branching ratio. Some limits depend on additional assumptions on the mass of the intermediate states, as described in the references provided in the plots. Taken from Ref. [85].

limits on gluino and squark masses in the context of these simple decays, up to around 2 TeV for gluinos and beyond a TeV for squarks, corresponding to a LSP with mass around 1 TeV and 0.5 TeV, respectively (see figure 2.8).

Searches have been made to target squark and gluino pair production in more specific SUSY scenarios, with different kinds of final states. For example, in gauge-mediated SUSY breaking (GMSB) models [82–84], where SUSY breaking is communicated to visible sector through "messenger" fields that share the gauge interactions of the SM, squarks and gluino production may produce final states with hadronic jets, $\boldsymbol{p}_{\mathrm{T}}^{\mathrm{miss}}$ and one or two τ-leptons. Other searches consider GMSB models where the gravitino, the superpartner of the hypothetical graviton, is the LSP. In this scenario, squarks and gluinos can lead to final states with hadronic jets, $\boldsymbol{p}_{\mathrm{T}}^{\mathrm{miss}}$ and a Z boson or a photon. The exclusion limits placed by these searches are also shown in figure 2.8.

- **Third Generation Squark Production:** The searches considered in this thesis (excluding direct scharm pair production) fall into this category. The motivation for third generation searches has already been discussed in section 2.3.3. Third generation search strategies are largely dictated by the kinematic dependence on the targeted region in the stop / sbottom vs. LSP mass parameter space. A variety of methods are employed to target different regions, a number of which are described in chapters 5 and 6. Examples of novel methods used in third generation searches but not described later in this thesis are: tagging of top quarks, identification of hadronic jets originating from initial-state

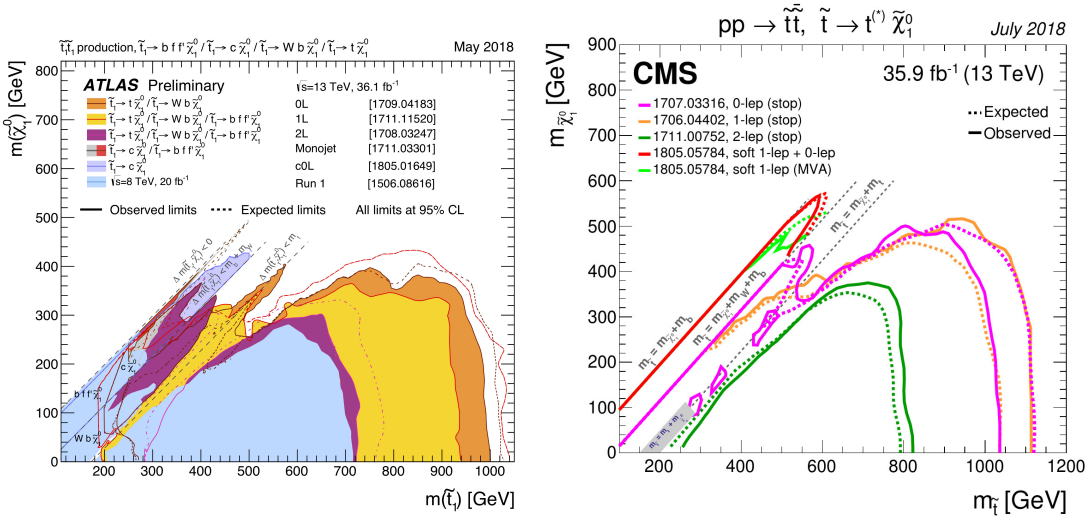

(a) (b)

Figure 2.9: (a) ATLAS and (b) CMS exclusion limits at 95% confidence limit based on 13 TeV data in the stop versus LSP mass plane. Three kinematic regions are shown corresponding to decays of the stop quark to: a top quark and a LSP, a bottom quark, W boson and a LSP and either a charm quark and a LSP or a bottom quark, fermion-antifermion pair and a LSP. Taken from Refs. [85, 86].

radiation (ISR) and a wide range of dedicated kinematic variables. As can be seen in figure 2.9, third generation searches at ATLAS and CMS disfavour direct stop pair-production up to a mass of around a TeV, for a LSP with mass of around 400 GeV. The results from the analysis presented in chapter 5 are included in the ATLAS limits, the methodology will be presented in chapter 5.

- **Direct Electroweak:** This category concerns the direct production of electroweakinos or sleptons. In SUSY models with heavy coloured sparticles, direct electroweak production may be the dominant mechanism for SUSY processes at the LHC. Production of a pairs of the lightest neutralino and second lightest neutralino are favoured by a relatively large cross-section. A number of searches exploit final states with $\boldsymbol{p}_{\mathrm{T}}^{\mathrm{miss}}$ and multiple leptons, which can result from slepton mediated decay or production of the second lightest neutralino and lightest chargino, decaying to a Z boson and a LSP and a W and a LSP, respectively. Another important signature has the second lightest neutralino decaying to a Higgs and a LSP and the lightest chargino decaying to a W and a LSP, with a number of signal topologies possible due to the many decay modes of the Higgs. A summary of CMS exclusion limits based on searches for the Higgs final state is given in figure 2.10b.

  Searches for direct slepton production are challenging due to low cross-sections. Compressed scenarios, with a small mass splitting between the slepton and the LSP are of particular interest, since, as for the case of compressed third generation models, they can satisfy the dark matter relic density through slepton-neutralino co-annihilation. Simplified models are considered where the sleptons are assumed to decay to a lepton and a LSP, with the final state char-

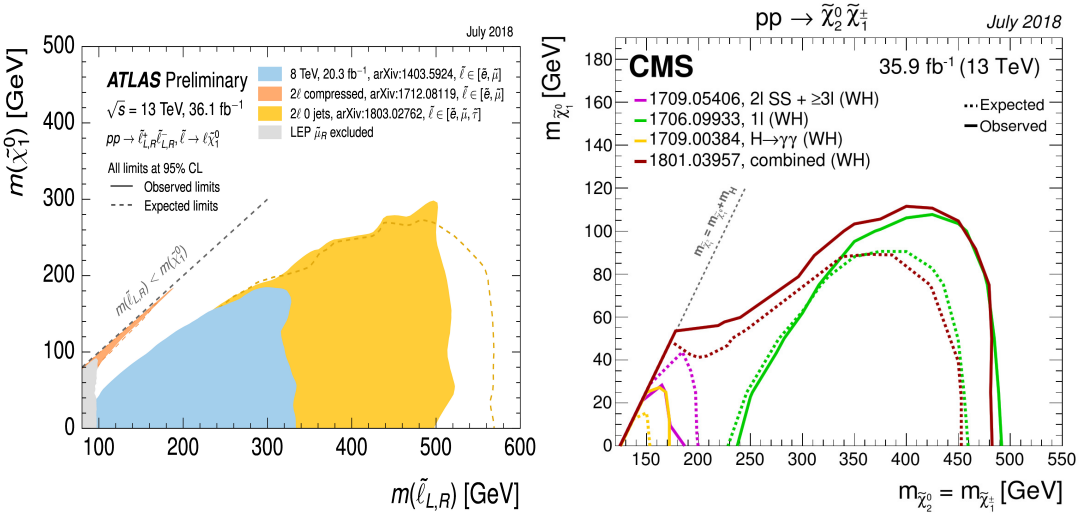

(a) (b)

Figure 2.10: (a) ATLAS and (b) CMS exclusion limits at 95% confidence limit based on 8 TeV and 13 TeV data. (a) Exclusion limits in the slepton versus LSP mass plane, probing the direct production of sleptons decaying to a lepton and a LSP. (b) Mass limits for the production of pairs of the lightest chargino and second lightest neutralino with decays to W and H bosons, respectively, and the LSP. The two gauginos are assumed to have the same mass. Taken from Refs. [85, 86].

acterised by the corresponding SM lepton and $\boldsymbol{p}_{\mathrm{T}}^{\mathrm{miss}}$. Recent ATLAS results from direct slepton searches are shown in figure 2.10a.

- **Long-lived Particles:** Long-lived particles (LLPs) can appear in supersymmetric extensions to the SM. In split SUSY [87, 88], SUSY breaking occurs at $\gg$ 1000 TeV and scalars acquire mass at this high scale, with fermions protected by chiral symmetry. As a result gluinos decay via highly virtual heavy scalar quarks, resulting in a long lifetime, long enough to produce bound states known as R-hadrons. R-hadrons can also result from long-lived LSPs in weakly R-parity violating models. The R-hadrons lifetime can be sufficiently long to allow them to produce a characteristic displaced vertex in the detector, which can be exploited in dedicated searches. They can also be targeted by their characteristic ionisation loss.

  In SUSY models where the lightest chargino and neutralino are almost pure wino or higgsino, for example anomaly-mediated SUSY breaking (AMSB) [89, 90], they become almost mass-degenerate. This results in a chargino LLP that can radiate a soft pion when decaying to the LSP. Since the pion is too soft to be detected, this leads to a disappearing track in the detector, providing a handle by which to form a search.

  Figure 2.11 shows limits on the gluino and chargino mass as a function on the LLP lifetime. These limits demonstrate another approach used by ATLAS and CMS, reinterpreting results from a collection of existing searches for combined sensitivity to selected models. In these figures, the sensitivity is scanned over different values of the gluino and chargino lifetime, with stringent limits set for a range of values.

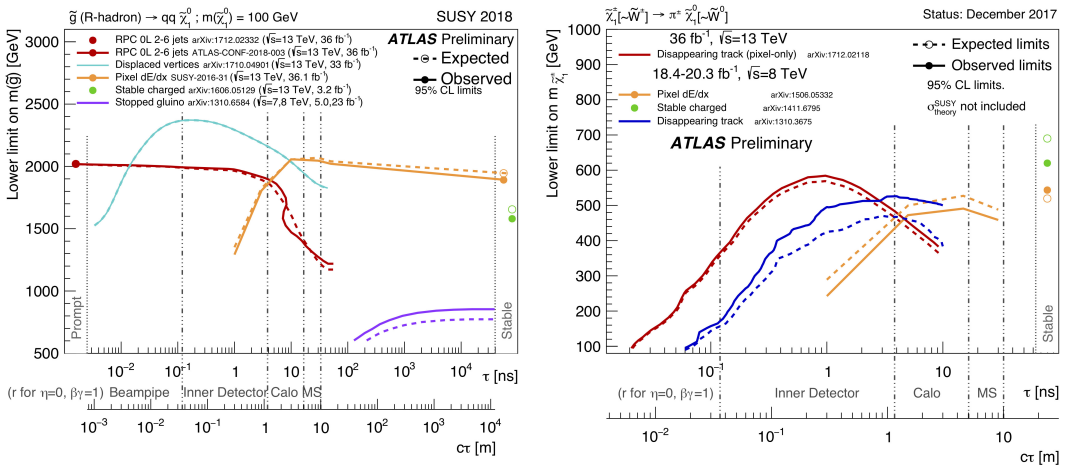

(a) (b)

Figure 2.11: ATLAS constraints on (a) gluino and (b) chargino mass-vs-lifetime plane. (a) Split SUSY with the gluino R-hadron decaying into a gluon or light quarks and a neutralino with mass of 100 GeV. (b) AMSB model with $\tan\beta = 5$ and $\mu > 0$. The wino-like chargino is pair-produced and decays to the wino-like neutralino and a very soft charged pion. In this context, stable means leaving the detector. Taken from Ref. [85].

- **R-Parity Violating:** Most of the searches considered so far assume R-parity conservation. In fact, much of the SUSY parameter space is R-parity violating (RPV), and many searches at ATLAS and CMS are dedicated to these kinds of models. If R-parity is not assumed, the following Yukawa and bilinear couplings:

$$\mathcal{L}_{\text{RPV}} = \frac{\lambda_{ijk}}{2} L_i L_j \bar{E}_k + \lambda'_{ijk} L_i Q_j \bar{D}_k + \frac{\lambda''_{ijk}}{2} \bar{U}_i \bar{D}_j \bar{D}_k + \kappa_i L_i H_u \tag{2.43}$$

  which can violate baryon and lepton number, appear in the SUSY Lagrangian. The i, j and k are quark and lepton generational indices, the L_i and Q_i represent lepton and quark $SU(2)_L$ doublet superfields, respectively, and H_u is the Higgs superfield that couples to up-type quarks. $\bar{E}_i$, $\bar{D}_i$ and $\bar{U}_i$ are lepton, down-type quark and up-type quark $SU(2)_L$ singlet superfields, respectively. κ is a dimensional mass parameter. The λ, λ' and λ'' couplings quantify the degree to which baryon and lepton number are violated.

  A variety of signal topologies are possible in RPV models, depending on assumptions made about the λ couplings in equation 2.43. An important difference with respect to R-parity conserving models is the decay of the LSP to SM particles. As mentioned above, weakly R-parity violating models may lead to LLPs. Some examples of RPV models are given below:

  - **Gqq model:** In models where the λ''_{112} is nonzero and the other RPV couplings are set to zero, with light gluinos and the lightest neutralino is the LSP, the gluino can decay as $\tilde{g} \to qq\tilde{\chi}_1^0$ with subsequent LSP decay as $\tilde{\chi}_1^0 \to qqq$. For larger values of λ''_{112}, the gluino can decay as $\tilde{g} \to qqq$.
  - **Gtt model:** If instead the λ''_{323} coupling is nonzero, the decay $\tilde{g} \to tt\tilde{\chi}_1^0$

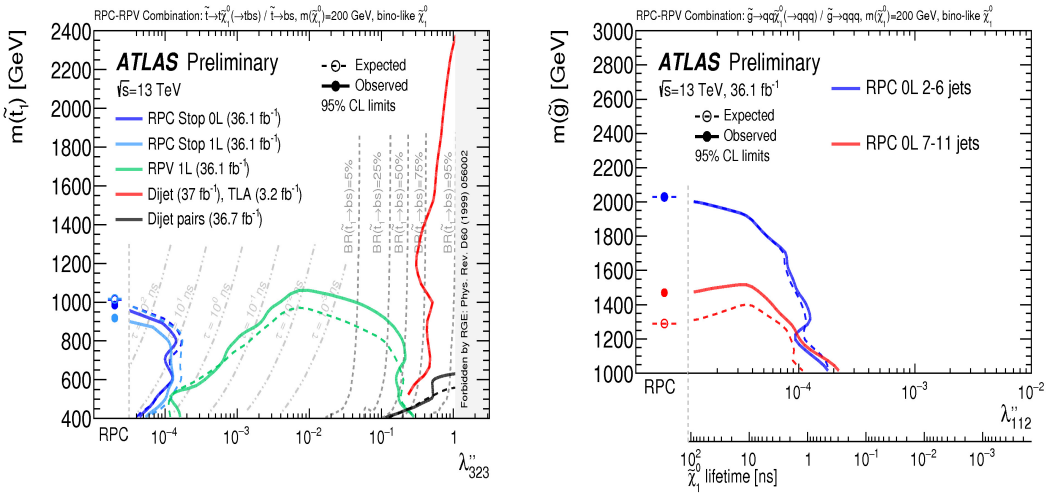

(a) (b)

Figure 2.12: ATLAS limits as a function of RPV parameters. (a) Limits for the Gtt model as a function of λ''_{323} and the gluino mass. (b) Limits for the Gqq model as a function of λ''_{112} and the gluino mass. For (b) the LSP lifetime is also shown. Taken from Ref. [91].

is possible, with the LSP decaying as $\tilde{\chi}_1^0 \to tbs$. For larger values of λ''_{323}, the gluino may decay as $g \to tbs$.

– **Stop model:** Again, the λ''_{323} coupling is nonzero and the other λ couplings are set to zero. The lightest neutralino is assumed to be the LSP, and a light $\tilde{t}_1$ is assumed. Stops are pair-produced, decaying as $\tilde{t}_1 \to t\tilde{\chi}_1^0$ for a low RPV coupling, or as as $\tilde{t}_1 \to bs$ for a high coupling. The LSP decays as $\tilde{\chi}_1^0 \to tbs$.

Figure 2.12a shows limits set on the mass of the stop and figure 2.12b limits set on the mass of the gluino, as a function of the appropriate RPV coupling. These limits are obtained by reinterpreting the results of existing analyses that offer sensitivity to the RPV models considered.

2.4 Summary

This chapter serves as an introduction to the work of this thesis. The relevant theoretical background has been reviewed, from QFTs and symmetries, the theoretical foundations of modern particles physics, to the SM, which provides a complete calculational apparatus for making phenomenological predictions for collider experiments. The key limitations of the SM motivating the work of this thesis have been outlined, and a theoretical overview of SUSY and its ability to address these limitations has been given.

The results shown in section 2.3.6 provide the backdrop for the analyses presented in chapters 5 and 6. Despite its theoretical appeal, SUSY below the TeV level is becoming increasingly disfavoured by LHC data, with much of the parameter space excluded for squark and gluino masses up to 1 TeV. These results suggest that, if SUSY is a realistic description of nature, SUSY particles are too heavy for it

to provide answers to the questions that it promised to solve. Low mass SUSY, if it exists, is likely to occupy regions of the parameter space that are difficult to probe. It is therefore crucial to improve searches and extend the reach of particle identification methods to probe as much of the parameter space as possible with the current LHC dataset. The analysis presented in chapter 5 is an important component of the ATLAS third generation search effort and provides sensitivity to scharm pair production. The most compressed SUSY scenarios are currently beyond the reach of ATLAS searches; the analysis in chapter 6 presents a novel method for recovering sensitivity in these regions.

3 | The ATLAS Experiment

The analyses presented in this thesis make use of data collected by the ATLAS detector [92], one of seven detectors located at the LHC [93]. This chapter gives an introduction to the LHC in section 3.1 and an overview of the ATLAS detector and its sub-detectors in section 3.2.

3.1 The Large Hadron Collider

The LHC is a two-ring superconducting-hadron particle accelerator located at CERN, straddling the Franco-Swiss border. Installed in a pre-existing tunnel constructed for LEP [94], it has a circumference of 26.7 km, lies at a depth of between 45 m and 170 m and houses seven detector experiments: two general purpose detectors: ATLAS and CMS [95], and five specialised detectors: ALICE [96], LHCb [97], TOTEM, [98], LHCf [99] and MoEDAL [100]. It is the most powerful particle accelerator ever built, colliding protons at a centre-of-mass energy of $\sqrt{s} = 13$ TeV. The LHC was built with two key goals in mind: to discover the Higgs boson, and to reveal new phenomena beyond those predicted by the SM.

Protons are supplied to the LHC through an *injection chain*. They are obtained by stripping the electrons from hydrogen gas by the application of an electric field. The resulting protons are accelerated to 50 MeV using LINAC2, a linear accelerator. They are then accelerated to higher energies by a series of synchrotron rings of increasing size. The first of these is the Proton Synchrotron Booster, with a radius of 25 m, which accelerates the protons to 1.4 GeV. The next is the Proton Synchrotron (PS), with radius 100 m, which further accelerates the protons to 25 GeV. The PS was once the world's most powerful particle accelerator, and over the years has accelerated a variety of particles either directly to experiments, or to feed larger accelerators. The final step in the injection chain is the Super Proton Synchrotron (SPS). The SPS feeds a number of experiments at the LHC, and, operating as a proton-antiproton collider, led to the discovery of W and Z bosons [101]. The SPS has a radius of 7 km and accelerates the protons to 450 GeV before injection into the LHC. The LHC injection chain forms part of the CERN accelerator complex, shown in figure 3.1.

The pre-accelerated protons are injected from the SPS into the LHC in both clockwise and anti-clockwise directions, in vacuum beam pipes. The beams are guided in a circular path through the beam pipes by superconducting dipole magnets, maintained at around 2 K using liquid helium coolant. The beams are focused transversely using pairs of quadrupole magnets, with a total of 858 quadrupole magnets along the beam pipe. Sextupole and octopole magnets are used to correct for other beam interactions, for example EM interactions within the beam and EM interactions between the beam and electron clouds from the pipe wall.

The orbiting protons are accelerated to 6.5 TeV using RF cavities operated by high power klystrons. To ensure that the protons are always accelerated by the RF pulses, the RF frequency f_{RF} must be an integer multiple of the revolution frequency

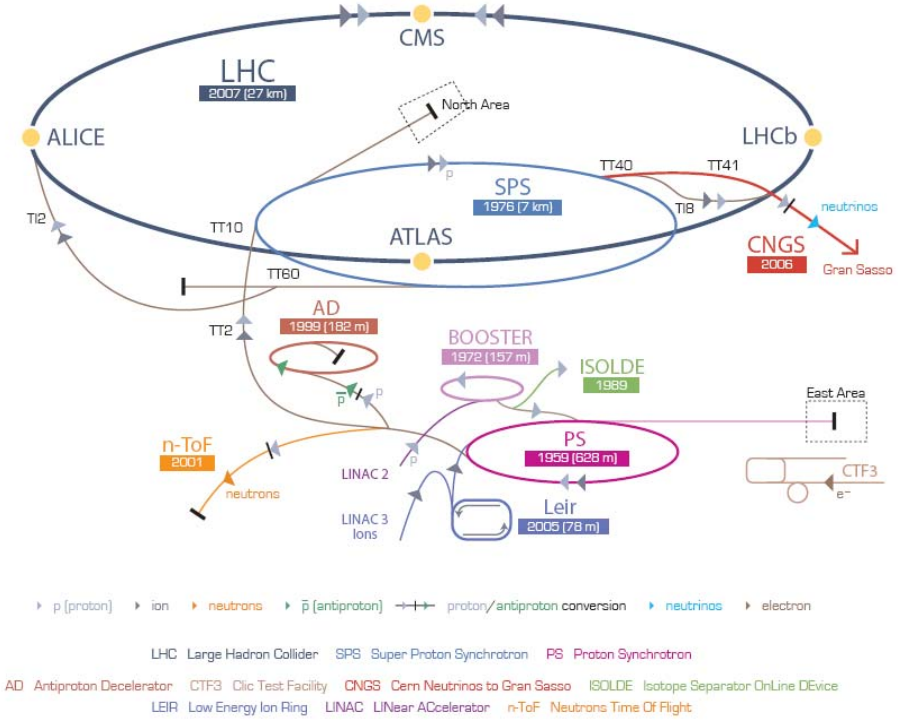

Figure 3.1: Schematic of the LHC accelerator complex. Image taken from Ref. [102].

f_{rev}. With protons travelling at close to c, f_{RF} should then satisfy:

$$f_{\text{RF}} = h f_{\text{rev}} = h\frac{c}{2\pi R}; \qquad h \in \mathbb{N}, \tag{3.1}$$

where R is the radius of the LHC. The applied RF frequency of 400 MHz gives a harmonic number $h = 35640$. The harmonic points around the LHC are called *buckets* and around 10% are filled with protons. Thus the RF cavities also serve to organise the proton beam into a *bunch* structure. This ensures high luminosity $\mathcal{L}$, which is proportional to the number of collisions per second. The LHC is designed to operate a beam of up to 2808 bunches, each consisting of up to 1.15×10^{11} protons.

The protons are accelerated until they reach maximum energy, at which point the beam is declared stable, and collision data can be taken at the four collision points. The beam intensity decays over time, primarily due to Coulomb scattering within the beam, where the momentum transfer is enhanced longitudinally due to relativistic effects. This causes protons to be lost from the beam, for example if the longitudinal momentum deviation exceeds the RF bucket. This is known as the *Touschek Effect* [103]. Other factors that contribute to the beam lifetime are the limited efficiency of beam focalisation, loss of protons at the collision points and proton collisions with residual gas molecules in the vacuum beam pipes. Typically the beam will last for $\mathcal{O}(10)$ hours, after which it is *dumped* into an absorbing material.

The luminosity delivered by the LHC depends on a number of design parameters

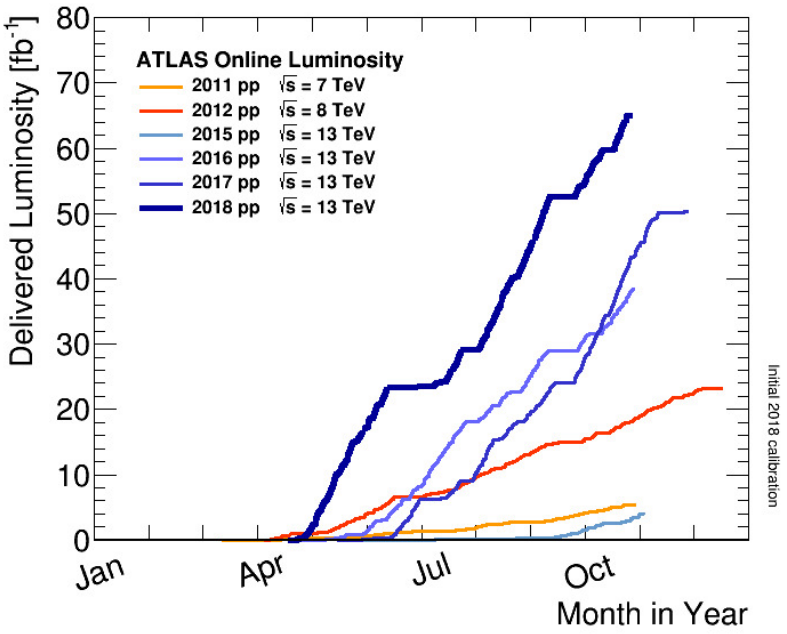

Figure 3.2: Delivered luminosity (pp collisions) to ATLAS by the LHC for years 2011-2018. Taken from Ref. [104].

[93]:

$$\mathcal{L} = \frac{N_b^2 n_b f_{\text{rev}} \gamma}{4\pi\epsilon\beta^*} F, \tag{3.2}$$

where N_b is the number of particles per bunch, n_b is the number of bunches per beam, f_{rev} is the revolution frequency and γ is the relativistic gamma factor. ϵ is the normalised transverse beam emittance, a measure of the spread of the beam particles in position and momentum phase-space, which remains constant as the beam changes energy. β^* is the beta function at the collision point, defined as the distance between the collision point and the point where the beam width has double the width at this point, giving a sense of how "squeezed" the beam is. F is a reduction factor in the luminosity due to the beams crossing at an angle at the collision point. The total number of pp collision events is given by

$$N_{\text{events}} = \sigma \int dt\mathcal{L}, \tag{3.3}$$

where σ is the total pp cross-section and $\int dt\mathcal{L}$ is the instantaneous luminosity integrated over time. Thus $\mathcal{L}$ is crucial for any measurement made using LHC data and must be determined as accurately as possible.

To measure the $\mathcal{L}$ delivered to ATLAS, it is useful to use the bunch luminosity

$$\mathcal{L}_b = \frac{\mu f_{\text{rev}}}{\sigma_{\text{inel}}}, \tag{3.4}$$

where μ is the number of interactions per bunch crossing (referred to as in-time *pileup*), to recast equation 3.2 as:

$$\mathcal{L} = \sum_{b=1}^{n_b} \mathcal{L}_b = n_b \langle \mathcal{L}_b \rangle = \frac{\langle \mu \rangle n_b f_{\text{rev}}}{\sigma_{\text{inel}}}, \tag{3.5}$$

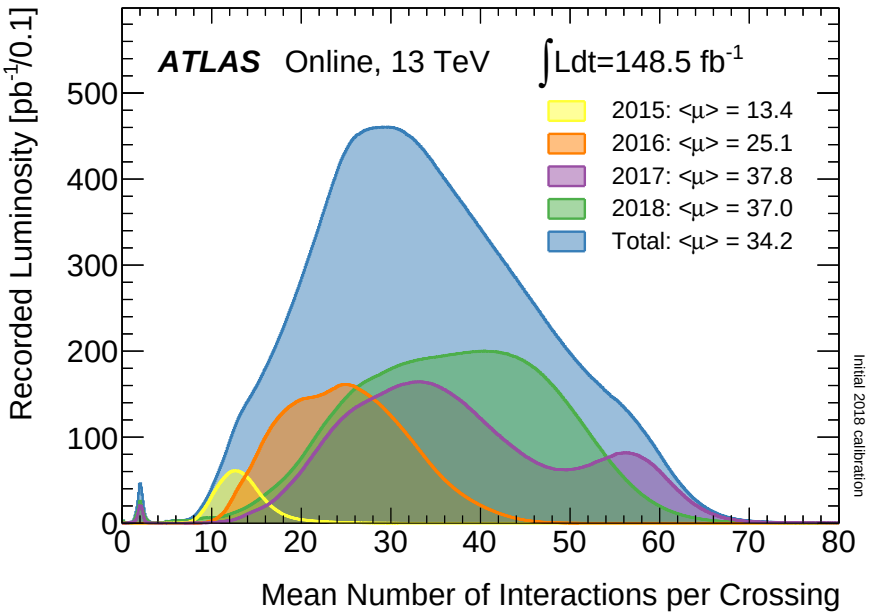

Figure 3.3: Luminosity-weighted distribution of the mean number of interactions per crossing for the years 2015-2018, in pp collision data at 13 TeV centre-of-mass energy. All data recorded by ATLAS during stable beams is shown, and the integrated luminosity and the mean μ value are given in the figure. Image taken from Ref. [104].

where σ_{inel} is the inelastic pp cross-section. The bunch luminosity recorded by ATLAS is then given by:

$$\mathcal{L}_b^{\text{recorded}} = \frac{\mu_{\text{vis}} f_{\text{rev}}}{\sigma_{\text{vis}}}. \tag{3.6}$$

$\mu_{\text{vis}} = \varepsilon\mu$ and $\sigma_{\text{vis}} = \varepsilon\sigma_{\text{inel}}$ are the visible pileup and inelastic cross-section obtained from re-scaling by the detection efficiency ε. μ_{vis} is measured using a combination of algorithms, the main ATLAS detector and additional dedicated detectors [105]. The dedicated detectors are described in section 3.2.5. The absolute luminosity scale is determined by performing *Van der Meer* scans [106], where the beams are scanned transversely across each other to estimate the beam profile $\epsilon\beta^*$, allowing the reference luminosity to be determined (see equation 3.2).

The instantaneous luminosity has increased throughout the operation of the LHC, as shown in figure 3.2. For a fixed filling scheme, the mean number of pileup collisions is proportional to $\mathcal{L}$, and quantified by $\langle\mu\rangle$. Pileup collisions are pp collisions not associated to the hard pp scattering of interest, leading to unwanted background physics objects that can degrade the performance of particle identification procedures. Distinguishing between objects arising from pileup collisions and hard pp scatterings is therefore an important consideration in recorded data and simulation. The $\langle\mu\rangle$ distribution for each year of Run 2 is shown in figure 3.3.

The LHC has been running since 2011, first at $\sqrt{s} = 7$ TeV, then $\sqrt{s} = 8$ TeV in 2012 and increasing to $\sqrt{s} = 13$ TeV for 2015-2018. The operating periods 2011-2012 and 2015-2018 are known as Run 1 and Run 2, respectively. The analyses presented in this thesis make use of data collected by the ATLAS detector during Run 2 in years 2015-2016, and builds on previous analyses based on data from Run 1. The

ATLAS detector is described in the next section.

3.2 The ATLAS Detector

The ATLAS detector is one of two general purpose experiments located at the LHC, the other being CMS. The physics goals of these experiments were the same at the outset: to search for the Higgs and to reveal physics beyond the SM. Having two independent detector experiments allows for healthy competition and innovation, and provides an important cross-check for significant physics results. In addition, their independent design led to different tradeoffs decisions for the finished detectors, for example, the ATLAS collaboration invested more resources for a precise muon chamber, while CMS invested heavily in the highest possible magnetic field for improved tracking of charged particles.

The toroidal geometry of the ATLAS detector [92] can be seen in figure 3.4. Its sub-detectors (described in detail in the following sections) are arranged in cylindrical layers surrounding the collision point. From the centre of the detector moving outwards, the sub-detectors are:

- The **Inner Detector** (ID), consisting of a pixel detector, semiconductor tracker and transition radiation tracker. The ID allows for the tracking of charged particles.
- The **Calorimeter System**, with a liquid argon (LAr) electromagnetic (EM) calorimeter, LAr end-cap and forward hadronic calorimeters and tile calorimeters. The calorimeter system allows for the the measurement of energy deposits from EM and strongly interacting particles.
- The **Muon Spectrometer**, for the tracking and measurement of muons.

The ATLAS magnet system can also be seen in figure 3.4. It provides a magnetic field for momentum reconstruction in the ID and muon chamber. It includes:

- A thin central superconducting solenoid which surrounds the ID cavity, providing a 2 T magnetic field. Its thin design keeps the additional material in front of the calorimeter system as low as possible, with the solenoid contributing ~ 0.66 radiation lengths at normal incidence.
- A barrel toroid magnet, which provides a magnetic field to the cylindrical volume surrounding the calorimeters and both end-cap toroids.
- Two end-cap toroidal magnets which provide the magnetic field for the bending of muon trajectories in the end-cap region of the muon chamber.

The toroidal magnets provide ~ 0.5 T for the muon detectors in the central region, and ~ 1 T for the muon detectors in the end-caps.

3.2.1 Coordinate System

The ATLAS coordinate system is defined with the nominal interaction point as the origin. The x, y and z axes are defined right-handed, as follows: the z-axis is defined by the beam direction, the x-direction points from the collision point to the centre

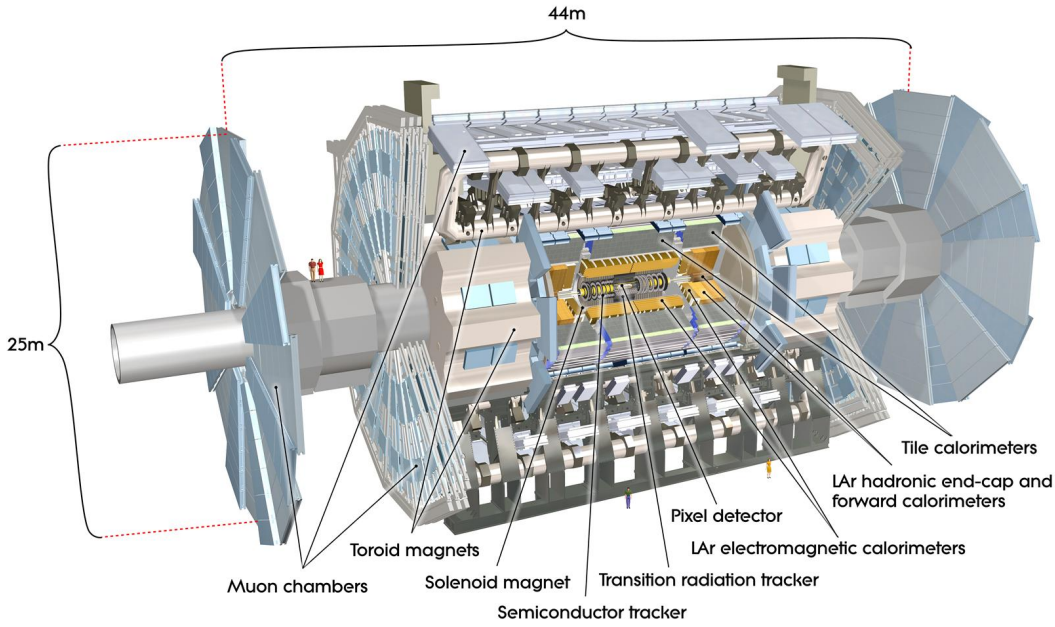

Figure 3.4: Cut-away view of the ATLAS detector, with cartoon humans to give a sense of scale. The ATLAS detector is 25 m in height and 44 m in length. The overall weight of the detector is approximately 7000 tonnes. Taken from Ref. [92].

of the LHC ring and the y direction points upwards from the collision point. The azimuthal angle ϕ is measured around the beam axis, in the $x-y$ plane, and the polar angle θ is measured from the beam axis. For LHC physics it is useful to recast θ in terms of rapidity y, defined as:

$$y = \frac{1}{2}\ln\left(\frac{E+p_z}{E-p_z}\right), \tag{3.7}$$

where p_z is the z component of the particle momentum, since it is additive under Lorentz boosts in the z direction. A related quantity is pseudorapidity η, defined:

$$\eta = -\ln\left[\tan\left(\frac{\theta}{2}\right)\right]. \tag{3.8}$$

For the case $m \ll |\mathbf{p}|$, where particles can be treated as approximately massless, the pseudorapidity converges to η. Where this is not the case, y is more appropriate. Transverse quantities, denoted by the subscript T, for example transverse momentum p_{T} , are defined in the $x-y$ plane. The angular separation between two objects ΔR is defined:

$$\Delta R = \sqrt{\Delta\eta^2 + \Delta\phi^2} \tag{3.9}$$

where ϕ is measured in radians.

3.2.2 Inner Detector

The purpose of the ID, shown in figure 3.5, is the precise measurement of charged tracks and their momenta, and for reconstruction of primary decay vertices originating from the pp interaction region and secondary vertices originating from intermediate particle decays. It surrounds the beam pipe, extending radially to a distance

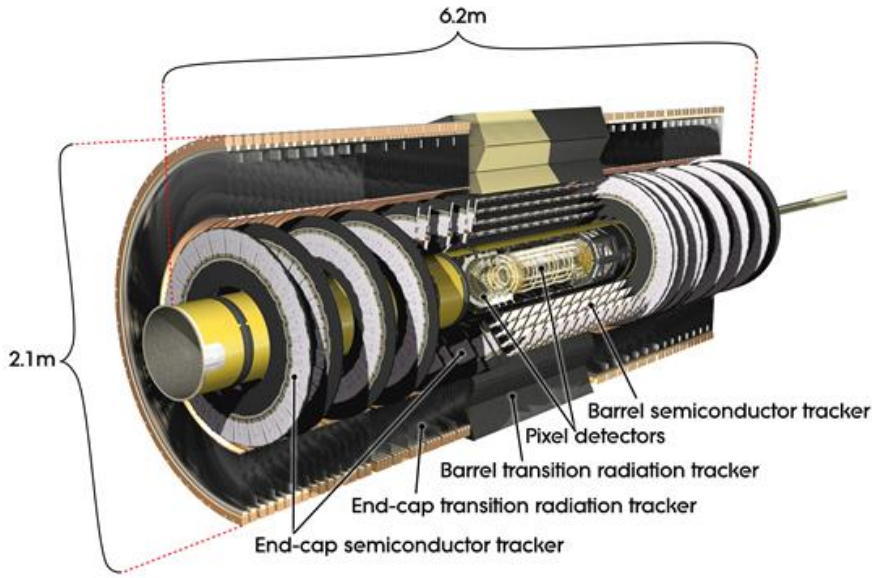

Figure 3.5: Cut-away view of the ATLAS inner detector (the IBL is not shown). Taken from Ref. [92].

of 1150 mm, and to $|z| = 3512$ mm along the beam axis, with an overall coverage of $|\eta| < 2.5$. It consists of three complementary subsystems: a pixel tracker, which includes an insertable B-layer (IBL) installed during the LHC shutdown between Run 1 and Run 2 [107], a semiconductor tracker (SCT) and the TRT. The radial structure of the ID is shown in figure 3.6. Each subsystem is detailed below:

- The **pixel detector** is the the innermost element of the ID, extending from a radius of 45.5 mm to 242 mm. For comparison, the beam pipe outer radius was originally 36 mm (the beam pipe was later refitted with a smaller radius of 33 mm to facilitate the installation of the IBL, discussed later in this section). It is designed to produce at least three points for a charged track originating from the collision point. It consists of modules arranged in three barrel layers and two sets of end-cap layers. Each module is made up of pixel sensors, each with a minimum length of 400 μm in the z-direction and 50 μm along ϕ. There are 47080 readout channels per module and a total of 67 million readout channels in the barrel and 13 million in the end-caps. The pixel detector has an intrinsic accuracy of 10 μm in the $R - \phi$ direction and 115 μm in the z-direction.

  A pixel sensor is made by implanting positive and negative dose regions on each side of an n-type bulk. The $p - n$ junction is configured in reverse bias, with the depletion region extending over the whole of the bulk volume. Charged particles traversing the sensor generate charge carriers in the depletion region, which can be collected to measure a "hit" in the pixel detector. Over the course of the operational lifetime of the pixel detector ($\sim$ 10 years), the sensors sustain intense irradiation due to their close proximity to the beam. Over time, this leads to bulk damage, increased leakage current and increased depletion voltage. Oxygen impurities are introduced in the bulk to improve tolerance to radiation damage due to charged hadrons. In addition, the silicon sensors

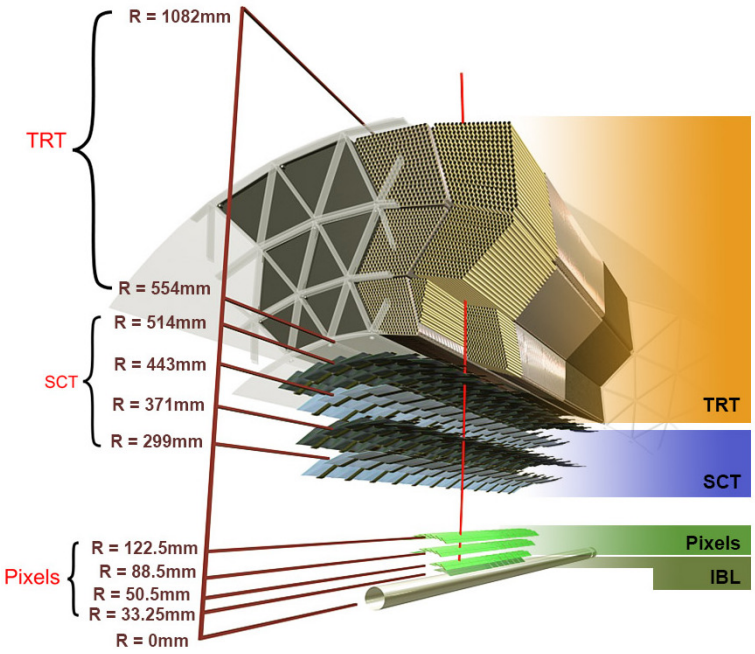

Figure 3.6: Diagram showing the sensors and structural elements traversed by a 10 GeV charged track in the barrel ID at $\eta = 0.3$. The radial distance from the beam is also shown. Taken from Ref. [108].

are maintained at a low temperature ($-5°$ to $-10°$C) to mitigate radiation damage.

The IBL is an extra fourth layer added between Run 1 and Run 2, closest to the interaction point. It makes use of the same pixel sensor technology as the pixel detector and adds approximately 12 million additional readout channels. The addition of the IBL was motivated by a number of considerations. First, the close proximity of the IBL to the collision point improves impact parameter reconstruction (see figure 3.7), essential in jet flavour and secondary vertex identification. The IBL will also maintain impact parameter resolution capabilities in the case of module failures in the current pixel detector, which are anticipated to emerge during the operational lifetime of the ATLAS detector. Finally, the existing pixel detector was designed for a peak luminosity of 1×10^{34} cm^{-2}s^{-1}. The IBL was built to improve the robustness of tracking to increasing pileup and luminosity, which reached more than 2×10^{34} cm^{-2}s^{-1} by the end of Run 2.

- The **SCT** [110] is the intermediate element of the ID, spanning from radius 255 mm to 549 mm in the barrel and 610 mm in the end-cap. It is made up of 4088 two-sided modules containing silicon strips that are on average 80 μm wide and 13 cm in length, giving a total of $\sim$ 6 million silicon strips. The sensors of the SCT are similar in design to the those of the pixel detector, with the pixels replaced by strips in order to cover the larger area necessary at the greater radius occupied by the SCT. The sides of the modules are offset by an angle of 40 mrad to allow for accurate measurement in both z and $R - \phi$. The modules are distributed over 4 cylindrical barrel layers and 18 planar discs on the end-caps. The SCT has an intrinsic accuracy of 17 μm in $R - \phi$ and

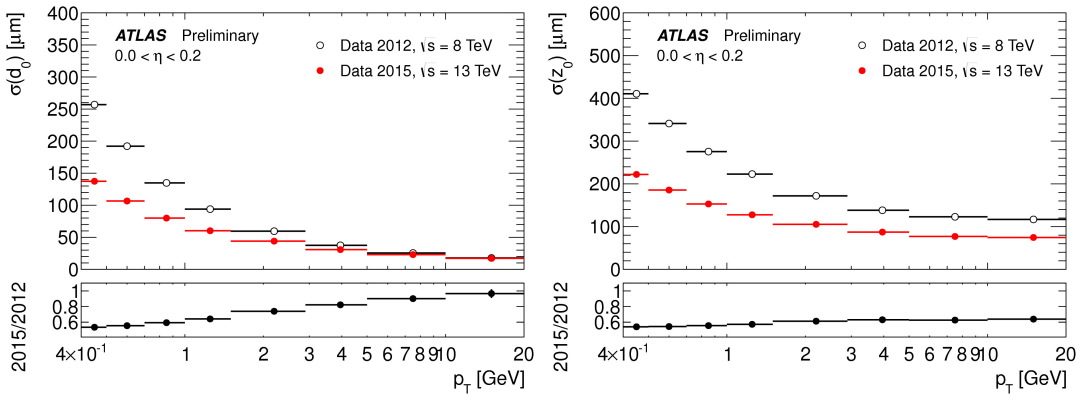

(a) (b)

Figure 3.7: (a) Transverse and (b) longitudinal impact parameter resolution with the ID, including the IBL in Run 2. Tracking parameters are described in detail in section 4.4.1. Taken from Ref. [109].

580 μm in z. The reduction in accuracy compared to the pixel detector is due to the replacement of pixels with strips.

- The **TRT** [111] occupies the region with radius 554 mm $< R <$ 1082 mm. The basic elements that make up the TRT are straw tubes 4 mm in diameter, with walls made of two multi-layer films, each 35 μm thick. The tubes contain a 31 μm diameter tungsten wire plated with 0.5-0.7 μm of gold, and a mixture of 70% Xe, 27% CO_2 and 3% O_2, maintained at a pressure of $5 - 10$ mbar. Charged particles passing through the TRT ionise the gas mixture in the straw tubes, generating electron charge carriers. The metal cladding is maintained at a high negative voltage, guiding the electrons to the tungsten wire. The electrons may take up to 48 ns to reach the wire, allowing the proximity of the traversing particle to be determined from the time of arrival of the first electron. The Xe gas is particularly sensitive to low-energy transition radiation photons; in this way the TRT provides additional discrimination between electrons and hadrons. In total there are $\sim$ 350000 readout channels. The TRT is designed to provide a large number of hits, typically 36 per track, with a coverage of $|\eta| < 2.0$. It has an intrinsic accuracy of 130 μm in $R - \phi$, providing no information in the z-direction.

3.2.3 Calorimeter System

The ATLAS calorimeter system surrounds the ID, covering the range $|\eta| < 4.9$. The components of the calorimeter system are shown in figure 3.8. The calorimeter system consists of an EM calorimeter surrounding the ID, which is in turn surrounded by the hadronic calorimeter. Both operate on the same principle, an incoming particle interacts with the detector, producing secondary particles, which in turn lead to further interactions with the detector material. Thus the incoming particle initiates a chain reaction in the calorimeter, producing a *shower* of subsidiary particles that will terminate when the energy of the particles falls below the energy threshold required to initiate further interactions with the detector material. The energy of the incoming particle can be measured by the response of the

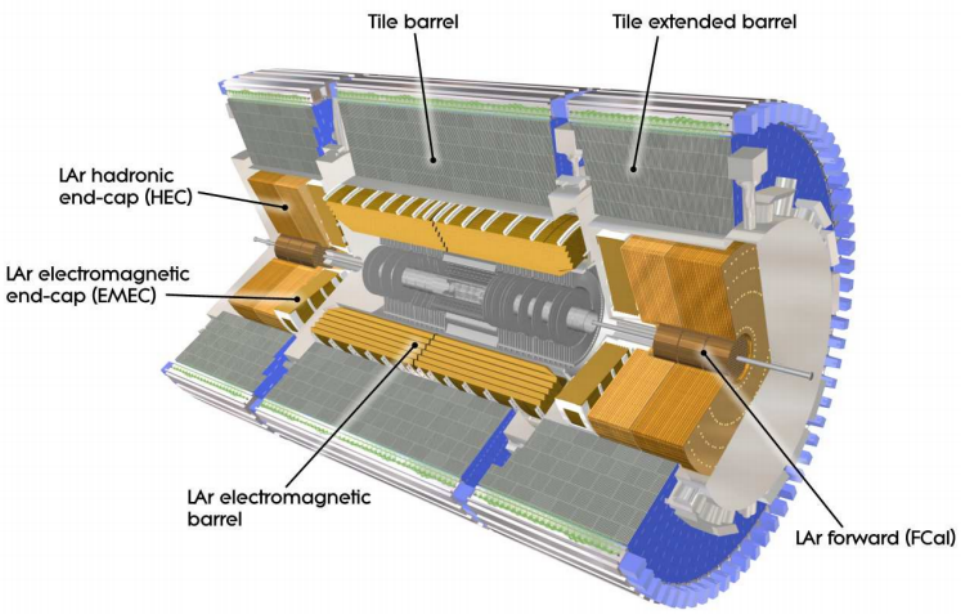

Figure 3.8: Cut-away view of the ATLAS calorimeter system. Taken from Ref. [92].

detector, and particles can be identified by their characteristic shower development. The differences in design for the EM and hadronic calorimeters are motivated by the kinds of particle that they target.

Electrons and photons develop EM showers through bremsstrahlung and electron-positron pair-production, continuing to develop until the energy falls below the threshold for photon conversion, at which point the shower terminates. Electrons and photons are identified with EM showers, with electrons distinguished by associated tracks in the ID. The effective thickness of the detector for EM particles can be parameterised in terms of the *radiation length*, X_0, the distance over which the energy of an incoming electron is reduced to $1/e$ of its initial value by radiation losses only.

The calorimeter energy resolution $\frac{\sigma_E}{E}$ is governed by a number of factors:

- The measured energy is proportional to the number of signal-generating interactions N. Since this is an intrinsically random process, N will be subject to Poisson fluctuations. These statistical fluctuations in the shower development contribute the so-called *stochastic term* $\frac{A}{\sqrt{E}}$ to the energy resolution, where A depends on the calorimeter design.

- The electronic readout chain results in a flat contribution to σ_E. The resulting contribution to the energy resolution is $\frac{B}{E}$, referred to as the *noise term*, where the constant B is a characteristic of the detector readout technique.

- The *constant term*, which does not depend on the energy of the incoming particle. This term parameterises instrumental effects which cause smearing of the calorimeter response to particles distributed over large areas of the detector.

The resolution of a calorimeter can thus be parameterised as:

$$\frac{\sigma_E}{E} = \frac{A}{\sqrt{E}} \oplus \frac{B}{E} \oplus C, \tag{3.10}$$

where $\oplus$ indicates that the sum should be performed in quadrature. At high enough energies, the overall resolution becomes dominated by the stochastic and constant terms. Neglecting the noise term, the design resolution for electrons in the ATLAS EM calorimeter is

$$\frac{\sigma_E}{E} = \frac{10\%}{\sqrt{E}} \oplus 0.7\%. \tag{3.11}$$

Hadronic showers are initiated by inelastic nuclear scattering, with subsequent interactions proceeding either by further inelastic nuclear scattering (typically around 2/3 of the shower) or EM showers from photons arising from intermediate neutral pions. Typically a significant fraction of the shower energy is lost, for example due to the energy required to break up atomic nuclei, ~ 1 GeV per nucleus. Energy may also be lost to "invisible" secondary particles leaving the calorimeter undetected, for example muons and neutrinos from charged pion decays. The effective thickness of the detector is governed by the radiation length for the EM fraction of the shower, whilst for the hadronic fraction of the shower it is determined by the *interaction length* λ, defined as the mean free path before a hadronic interaction takes place. For heavy materials, with a high atomic number, the interaction length is typically large compared with the radiation length. Due to the varying EM fraction, hadronic showers display large fluctuations in spatial energy distribution. As a result of these different factors, the energy resolution for hadronic showers tends to be significantly worse than for EM showers. For example, the design resolution for hadronic showers in the end-cap hadronic calorimeters is

$$\frac{\sigma_E}{E} = \frac{50\%}{\sqrt{E}} \oplus 10\%. \tag{3.12}$$

Both the EM and hadronic components of the ATLAS calorimeter system are *sampling* calorimeters, with separate materials used to initiate the shower (absorbing material) and measure the deposited energy (active material). The depth of the detector is an important design consideration; the EM calorimeter should fully absorb electrons and photons and hadronic particles should reach, and be fully contained by, the hadronic calorimeter. The large value of the interaction length compared to the radiation length therefore dictates the structure of the calorimeter system, with the EM calorimeter surrounded by the hadronic calorimeter. A hadronic calorimeter requires more material than an EM calorimeter to achieve the same level of containment of targeted incoming particles.

The individual components of the ATLAS calorimeter system are:

- The **EM calorimeter (ECAL)** which consists of a barrel and end-cap sections. Both are designed with an "accordion" geometry, allowing for homogeneity of the detector in the azimuthal direction and improved signal extraction times. The active material is LAr, chosen for its intrinsic hardness and linear dependence on energy, interleaved with copper and kapton readout electrodes. The absorbing material is lead, reinforced with 0.2 mm thick stainless steel sheets. The lead thickness is reduced at $|\eta| > 0.8$ from 1.53 mm to 1.13 mm to

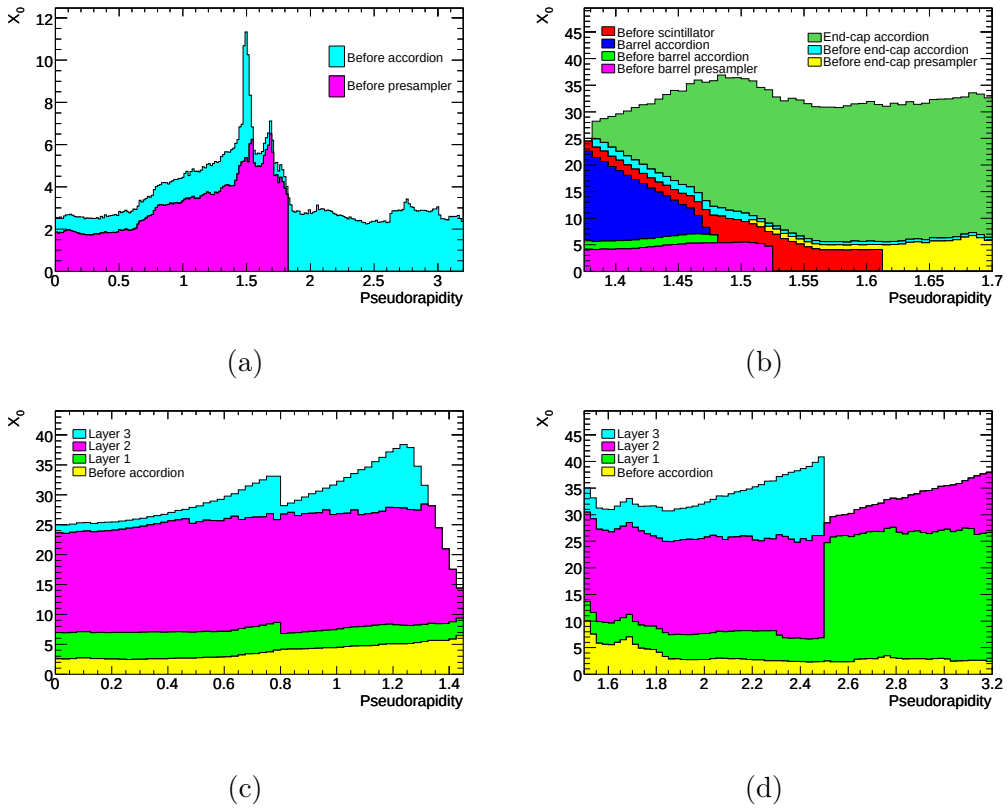

Figure 3.9: Cumulative amounts of material, measured in units of interaction length X_0, as a function of $|\eta|$, in front of and in the EM calorimeters. (a) Amount of material in front of the presample layer and in front of the accordion itself, over the full η coverage and (b) full details for the crack region. The lower panels show the thickness of each accordion layer and the amount of material in front of the accordion for (c) the barrel and (d) the end-cap. Taken from Ref. [92].

mitigate the reduced fraction of energy absorbed by the active material, the *sampling fraction*. The barrel section is made up of two identical half-barrels, with combined coverage $|\eta| < 1.475$. The EM end-cap (EMEC) calorimeters are arranged either side of the barrel calorimeters in two wheels, covering the range $1.375 < |\eta| < 2.5$.

A presampler is placed in front of the ECAL, a thin layer of active LAr with no lead absorber, to correct for energy loss in the ID, solenoid and its servicing cryostat. The thickness, measured in radiation lengths, of the ECAL is shown in figure 3.9. The "crack" region $1.37 < |\eta| < 1.5$, where the barrel meets the end-cap can clearly be seen in the 3.9a, where additional servicing material is present. The crack region is important in analyses that are sensitive to EM particle identification, and is often vetoed in these cases.

- The **tile calorimeter** surrounds the ECAL. It uses steel as the absorbing material and plastic scintillator tiles for the active material. It is arranged as a central barrel covering $|\eta| < 1.0$ with two extended barrels either side, together covering $0.8 < |\eta| < 1.7$. Each of the barrels has a radial depth corresponding to 7.4 λ. The scintillating tiles are arranged radially and in the $x - y$ plane, allowing for full azimuthal coverage. It is segmented into three

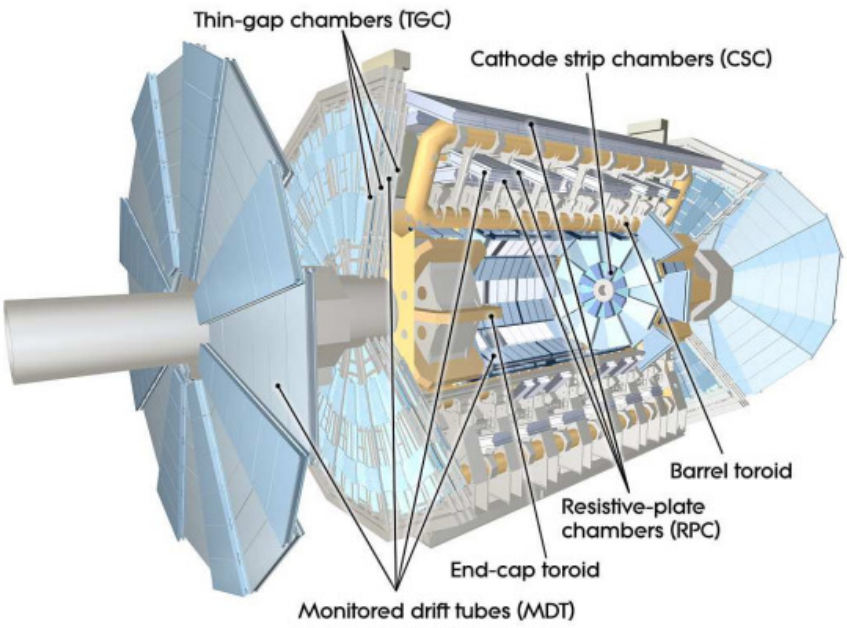

Figure 3.10: Cut-away view of the ATLAS muon system. Taken from Ref. [92].

layers of 1.5, 4.1 and 1.8 interaction lengths in the barrel and layers of 1.5, 2.6 and 4.4 interaction lengths in the extended barrels, for $\eta = 0$. Wavelength shifting fibres are used to readout the UV light produced by particles passing through the scintillators. This signal is fed to photomultiplier tubes (PMTs) for amplification.

- The **hadronic end-cap (HEC) calorimeters** are LAr calorimeters arranged in pairs of wheels behind the end-cap EM calorimeters. Like the EMEC calorimeters, they use LAr as the active medium and copper and kapton readout electrodes. The absorbing material for the HEC is copper. The HEC covers the range $1.5 < |\eta| < 3.2$, overlapping with the tile and forward calorimeters to mitigate the drop in material density in the gap between the end-cap and forward components.

- The **forward calorimeters (FCAL)** are integrated into the end-cap cryostats, providing coverage for the range $3.1 < |\eta| < 4.9$. They consist of three modules in the longitudinal direction, with LAr for their active media. The first, optimised for EM showers, uses a copper absorber. The second and third use tungsten absorbers and are designed primarily for the measurement of hadronic showers. The position of the FCAL at high $|\eta|$ means that it receives a very high flux of particles, motivating the small LAr gap design, to limit ion build up. It is designed to have a high thickness, corresponding to 10 λ, to suppress background radiation in the muon chamber.

3.2.4 Muon Spectrometer

Muons leave tracks in the ID and pass through the calorimeter system, leaving a small energy signature. Beyond the calorimeter system, they are measured using a dedicated muon spectrometer, shown in figure 3.10. The superconducting toroidal

magnets deflect the trajectory of the muons for momentum reconstruction. The muon spectrometer consists of four main sub-detector elements: *thin gap chambers* (TGCs) and *resistive plate chambers* (RPCs) for triggering information (the ATLAS trigger system is discussed further in section 4.2), and *monitored drift tube chambers* (MDTs) and *cathode-strip chambers* (CSCs) for precision tracking information. Each element is described below:

- **MDTs** allow for precision tracking and momentum measurements. MDTs are pressurised tubes of diameter 29.970 mm and length 0.85-6.5 m, which contain a mixture of Ar and CO_2 in the ratio 93 : 7. They measure the ionisation effects of passing charged particles, collecting electrons with a central a tungsten-rhenium wire of diameter 50 μm. The coverage of the MDTs extends to $|\eta| < 2.7$ except in the innermost end-cap layer where they are limited to $|\eta| < 2.0$, and replaced by CSCs in the range $2.0 < |\eta| < 2.7$. There are a total of 1171 MDT chambers, with a combined total of 354240 tubes. The overall tube resolution is 80 μm.

- The **CSC** replacement in the region $2.0 < |\eta| < 2.7$ in the innermost layer corresponds to the region of the muon spectrometer where the incoming neutron rate is expected to exceed 150 Hz/cm^2, the maximum for safe operation of the MDTs. The CSC can withstand a much higher rate of 1000 Hz/cm^2. They are multiwire proportional chambers, using the same gas mixture as the MDTs. The anode wires of the CSCs are directed in the radial direction, with the cathode strips arranged perpendicularly in order to provide a two-coordinate position measurement. The CSCs correspond to about 70000 readout channels and give a resolution of 60 μm.

- The **RPCs** are used for triggering in the central region $|\eta| < 1.05$. The muon triggering system is required to provide transverse momentum discrimination, bunch-crossing identification, fast and coarse tracking information and complementary second coordinate measurement in the no-bending ϕ-projection to complement the MDTs, whilst being robust in the presence of neutron and photon background. RPCs are made of two parallel bakelite plates, separated by 2 mm with insulating spacers enclosing a volume of gas mixture: $C_2H_2F_4$ (94.7%), C_4H_10 (5%) and SF_6 (0.3%). They are chosen for their simple construction, good spatial and time resolution and rate capability. The total arrangement of RPCs corresponds to 380000 readout channels.

- For the range $1.05 < |\eta| < 2.4$, **TGCs** are used for triggering. This is motivated by the same triggering requirements as the RPCs, with increased momentum resolution needed at high pseudorapidity, due to the larger relative increase in p_{T} compared to the bending power of the magnetic with rising $|\eta|$. The TGCs measure muons in a similar way to the multiwire proportional chambers. The resolution of the TGC arrangement is determined by the number of readout channels, in total there are 440000 channels.

3.2.5 Forward Detectors

In addition to the main ATLAS detector, three smaller, forward detectors are installed: LUCID (LUminosity measurement using Cherenkov Integrating Detector),

the Zero Degree Calorimeter (ZDC) and ALFA (Absolute Luminosity For ATLAS). They are located, respectively, ±17 m, ±140 m and ±240 m from the collision point. Each is described in more detail below:

- The **LUCID** detector is dedicated to the measurement of luminosity, both for monitoring instantaneous luminosity, and the total integrated luminosity over time. It measures inelastic *pp* scattering in the forward direction by Cherenkov radiation, the characteristic signal emitted by a charged particle passing through a dielectric medium at a greater speed than the phase velocity of light in that medium. The detector is designed to have a high acceptance, sufficient time resolution for 25 ns bunch spacing, robustness against intense radiation levels and sufficient resolution for the counting of individual charged particles. It consists of 20 aluminium tubes, 1.5 m in length and 15 mm in diameter, filled with C_4F_{10} maintained at a pressure of $1.2 - 1.4$ bar. This gives a Cherenkov threshold of 2.8 GeV for pions and 10 MeV for electrons. The Cherenkov pulses are picked up by PMTs for readout.

- The **ALFA** detector is used to determine the absolute luminosity scale by measuring elastic scattering at low angles. These measurements require high β^* and reduced emittance to ensure that the beam does not diverge beyond the required measurement angles, and must therefore be performed during dedicated runs. The detector consists of "Roman pots", detectors with their volume separate from the vacuum of the beam pipe, but connected by bellows, allowing them to be moved close to the beam. Along with the large separation from the collision point (240 m), this allows extremely small angle scatterings of $\mathcal{O}(3)$ μrad to be measured.

- The **ZDC** is designed to detect neutrons from heavy-ion collisions in dedicated runs of the LHC, and can also be used as an extra minimum-bias trigger during *pp* runs.

3.2.6 The ATLAS Trigger System

During Run 2, the LHC operated with 25 ns bunch-spacing, equivalent to a crossing rate of 40 MHz. Only a fraction of these collisions are expected to produce "interesting" physics. SUSY production cross sections are expected to be below the nanobarn scale; the total inelastic *pp* cross section is 68.1 ± 1.4 mb [112]. The ATLAS TDAQ (Trigger and Data AcQuisition) system is designed to select potentially interesting collision events from the vast background with high efficiency, with a recording rate of ~ 1 kHz.

The ATLAS TDAQ system is shown in figure 3.11. It consists of the hardware-based Level 1 (L1) trigger system and the software-based High Level Trigger (HLT) system, which runs on a dedicated computer farm. In Run 1, the HLT was made up of separate Level 2 (L2) and Event Filter (EF) farms. The L2 farm used partial event data, while the EF used full event information in dedicated nodes. For Run 2, the L2 and EF are merged to run on a single computer farm, for improved resource sharing and simplification of the overall system.

The L1 trigger system consists of the L1 Calorimeter (L1Calo) trigger, based on input from the full calorimeter system, and the L1 muon (L1Muon) trigger,

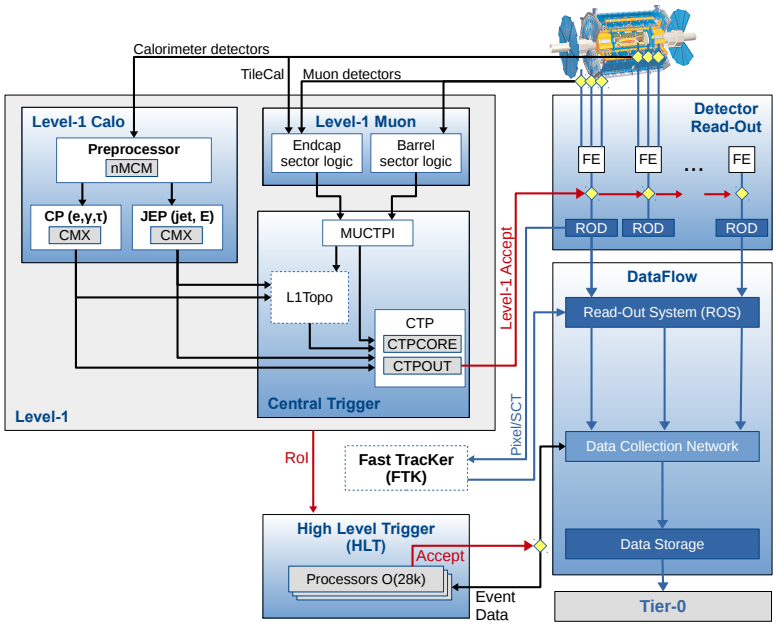

Figure 3.11: The ATLAS TDAQ system in Run 2, focusing on components relevant for triggering. Taken from Ref. [113].

based on information from the muon detector and Tile calorimeters. The central trigger processor (CTP) performs the initial event selection, calculating the "L1 Accept" trigger decision. The L1 trigger decision is based on inputs from L1Calo and L1Muon as well as other subsystems such as the LUCID and ZDC detectors. Accepted events are buffered in the readout system (ROS) to be processed at HLT. The geometric location of trigger objects, regions-of-interest (ROIs) are also passed to HLT to seed trigger reconstruction algorithms.

The L1Calo trigger uses input from all calorimeters to target high E_{T} calorimetric objects: electrons and photons (hereafter referred to collectively as e/γ), jets from hadronically decaying taus and jets from fragmenting quarks and gluons. The L1Calo also targets events with high total E_{T} or missing transverse energy, $E_{\mathrm{T}}^{\mathrm{miss}}$. Analogue L1Calo signals are digitised by the preprocessor system, which then associates them to specific bunch crossings using a digital filter. In Run 2 a new multi-chip module (nMCM) based on FPGAs was developed to replace the Run 1 ASIC-based multi-chip modules (MCMs). The nMCM offers improved flexibility and functionality, for example capability for bunch-by-bunch pedestal corrections. For improved processing time, the preprocessor uses a look-up table to assign values for E_{T} . The pre-processed data are then transmitted to the Cluster Processor (CP) and Jet/Energy-sum Processor (JEP) in parallel.

The CP applies e/γ and tau trigger algorithms to build ROIs consisting of 4×4 trigger towers (see figure 3.12), analogue summations of calorimeter cells. In total there are $\sim$ 7000 towers with granularity 0.1×0.1 in η and ϕ. A E_{T} threshold is applied for object selection, which can be η dependent to take into account energy losses and detector geometry (for example see figure 3.9). A sliding-window algorithm identifies the local energy minimum using four overlapping towers within a 2×2 central region for energy reconstruction. EM and hadronic rings are formed from the 12 towers surrounding the central cluster in the EM and hadronic layers,

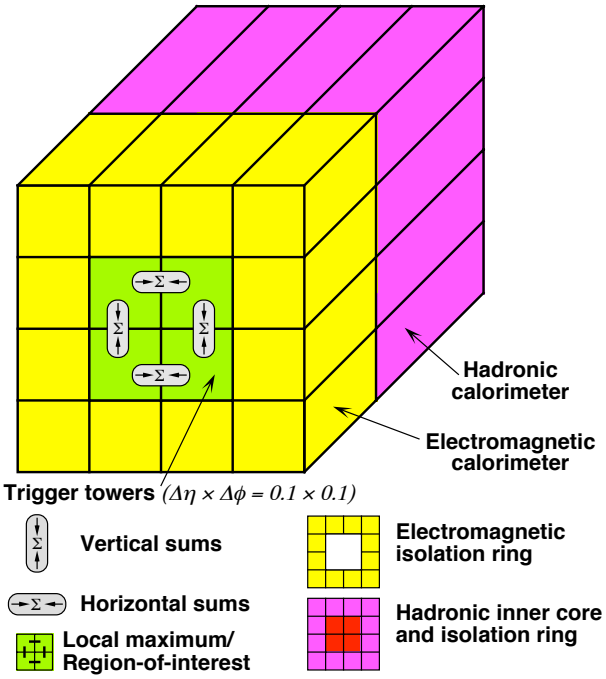

Figure 3.12: Schematic view of the trigger towers used as input to the L1Calo trigger algorithms. Taken from Ref. [92].

respectively, and are used for object isolation tests. The JEP receives jet trigger elements, 0.2×0.2 summations in η and ϕ. These are used to identify jet objects and compute the total scalar and missing transverse energy for the event. Extended cluster merger modules (CMXs) are used to transmit the location and energy of trigger objects to the L1 central trigger.

The L1Muon trigger is based on input from the RPCs in the barrel and the TGCs in the end-caps (section 3.2.4). The muon trigger chambers are arranged into three planes, each consisting of 2 or 4 layers. L1 muon trigger candidates are required to have coincident hits in multiple detector layers: 2 and 3 layers for low and high p_{T} muons, respectively. The muon candidate is identified with a ROI, approximately 0.1×0.1 in η and ϕ, in one of the layers. The algorithm proceeds by searching for additional hits within a window of additional ROIs consistent with the trajectory of a muon with minimum p_{T} defined by a preset, programmable trigger threshold. The end-cap and barrel sector logic proceed in parallel, providing the input for the L1 central trigger, including information about the position and p_{T} threshold passed by the muon candidate.

The L1 central trigger consists of the L1 topological processor (L1Topo), the Muon to Central Trigger Processor Interface (MUCTPI) and the central trigger processor (CTP). The MUCTPI uses information from all muon detector regions, providing muon track multiplicity for six p_{T} thresholds to the CTP for each bunch-crossing. The L1Topo receives input from L1Calo and L1Muon and comprises two FPGA-based modules, each programmed to perform additional selections based on geometric and kinematic associations between trigger objects.

The CTP uses information from the MUCTPI and L1Topo and additional subsystems to compute the L1 accept decision. This is performed using look-up tables from the input signals to form boolean trigger conditions, corresponding to, for ex-

ample, the multiplicity of an object type with a given E_{T} threshold. The trigger conditions are used to form up to 256 L1 trigger *items*, sets of selection criteria based on combinations of trigger conditions. Each item may be assigned a *prescale* factor, which can be used to limit the acceptance of triggers that would otherwise select events at an unmanageable rate. After a L1 Accept decision, the event is passed from the detector front-end (FE) electronics to the ROS via detector specific readout drivers (ROD). ROIs are also supplied directly to the HLT system, where a dedicated ROI builder merges them into a single data structure. Event fragments are stored temporarily in the ROS and passed to the HLT system if requested based on ROI information, which corresponds to $\sim 1-2\%$ of the full event information. The HLT system applies dedicated software-based algorithms to provide reconstructed physics objects and a trigger decision on whether the event is to be recorded. This information is passed back to the data collection network and, if the event is accepted, the event information is directed to Tier-0, the ATLAS computing facility for the first-pass processing of detector data. Further details of the HLT reconstruction are given in section 4.2.

3.3 Summary

The work of this thesis is based entirely on data collected by the ATLAS detector and simulations thereof. This chapter has provided a description of the LHC which accommodates the ATLAS detector, followed by a description of ATLAS itself. The analyses of chapter 5 and 6 use information from all of the subsystems of the ATLAS detector, each of which has been given individual attention. This includes the hardware of the ATLAS trigger system, which is crucial for selecting events for every measurement described later in this thesis.

4 | Data Acquisition and Reconstruction

This thesis makes use of both data collected by the ATLAS detector, and data simulated using Monte Carlo (MC) methods. This chapter describes the methods used for data quality (DQ) and processing in section 4.1, reconstructing and selecting events at HLT level in section 4.2 and data simulation in section 4.3. Finally, offline object- and event-level reconstruction methods are described in section 4.4.

4.1 Data Quality and Processing

Collision events selected by the ATLAS trigger system can be placed into a number of different offline *streams*, for processing at Tier-0 using the ATLAS `Athena` software framework [114]. These streams include:

- The `physics_main` stream, the primary data stream used for analyses, containing all physics objects and full detector information.
- The `express` stream, a subset of the `physics_main` stream, corresponding to around 2% of its events. This stream is used for prompt reconstruction, allowing for a first look at collected data for monitoring and data quality purposes, available within hours of the end of a data-taking run.
- The `calibration` stream, which contains events that are only partially rebuilt, containing the minimum information required for detector calibration.
- The `debug` stream, containing events where the trigger failed to make a decision due to failures in the online system.
- The `CosmicCalo` stream, which receives events matching a cosmic ray signature. This stream is triggered by large energy deposits in the calorimeter system, restricted to empty bunches.

The streams enumerated above are a subset of the numerous specialised physics and detector calibration and monitoring streams. A rate of 1 kHz is allocated to `physics_main`, with lower rates assigned for other streams.

During data taking, a small fraction of events are selected for fast reconstruction (around 1 minute) for online DQ monitoring. At the end of a data-taking run, the primary calibration loop (PCL) commences. A first calibration pass is performed, on the timescale of 48 hours, using the express and calibration streams. This "best effort" initial calibration updates the information stored at Tier-0. The first pass also allows an initial offline DQ assessment, allowing the PCL to be delayed if any issues are flagged for further investigation.

The second pass typically takes place on the timescale of ~ 1 week. During this pass the bulk data processing is performed, along with the final calibration, which

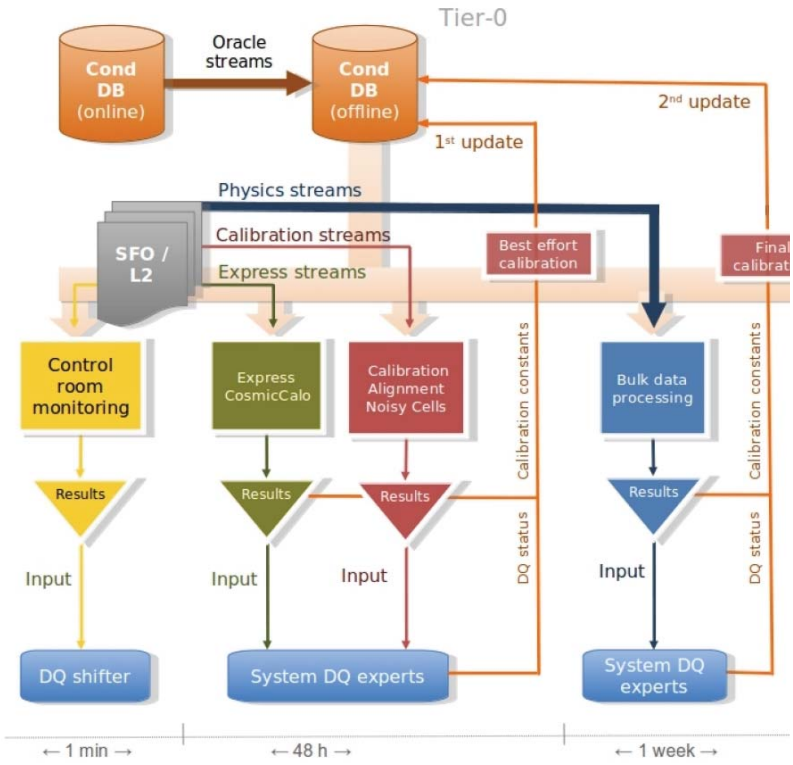

Figure 4.1: Overview of the ATLAS prompt calibration loop and online DQ. Taken from Ref. [115].

is used for a second update at Tier-0. The final calibration procedure includes the finalisation of the ID alignment, correcting for displacements and deformations of the ID subdetectors that take place during a run, and the beamspot determination, which must follow the ID alignment step. The quality of the physics data is assessed in this final step, with a granularity of 1 luminosity block (LB), equivalent to approximately 1 minute of data taking, to produce a "good runs list" (GRL), specifying which LBs are suitable for for physics analysis. The final updated calibrations are used to write the data to the primary ATLAS data format, Analysis Object Data (AOD). An overview of the online DQ and PCL can be seen in figure 4.1.

The output AOD is passed through the ATLAS derivation framework to produce "derived" AODs (DAODs). The derivation framework produces analysis specific DAODs with reduced size, filtering events from the primary AOD and storing a subset of event information, targeting a particular range of signal topologies. The derivation framework can also add additional calibrations and physics objects that can be calculated from the primary event information, but may not be required by all offline analyses. The DAOD is the final data format used in combination with GRLs for physics analysis.

4.2 ATLAS Signature Triggers

This section extends the discussion in 3.2.6, describing trigger selections targeting specific physics signatures. A complete trigger selection, from L1 to HLT is referred to as a trigger *chain*, and the complete list of triggers active during a given data taking period is called the trigger *menu*. The ATLAS trigger menu includes many

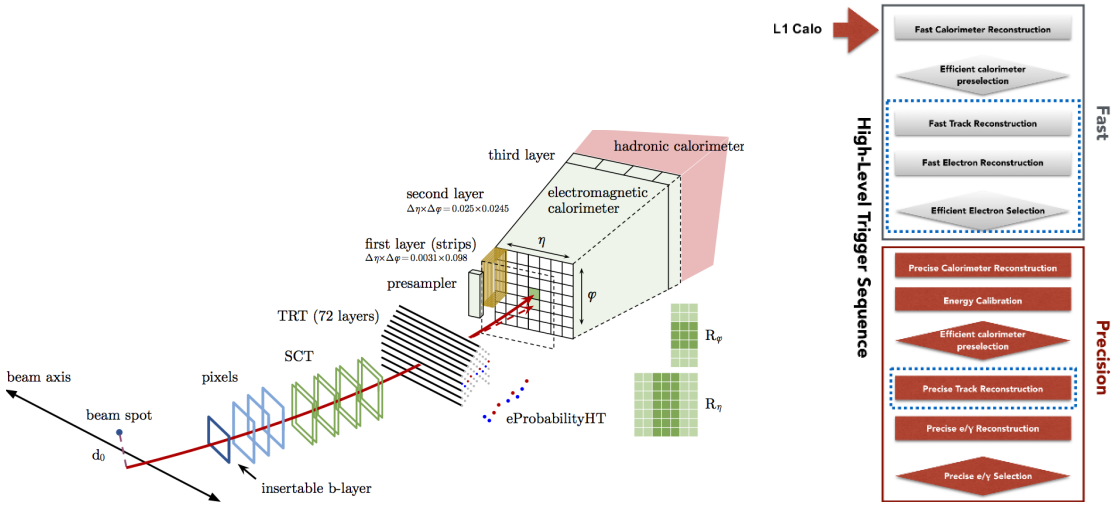

(a) (b)

Figure 4.2: (a) Schematic of the overall e/γ trigger sequence and (b) outline of the individual steps in the e/γ trigger sequence, where the blue dashed line indicates parts of the sequence that apply to electrons only. (a) Taken from Ref. [116] and (b) taken from Ref. [117].

triggers dedicated to a variety of processes. This section focuses on the triggers relevant to the analyses presented later in the text: e/γ , muon, jet and $E_{\mathrm{T}}^{\mathrm{miss}}$ triggers.

4.2.1 Electron and Photon Triggers

The ATLAS e/γ trigger is allocated around 20% of the total 1 kHz trigger rate. At HLT, the full detector granularity is used in the ROI (the ROI structure for e/γ has been described in section 3.2.6). The HLT trigger sequence, illustrated in figure 4.2, proceeds in two main steps: the first step uses fast algorithms to reject events early and the second step applies precision algorithms for efficient identification. This design allows the more time-consuming algorithms to take place at a reduced rate, later in the trigger sequence. This approach is common to all online signature strategies.

The first step in the HLT sequence is the fast calorimeter preselection, which builds energy clusters from from calorimeter cells, of size 0.025×0.025 in η and ϕ, within the ROIs. Electrons and photons deposit most of their energy in the second ECAL layer (see figure 3.9), which is used to find the cell with the largest E_{T} in the ROI. The cluster size depends on the region of the detector: 3×7 cells in the barrel and 5×5 cells in the end-caps. Electron and photon identification is based on the total cluster E_{T} and a number of shower shape variables. Shower shape variables are based on ratios and widths (defined in terms of the energy weighted RMS) of grouped calorimeter cells within the cluster, and are described in more detail in section 4.4.2. Following the fast calorimeter preselection is the fast track reconstruction, using hits from the silicon detectors. Tracks with $p_{\mathrm{T}} > 1$ GeV are matched to calorimeter clusters if they satisfy angular separation requirements. Electron and photon candidates are identified with calorimeter clusters with and without matching tracks, respectively.

Precision reconstruction follows the fast HLT sequence, with the online iden-

tification procedures kept as close as possible to offline selections, within resource constraints. A cut-based selection is applied for photon identification and a likelihood (LH) based discriminant is used for electron identification. The LH method is a simple multi-variate analysis (MVA) technique based on the *projective likelihood estimator approach* [118]. The LH method builds a likelihood discriminant:

$$d_{\mathcal{L}} = \frac{\mathcal{L}_S}{\mathcal{L}_S + \mathcal{L}_B} \tag{4.1}$$

from geometric sums $\mathcal{L}_{S(B)}$ of probability density functions $P_{S(B)}$, defined by:

$$\mathcal{L}_{S(B)}(\vec{x}) = \prod_{i=1}^{n} P_{S(B),i}(x_i), \tag{4.2}$$

where the subscript S (B) denotes signal (background), and $\vec{x}$ is a vector of 22 electron track- and shower-based variables. The discriminant $d_{\mathcal{L}}$ displays a sharp peak at zero for background and unity for signal; it is transformed into a broader distribution using the inverse sigmoid function:

$$d'_{\mathcal{L}} = -\tau^{-1} \ln\left(d_{\mathcal{L}}^{-1} - 1\right), \tag{4.3}$$

where τ is a parameter fixed to 15, to form the following operating points (OPs): *lhvloose*, *lhloose*, *lhmedium* and *lhtight*. Here the *lh* simply denotes the LH-based selection, and the *vloose* denotes "very" loose. Each working point selects on a higher value of $d'_{\mathcal{L}}$, such that the sample of electrons selected by tighter OPs are subsets of those selected by looser OPs. The LH method was introduced online for electrons in Run 2, and offers a significant rate reduction for an equivalent efficiency compared with the cut-based selection used for electrons in Run 1.

Isolation requirements can be applied at HLT to improve discrimination against hadronic activity. For electrons, track isolation is used, defined as the ratio of the p_{T} sum of non-electron associated tracks in a given ΔR cone, to the p_{T} of the electron candidate. The cone is optimised for different triggers: from 2016 on wards variable track isolation is used, where the cone radius is defined as 10 GeV / p_{T} where the p_{T} is that of the electron candidate, up to a maximum radius of 0.2, describing a cone that narrows as the electron candidate p_{T} increases. Thus the isolation requirement becomes stricter for electrons with high p_{T} , which are expected to be more isolated from hadronic activity.

HLT items with loose selection criteria are required by ATLAS for a number of purposes, for example as part of a multi-object trigger chain. Loose triggers with high rates can be set a *prescale*, as for L1 items, to control the rate. The quoted trigger prescale is the reciprocal of the fraction of events that the trigger in question is permitted to select during data-taking. The analyses presented in the main body of this text use only the lowest E_{T} threshold, *unprescaled* electron trigger. As the instantaneous luminosity of the LHC increased during Run 2, the lowest unprescaled single electron trigger selection was tightened in order to control the rate. The following triggers were used in 2015 and 2016:

- `e24_lhmedium_nod0` was used in 2015. Here e denotes that it is an electron trigger, 24 denotes a 24 GeV E_{T} treshold and *nod0* denotes that no transverse impact parameter requirements are applied (in contrast to offline electron identification).

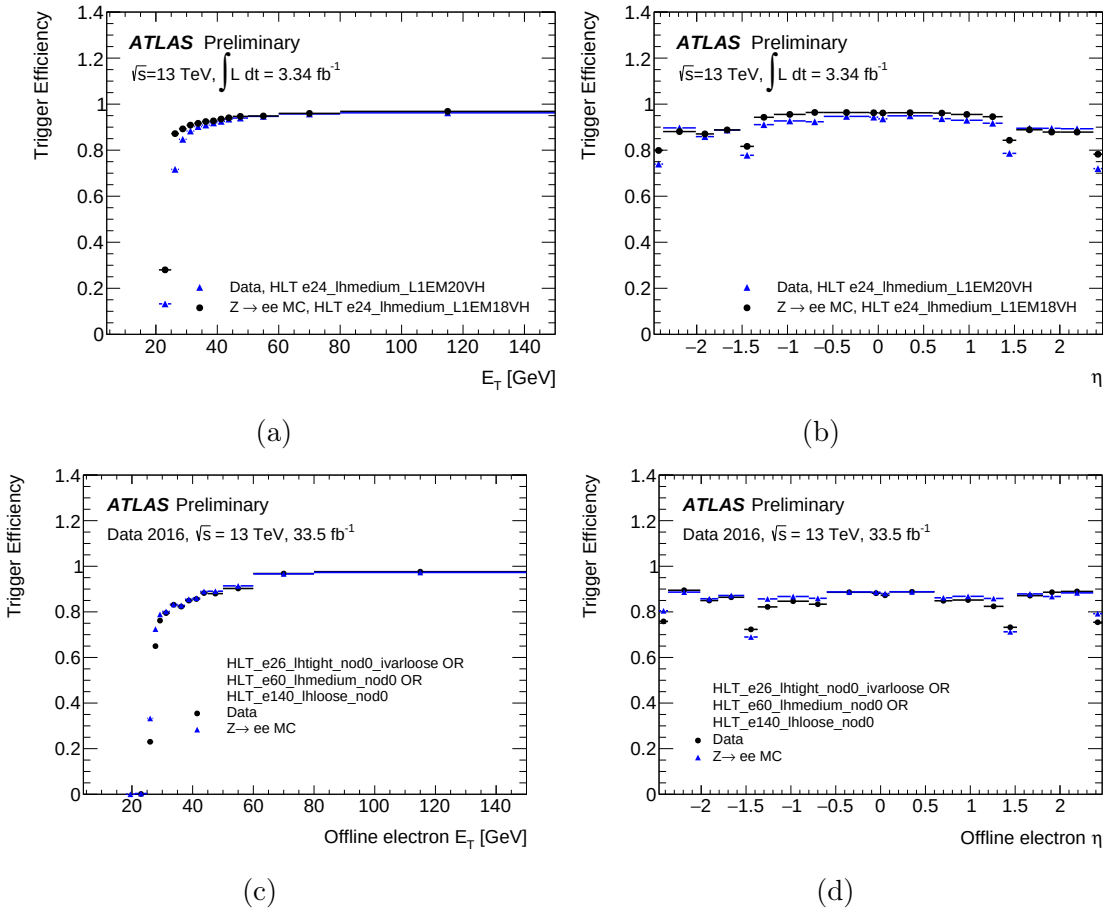

Figure 4.3: Primary electron trigger performance in 2015 and 2016. Efficiencies are shown for 2015 data as a function of (a) E_{T} and (b) η and for 2016 data as a function of (c) E_{T} and (d) η. The efficiency for the primary trigger in 2016 is shown as a logical OR with looser, higher threshold triggers. All efficiencies are measured with respect to offline isolated electrons, with tight selection criteria, using the Tag-and-Probe method, described in detail in appendix A. The efficiency in data is compared to the efficiency in simulated $Z \rightarrow ee$ decays. The error bars show binomial uncertainties. Taken from Ref. [121].

- `e24_lhtight_nod0_ivarloose` was used in 2016 until the peak instantaneous luminosity reached 10^{34} cm^{-2}s^{-1}. The *ivarloose* in the name of the trigger indicates that variable track-based isolation requirements are applied. The tighter identification criteria represent a tradeoff, sacrificing efficiency in order to control the trigger rate.

- `e26_lhtight_nod0_ivarloose` was used after the peak instantaneous luminosity exceeded 10^{34} cm^{-2}s^{-1}. The increased trigger threshold further reduces the trigger rate for the increased luminosity [119, 120].

These triggers are used as part of a logical OR with higher threshold, looser identification and non-isolated triggers. This strategy gives a significant improvement in efficiency at high E_{T}, where track-isolation losses become important. The cost in additional trigger rates is low due to the significantly lower cross section for production of high E_{T} electrons.

The HLT items are used in conjunction with L1 items to form a complete trigger chain. The same strategy is employed for the L1 items, with the same tradeoff between maximising efficiency and keeping the overall rates under control. The following L1 items were used in 2015 and 2016 [119, 120]:

- `L1EM18VH` was the L1 item used in 2015. The nomenclature is as follows: *L1* indicates an L1 item, *EM* indicates an e/γ selection, 18 is the E_{T} threshold in GeV, *V* indicates that the threshold is η dependent and *H* that a hadronic core isolation threshold is applied.

- `L1EM18VHI` was used in 2016 until the peak instantaneous luminosity reached 10^{34} cm^{-2}s^{-1}. The additional *I* in the L1 item name indicates that electromagnetic isolation thresholds are also applied.

- `L1EM22VHI` was used in 2016 after 10^{34} cm^{-2}s^{-1} was reached. Again, the increased threshold is to reduce the trigger rate at the higher luminosity.

The primary electron trigger performance at HLT is summarised in figure 4.3. In 4.3c the boost in efficiency from the logical OR with looser, higher threshold triggers can clearly be seen by the discontinuity at 60 GeV where the looser triggers become efficient. The performance versus η shows a drop in efficiency at the end-caps and crack region $1.37 < |\eta| < 1.5$, where additional material is present to service the detector.

For offline analysis, scale factors are applied to correct for deviations between the trigger efficiency measured in data, and the efficiency predicted by MC simulation. The measurement of electron trigger efficiencies in data and MC, and the derivation of these scale factors for the whole electron trigger menu formed the bulk of the author's qualification work for the ATLAS Collaboration. In appendix A, a complete discussion of the methodology and results of this work is given. Furthermore, the discussion of the electron trigger menu and strategy is extended to place this work in context.

4.2.2 Muon Triggers

The HLT muon trigger sequence [122] begins with the fast reconstruction of tracks using only the muon spectrometer. The muon candidate is built by fitting the drift times and track hit positions from the MDTs. The muon candidate p_{T} is assigned using a look-up table. Next, the muon candidate is updated by performing a combined fit, using tracks from the muon spectrometer and tracks from the ID.

The next stage is the precision reconstruction in the ROI, using information from all regions of the muon spectrometer. The muon candidate is extrapolated to the ID to form a combined muon candidate, this time using precision reconstruction. If the combination fit fails, which may happen for softer muon candidates, another fitting stage takes place, extrapolating instead from the ID out to the muon spectrometer. Muon candidates are required to pass a set of identification criteria based on track fit quality, the p_{T} difference in the ID and muon spectrometer and charge and momentum significance, defined as the measured value normalised to its measured uncertainty. Finally, isolation requirements can be applied for improved rejection against hadronic activity. The lowest unprescaled muon triggers used in 2015 and 2016 are [119, 120]:

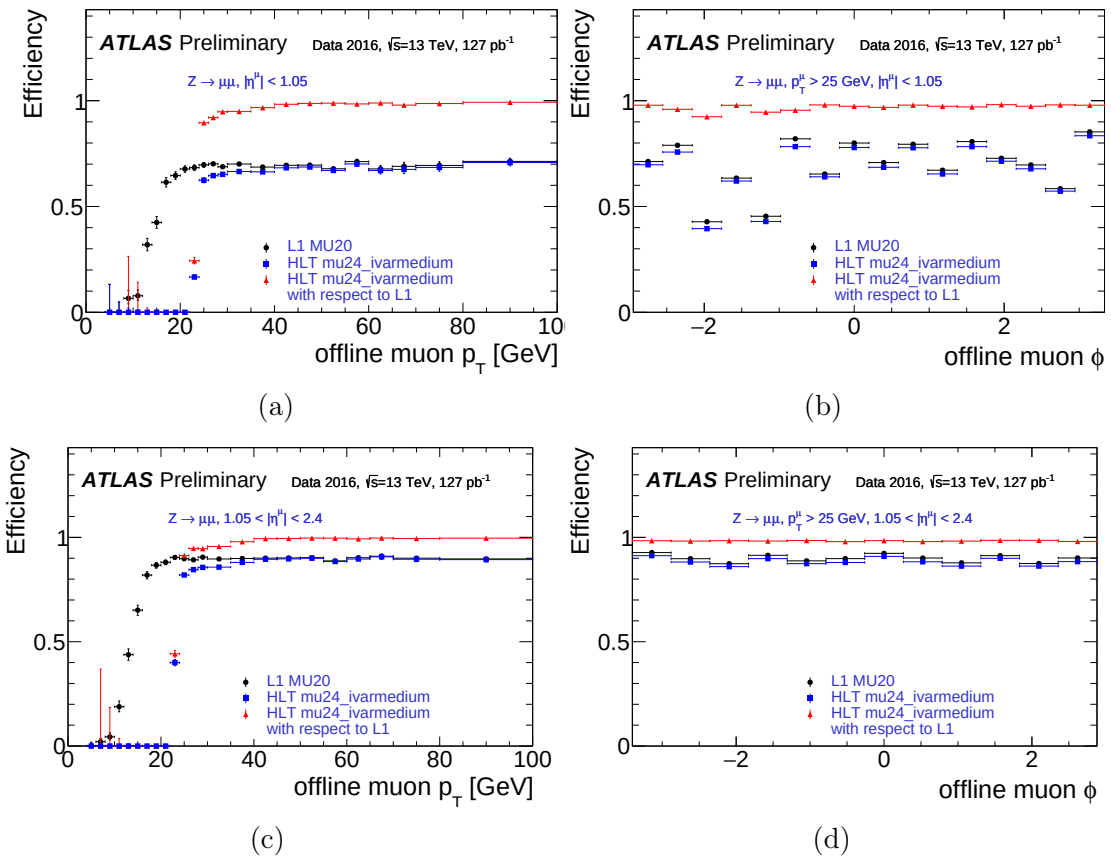

Figure 4.4: Primary muon trigger performance in 2016. Efficiencies are shown in the barrel as a function of (a) p_{T} and (b) ϕ and in the end-caps as a function of (c) p_{T} and (d) ϕ. All efficiencies are measured using the Tag-and-Probe method, described in detail in appendix A, with respect to offline isolated muons satisfying medium identification criteria. The efficiency in data is compared to the efficiency in simulated $Z \to \mu\mu$ decays. The error bars show binomial uncertainties. Taken from Ref. [123].

- `mu20_iloose` in 2015, where *iloose* refers to a loose, fixed isolation requirement.
- `mu24_ivarmedium` in 2016, until an instantaneous luminosity of 10^{34} cm^{-2}s^{-1} was reached.
- `mu26_ivarmedium` in 2016, after an instantaneous luminosity of 10^{34} cm^{-2}s^{-1} was exceeded.

As for the single electron triggers, these are used as part of a logical OR with non-isolated triggers to regain efficiency from isolation losses at higher p_{T} . These primary HLT muon triggers were used in combination with the following L1 items:

- `L1MU15` in 2015, where *MU* indicates that the L1 muon trigger is being used.
- `L1MU20` in 2016.

The performance of the HLT muon triggers in 2016 data is summarised in figure 4.4. The differences in efficiency between the barrel and the end-caps arise from

differences in the geometric acceptance and local detector inefficiencies. The lower efficiency seen in figure 4.4b in the range $-2.0 < \phi < -1.6$ corresponds to the barrel region containing toroid coils.

4.2.3 Jet Triggers

For jet reconstruction at HLT the full calorimeter system is scanned for *topological clusters* [124, 125]. The clustering algorithm proceeds as follows:

- **Seed Finding:** Clusters with an energy to noise ratio meeting a particular threshold t_{seed} are identified as seed clusters, or *proto-clusters*. The noise is computed as the sum in quadrature of the estimated RMS of electronic noise and the estimated pileup contribution.
- **Neighbouring Cluster Finding:** Starting from the seed with highest energy to noise ratio, topological clusters are built from proto-clusters by considering the (approximately) eight neighbouring cells in the same calorimeter layer. Neighbouring cells are incorporated into the cluster if they meet a given energy to noise ratio $t_{\text{neighbour}}$, with proto-clusters merged if they share a neighbour that meets the threshold.
- **Finalise:** Remaining proto-clusters that meet a given E_{T} threshold are added to the collection of topological clusters. The rest are discarded.

Topological clusters are used as inputs for offline-like jet reconstruction. The offline choice for jet reconstruction at ATLAS in 2015 and 2016 was the anti-k_t algorithm [126], which is further described in section 4.4.4. Jet triggers are sensitive to pileup interactions, both in-time pileup interactions from the same bunch crossing, and out-of-time pileup interactions that arrive earlier or later than the nominal beam crossing. Pileup suppression is applied using noise thresholds, which are tuned to each data-taking period to reflect pileup conditions.

For the purposes of the analyses presented in this thesis, jet triggers with low energy thresholds are required. The acceptance rate for jet triggers with low thresholds is high, leading to unmanageable trigger rates. As a result, low threshold jet trigger chains are typically prescaled for the L1 and HLT items. The nomenclature for jets is simply L1 or HLT with j used to denote a jet trigger, followed a number indicating the threshold. The ATLAS single jet trigger performance is summarised in figure 4.5. At the L1 jet objects are calibrated at the EM scale, resulting in a large difference between the L1 trigger threshold and the p_{T} at which full efficiency is reached. The HLT triggers reach full efficiency quickly, even in 2016 with harsher pileup conditions, demonstrating the effectiveness of pileup suppression procedures.

4.2.4 Missing Transverse Energy Triggers

The $E_{\text{T}}^{\text{miss}}$ triggers primarily target events with energetic invisible particles. The basic definition of the $E_{\text{T}}^{\text{miss}}$ variable is

$$E_{\text{T}}^{\text{miss}} = |\boldsymbol{p}_{\text{T}}^{\text{miss}}| = |-\sum_{i} p_{\text{T}}(i)|, \tag{4.4}$$

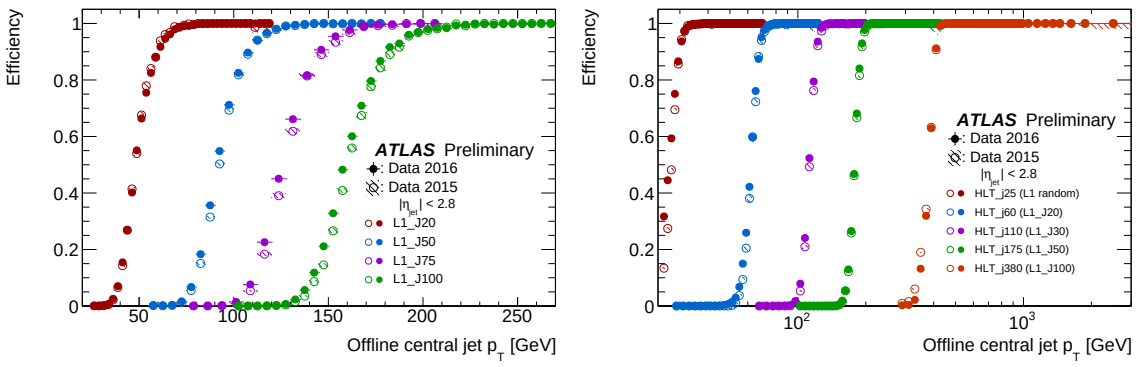

(a) (b)

Figure 4.5: Single jet trigger performance in 2015 and 2016. The efficiency is shown in the central region $|\eta| < 2.8$ for (a) L1 and (b) HLT single jet triggers. The samples used for the efficiency measurements are selected by a fully efficient, lower threshold jet trigger. Taken from Ref. [127].

where i runs over all physics objects in the event. Since the transverse momentum is conserved, a large value for $E_{\mathrm{T}}^{\mathrm{miss}}$ indicates an invisible object that was not reconstructed by the ATLAS detector. High $E_{\mathrm{T}}^{\mathrm{miss}}$ can also be caused by mis-measurement of jets, for example in energetic dijet events where the measurement of each of the jet energies fluctuates in the opposite direction. The production cross section for events with mis-measured $E_{\mathrm{T}}^{\mathrm{miss}}$ is relatively high. This has the consequence that the trigger rates cannot be controlled by the trigger threshold only without seriously affecting the efficiency for $E_{\mathrm{T}}^{\mathrm{miss}}$ based analyses. This has motivated the development of a variety of $E_{\mathrm{T}}^{\mathrm{miss}}$ calculation methods for online data collection [113]. The techniques most relevant to the analyses described in following chapters are described below:

- **Cell algorithm (`xe`):** this is calculated from individual cells in the Tile and LAr calorimeters, in the massless approximation $E \approx |\vec{p}|$ so that

$$p_{x,i} = E_i \sin\theta_i \cos\phi_i, \quad p_{y,i} = E_i \sin\theta_i \sin\phi_i. \tag{4.5}$$

  Noise suppression is applied with the following requirements:

$$|E_i| > 2\sigma_i, \quad E_i > -5\sigma_i \tag{4.6}$$

  for a cell to be considered in the $E_{\mathrm{T}}^{\mathrm{miss}}$ calculation. The final result is the magnitude of the 2-dimensional vector obtained in this way.

- **Jet-based algorithm (`xe_tc_mht`):** the $E_{\mathrm{T}}^{\mathrm{miss}}$ is directly taken from the $\boldsymbol{p}_{\mathrm{T}}^{\mathrm{miss}}$ calculated as the negative sum of all jet objects identified using the jet trigger algorithm described in the previous section.

- **Topo-cluster algorithm (`xe_tc_lcw`):** again the massless approximation is used. The $\boldsymbol{p}_{\mathrm{T}}^{\mathrm{miss}}$ is instead built from topological clusters (see section 4.4.4), used in jet reconstruction algorithms.

- **Pileup suppression algorithm (`tc_tc_pueta`):** as `xe_tc_lcw` with additional pileup suppression to improve $E_{\mathrm{T}}^{\mathrm{miss}}$ resolution in the harsher pileup

conditions seen in 2016 and later. The pileup suppression algorithm calculates the mean and RMS energy of topological clusters in ten equally spaced η bins in the range $-5.0 < \eta < 5.0$, defining "rings" in the detector. The mean for each region is then recalculated using only clusters with $E < 2\sigma$, representing an estimate of the pileup contribution to the energy of the ring. The pileup contribution to the energy of a given cluster is then estimated as:

$$E_{\text{cluster}}^{\text{pileup}} = \frac{E_{\text{avg,ring}}^{\text{pileup}}}{\Omega_{\text{ring}}} \times \Omega_{\text{cluster}}, \tag{4.7}$$

where $E_{\text{avg,ring}}^{\text{pileup}}$ is the average pileup energy in a given ring, calculated as described above, Ω_{cluster} is the solid angle occupied by a given cluster and Ω_{ring} is the solid angle occupied by the corresponding ring. $E_{\text{cluster}}^{\text{pileup}}$ is subtracted from each cluster, and the $E_{\text{T}}^{\text{miss}}$ recalculated to give the final pileup corrected value.

- **Pileup fit algorithm (`tc_tc_pufit`):** again as `xe_tc_lcw`, using a different pileup suppression algorithm. The pileup fit algorithm calculates the p_{T} and E_{T} in 112 towers, each approximately 0.71×0.79 in η and ϕ. Any tower with E_{T} less than 45 GeV is assumed to result from pileup. The average pileup energy density is computed as the sum of all towers below this threshold scaled by the total area in η and ϕ space of those towers. The pileup contribution for each tower is then estimated by performing a fit, using the average pileup density and constraining the total $E_{\text{T}}^{\text{miss}}$ from pileup contributions only to be zero within resolution. As for `xe_tc_lcw`, the pileup contribution in each cell is subtracted, and the $E_{\text{T}}^{\text{miss}}$ recalculated.

Since the methods described above are based on calorimeter information only, muons are not included in the $E_{\text{T}}^{\text{miss}}$ calculation. For this reason, $E_{\text{T}}^{\text{miss}}$ triggers can be the most efficient way to select highly energetic muons online.

In 2015, the lowest threshold unprescaled $E_{\text{T}}^{\text{miss}}$ trigger used was the jet-based algorithm, with a threshold of 70 GeV. In 2016 a variety of $E_{\text{T}}^{\text{miss}}$ triggers based on the different algorithms described above were used, with the trigger threshold increased from 2015 to control rates, but also depending on which algorithm was used. These triggers were all unprescaled, with the topological clustering component of the algorithm shared between them, so that running them all in parallel was relatively inexpensive in terms of trigger rates.

Figure 4.6 shows $E_{\text{T}}^{\text{miss}}$ trigger efficiencies in 2015 and 2016. In 4.6a, the trigger turn-on curve is compared for the same threshold, using different calculation algorithms. In 4.6b the comparison is for different trigger thresholds and algorithm combinations with similar rates that were left unprescaled during data-taking. The cell algorithm requires a much higher threshold for a manageable rate, which results in a slow turn-on and a lower plateau efficiency. The topological clustering and jet-based algorithms allow for a lower threshold, reaching full efficiency by ~ 200 GeV.

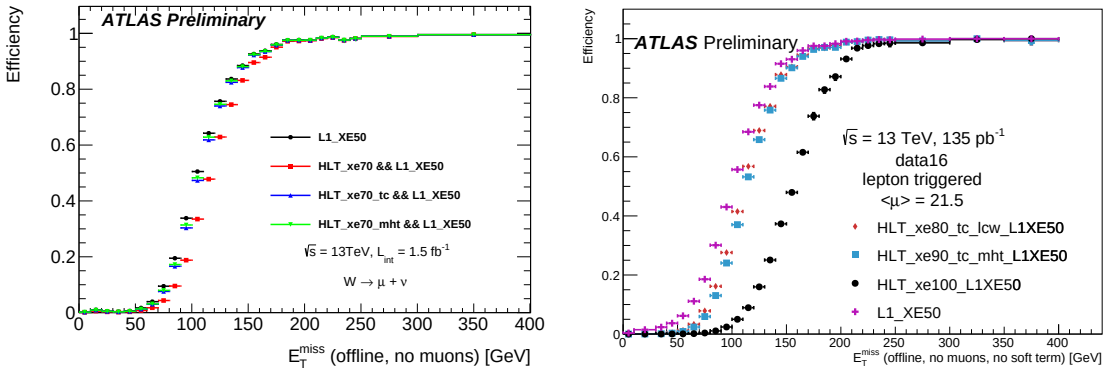

(a) (b)

Figure 4.6: Missing transverse energy trigger performance in 2015 (a) and 2016 (b). The efficiencies shown in (a) are calculated using events selected by a single lepton trigger and applying $W \to \mu\nu$ selection criteria. The efficiencies for (b) are calculated from events selected by single lepton triggers. Taken from Ref. [128].

4.3 Monte Carlo Simulation

So far in this chapter, the acquisition of data from pp collisions using the ATLAS detector has been described. A key tool in interpreting the data is MC simulation of signals and individual background processes. MC methods use pseudo-random numbers to evaluate integrals. Due to the statistical nature of these methods, the integral converges like $1/\sqrt{N}$, independent of the number of dimensions [129]. Thus they are particularly useful in particle physics calculations, where integrals with complex integrands and many dimensions are common.

4.3.1 Event Generation

The physics of pp scattering involves QCD processes at very different energy scales. At low energy scales, due to asymptotic freedom (section 2.1.5), perturbative QCD breaks down. In particular, the momentum distribution of partons within the protons, the PDF, is non-perturbative. To simulate pp collision events, the *factorisation theorem* [130] is exploited. The factorisation theorem states that a cross section can be computed through a product of probability functions [131]:

$$\sigma_{pp\to X} = \sum_{i,j} \int dx_i dx_j f_i(x_i, \mu_F^2) f_j(x_j, \mu_F^2) \hat{\sigma}_{ij\to X}(x_i, x_j, \mu_F^2, \mu_R^2). \tag{4.8}$$

Here $\sigma_{pp\to X}$ is the cross section for the pp collision to produce X and the sum runs over all combinations of partons that can initiate the process. The function $f_i(x_i, \mu_F^2)$ is the PDF for the parton i, more precisely the probability for the parton i to be found with momentum fraction x_i. μ_F^2 and μ_R^2 are the factorisation and renormalisation scales, respectively. The factorisation scale is somewhat arbitrary, representing a scale that separates the high- and low-energy processes. Since the cross section depends on this scale, it must be varied to determine the associated systematic uncertainty.

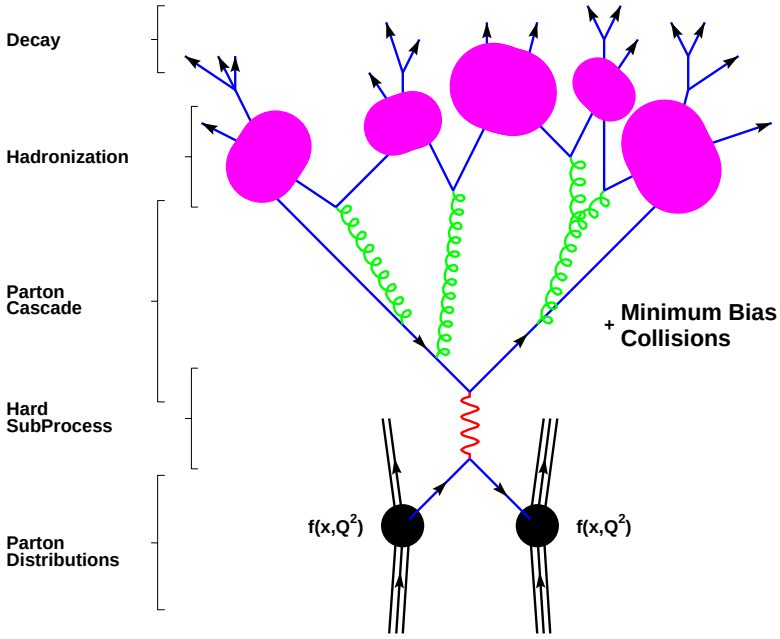

Figure 4.7: Diagram showing the stages of MC simulation of pp collisions. Taken from Ref. [132].

The factorisation theorem allows the pp interaction to be divided into distinct steps, with the modelling of the partons within the proton factorised out. The steps for simulating a pp scattering event for a given process, shown in figure 4.7, are thus:

- **Parton Distributions:** The PDFs can be applied universally since they are independent of the process. They are determined using data from hadron collider and deep inelastic scattering experiments at fixed energy scales. The evolution of the PDF to LHC energy scales is calculated using the DGLAP equations [133–135]. The PDFs used for this thesis are presented in Refs. [136–138].

- **Hard Subprocess (Matrix Element):** The next stage is to calculate the cross section for two of the partons from the colliding protons undergo hard-scattering to initiate process X. This amounts to calculating the scattering matrix relating the final and initial states, and is also referred to as the Matrix Element (ME) calculation. Due to the high energy of the hard subprocess it can be calculated perturbatively.

  The cross section for partons to initiate the process X from equation 4.8 can be expressed [131]

$$\hat{\sigma}_{ij\to X} = \int \mathrm{d}\Phi_n \frac{1}{2\hat{s}} |\mathcal{M}_{ij\to X}(\Phi_n; \mu_R, \mu_F)|^2. \tag{4.9}$$

  Thus the partonic cross section to produce the final state X depends on the final state phase space Φ_n and the corresponding ME squared, averaged over

the initial spin-states and colour degrees of freedom, $|\mathcal{M}_{ij\to X}|^2$. It also depends on the parton flux $1/(2\hat{s}) = 1/(2x_i x_j)$ where $\hat{s}$ is the hadronic centre-of-mass energy squared. The ME can be expressed as a sum over Feynman diagrams:

$$\mathcal{M}_{ij\to X} = \sum_k \mathcal{F}^{(k)}_{ij\to X}, \tag{4.10}$$

where $\mathcal{F}^{(k)}_{ij\to X}$ is the kth diagram and the sum runs over all possible diagrams for the process at a given order.

The ME calculation is usually truncated to a fixed order in perturbation theory, including effects from virtual corrections (loops) and real emissions (legs). At fixed order, according to the Kinoshita-Lee-Nauenberg (KLN) theorem [139, 140], order by order, the divergences from final-state collinear splitting and soft emissions exactly cancel against virtual corrections to the total cross-section. If the multiplicity of legs exceeds the multiplicity of loops, this cancellation is spoiled, leading to infrared divergences. This can be handled by including only hard contributions that yield finite results in the ME calculation. The soft contributions are then calculated in the parton shower stage.

- **Parton Cascade or Shower:** The partons participating in the hard collision may emit further partons due to their colour charge. This can be due to incoming partons of the hard subprocess (initial state) or outgoing partons from the hard subprocess (final state), which may in turn radiate further partons. As a result, a parton *cascade*, or parton *shower* develops.

  An approximation scheme is used to simulate parton showering, which includes only the dominant contributions associated with soft emissions at each order. If the hard subprocess produces partons of type i, with cross section σ_0, the cross section for collinear splitting to produce a parton of type j with momentum fraction z is given by [131]:

$$\mathrm{d}\sigma \approx \sigma_0 \sum_i \frac{\alpha_s}{2\pi}\frac{\mathrm{d}\theta^2}{\theta^2}\mathrm{d}z\mathrm{d}\phi P_{ij}(z,\phi), \tag{4.11}$$

  where θ and ϕ are the angles of splitting, z is the momentum fraction carried by j and P_{ij} is the *splitting function*, describing the probability distribution for the splitting process $i \to ij$. Examples of such processes are $q \to qg$, $g \to gg$ and $g \to qq$. Based on equation 4.11, a Sudakov form factor [141] can be derived:

$$\Delta_i(Q^2, q^2) = \exp\left\{-\int_{q^2}^{Q^2}\frac{\mathrm{d}k^2}{k^2}\frac{\alpha_s}{2\pi}\int_{Q_0^2/k^2}^{1-Q_0^2/k^2}\mathrm{d}z P_{ij}(z)\right\}, \tag{4.12}$$

  which describes the probability for a virtual gluon at scale Q^2 to evolve to a scale q^2 without radiating. Q_0 is a resolution criterion: two partons are considered resolvable only if they meet this threshold. In the MC simulation, a parton shower is developed for each parton involved in the hard subprocess by sequential application of equation 4.12 to determine if splitting takes place, until all partons fall below a resolvable threshold $Q_0 \approx 1$ GeV.

The above procedure applies to final state radiation from partons emerging from the hard subprocess. For initial state radiation from incoming partons, PDFs must be included in the Sudakov form factor calculation. In this case it is therefore more efficient to use *backward evolution*. Here, the momentum fraction of each incoming parton is chosen, within kinematic constraints. The incoming partons are then propagated backwards, gaining energy at each stage until again a suitable threshold is reached.

- **Parton Shower to Matrix Element Matching:** The results of the ME and parton showering must be combined in the event generation. Since both procedures are carried out independently, and have overlapping phase space, care must be taken not to double count physics objects. Two matching schemes widely used by ATLAS are the those developed by Michelangelo L. Mangano *et al.* [142] and Catani-Krauss-Kuhn-Webber [143], known as the MLM and CKKW schemes, respectively.

  The general procedure [144] for ME-parton shower merging is to first define a jet measure. This can then be used to calculate cross sections for the process under consideration, in association with n jets, up to some maximum number. Samples of hard partons can then be generated according to these cross sections, with each kinematic configuration of partons rejected or accepted according to probability distributions based on Sudakov form factors and running couplings. If the sample of partons is rejected then a new sample must be generated. Once a sample of partons is accepted, the showering is initiated, with shower configurations that overlap with the ME phase space vetoed. Matching schemes differ in the jet definition used for the ME, the acceptance of parton samples, the initiation of the parton shower and the method of phase space separation.

  In the CKKW matching, "shower history" is built by clustering the partons according to the k_t algorithm, forming a tree-like structure of vertices connected by branches. Weights are attached to each branch based on the Sudakov factor and α_s connecting the vertices. Thus each ME is re-weighted according to the shower history. The initialisation of the shower is chosen to give a smooth transition between the ME and parton shower, and any parton shower emission is vetoed if it is harder than some threshold.

  The MLM procedure clusters partons instead based on a cone algorithm defined by some radius R_{min}. A similar tree-like structure is formed in this way, again with weights attached to each branch. An event is considered matched if each parton is contained within a jet. If the event is not matched, it is rejected. This can happen if, for example, two partons are too close to produce independent jets according to the R_{min} measure, or if a parton is too soft to generate its own jet and is not matched. The removal of events containing such partons prevents double counting of collinear double logarithms and single logarithms in the ME and parton shower.

- **Hadronisation and Decay:** As the parton showers develop, the interaction scale falls due to the running coupling of the strong force (section 2.1.5). When the energy scale falls below $\sim$ 1 GeV, hadronisation becomes dominant and the partons begin to form colourless states from the vacuum. Hadronisation is

governed by non-perturbative processes so that phenomenological models must be used for this stage of the simulation. The most commonly used models are the string model [145, 146] and the cluster model [147, 148].

Based on non-perturbative QCD simulations, the potential energy due to colour charge between partons is expected to grow linearly with the parton separation for large distances. In the string model, the potential energy between partons is represented by a gluonic string. As the separation increases, partonic kinetic energy is converted to potential energy of the string. Once the potential energy is of the order of hadronic masses, it can break to produce a new $q\bar{q}$ pair from the vacuum. A new string will form between the new pair as their separation increases; this process will continue to produce new particle pairs until only colour singlet states remain.

The cluster model exploits the *preconfinement* property of QCD [149], where partons in showers developing at scales much lower than that of the hard subprocess cluster into colour singlet combinations with an invariant mass distribution that depends on the parton shower scale but not on the properties of the hard subprocess. These colour singlet states are identified with the stable final state hadrons.

- **Underlying Event:** This refers to additional hadronic activity in the final state that is not associated to the hard subprocess itself. The underlying event originates primarily from *spectator* partons within colliding hadrons that do not participate directly in the hard-scattering. This component is simulated by phenomenological models, using measurements of the underlying event as inputs. The underlying event is measured in data collected by minimum-bias triggers [150], which is primarily composed of events with no identifiable hard collision. A secondary source is colour connection [151] between hard partons and beam remnants, which is also simulated using phenomenological models [152, 153].

- **Pileup:** Further hadronic activity is present in the final state due to pileup collisions. These can be from in-time or out-of-time pileup. In-time pileup arises from soft interactions between protons in the same bunch crossing, and is simulated using minimum-bias data in a similar way to the underlying event. Out-of-time pileup is simulated by considering previous bunch crossings and detector time response. The pileup collisions are simulated and then overlaid on to the MC event generated by the previous steps.

4.3.2 Monte Carlo Generators

The MC simulation steps outlined above are implemented in a number of existing programs. Included below is a brief description of the MC generators used in this thesis:

- `Sherpa` **[154]:** a general purpose tool for simulating pp collisions, capable of multi-leg ($2 \to n$) leading-order (LO) and next-to-leading-order (NLO) calculations. The CKKW matching scheme is used and a phenomenological cluster-hadronisation model is used for parton fragmentation.

- `Pythia` **[155]:** a standard tool for LO simulation of $2 \to 2$ processes. Initial- and final-state parton shower algorithms are based on p_{T} ordered evolution [156] and hadronisation is based on the string model.

- `Herwig` **[157]:** another general purpose generator for $2 \to 2$ processes at LO. The parton showering is ordered by opening angle and the cluster model is used for hadronisation and the underlying event.

- `MadGraph` **[158]:** capable of handling LO and NLO calculations for $2 \to n$ processes, with no parton showering. In this thesis `MadGraph5_aMC@NLO` is used for the ME calculation, interfaced to `Pythia` for parton showering, hadronisation and simulation of the underlying event.

- `Powheg` **[159]:** used for calculating the ME at NLO. For the analyses in this thesis, it was interfaced to either `Pythia` or `Herwig` for showering, hadronisation and the underlying event.

4.3.3 ATLAS Simulation

The output of the MC generators is a sample of events recorded in the `HepMC` format [132]. An event is essentially a list of particles with corresponding four-vectors. The next stage is to simulate the detector response to these particles, using the ATLAS simulation infrastructure [160], which is integrated into the ATLAS software framework `Athena` [114]. The detector simulation is implemented using `Geant` [161], a toolkit for simulating the passage of particles through matter. The processing time for full ATLAS simulation using `Geant` is on the order of several minutes per event. The calorimeter system takes up more than 90% of this time. Fast simulation (`ATLFAST-II`) is available using the ATLAS `FastCaloSim` package [162], which parameterises the calorimeter response, reducing processing time to seconds per event.

4.4 Event Reconstruction

Processed ATLAS data contain event-by-event detector response information. MC has the same information, with an additional *truth* record of the particle inputs and their corresponding four-vectors. The next stage is to reconstruct physics objects based on the detector response. The same reconstruction is applied in data and MC, and is less restricted by time considerations than the trigger reconstruction described in section 4.2. This section describes the reconstruction of physics objects important for this thesis.

4.4.1 Tracking and Vertex Reconstruction

ATLAS track reconstruction employs an "inside-out" strategy [163], beginning with the silicon detectors and extending tracks to the TRT. Raw measurements in pixels and strips in the same sensor are merged into clusters based on a connected component analysis [164]. These clusters are used to define three-dimensional *space-points* describing where charged particles have traversed the active material of the detector.

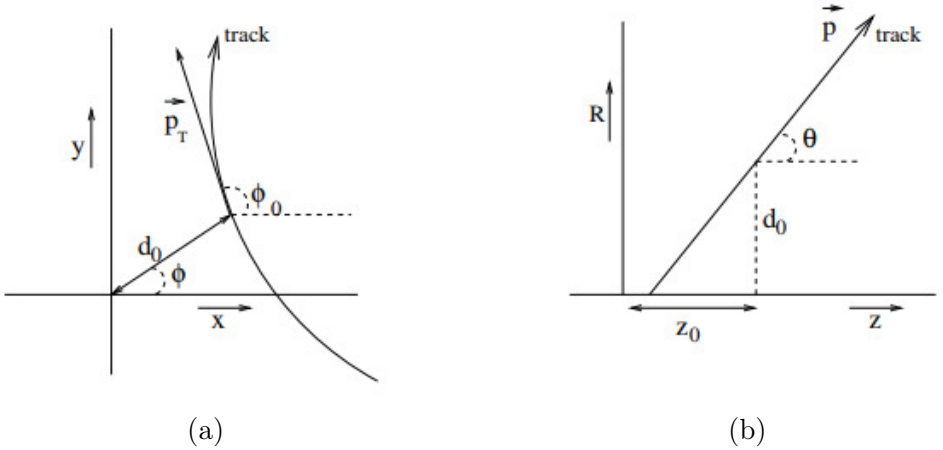

(a) (b)

Figure 4.8: Illustration of the perigee track parameterisation in (a) the transverse plane and (b) the $R-z$ plane. Taken from Ref. [168].

Seed tracks are then defined from sets of three space-time points. Quality requirements, based on impact parameter, reconstructed p_{T} and overlapping space-points, are applied to obtain a sample of seeds that are likely to produce high-quality tracks. Selected seeds are then passed to a Kalman filter [165] which incorporates space-points that are consistent with the trajectory of the seed.

The resulting collection of track candidates may include many overlapping, incomplete and fake tracks. Fake tracks result primarily from mis-allocation of hits from other tracks, but in some cases may arise from randomly coincidental silicon hits. An ambiguity solving algorithm [166] is applied which builds a quality score for each track candidate based on: p_{T} , η, minimum hits in the pixel detector and SCT, maximum number of shared hits and a maximum number of "holes", sensitive regions of the detector lying within the track trajectory with no reading. If multiple tracks overlap, the track with the highest score is chosen for further processing and the others removed. The solver also applies a set of selection criteria, based on the same variables as the quality requirements described above, to further reject incomplete and fake tracks. A neural network clustering algorithm (NN) assists the ambiguity solver [167] in cases where a cluster is shared by multiple track candidates. The NN identifies merged clusters based on the measured charge, relative positions of pixels within the cluster and the incident angle of track candidates.

Remaining tracks are then used as inputs for an extension algorithm, which looks for compatible track segments in the TRT. The algorithm extrapolates the track trajectory to build a road through the TRT, and performs a line fit to determine the compatibility of TRT hits with the input track. The silicon track segment is not modified at this stage, the algorithm only extends the track. Finally, an "outside-in" reconstruction sequence is performed. This can recover tracks that did not produce a seed in the silicon detectors, for example tracks that result from secondary decays. Hits already associated to tracks in the first pass are not considered at this stage. The tracks resulting from the above procedures are fitted and their parameters estimated.

With the magnetic field directed along the beam axis, charged particles trace a helical trajectory in the detector. A helix can be fully determined by five parameters. A track is defined in terms of its *perigee*, the point of closest approach to the beam

axis. The perigee parameterisation is defined as follows (see also figure 4.8):

- $\frac{q}{p}$**:** The charge / momentum ratio.
- d_0**:** The transverse impact parameter. The sign of d_0 indicates the direction of the angular momentum of the track around the beam. It is negative for a positive angular momentum.
- z_0**:** The longitudinal impact parameter.
- ϕ_0**:** The angle with the x-axis in the $x - y$ plane at the perigee.
- θ**:** The angle with the z-axis in the $R - z$ plane.

Tracks are one of the basic quantities for analyses based on ATLAS data. Primary decay vertices are another, defined as positions in the detector where a pp interaction has occurred. One of the primary vertices is of particular interest: the hard-scatter vertex, from which the hard objects in the event are expected to originate. By extrapolating multiple tracks to a point in space, primary vertices can be identified and their properties reconstructed from the constituent track parameters.

To reconstruct primary vertices a selection is applied to the tracks in the event [169], based on the same quantities as the track quality requirements described previously. Vertex reconstruction is applied to the remaining tracks as follows:

1. A seed position for the vertex is defined, with the x and y coordinates taken from the beam spot. The z coordinate of the seed position is the mode of the longitudinal impact parameters of the selected tracks.

2. An iterative fitting procedure is applied. Using the seed position as input, a χ^2 minimisation is used to find an optimal vertex position. The following weights are calculated for each track:

$$\omega(\hat{\chi}^2) = \frac{1}{1 + \exp\left(\frac{\hat{\chi}^2 - \chi^2_{\text{cutoff}}}{2T}\right)}, \tag{4.13}$$

   where $\hat{\chi}^2$ is the χ^2 comparing the closest approach of the track and the vertex position in three dimensions. The parameters χ^2_{cutoff} and T determine the value of $\hat{\chi}^2$ for which the weight is zero and the smoothness of the weight, respectively. Thus ω is a metric for the compatibility of a track with a given position. The vertex position is recalculated using the weighted tracks and this process iterated, with incompatible tracks contributing less to the position calculation in later iterations. A predefined sequence of iterations is applied with varying values of T to avoid convergence in a local minimum.

3. Any tracks with $\hat{\chi}^2$ corresponding to more than seven standard deviations after the final iteration are removed from the vertex and returned to the collection of selected tracks to be considered for the next pass in primary vertex (PV) reconstruction. This loose requirement reduces the number of pp interactions reconstructed twice as two separate primary vertices.

Steps 1-3 are repeated until no tracks remain, or no new primary vertices can be reconstructed.

The hard-scatter vertex is identified as the PV with the largest $\sum p_{\mathrm{T,track}}^2$. After the identification of the hard-scatter vertex, all tracks can be classified as one of the following:

- Matching the hard-scatter vertex.
- Matching a pileup vertex.
- Unmatched. These are primarily combinatoric fakes.

These categories are useful for track selection when reconstructing higher-level physics objects.

The reconstruction of secondary vertices within jets is useful for identifying the flavour of the initiating particle (flavour tagging). This is left to section 4.4.5. Reconstructing secondary vertices independently of jets is also a key component of the soft b-tagging analysis and is described in detail in chapter 6.

4.4.2 Electrons

Offline electron reconstruction at ATLAS [170] is similar to the online reconstruction described in section 4.2.1. Indeed, the online identification is kept as close to the offline as possible, within processing constraints. The key differences are:

- For offline reconstruction, an upper threshold is applied on the d_0 and $|d_0/\sigma_{d0}|$ of tracks associated to the electron candidate, where σ_{d0} is the uncertainty on the transverse impact parameter. Online, where the NN clustering algorithm (see 4.4.1) cannot be used due to time constraints, these variables tend to have poorer resolution and are therefore not used.
- Offline reconstruction uses an optimised Gaussian Sum Filter (GSF) [171], a generalisation of the Kalman filter which splits noise into Gaussian components, applying a Kalman filter to each one. The GSF is used to refit tracks associated to the electron candidate, recovering radiative energy losses and significantly improving tracking variables. The GSF is time consuming and cannot be applied for electron triggers. The offline variable $\Delta p/p$, the momentum lost by the track between the perigee and the last measurement point, relies on the GSF and is therefore not used online.
- The ratio of the cluster energy to the track momentum is used offline at high E_{T} for improved signal / background separation. As described in section 4.2.1, a logical OR with looser triggers is used online, which minimises efficiency losses with little cost in terms of the trigger rate.
- The average μ is used for pileup correction online. Offline the number of reconstructed vertices is used instead.

A larger selection of isolation OPs is available offline, which can be based on calorimetric- and track-based isolation variables. Offline, calorimetric isolation is defined as the E_{T} sum of topological clusters, calibrated at the EM scale, in a ΔR cone around electron candidate cluster. Offline track isolation is defined in a similar

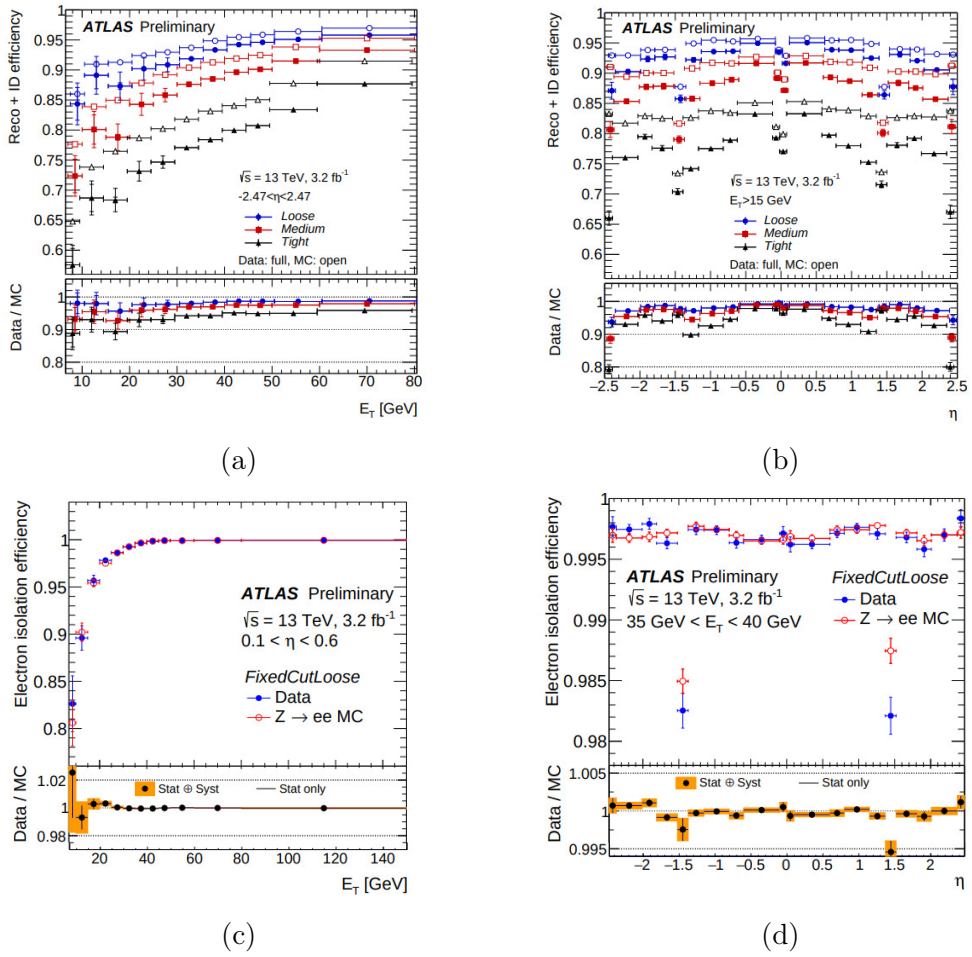

Figure 4.9: Offline electron reconstruction and identification efficiencies in $Z \to ee$ electrons as a function of E_{T} (a) integrated over the entire pseudorapidity range and (b) as a function of η. The uncertainties are determined from pseudo-experiments, assuming uncorrelated statistical uncertainties in separate E_{T} and η bins. The isolation efficiency in $Z \to ee$ electrons is shown for the `FixedCutLoose` isolation OP with respect to the `Tight` identification OP (c) versus E_{T} in the range $0.1 < \eta < 0.6$ and (d) versus η, with statistical uncertainties only. Taken from Ref. [170].

fashion to online (section 4.2.1), using offline tracks. Isolation OPs are defined using both variables described above, based either on fixed thresholds or with a linear E_{T} dependence, amounting to a tighter threshold for harder electrons.

The overall electron identification efficiency, from trigger to isolation, is the product of the individual selection efficiencies:

$$\epsilon_{\mathrm{total}} = \epsilon_{\mathrm{trigger}} \times \epsilon_{\mathrm{identification}} \times \epsilon_{\mathrm{isolation}}. \tag{4.14}$$

Scale factors are applied for each component of the total efficiency to account for the mis-match between data and MC. The trigger scale factor measurements are performed for all trigger/identification/isolation combinations, as described in appendix A. Examples of offline identification and isolation efficiencies are shown in figure 4.9.

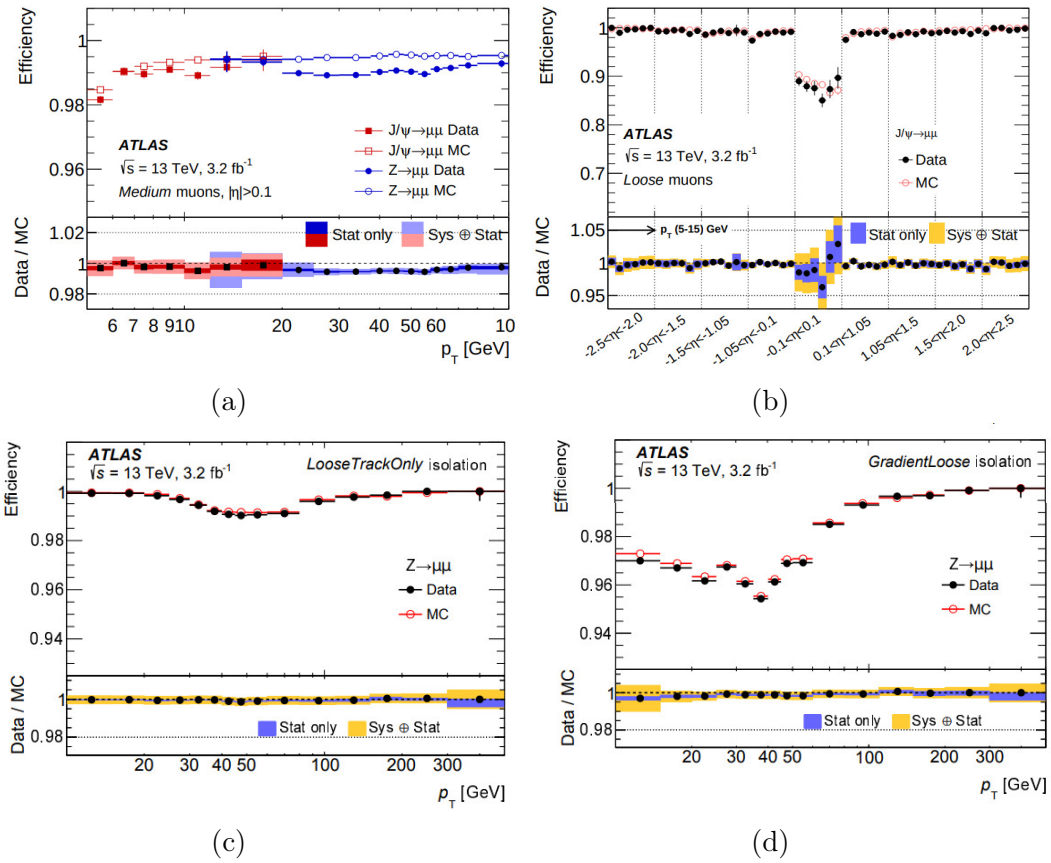

Figure 4.10: Muon identification efficiency (a) for the `Medium` offline OP as a function of p_{T} , using $J/\psi \to \mu\mu$ and $Z \to \mu\mu$ events and (b) for the `Loose` OP in $J/\psi \to \mu\mu$ events, versus p_{T} for separate η slices. The efficiency versus p_{T} in $Z \to \mu\mu$ events for (c) loose, track-based isolation and for (d) variable calorimetric- and track-based isolation. Only statistical uncertainties are shown. Taken from Ref. [172].

4.4.3 Muons

The offline muon reconstruction is similar to the online reconstruction, combining separate measurements from the muon spectrometer and the ID [172]. Muons are reconstructed using tracks from the ID reconstructed as described in section 4.4.1. Track reconstruction in the muon spectrometer can be thought of as a more refined version of the online procedure. The combined reconstruction proceeds rather differently, applying a set of algorithms based on ID, muon spectrometer and calorimeter information. Four muon types are defined:

- **Combined (CB) Muon:** reconstructed from independent ID and muon spectrometer tracks matched by a global fit.
- **Segment-Tagged (ST) Muon:** an ID track with at least one associated track segment in the MDT or CSC chambers. These are used if the muon crosses only one layer of the muon spectrometer, which may happen for soft muons or muons in regions of the muon spectrometer with reduced acceptance.
- **Calorimeter-Tagged (CT) Muon:** muons typically leave a small (order of a few GeV), narrow deposit in the calorimeter. ID tracks are identified as

CT muons if they are consistent with a minimum-ionising-particle (MIP). CT muons recover efficiency in regions where the muon spectrometer is deficient due to material servicing upstream subdetectors, approximately $|\eta| < 0.1$.

- **Muon, Extrapolated (ME):** tracks in the muon spectrometer with no matching ID track that are compatible with the interaction point. MEs recover efficiency in the region $2.5 < |\eta| < 2.7$, which is not covered by the ID.

The samples of muons fulfilling the definitions above overlap. An overlap removal procedure is therefore applied to avoid double counting.

Muons reconstructed using the above procedure are required to fulfil a set of identification criteria designed to select prompt muons from the primary interaction, and to reject non-prompt muons, primarily from light hadronic decays. For CB muons, the selection is based on the following:

- $\boldsymbol{q/p}$ **significance:** the charge to momentum ratio, normalised to the combined uncertainties of each.
- $\boldsymbol{\rho'}$**:** the ratio of the absolute difference between the momenta of the tracks in the muon spectrometer and the ID to the combined p_{T}.
- $\boldsymbol{\chi^2}$**:** the normalised χ^2 of the combined track fit.

These criteria are used to defined `Loose`, `Medium` and `Tight` muon identification OPs. An additional `High-`p_{T} OP is defined to target maximum resolution for tracks with $p_{\mathrm{T}} > 100$ GeV. Isolation requirements offer additional background rejection, and are defined in the same way as for electron candidates. Offline muon identification and isolation efficiencies in 2015 data are shown in figure 4.10. The region covered by CT muons can clearly be seen in figure 4.10b, with a significant drop in efficiency. As for electrons, correction factors are applied to account for efficiency differences in data and MC.

4.4.4 Jets

Offline jet reconstruction uses the anti-k_t [126] algorithm to combine objects into jets. The anti-k_t algorithm uses the following distance metrics:

$$d_{ij} = \min(k_{ti}^{-2}, k_{tj}^{-2}) \frac{\Delta R_{ij}^2}{R^2}, \tag{4.15}$$

$$d_{iB} = k_{ti}^{-2}, \tag{4.16}$$

where d_{ij} is the distance between objects i and j and d_{iB} is the distance between object i and the beam. k_{ti} is the transverse momentum of the ith particle and R is a parameter that defines the radius in $\eta - \phi$ space for the jet cone. Starting from an object i, additional objects are added to the jet if they have the minimum d_{ij}, until d_{iB} is the minimum distance, at which point the collection of objects is called a jet. This algorithm gives the same output in the case of soft or collinear emissions; as such it is said to be infrared and collinear *safe*.

The collection of jets returned by the anti-k_t algorithm is dependent on the input objects and the size parameter. Two categories of jet collection are used in this thesis:

- **Calorimeter jets:** The input objects for the calorimeter jets used in this thesis are topological clusters (see 4.2.3) and the radius parameter is $R = 0.4$. Calorimeter cell energies are measured at the EM scale and jets are only reconstructed if they meet the threshold $p_{\mathrm{T}} > 7$ GeV. The calibration procedure for calorimeter jets is described later in this section.

- **Track jets:** The input objects for track jet reconstruction are ID tracks down to a threshold of 0.4 GeV. The studies made in this thesis make use of a number of different track collections differing only by the radius parameter. Two collections based on a fixed radius are used, with $R = 0.2$ or $R = 0.4$. A variable radius VR track collection is also used, where a dedicated VR algorithm [173] is applied. The radius parameter scales as ρ/p_{T} with $\rho = 30$ GeV, with cutoffs $R_{\mathrm{min}} = 0.02$ and $R_{\mathrm{max}} = 0.4$ for very hard and soft jets, respectively.

Calorimeter jets are initially measured at the EM scale. They are then calibrated using a jet energy scale (JES) calibration scheme [174] to recover hadronic energy, account for detector related effects and correct for energy due to pileup interactions. The calibration scheme proceeds as follows:

- **Origin correction:** The four-vector of the jet is adjusted so that it originates from the hard-scatter PV instead of the nominal interaction point. The adjustment is done in such a way as to keep the energy of the jet constant.

- **Pileup correction:** After the origin correction, the pileup contribution to jet energy is estimated. First a jet area-based method is used, followed by a further correction to remove residual pileup dependence as a function of μ and the number of primary vertices. The area of the jet is calculated using *ghost association* [175, 176] a method which will be referred to again repeatedly in this text. In this method, particles with infinitesimal momenta are added to the event with uniform density in solid angle. After jet reconstruction is re-applied to the event, the jet area is defined proportional to the number of ghost particles associated to it. This area is used to define the momentum density from which pileup corrections are derived.

- **Jet energy scale and η calibration:** An absolute energy scale, derived from MC simulation, is used to recover the energy, initially measured at the EM scale, at the particle-level. The η of the jet is also corrected for to account for detector effects, such as the transitions between different detector designs and regions of granularity, biasing the energy and η of the jet. The energy response in ATLAS simulation is shown in figure 4.11a.

- **Global sequential calibration (GSC):** Additional corrections to the jet four-momentum are derived using five variables which are found to improve the resolution of the JES. These variables are based on the fraction of the jet energy deposited in particular regions of the detector, constituent track-based variables and the number of muon track segments associated to the jet. The track and muon track segment multiplicities are determined by ghost association, treating all tracks as infinitesimal four-vectors and re-running jet reconstruction, assigning tracks to a jet if they are included as constituents by the anti-k_t algorithm.

- **In-situ calibration:** Scale factors are derived to correct for differences in the jet response between data and MC. They are evaluated by comparing the average detector response to central jets with well measured reference objects. Different reference objects are used to focus on different p_{T} regions: Z+jet and γ+jet events are used to calibrate up to 950 GeV and multijet events are used to extend the calibration to 2 TeV. The scale factors are shown as a function of jet p_{T} in figure 4.11b.

  Jet cleaning criteria [177] are applied during the in-situ calibration to discriminate against mis-reconstructed "fake" jets from, for example, detector noise, beam background and cosmic particles. Fake jets from detector noise spikes in the HEC are suppressed by vetoing jets with a fraction of energy deposited in the HEC greater than 90%. Fake jets originating from unwanted communication between neighbouring cells are suppressed by rejecting jets if five or less cells account for 90% of the total energy. A less dominant source of noisy fakes is coherent noise in the EM calorimeter. The fraction of jet energy in the ECAL and the fraction of energy measured in bad-quality calorimeter cells can both be used to reject such jets. Finally, out-of-time jets are rejected if they have an energy-weighted cell time greater than two bunch crossings, or 50 ns.

  A jet vertex tagger (JVT) [178] is applied at this stage for additional suppression of pileup jets. It is based on the variables $R_{p_{\mathrm{T}}}$ and corrJVF. The variable $R_{p_{\mathrm{T}}}$ is defined:

$$R_{p_{\mathrm{T}}} = \frac{\sum_k p_{\mathrm{T}}^{\mathrm{trk}_k}(\mathrm{PV}_0)}{p_{\mathrm{T}}^{\mathrm{jet}}}, \tag{4.17}$$

  where the sum runs over all tracks associated to the jet and the hard-scatter PV, PV_0. The jet momenta are fully calibrated. $R_{p_{\mathrm{T}}}$ peaks sharply at zero for pileup jets since the jet tracks should be associated to other PVs, and is broadly distributed for jets originating from the primary interaction, where it amounts to a measure of the charged fraction of the jet. The variable corrJVF is defined as follows:

$$\mathrm{corrJVF} = \frac{\sum_k p_{\mathrm{T}}^{\mathrm{trk}_k}(\mathrm{PV}_0)}{\sum_k p_{\mathrm{T}}^{\mathrm{trk}_k}(\mathrm{PV}_0) + \frac{p_{\mathrm{T}}^{\mathrm{PU}}}{(k.n_{\mathrm{trk}}^{\mathrm{PU}})}}. \tag{4.18}$$

  The scalar sum of momenta of tracks associated to PV_0 and the weighted scalar p_{T} sums of each of the pileup vertices contribute to the denominator in corrJVF. Thus the corrJVF gives a measure of the fraction of tracks in the jet coming from the PV_0, compared to the total number of tracks matched to PVs. The weighting $(k.n_{\mathrm{trk}}^{\mathrm{PU}})$, with the parameter $k = 0.01$ and the multiplicity of tracks associated to pileup vertices $n_{\mathrm{trk}}^{\mathrm{PU}}$, is added to account for the linear dependence of the average p_{T} of pileup jets on the total pileup. The variables $R_{p_{\mathrm{T}}}$ and corrJVF are combined into a 2-dimensional likelihood using a k-nearest neighbour algorithm [118], which is used to reject pileup jets.

4.4.5 Flavour Tagging

Hadronic jets can be initiated by a variety of different sources, and can be organised into four main categories:

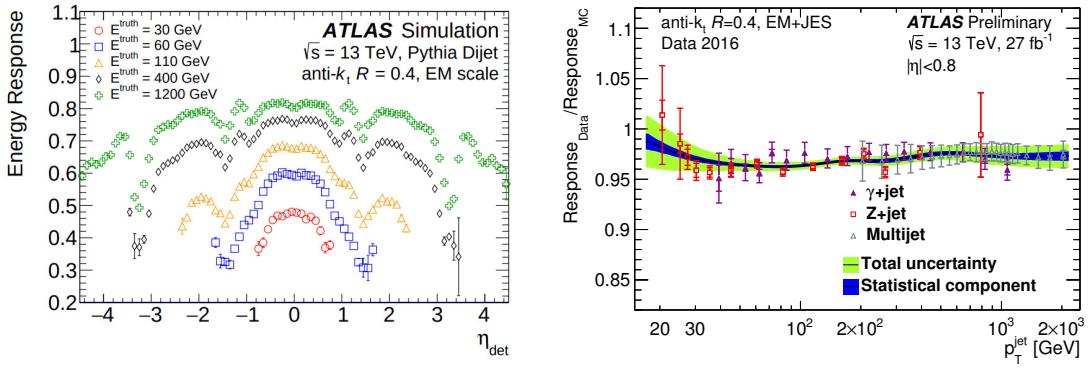

(a) (b)

Figure 4.11: (a) Average energy response as a function of the detector pseudorapidity η_{det} for jets with a truth energy of 30, 60, 110, 400 and 1200 GeV. The energy response is shown after origin and pileup corrections, but not the JES calibration, are applied. (b) Data / MC ratio of the EM+JES response as a function of jet p_{T} for Z+jets, γ+jets and multijet calibrations. Taken from Ref. [174].

- ***b*-jets:** Jets which arise from the hadronisation of bottom quarks. b-hadrons have a relatively long lifetime of $\sim$ 1.5 ps, corresponding to $c\tau \sim 0.45$ mm. In many cases this results in a displaced secondary vertex (SV) that can be resolved from the PV_0, a fact that will be exploited in many of the techniques discussed later.

- ***c*-jets:** Initiated by charm quarks. c-hadrons have a shorter lifetime than b-hadrons, but in many cases they may also lead to a resolved SV. The properties of c-jets are similar to b-hadrons and distinguishing them can be difficult. As a result, b- and c-tagging methods tend to select samples with high mutual contamination.

- ***l*-jets:** Initiated by lighter quark flavours and gluons. These are easier to distinguish from heavier flavour jets and have similar properties and as such are grouped together.

- **τ-jets**: Jets resulting from hadronic τ decays. τ-leptons decay hadronically with a branching fraction of $\sim$ 65%, to pions and neutrinos. In more than 90% of cases the hadronic component consists of either one or three charged hadrons, with a possible contribution from neutral hadrons. As a result τ-jets have one or three associated tracks in the ID with a high probability. The flavour tagging methods described below are not optimised with τ-leptons in mind. Instead, hadronic τ-leptons are typically identified using a dedicated BDT tagger based primarily on shower shape variables [179]. Indirect methods based on the parent of the τ-lepton can also be used, as described in chapter 5.

The analyses presented in this thesis are motivated by signals with c- and / or b-jets in the final state, with significant SM backgrounds containing jets from all of the above categories. Identifying b- and c-jets as efficiently as possible is therefore of crucial importance.

Flavour tagging at ATLAS aims to identify $b-$ and / or $c-$jets and is based on a set of dedicated algorithms which are combined using a boosted decision tree (BDT) [118]. A decision tree takes as input signal and background training samples and a set of descriptive variables, or *features*. A sequence of selections is applied, dividing the phase space into a set of regions which are classified as signal or background according to the number of signal or background events they contain. A *boosted* decision tree is formed from an ensemble of decision trees formed by re-weighting events and taking the average of the individual decision trees to form an improved classifier. Thus a BDT takes as input a training sample and outputs event weights, which are used to estimate the probability of an event being signal or background. The input algorithms are described below:

- **Impact parameter based algorithms [180]:** These algorithms aim to identify b- and c-hadrons by exploiting their long lifetimes, which results in tracks that are displaced from the hard-scatter vertex. A common track selection is applied, based on p_{T}, d_0, $z_0 \sin\theta$ and pixel detector hits. There are two algorithms used: IP2D and IP3D. Both taggers are based on the impact parameter significance, defined as d_0/σ_{d0} and $z_0 \sin\theta/\sigma_{z0\sin\theta}$ for the transverse and longitudinal impact parameter significance, respectively, where σ_{d0} and $\sigma_{z0\sin\theta}$ are the associated uncertainties. The d_0 variable is signed such that it is positive for a point of closest approach on the same side as the direction of the jet, with respect to the PV_0. The impact parameter significance variables are used to build probability density functions, which are combined into a log-likelihood ratio (LLR) based discriminant.

- **Secondary vertex finding (SVF) algorithm [181]:** This algorithm aims to tag b-jets by explicitly reconstructing a secondary vertex within the jet. The inputs to the SVF algorithm are the jet cone, four-momentum and selected tracks associated to the jet. The SVF algorithm first attempts to identify two-track vertices within the jet, which can then be merged if they lie close in space to form a secondary vertex.

  There are several sources of fake SVs, for example hadronic interactions in detector material, photon conversions, neutral strange decays, referred to as V^0 decays, and combinatoric fakes from dense track environments. A cleaning procedure is applied in order to reject these backgrounds:

  1. A two-track vertex should not have associated to it any tracks with pixel hits at a radius smaller than radius of the vertex. Vertices are rejected if they contain tracks with hit patterns that are inconsistent with the vertex position. This step suppresses primarily the background contribution from combinatoric fakes.
  2. The invariant mass of a two-track vertex is calculated from its constituent tracks. It is then rejected if the invariant mass is consistent with the invariant mass of the characteristic V^0 decays: $K^0 \to \pi^+\pi^-$ or $\Lambda^0 \to p\pi^-$.
  3. A two-track vertex radius from the interaction point is compared with the known radii of cylindrical detector material layers. If they are consistent, the two-track vertices are removed. This requirement greatly enhances the purity at the cost of rejecting true b- and c-hadron vertices, which cannot be further distinguished from material interaction vertices.

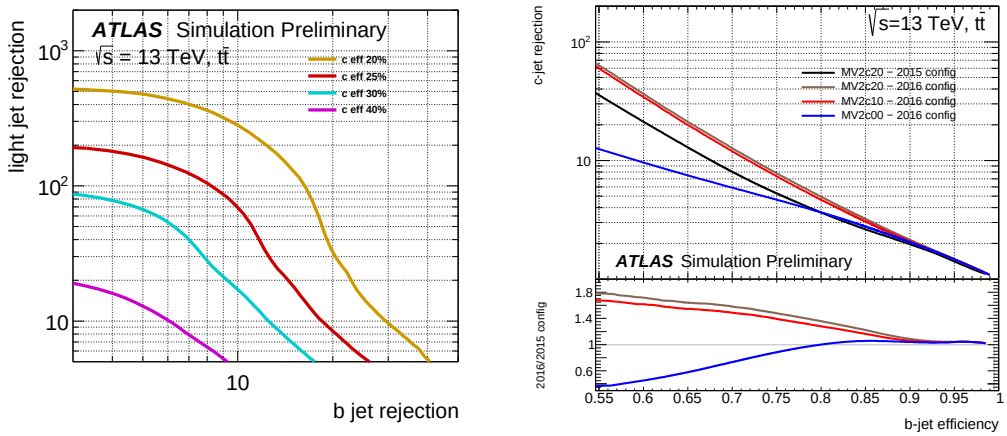

(a) (b)

Figure 4.12: (a) c-jet tagging efficiency (coloured scale) as a function of b-jet and l-jet rejection obtained from $t\bar{t}$ events. The solid lines indicate contours of constant c-tagging efficiency in the b- and l-jet rejection space. (b) b-jet tagging performance versus light flavour rejection, measured in $t\bar{t}$ events. The ratio of the performance for the 2016 and 2015 performances is shown in the lower panel. Taken from Refs. [182, 183].

After the cleaning procedure, all tracks associated with two-track vertices are combined into a single collection of tracks. This collection is the input for the vertex fitting procedure described in section 4.4.1. After fitting, if the resulting SV has only two associated tracks, the cleaning procedure is re-applied. Multiple SVs may be present due to subsequent decay of the b-hadron to a c-hadron, although the two vertices may not always be resolved. If multiple SVs are reconstructed, they are merged if close by, otherwise the SV with the greatest track multiplicity is chosen.

- **Decay chain multi-vertex algorithm (JetFitter) [184]:** This algorithm attempts reconstruct the $b-c$ decay cascade based on the assumption that the b- and c-hadron decay vertices lie on the flight path of the b-hadron. A Kalman filter is used to fit the cascade trajectory, updating the position of the SV iteratively. The cascade flight axis is used in the vertex fitting procedure, once again based on the merging of two-track vertices. This approach can recover SVs from incomplete topologies, for example due to missed tracks.

Variables based on the outputs of the above algorithms, amounting to 24 in total, are used as features for the BDT. The output of the BDT depends also on the composition of the training samples. The basic algorithm used is named MV2. The following variants of the MV2 tagger were used in this thesis: MV2c10, which uses a background composition of 7% c-jets and 93% l-jets, MV2c20, which uses 15% c-jets and 85% l-jets, and the MV2c(l)100 taggers, designed for charm-tagging, which use 100% for $c(l)$-jets. The signal composition is always 100% b-jets. The performance of charm-tagging working points formed from the MV2c(l)100 taggers is shown in figure 4.12a, and the performance for b-tagging working points versus c-jet rejection is shown in figure 4.12b. The addition of the IBL to the ID and upgraded tracking performance for Run 2 yielded an improvement in charm and light flavour rejection

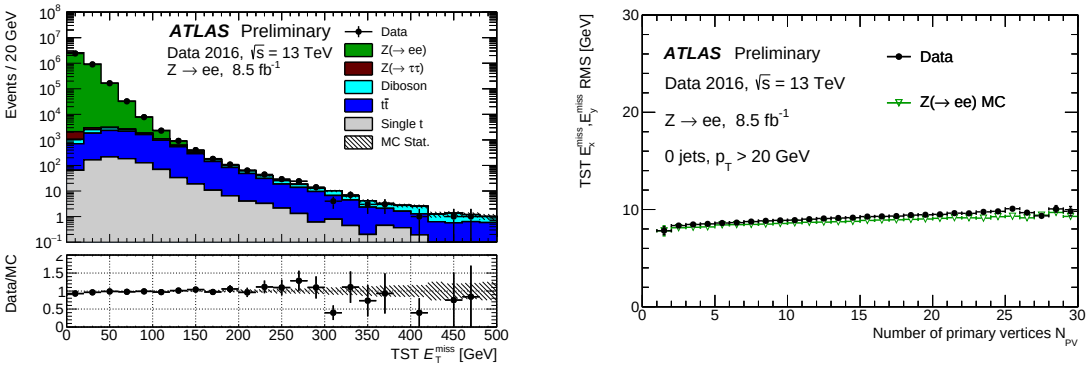

(a) (b)

Figure 4.13: (a) $E_{\mathrm{T}}^{\mathrm{miss}}$ distribution for a dilepton selection targeting $Z \to ee$ decays, comparing 2016 data to MC expectation. (b) $E_{\mathrm{T}}^{\mathrm{miss}}$ resolution as a function of the number of reconstructed primary vertices in the event. TST indicates that track based soft term, based on unmatched tracks from the hard-scatter vertex, is included in the $E_{\mathrm{T}}^{\mathrm{miss}}$ calculation. Taken from Ref. [185].

for b-tagging. This corresponded to a 10% improvement in efficiency for the same rejection factors.

4.4.6 Missing Transverse Energy

Two main contributions are considered for $E_{\mathrm{T}}^{\mathrm{miss}}$ calculation: a *hard* contribution from fully reconstructed and calibrated physics objects and a *soft* contribution from reconstructed tracks in the ID which are matched to the PV_0, but not to any of the hard objects. In this thesis, the hard $E_{\mathrm{T}}^{\mathrm{miss}}$ contribution is reconstructed using the following objects: electrons, muons and jets. Any unidentified photons or τ-leptons will have associated jets which will contribute to the $E_{\mathrm{T}}^{\mathrm{miss}}$ calculation. The calculation of $E_{\mathrm{T}}^{\mathrm{miss}}$ thus proceeds as follows:

$$E_{\mathrm{T}}^{\mathrm{miss}} = \left\| \boldsymbol{p}_{\mathrm{T}}^{\mathrm{miss}} \right\| = \left\| -\sum_{\text{electrons}} \vec{p_{\mathrm{T}}}^{\,e} - \sum_{\text{muons}} \vec{p_{\mathrm{T}}}^{\,\mu} - \sum_{\text{jets}} \vec{p_{\mathrm{T}}}^{\,\text{jet}} - \sum_{\substack{\text{unmatched} \\ \text{tracks}}} \vec{p_{\mathrm{T}}}^{\,\text{track}} \right\| . \tag{4.19}$$

From $\boldsymbol{p}_{\mathrm{T}}^{\mathrm{miss}}$ the additional derived variable can be recovered:

$$\phi^{\mathrm{miss}} = \arctan\left(E_y^{\mathrm{miss}} / E_x^{\mathrm{miss}}\right) . \tag{4.20}$$

To avoid the double counting of objects an overlap-removal procedure is applied, using reconstructed electrons preferentially if they overlap with a reconstructed jet. Muons have very little overlap with electrons and jets and are not considered for overlap removal.

The reconstructed $E_{\mathrm{T}}^{\mathrm{miss}}$ includes contributions from physics objects with different p_{T} resolutions. The set of objects contributing to the $E_{\mathrm{T}}^{\mathrm{miss}}$ calculation also fluctuates significantly on an event-by-event basis. The intrinsic dependence of $E_{\mathrm{T}}^{\mathrm{miss}}$ on the event composition results in a strong dependence of the performance on the event type and pileup activity. The reconstruction performance and associated systematic uncertainty is assessed [186] using data / MC comparisons of $E_{\mathrm{T}}^{\mathrm{miss}}$ based

quantities. The quality of MC simulation is independently determined for individual type of physics object, including the soft contribution, and then propagated to the final $E_{\mathrm{T}}^{\mathrm{miss}}$ calculation at event level.

Figure 4.13a shows the $E_{\mathrm{T}}^{\mathrm{miss}}$ distribution for a selection targeting $Z \to ee$ decays. At low $E_{\mathrm{T}}^{\mathrm{miss}}$ Z+jets events dominate through resolution effects. Similar distributions can be seen for single and pair produced top quarks, with $E_{\mathrm{T}}^{\mathrm{miss}}$ produced from leptonic W decays. Figure 4.13b shows the pileup dependence of the $E_{\mathrm{T}}^{\mathrm{miss}}$ resolution in 2016 data. The resolution is robust in the range $0 < N_{\mathrm{PV}} < 30$, with some deterioration at higher values.

4.5 Summary

Data processing at ATLAS begins with the hardware-based L1 trigger, which selects candidate events for further reconstruction. This chapter gives an account of the data processing from a L1 accept decision, to efficient reconstruction at HLT and storage for further analysis, as well as the different streams used to monitor and calibrate the data as it is collected. Essential for the interpretation and analysis of the data is MC simulation of individual SM and signal processes. An overview of the procedure for producing samples of MC data, from event generation to propagation through detector simulations, has been given. Once the data has been collected and processed and sufficient MC events generated, the same event reconstruction procedures are applied to both, to obtain tracks, vertices and higher level physics objects from the detector response. The event reconstruction has been outlined for all of the physic objects used by the analyses in chapter 5 and 6. The full sequence of data acquisition, MC generation and event reconstruction results in data, background MC and signal MC samples. The data and MC samples differ in that the MC contains a truth record with information about the particles that initiated the detector response. These data and MC samples are the inputs for the analyses of the following chapters.

5 | Search for SUSY in Final States with Jets from Charm Quarks

This chapter presents searches for direct pair production of the stop or scharm with c-jets in the final state, inspired by the models described in section 2.3.3 and shown in figures 2.6b and 2.6d, using 36.1 fb^{-1} of data collected by the ATLAS detector at 13 TeV. This analysis is published in Ref. [1]. It formed a significant part of the PhD work of the author and is described in detail, with additional focus on the aspects that the author contributed the most to.

5.1 Introduction

As described in chapter 2, SUSY can address many of the limitations of the SM. If SUSY were found to be a true description of nature, the degree to which it would address these limitations would depend on the particular model that manifests. The channels targeted by this search are simplified models that are accessible to the ATLAS experiment by virtue of the high $E_{\mathrm{T}}^{\mathrm{miss}}$ and heavy flavour (c or b) jet from a charm quark and represent a class of SUSY scenarios that can provide a solution to particular limitations of the SM. If discovered, such signatures could provide a handle to further study the nature of SUSY. On the other hand, considered with the wider SUSY search effort being undertaken at the LHC, the null result provides further coverage of the SUSY parameter space that is disfavoured.

Both the stop and scharm signals assume R-parity conserving SUSY and that the lightest neutralino is the LSP. If a significant signal was discovered, both stop and scharm signals would provide evidence for an electrically neutral, massive and stable new particle: a WIMP candidate for dark matter. Furthermore, in the case where the mass splitting between the squark and LSP is 15-30 GeV, the dark matter relic abundance can be neatly satisfied through squark-neutralino co-annihilation.

The mass of the stop is an important parameter for SUSY as a solution to the limitations of the SM. Due to the strong Yukawa coupling of the top quark to the Higgs, the stop mass has strong implications for naturalness and the utility of SUSY as an answer the Hierarchy problem. Naturalness arguments strongly favour a top quark with mass at the TeV scale. A stop mass below the TeV scale may also be required for SUSY to generate sufficient baryon asymmetry to explain baryogenesis. Finally, with a stop mass at the TeV scale SUSY may provide a perfect unification of running couplings at the GUT scale.

The decay of the stop depends on its mass difference with the LSP. The decay to a charm quark and LSP is mostly restricted to the case where the mass difference $\Delta m = m_{\tilde{t}_1/\tilde{c}_1} - m_{\tilde{\chi}_1^0}$ is less than $\Delta m < m_W + m_b$. In this region of the parameter space, the flavour violating decay to a charm quark competes with four-body decay to $bff'\tilde{\chi}_1^0$. Despite the flavour violating nature of the charm process, in many regions of the MSSM parameter space its branching ratio can be as important as that of four-body decay.

Despite second generation squarks being excluded at the 95% confidence level already by CMS and ATLAS, searching for direct scharm production can be motivated by relaxing the simplifying assumption of mass degeneracy for second generation squarks with which these limits are derived. These assumptions are motivated by flavour violating constraints on SUSY, however in some general SUSY models these constraints may be satisfied in other ways, for example by imposing additional horizontal symmetries to align second generation squark and quark mass matrices. Relaxing the assumption of mass degenerate second generation squarks can weaken the coverage of existing limits for low mass scharm production, motivating dedicated searches for such signals.

5.2 Run 1 Status

This analysis builds on previous searches conducted using Run 1 data collected by ATLAS. The first of these searches targets stop pair production [187] and the second targets scharm pair production [188]. Both signals are considered together for this analysis due to their similar topologies. The results of the Run 1 analyses are shown in figure 5.1. Figure 5.1b also shows the results of a monojet search, based on $E_{\mathrm{T}}^{\mathrm{miss}}$ and a single, high p_{T} jet, which has sensitivity in the compressed region with small mass-splitting between the squark and LSP [189]. The mass of the stop was excluded up to ~ 290 GeV for a LSP of mass ~ 200 GeV at the 95% confidence level and the scharm to ~ 500 GeV for a LSP of the same mass (see figure 5.1). Both sets of limits assumed a 100% branching ratio to the charm final state. CMS also published exclusion limits for the stop to charm final state with full Run 1 data, with similar results [190].

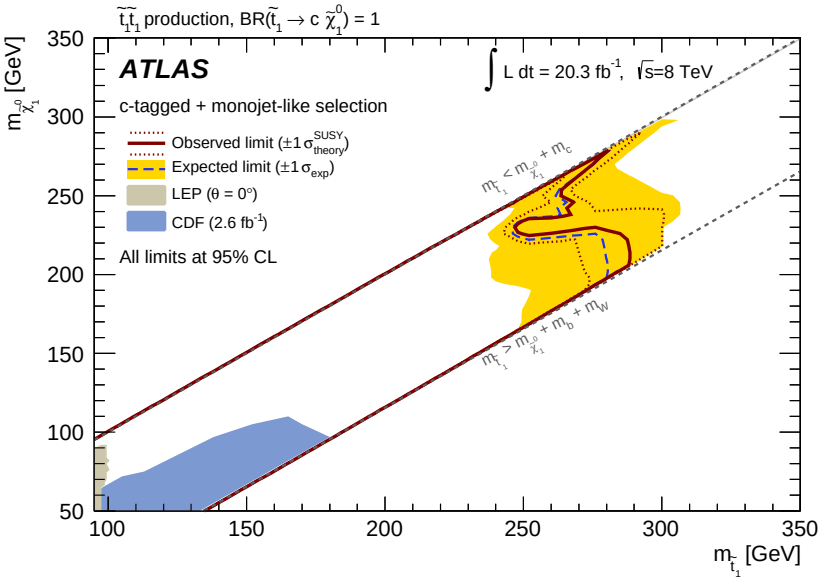

(a)

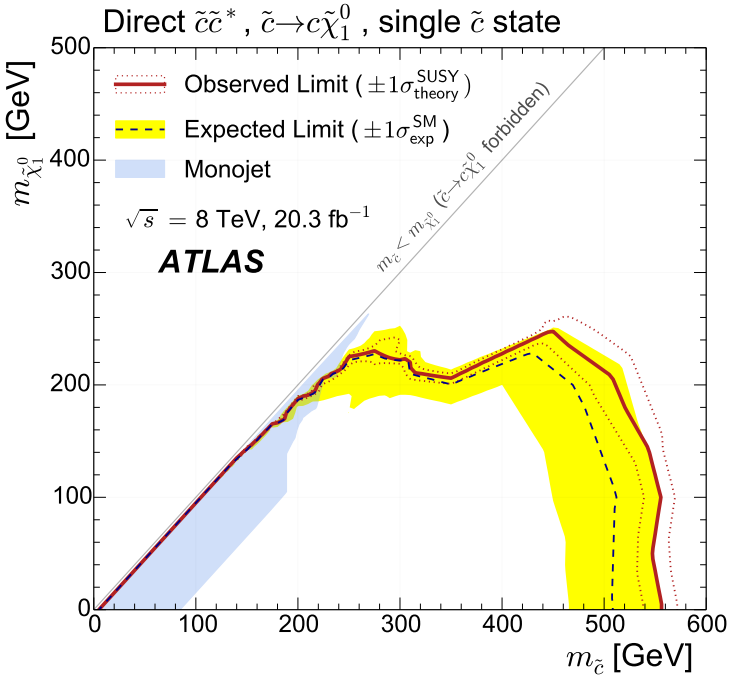

(b)

Figure 5.1: Exclusion limits in (a) the stop, LSP mass plane and (b) the scharm, LSP mass plane. These limits assume a 100% branching ratio for decay to charm quarks and the LSP. The red lines show the observed limits and the blue dashed lines the expected limits. For (a) previous results from LEP [94] and Tevatron [191, 192] are shown in grey and blue, respectively. The limits in (b) have superimposed limits from a monojet-based analysis, also conducted by ATLAS. Taken from Ref. [187, 188].

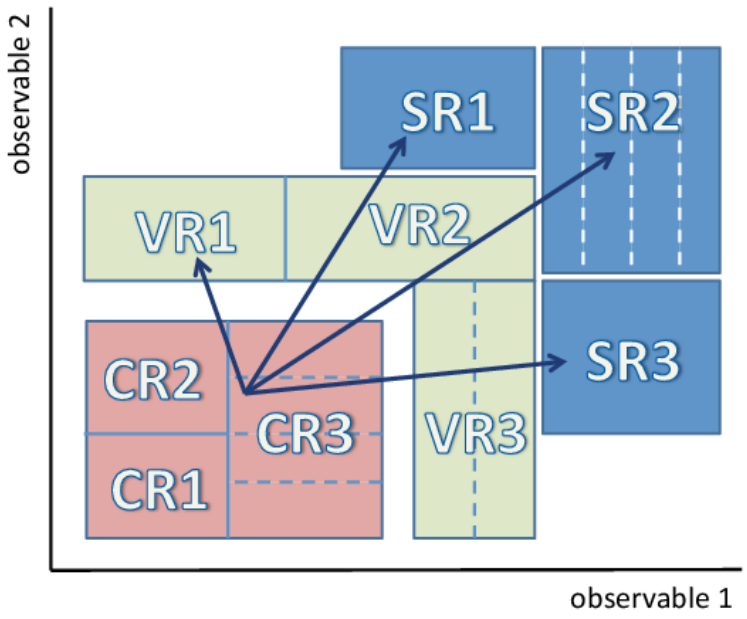

Figure 5.2: Overview of the signal, control and validation region approach. The dashed line illustrates that any given region may have multiple bins. Taken from Ref. [193].

5.3 Analysis Strategy

This analysis follows a *cut-and-count* approach. In this approach, MC generators are used to produce samples of events for signal processes and for the most important SM backgrounds. These are then compared in order to design kinematic selections based on reconstructed physics objects. These selections define *regions* targeting specific processes. Three main types of region are defined:

- **Signal regions:** kinematic selections designed to enhance signal events and suppress SM backgrounds in order to maximise the probability of discovery, or in the case of a null result, maximise the exclusion limits that can be placed on the mass of the squark and LSP. Unlike the other regions, the signal regions are designed without considering the data, using only MC simulation.

- **Control regions:** auxiliary measurements designed to target specific SM backgrounds that are expected to contribute significantly to the signal regions (SRs). The background estimates are extrapolated to the signal regions for the estimate of the total background.

- **Validation regions:** kinematic selections that lie in the phase space between the SRs and control regions (CRs). SM backgrounds are fitted in the CRs and used to predict the yield in the validation regions (VRs) in order to validate the extrapolation procedure.

The SR, CR and VR approach is illustrated in figure 5.2. Once these regions have been defined, the impact of systematic uncertainties on the predicted yields for each process must be evaluated. Once the uncertainty on the predictions for each of the regions is known, the SM predictions are normalised by fitting the CR yields to the data using a maximum likelihood estimation. These normalisations are then used to predict the yield in each of the VRs. Only after the CR extrapolations have been validated in this way is the data revealed in the SRs. The SR and CR yields are then used to assess whether there is evidence in the data for new physics that cannot be accounted for by the SM. If no significant excess of data is observed, exclusion limits are derived at a confidence level of 95% in the squark and LSP mass plane.

The remainder of this chapter is organised as follows: in section 5.4 the benchmark signal models considered for this analysis and the MC simulated samples are described. This is followed in section 5.5 by a description of the key SM processes in this analysis and the MC simulated samples used for each. In section 5.6 the definitions are introduced for physics objects reconstructed from simulated and data samples. In section 5.7 the SR event selection strategy is described and in section 5.8 the strategy used to estimate each of the important backgrounds is described. Section 5.9 details the strategy for evaluating the experimental and theoretical uncertainties and in section 5.10 the statistical procedure for interpreting the signal and background yields in the SRs is given. Finally, in section 5.12, the results and interpretation for the analysis are given.

5.4 Benchmark Signal Models

As described in section 2.3.3 the signals considered for this analysis represent simplified models, where the signals shown in figures 2.6b and 2.6d are assumed to proceed with a 100% branching ratio, and all SUSY particles not taking part in the process of interest are assumed to be heavy. A grid of signals in the $m_{\tilde{q}_1}$, $m_{\tilde{\chi}_1^0}$ mass plane, where $\tilde{q}_1$ indicates either $\tilde{t}_1$ or $\tilde{c}_1$, was generated, starting from grid points lying at the boundary of the exclusion limits set by the Run 1 analyses. For a fixed centre-of-mass energy, the production cross section depends on the mass of the squark, falling quickly (see figure 5.4) as the mass increases. At 1100 GeV the cross section is (3.07 ± 0.53) fb, which, for an integrated luminosity of 36.1 fb^{-1}, corresponds to a total of approximately 111 events. At greater masses, with fewer events, there is little sensitivity for any selection after detector efficiency is taken into account, so the signal production was limited to 1100 GeV in mass. For a mass difference $\Delta m < m_W + m_b$ stop simplified models are considered. Beyond this region (see section 2.3.3) scharm models are considered, which are not restricted by Δm. The region $\Delta m < m_{\tilde{\chi}_1^0}$ is forbidden since $\tilde{\chi}_1^0$ is assumed to be the LSP. The full grid of generated signals and corresponding cross sections is shown in figure 5.4.

The signal samples used for this analysis were generated using `MadGraph5_aMC@NLO` v2.2.3 [158] for the ME calculation, which is performed at tree level, with the inclusion of up to two parton emissions. For the stop decay, parton showering, hadronisation and description of the underlying event, `Pythia` 8.8126 [155] is used with the A14 set of tuned parameters [194]. ME to parton matching is implemented using a CKKW prescription [195] (see section 4.3.1). The matching scale $m_{\tilde{q}_1}/4$ is used and the top quark mass is set to 172.5 GeV. For PDF input, the NNPDF2.3LO PDF set [136] is used. The signal cross sections, shown in figure 5.4, are calculated

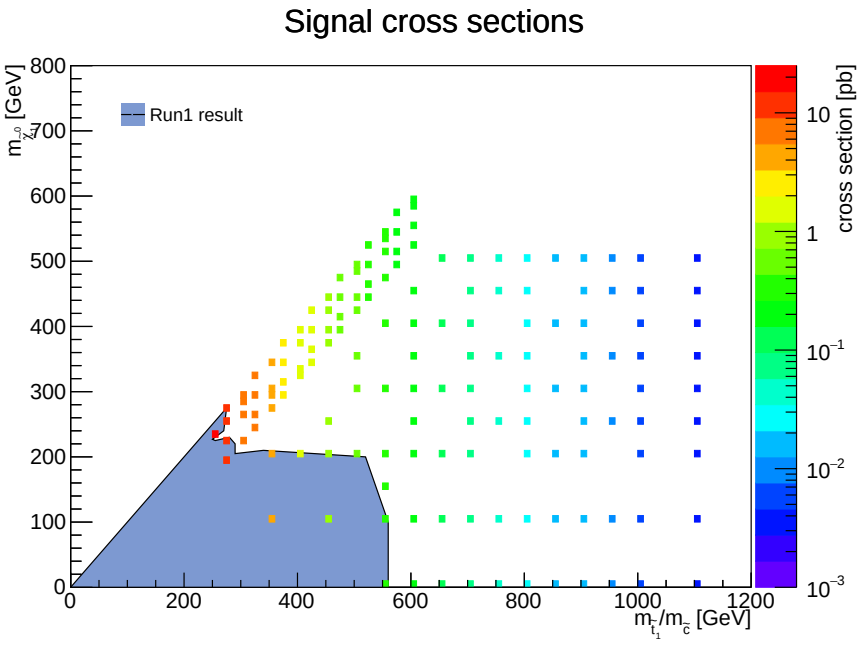

Figure 5.3

Figure 5.4: Production cross sections for benchmark SUSY models considered by this analysis. The Run 1 exclusion limits shown in figure 5.1 are superimposed.

at NLO in α_s with the addition of soft-gluon emission to next-to-leading-logarithm (NLO+NLL) accuracy [196–198]. The same signal cross sections are used for stop and scharm signal models. For the detector simulation, `ATLFAST-II` was used for all signal samples.

The experimental signature is characterised by high $E_{\mathrm{T}}^{\mathrm{miss}}$. To improve statistics in the high $E_{\mathrm{T}}^{\mathrm{miss}}$ region of parameter space, the samples were generated by applying a filter to the $E_{\mathrm{T}}^{\mathrm{miss}}$ calculated from the truth record in the MC. The stop signals are produced in two truth $E_{\mathrm{T}}^{\mathrm{miss}}$ slices: 100-250 GeV and $>$ 250 GeV. For the scharm signals, a single slice, filtering on truth $E_{\mathrm{T}}^{\mathrm{miss}} > 100$ GeV was used.

5.5 Standard Model Processes

The key distinguishing characteristics for the signals considered by this analysis are: high $E_{\mathrm{T}}^{\mathrm{miss}}$ from the LSP, two c-jets and zero leptons in the final state. Data-driven and MC methods are used to model backgrounds that are capable of producing signal-like experimental signatures, either because they have genuine $E_{\mathrm{T}}^{\mathrm{miss}}$ and at least one c-jet, or because they have a sufficient probability to "fake" the detector response, for example dijet events with mis-measured $E_{\mathrm{T}}^{\mathrm{miss}}$. The SM backgrounds considered for this analysis are:

- ***Z*+jets:** events where a Z boson is produced in association with jets. An example event in which a Z boson is produced in association with $b\bar{b}$ pair production is illustrated in figure 5.5a. The most important background is the decay of the Z to two neutrinos, with a heavy flavour initial-state radiation (ISR) jet. Such events are difficult to distinguish from the signal, since they

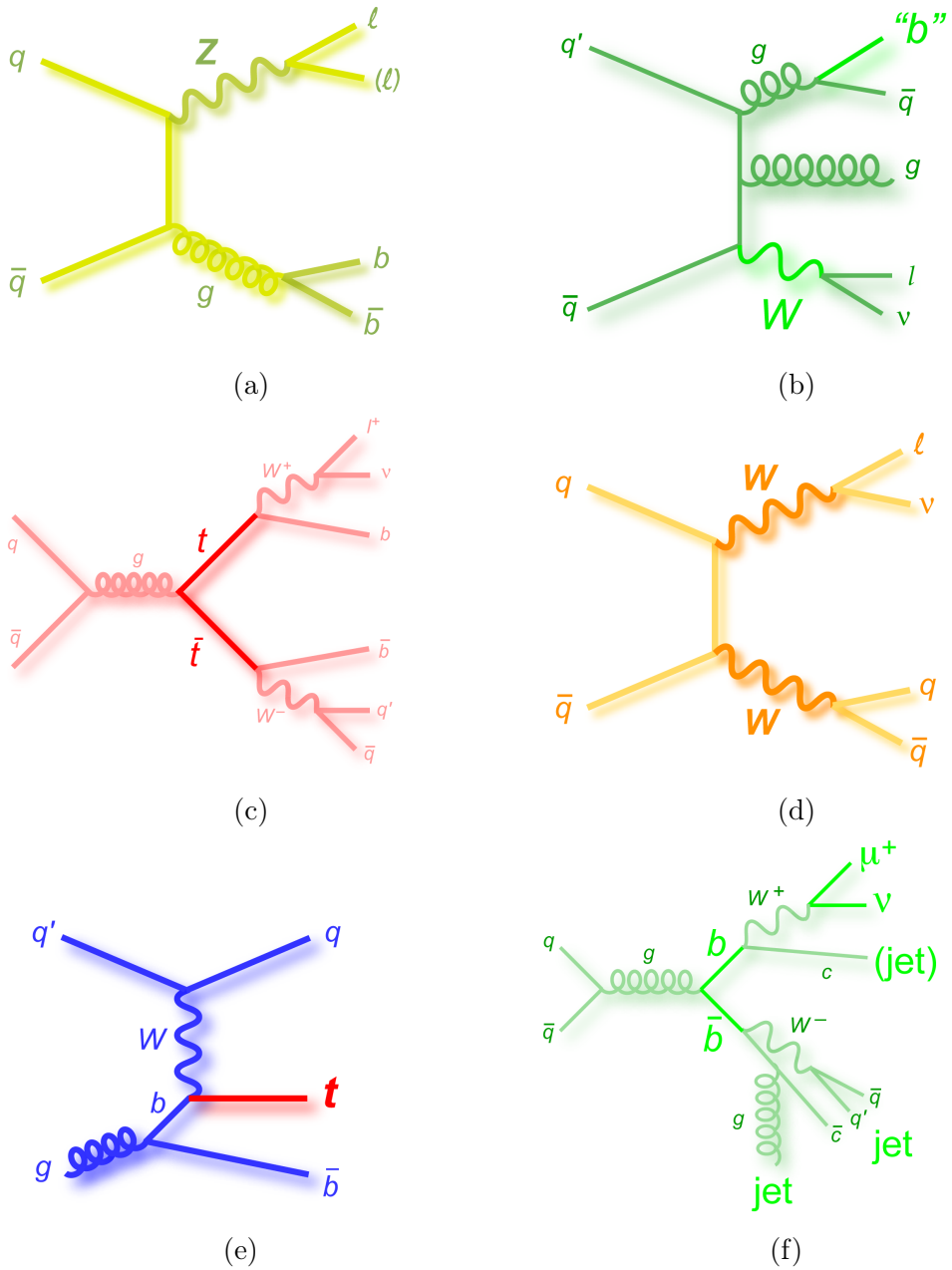

Figure 5.5: Production diagrams for important SM backgrounds. Images taken from Ref. [199].

can produce high $E_{\mathrm{T}}^{\mathrm{miss}}$ and c-tagged jets. The c-tagged jets can arise from real c production or mis-tags from b- or l-jets. A minor background is $Z \to \tau\tau$ in association with a heavy flavour jet, which can, with low probability, produce sufficient $E_{\mathrm{T}}^{\mathrm{miss}}$ in highly asymmetric leptonic decays or mis-measured $E_{\mathrm{T}}^{\mathrm{miss}}$ in double hadronic τ decays. Also considered in this analysis are $Z \to ee$ and $Z \to \mu\mu$. These backgrounds are easily suppressed by $E_{\mathrm{T}}^{\mathrm{miss}}$ requirements, but are useful for controlling the $Z \to \nu\nu$ background (see section 5.8.1). $Z \to q\bar{q}$ decays do not produce real $E_{\mathrm{T}}^{\mathrm{miss}}$ and can enter the SRs only through resolution effects. These events are included in the multijet estimation, described below.

Z+jets events were simulated with `Sherpa` 2.2.1 [154]. `Comix` [200] and `OpenLoops` [201] were used for the ME calculation, with up to two partons at NLO and four partons at LO. The ME to parton shower matching is implemented following Ref. [202] and the events are normalised using the `NNPDF3.0NNLO` PDF set [203].

- ***W*+jets:** events where a W boson is produced in association with jets. An example of a W boson produced in association with two gluons, with a b-tagged jet in the final state, is shown in figure 5.5b. This is an important background as it can produce high $E_{\mathrm{T}}^{\mathrm{miss}}$ from the W decaying to a lepton and a neutrino and a c-jet from heavy flavour ISR. Also important is the case of a τ-lepton decaying hadronically and being mis-tagged as a c-jet. The contribution from events where the W decays to an electron or muon can be highly suppressed by vetoing leptons, leaving only the small fraction of events where the electron or muon is mis-identified, missed by the detector altogether or out of acceptance. Events where the W decays hadronically do not produce real $E_{\mathrm{T}}^{\mathrm{miss}}$ and, like hadronic Z decays, are treated with mulitjet events as described below. Leptonic W+jets events are simulated using the same prescription as for Z+jets, described above.

- ***t*$\bar{t}$:** pair production of top quarks, as shown in figure 5.5c. Sufficient $E_{\mathrm{T}}^{\mathrm{miss}}$ can be produced by neutrinos from the W bosons from the top decays, with additional $E_{\mathrm{T}}^{\mathrm{miss}}$ contributions possible from τ-leptons from the W boson decays. c-jets can be produced by hadronic W decays, and mis-tagged c-jets can arise from b-jets and hadronically decaying τ-leptons. $t\bar{t}$ events are simulated using `Powheg-Box` v2 [159] with the `CT10` PDF [137] set used as input. Parton shower, hadronisation and the underlying event were simulated with `Pythia` 6.428 [204] with the CTEQ6L1 PDF set and the corresponding set of `Perugia2012` tuned parameters [205] and the mass of the top quark is set to 172.5 GeV. To improve the number of events available in the region of parameter space that is of interest, at least one leptonically decaying W boson was required in all $t\bar{t}$ events, since fully hadronic events will not produce sufficient $E_{\mathrm{T}}^{\mathrm{miss}}$.

- **Diboson:** events with two electroweak bosons: WW, ZZ or WZ. An example of WW production is illustrated in figure 5.5d. For ZZ events, a signal like final state can be produced if one of the Z bosons decays hadronically to heavy flavours and the other decays to two neutrinos, similar to the $Z \to \nu\nu$ case. A similar final state can arise from WZ if the W boson decays hadronically to heavy flavour quarks. WZ events can also produce $E_{\mathrm{T}}^{\mathrm{miss}}$ from the W decay

with heavy flavour quarks from a hadronic Z decay. Finally, WW events can produce $E_{\mathrm{T}}^{\mathrm{miss}}$ and heavy flavours from a mixture of hadronic and leptonic decays. Diboson backgrounds tend to be less dominant than $Z \to \nu\nu$, $W \to \tau\nu$ and $t\bar{t}$ due a relatively small cross section. Diboson events were simulated using the same generators as for V+jets, with the ME calculation performed using up to one parton at NLO and three partons at LO.

- **Single top:** production of a single top with an associated b-jet, with the possibility of either an additional jet or a W boson. An example of such an event is shown in figure 5.5e. Single top events can produce $E_{\mathrm{T}}^{\mathrm{miss}}$ from leptonic W decay, mis-tagged c-jets from a bottom quark or τ-lepton from a W decay, or tagged c-jets from hadronic W decay. Single top events are simulated with `Powheg-Box` v1. For the s-channel and Wt channel the CT10 PDF set was used and for the t-channel a four-flavour scheme was used for the NLO ME with the fixed four-flavour PDF set CT10f4 [206]. The parton shower is implemented as for $t\bar{t}$ and the same requirement of at least one leptonically decaying W is applied.

- $\boldsymbol{t\bar{t}+V}$**:** top pair production in association with a W or Z. Such events can produce $E_{\mathrm{T}}^{\mathrm{miss}}$ and c-tagged jets in a variety of ways, but are less dominant than other processes due to a low cross section. They are simulated to NLO using `MadGraph5_aMC@NLO` v2.2.3 interfaced with `Pythia` 8.212.

- **Multijet:** events with two or more jets, arising from QCD interactions between the constituent partons of the colliding protons. A multijet event arising from $b\bar{b}$ pair production is illustrated in figure 5.5f. Such events can produce real $E_{\mathrm{T}}^{\mathrm{miss}}$ from leptonic hadron decays or fake $E_{\mathrm{T}}^{\mathrm{miss}}$ due to resolution effects. If the jet energies are mis-measured then the $E_{\mathrm{T}}^{\mathrm{miss}}$ can be overestimated. In a small fraction of multijet events this mis-measurement is sufficient to reproduce the $E_{\mathrm{T}}^{\mathrm{miss}}$ of the signal. If a c-jet or mis-tagged jet is present then it closely resembles the signal. Due to the large multijet cross section, of the order of mb, it is impractical to simulate sufficient multijet events in the high $E_{\mathrm{T}}^{\mathrm{miss}}$ region of phase space. Instead, a data-driven approach is used, *jet smearing*, described in section 5.8.3.

The event selection described in section 5.7 is designed to maximise the chance of producing a significant excess of data in the presence of a signal. Many of the SM processes described above can be reduced to negligible levels with minimal impact on the signal efficiency by kinematic selections. For others, that resemble the signal closely, this is not possible and they must be estimated very precisely. The background estimation is described in detail in section 5.8.

5.6 Object Definitions

All events are required to have at least one PV, with the PV_0 identified as the PV with the highest $\sum p_{\mathrm{T,track}}^2$. Reconstructed physics objects are classified as either *baseline* or *signal*. Baseline objects are subject to a looser set of selection criteria and are used for the purpose of overlap removal, the procedure of removing double counted objects, described below. Baseline muons and electrons are also used for

vetoing leptons. Signal objects are required to pass tighter selection criteria and are used for the event selections described in section 5.7. The signal objects are by definition a subset of the baseline candidates. The definitions used for each type of physics object, based on the objects reconstructed as in section 4.4, are described below:

- **Electrons:** baseline electrons are required to have a minimum p_{T} of 7 GeV and to fall within $|\eta| < 2.47$, with a loose LH identification operating point (OP) applied. Signal electrons are required to satisfy a medium LH OP and to have $p_{\mathrm{T}} > 27$ GeV. For signal electrons an additional loose isolation requirement is applied, with a varying E_{T} requirement within the isolation cone.

- **Muons:** baseline muons must have $p_{\mathrm{T}} > 7$ GeV and $|\eta| < 2.7$ and pass loose identification criteria. Signal muons are required to satisfy an additional loose isolation requirement with a varying E_{T} threshold, and to have $p_{\mathrm{T}} > 27$ GeV.

- **Jets:** calorimeter jets are used, with baseline jets required to meet a p_{T} threshold of 20 GeV and $|\eta| < 2.8$. Signal jets must have $p_{\mathrm{T}} > 30$ GeV and $|\eta| < 2.5$. The tightened threshold on pseudorapidity is due to the acceptance of the ID and the requirement of tracking for flavour tagging, which is applied to all signal jets.

- **Missing transverse energy:** the missing transverse energy reconstruction follows exactly the procedure described in section 4.4.6.

- **Overlap removal:** this procedure removes ambiguities among jets, electrons and muons in the final state. First, CT muons are removed if they share an ID track with an electron candidate. Next, electrons that share ID tracks with remaining muons are removed. Jet that lie within $\Delta R = 0.2$ of an electron candidate and jets with less than three tracks falling within $\Delta R = 0.2$ of a muon candidate are discarded as they are likely to originate from calorimeter activity induced by the lepton. Any remaining electron candidate is removed if it lies within $\Delta R = 0.4$, and any remaining muon candidate removed if it lies within $\Delta R = 0.04 + 10\,\mathrm{GeV}/p_{\mathrm{T}}^{\mu}$, of a jet.

5.6.1 Charm Tagging

The identification of c-jets is of crucial importance for this analysis as they are one of the key distinguishing features of the final state of the signal. Charm-tagging is implemented using the MV2c100 and MV2cl100 discriminants described in section 4.4.5. The MV2c100 discriminant is optimised to distinguish c-jets from b-jets and is hereafter referred to as "AntiB", and the MV2cl100 discriminant is optimised to distinguish c-jets and l-jets. MV2cl100 is hereafter referred to as "AntiLight". c-tagging OPs are formed by applying thresholds in the AntiB, AntiLight parameter space, shown in figure 5.6 for each jet flavour in $t\bar{t}$ MC. The figure shows that c-jets have a very narrow peak at high values of AntiLight and have a broad distribution in AntiB, tending to smaller values. This reflects the difficulty of distinguishing between c- and b-jets due to their similar properties. Light jets peak sharply at low AntiB and AntiLight showing the effectiveness of lifetime based discrimination for

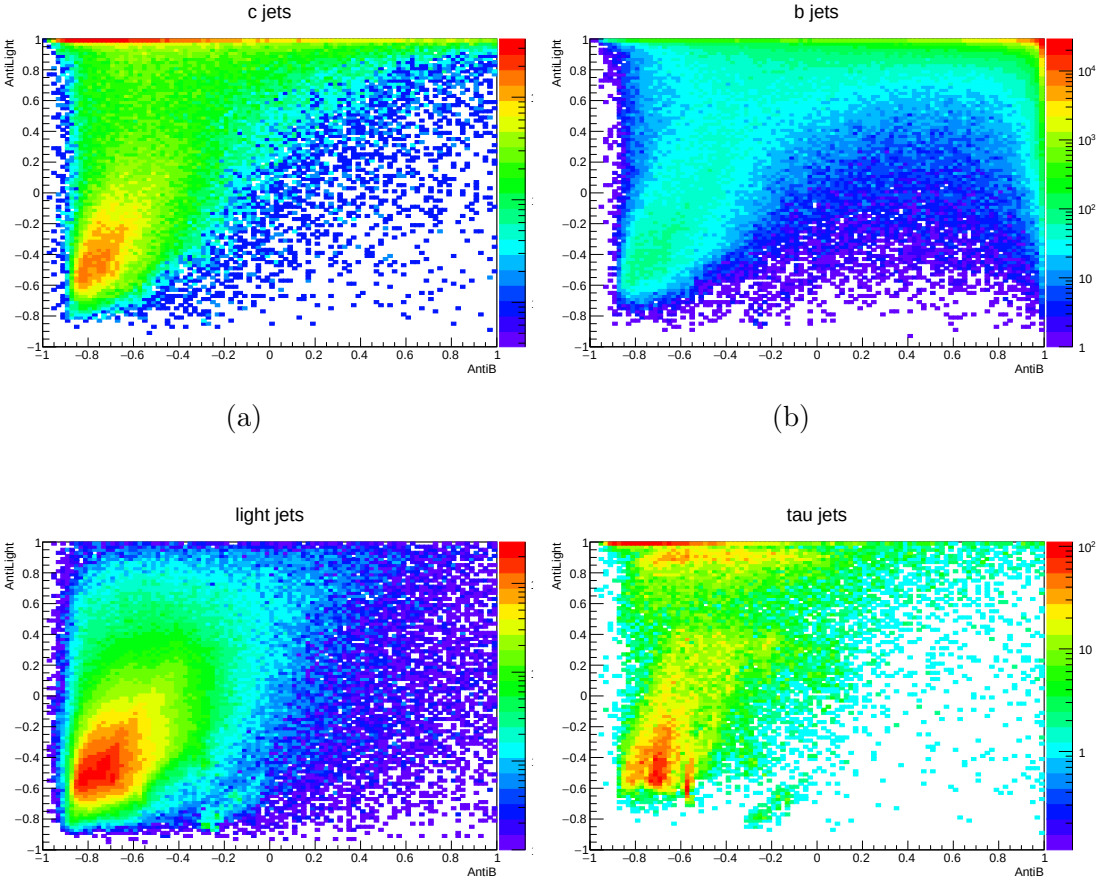

(a) (b)

(c) (d)

Figure 5.6: Distributions for charm-tagging weights for different jet flavours in the AntiB, AntiLight discriminant parameter space. Jet flavours are determined based on truth particles with $p_{\mathrm{T}} > 5$ GeV lying within $\Delta R < 0.3$ of the jet axis. If a truth b-hadron lies within this range, the jet is labelled as a b-jet. Otherwise if a truth c-hadron is found then the jet is labelled as a c-jet. If no truth heavy flavour hadron is found and a truth τ is found, the jet is labelled as a τ-jet. If no b, c or τ can be found the jet is labelled as a l-jet. These distributions are obtained from MC simulation of $t\bar{t}$ events.

distinguishing between light and heavy flavours. A secondary peak is visible in the same region for c-jets, and to a lesser extent for b-jets. This peak represents decays in which the heavy flavour hadron decays quickly and is therefore more difficult to distinguish with lifetime based methods. The figure also demonstrates that the tagger is optimised for rejection against b- and light-flavour jets only; hadronically decaying τ-leptons are not considered and are vetoed indirectly, as described in section 5.7.

Charm-tagging working points of arbitrary tightness can be formed from the AntiB and AntiLight outputs. The optimal choice represents a compromise between the following two considerations:

- **Calibration:** A tight OP can enhance the signal to background ratio S/B but can lead to very low yields for background events. If an OP is too tight this can increase the statistical uncertainty associated to the OP calibration.
- **Tagging strategy:** The chosen OP should be suitable for the tagging strategy used for the event selection. A number of tagging strategies were investigated. One approach is to use multiple c-tagging OPs: one loose OP optimised to reject b-jets with high c-jet efficiency and one tighter OP optimised to reject light jets with a high purity of c-jets. Multiple tagging OPs can enhance the sensitivity of the analysis, but presents technical challenges for calibration, due to cross-contamination of the samples obtained using the different OPs. Instead a single, tight OP was used.

The chosen OP, representing a tradeoff between the above considerations, is shown in table 5.1. It was obtained by restricting the tagging strategy to a single OP and leaving the AntiB and AntiLight thresholds as free parameters in the event selection optimisation (see section 5.7). In the optimisation, a tighter OP is favoured, thus the chosen OP is the tightest possible in line with the first of the above considerations.

OP	AntiLight	AntiB	ϵ_c	ϵ_b	ϵ_{light}
C Tight	> 0.7	< -0.3	0.18	0.05	0.005

Table 5.1: Charm-tagging efficiency and mis-tag rates for the OP selected for this analysis, determined using $t\bar{t}$ simulated events.

The efficiency dependence on p_{T} for this working point is shown in figure 5.8. The c-jet tagging efficiency is low in low p_{T} jets, where tracks may be too soft to be reconstructed, or the SV may not be resolved from the PV. It rises sharply with the reconstructed jet p_{T} to a peak at approximately 100 GeV. It is clear that the charm-tagging does not offer discrimination between c- and τ-jets, which are tagged with similar efficiencies. The c-tagging efficiency diminishes at high p_{T}; as the energy of the c-hadron increases its lifetime in the laboratory frame increases due to time dilation effects. This results in a larger fraction of c-hadrons decaying beyond the pixel detector, and fewer of the associated tracks being reconstructed, increasing the difficulty of distinguishing c-jets from l-jets. The b-jet mis-tag probability displays similar behaviour.

To account for deviations between the efficiency in MC simulation and in data, scale factors were derived separately for c, b and light flavoured jets. The MC events

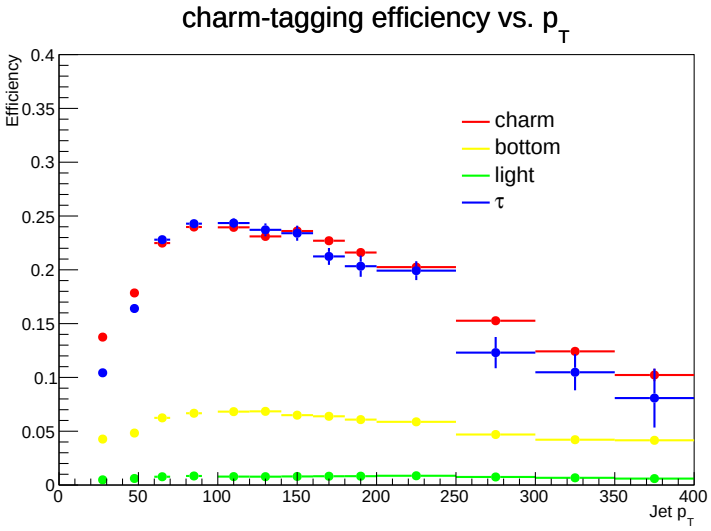

Figure 5.7

Figure 5.8: Charm tagging efficiency as a function of p_{T} for different jet flavours. The truth flavour of a jet is based on a matching of $\Delta R < 0.3$ to a truth particle of the corresponding flavour, considering only truth particles that satisfy $p_{\mathrm{T}} > 5$ GeV. These efficiencies are measured in MC simulation of $t\bar{t}$ events. Binomial uncertainties are shown.

were then given a weight w according to the formula:

$$w = \prod_{\text{jets}} \begin{cases} \mu_f, & \text{jet is tagged} \\ (1 - \mu_f \epsilon_f)/(1 - \epsilon_f), & \text{jet is not tagged} \end{cases} \tag{5.1}$$

where the sum runs over all jets in the event and μ_f and ϵ_f are the scale factor and efficiency corresponding to the jet flavour, respectively. The calibration procedure for each jet flavour is described below:

- ***l*-jets:** calibrated using the adjusted-MC method [207], where the ID tracking variables are adjusted such that they match the tracking performance observed in data. The corresponding updated tracking variables are used as inputs to re-evaluate the l-jet tagging rate in MC. The scale factors are then computed as $\epsilon_{\mathrm{MC}}^{\mathrm{adjusted}}/\epsilon_{\mathrm{MC}}$. The results of this calibration are shown in figure 5.9. The scale factors show an underestimate of the l-jet tagging rate from MC simulation, with scale factors consistently greater than unity. The uncertainties are large; the dominant source is the smearing of the longitudinal impact parameter, which is an important input for the tagging algorithm, and the correction for the number of fake tracks.

- ***b*-jets:** measured from fully leptonic $t\bar{t}$ events, using a combinatorial likelihood approach [208]. An $e\mu$ dilepton selection is applied to obtain a sample rich in b-hadrons. The AntiB and AntiLight weights are used as inputs for the likelihood, along with the jet flavour fractions for all permutations of the number of jets in the event and a probability distribution function of the p_{T} of jets in the event, taken from simulated data. The l-jet scale factors derived

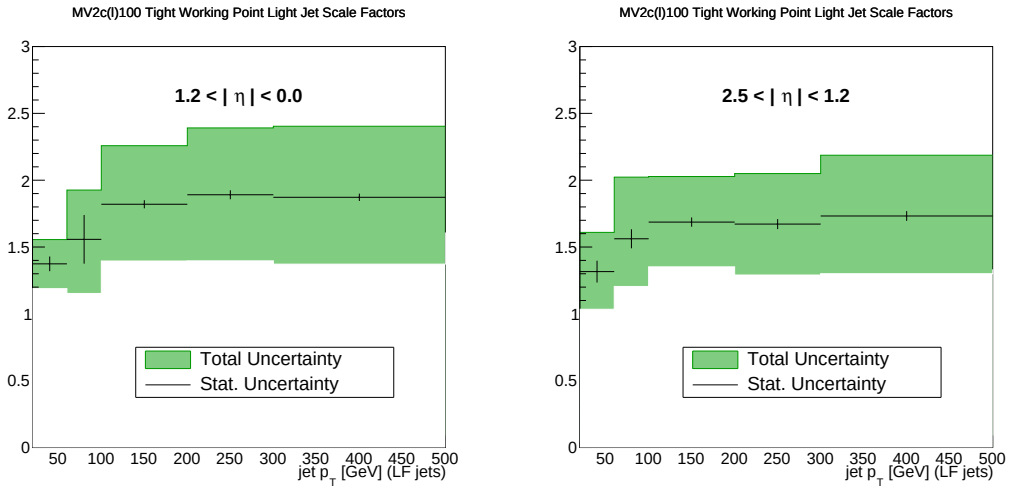

(a) (b)

Figure 5.9: Charm-tagging scale factors with relative uncertainties as a function of jet p_{T} for l-jets in (a) the central region and the (b) forward region.

previously are used as inputs for this calibration. The b-jet efficiency scale factors vary with jet p_{T}, this dependence is shown in figure 5.10a. The dominant uncertainties associated with this method are the ME calculation and the parton showering.

- ***c*-jets:** these are calibrated following [209] using semileptonic $t\bar{t}$ events. Given a hadronically decaying W, the probability for one of the daughters to be a charm-flavoured quark is 0.5 [210]. Thus c-jets make up 25% of the jets from W decays and in the single lepton channel the final state will contain a c-jet from the W decay 25% of the time. This is exploited by applying a selection targeting events where b-tagged jets, using MV2c10, and the remaining two jets, have a high probability to be correctly assigned to the top and W decays, respectively. The jet association is performed using a kinematic likelihood fitter (KLFitter) [211], which maximises a likelihood function derived from the jet-parton combination. Based on the jet assignments and the 25% probability of a jet associated to the hadronically decaying W, the scale factors and associated uncertainties can be extracted. This calibration uses the scale factors for b- and l-tagged jets and their uncertainties as inputs. The dominant uncertainties arise from theory modelling, in particular the ME and parton showering. The scale factors and their associated uncertainties are shown in figure 5.10b. The figure shows that the MC overestimates the tagging efficiency, with large associated uncertainties of around $\pm 10 - 20\%$.

The charm-tagging scale factors derived above are measured in a limited range of p_{T}, and then extrapolated to higher values, with an additional systematic associated to this extrapolation.

The measured c-jet tagging efficiency was found to be dependent on the MC generator used. This is due to the different ME calculation and parton showering scheme used, with the measured efficiency consistently higher in `Pythia` modelled events than in `Sherpa`. Additional MC-MC scale factors are applied to correct for

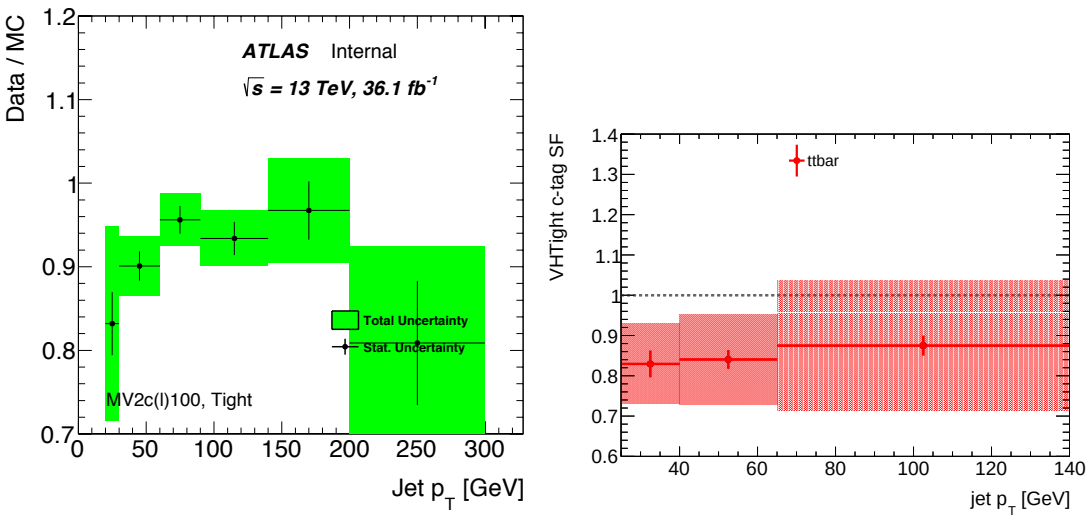

(a) (b)

Figure 5.10: Charm-tagging scale factors with relative uncertainties as a function of jet p_{T} for (a) b-jets and (b) c-jets.

these differences between generators, correcting to the efficiency measured in the `Pythia` generated $t\bar{t}$ sample used for the calibrations described above.

5.7 Event Selection

The event selection comprises five SRs designed to select signal events and to suppress SM backgrounds, in order to maximise the probability to detect, or the exclude in the case of the null hypothesis, the targeted signal model. The event selection is carefully optimised so that any remaining backgrounds can be estimated with sufficient accuracy; this condition limits how tight the selection criteria may be. The starting point for the optimisation of the event selection is to design a *preselection*, described in section 5.7.1, a relatively loose set of criteria designed to produce well-modelled distributions in a favourable region of the phase space to verify the modelling of the MC against data. A variety of different kinematic variables were considered in the optimisation of the SRs; all of the variables considered are described in section 5.7.2.

5.7.1 Preselection

The preselection is based on final state properties that are general to all of the benchmark processes. It includes soft kinematic selections targeting the signal and initial selections that easily suppress SM backgrounds that do not resemble the final state. These selection criteria are described below:

- **Cleaning criteria:** a set of basic quality requirements is applied to ensure that the data collected are adequate for physics analysis. All events in data are required to have been collected as part of a LB that is listed on a GRL, indicating that the initial ATLAS data quality assessment has been passed. The event must have at least one PV with two or more tracks associated to it, to reject beam background and cosmic ray events. A number of additional criteria relating to satisfactory detector conditions must also be met, and any events that contain jets labelled as being likely to originate from detector noise or out-of-time energy depositions (see section 4.4.4) are vetoed.

- **Trigger selection:** one of the key characteristics of the signal is the high $E_{\mathrm{T}}^{\mathrm{miss}}$ from the LSP. The data is selected by $E_{\mathrm{T}}^{\mathrm{miss}}$ triggers which, as described in section 4.2.4, vary by data taking period. For all of 2015 data taking, the `HLT_xe70_mht` trigger was used. For 2016 data taking, the transverse energy threshold was varied up to 110 GeV to control the trigger rate. Figure 4.6 shows the efficiency for $E_{\mathrm{T}}^{\mathrm{miss}}$ triggers in 2015 and 2016 data. The efficiency asymptotically approaches a maximum efficiency, close to 100%, by 250 GeV for all $E_{\mathrm{T}}^{\mathrm{miss}}$ triggers used by this analysis.

- **Reconstructed $\boldsymbol{E_{\mathrm{T}}^{\mathrm{miss}}}$:** to ensure that the online trigger efficiency is constant with respect to the offline reconstructed $E_{\mathrm{T}}^{\mathrm{miss}}$, an offline threshold of $E_{\mathrm{T}}^{\mathrm{miss}} > 250$ GeV is applied in the preselection.

- **Jet selection:** the signal is expected to produce two c-jets in the final state, with possible additional jets from initial and final state radiation. Since the c-quark and LSP participate in a two-body decay, for a squark decaying at rest, if the LSP is light, the c-jet is expected to have similar energy to the LSP, approximately 250 GeV after the $E_{\mathrm{T}}^{\mathrm{miss}}$ threshold is applied. As the mass of the

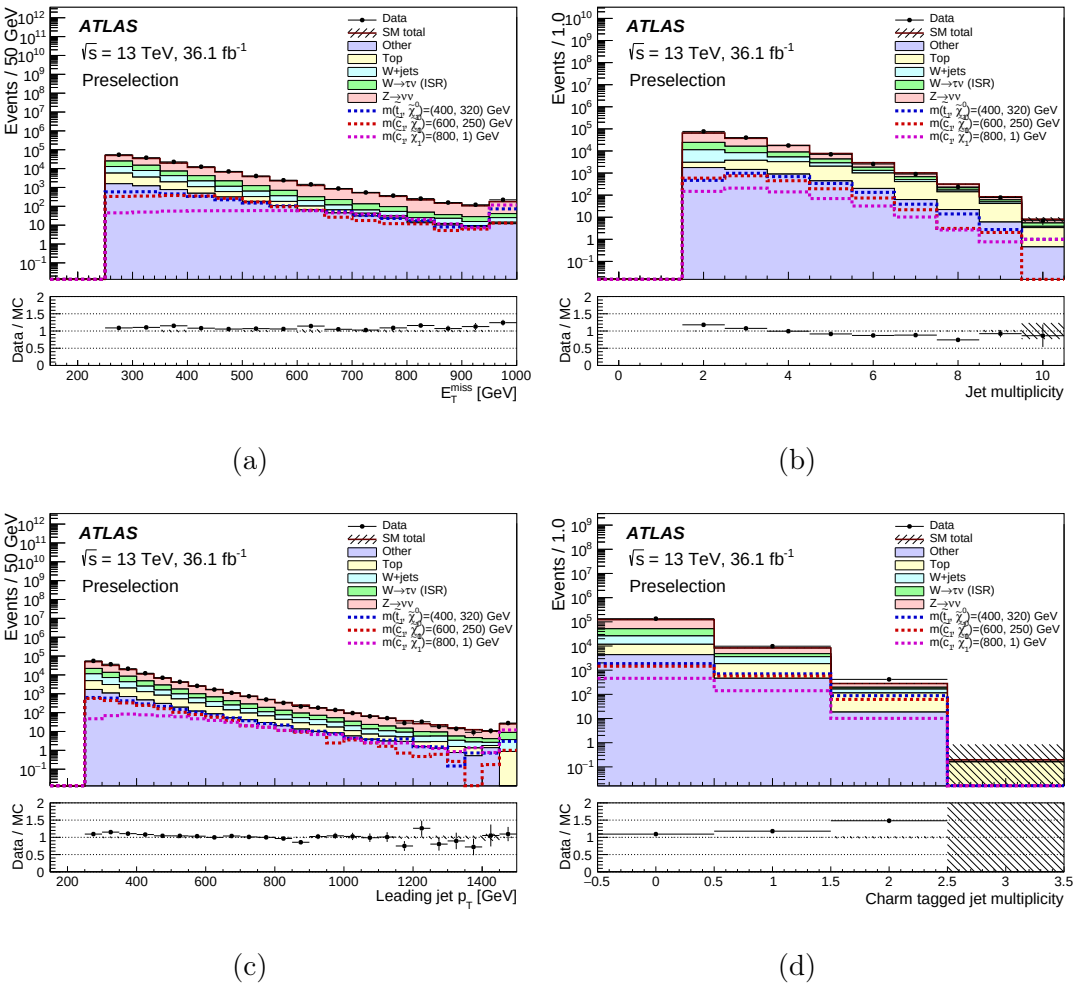

Figure 5.11: Data and MC distributions after the preselection has been applied. The dominant background processes are shown, with background contributing less than 5% combined into the "other" category. Only statistical uncertainties are shown.

LSP approaches the mass of the squark, the share of the energy carried by the c-jet falls and it becomes less likely to be reconstructed. In such cases, where no energetic jet from the squark decay is expected, the system is required to be boosted by an ISR jet. Thus it is useful in all cases to require at least two jets, with at least one with momentum comparable to the $E_{\mathrm{T}}^{\mathrm{miss}}$ requirement.

- **Angular separation between jets and $\boldsymbol{E}_{\mathbf{T}}^{\mathbf{miss}}$:** multijet events can survive the above selection due to mis-measurement of $E_{\mathrm{T}}^{\mathrm{miss}}$. The probability for this to happen is small, but since the cross section is relatively large, mutlijet events are a significant background after the above selections. In multijet events where the $E_{\mathrm{T}}^{\mathrm{miss}}$ measurement is a resolution effect, and not associated with an invisible particle, the direction of the $\boldsymbol{p}_{\mathrm{T}}^{\mathrm{miss}}$ vector should be collinear with the under-fluctuating jet in the transverse plane. A requirement on the minimum angular separation in ϕ between any signal jet and the $\boldsymbol{p}_{\mathrm{T}}^{\mathrm{miss}}$ vector, $\Delta\phi_{\mathrm{min}}(\mathrm{jets}, \boldsymbol{p}_{\mathrm{T}}^{\mathrm{miss}}) > 0.4$ is applied to veto such events. This selection is effective at suppressing the multijet background; the residual contribution was estimated (as described in section 5.8.3) and found to be negligible.

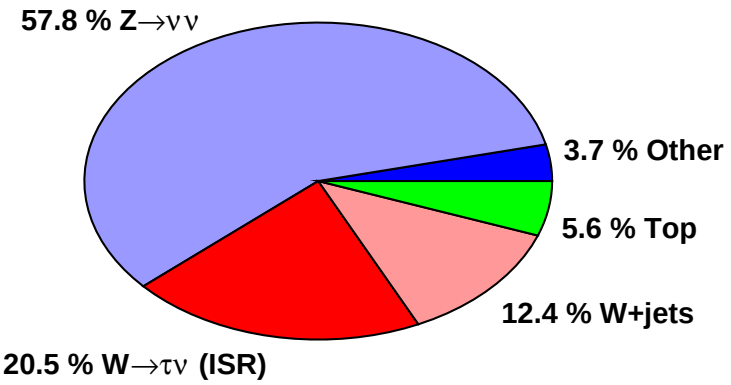

Figure 5.12: Breakdown of SM contributions to the total background after the preselection. The "other" category includes backgrounds that make up less than 5% of the total.

- **Lepton multiplicity:** no electrons or muons are expected in any signal model, so a lepton veto is applied. The baseline lepton veto is used for the veto for two reasons:

  1. Different definitions for the veto were tried and it was found that looser lepton OPs are favoured, without isolation requirements.
  2. In a fraction of multijet events, one of the jets may be mis-reconstructed as an electron. These fake electrons will not be isolated from hadronic activity and will fail to be meet the isolation requirements for signal electrons, which are not applied for the baseline identification. The corresponding jet is likely to then be discarded during overlap removal, so that the jet is not considered for the $\Delta\phi_{\text{min}}(\text{jets}, \boldsymbol{p}_{\text{T}}^{\text{miss}})$ requirement. Thus a veto on signal leptons can result in multijet background events being admitted into the preselection.

The SRs are optimised based only on simulation, in order to prevent biases being introduced by the analysis team, for example by targeting statistical excesses. No charm-tagging is applied at the preselection level, since this would be too close to the SRs and would amount to unblinding prematurely. The preselection is summarised in table 5.2.

Figure 5.11 shows comparisons of data and MC distributions after the preselection has been applied. SM processes with $E_{\text{T}}^{\text{miss}}$ and a heavy flavour jet or hadronically decaying τ-leptons are enhanced. Figure 5.12 shows the relative contribution of SM in the preselection. The main contributing SM processes are, in order of importance: $Z \to \nu\nu$, $W \to \tau\nu$ where the ISR jet is labelled as c-tagged, other W+jets events and top quark events. A $W \to \tau\nu$ event is identified as having a c-tagged ISR jet if no c-tagged jet can be found with a τ lepton within $\Delta R < 0.3$. In figure 5.11a and figure 5.11c the MC is modelling the data well, with the ratio close to unity for most bins. The modelling of the data by MC in figures 5.11b and 5.11d is imperfect, mostly due to the mis-modelling of jet multiplicity, which can be seen in figure 5.11b. The MC simulation underestimates the data for low jet multiplicity, with the ratio decreasing as the multiplicity increases. Poor agreement between

Selection	Threshold
Trigger	$E_{\mathrm{T}}^{\mathrm{miss}}$
$E_{\mathrm{T}}^{\mathrm{miss}}$ [GeV]	> 250
Jet multiplicity	≥ 2
Leading jet p_{T} [GeV]	> 250
$\Delta\phi_{\mathrm{min}}(\mathrm{jets}, \boldsymbol{p}_{\mathrm{T}}^{\mathrm{miss}})$	> 0.4
Lepton multiplicity	$= 0$

Table 5.2: Summary of kinematic selections applied in the preselection. The jet with the highest transverse momentum is referred to as "leading".

data and MC in the charm-tagged jet multiplicity can be seen in figure 5.11d. The discrepancies between data and simulation are corrected for by the statistical fitting procedure, described in 5.10.

The distributions for three benchmark signal models are also in figure 5.11. Figure 5.11a shows that for all three models, a high $E_{\mathrm{T}}^{\mathrm{miss}}$ region is most sensitive, with the peak of the distribution dependent on the mass difference between the squark and LSP, $\Delta m = m_{\tilde{t}_1/\tilde{c}_1} - m_{\tilde{\chi}_1^0}$. The jet multiplicity peaks at three for each of the models, as shown in figure 5.11b. This peak is due to events where the charm jets from the squark system recoil against an energetic ISR jet, which are favoured by the leading jet p_{T} requirement. The leading jet p_{T} distributions shown in figure 5.11c are similar for a mass difference of $\Delta m = 80$ GeV or $\Delta m = 350$ GeV, with a peak at larger values for the high Δm model, where the LSP is approximately massless and the squark mass is high, leading to an energetic leading charm jet. The charm-tagged jet multiplicity in figure 5.11d displays the power of charm tagging for separating signal from background, with the proportion of signal events increasing significantly in the charm-tagged bins.

5.7.2 Signal Region Optimisation

The SRs are defined by kinematic selections applied in addition to the preselection, designed to maximise the probability for observing a statistically significant excess of events for a range of benchmark signals. The signal characteristics are heavily dependent on Δm. From basic relativistic kinematics for a two-body decay, in the rest frame of the squark, the fraction of the energy carried by the LSP is given by:

$$\frac{E_{\tilde{\chi}_1^0}}{E_{\tilde{t}_1/\tilde{c}_1}} = \frac{m_{\tilde{t}_1/\tilde{c}_1}^2 + m_{\tilde{\chi}_1^0}^2 - m_c^2}{2m_{\tilde{t}_1/\tilde{c}_1}^2}. \tag{5.2}$$

For a given squark mass the fraction approaches unity as Δm approaches zero. As a result, the energy of the charm quark approaches zero. From the definition of $E_{\mathrm{T}}^{\mathrm{miss}}$, it is clear that it cannot be greater than the measured p_{T} sum of the physical objects in the event. Therefore as the jets become softer the $E_{\mathrm{T}}^{\mathrm{miss}}$ is reduced. Furthermore, very soft charm quarks are more likely to be missed by jet reconstruction altogether, by failing to meet the transverse energy threshold imposed for calibrated jets. Thus lower Δm scenarios are characterised by soft decay products and smaller $E_{\mathrm{T}}^{\mathrm{miss}}$ and,

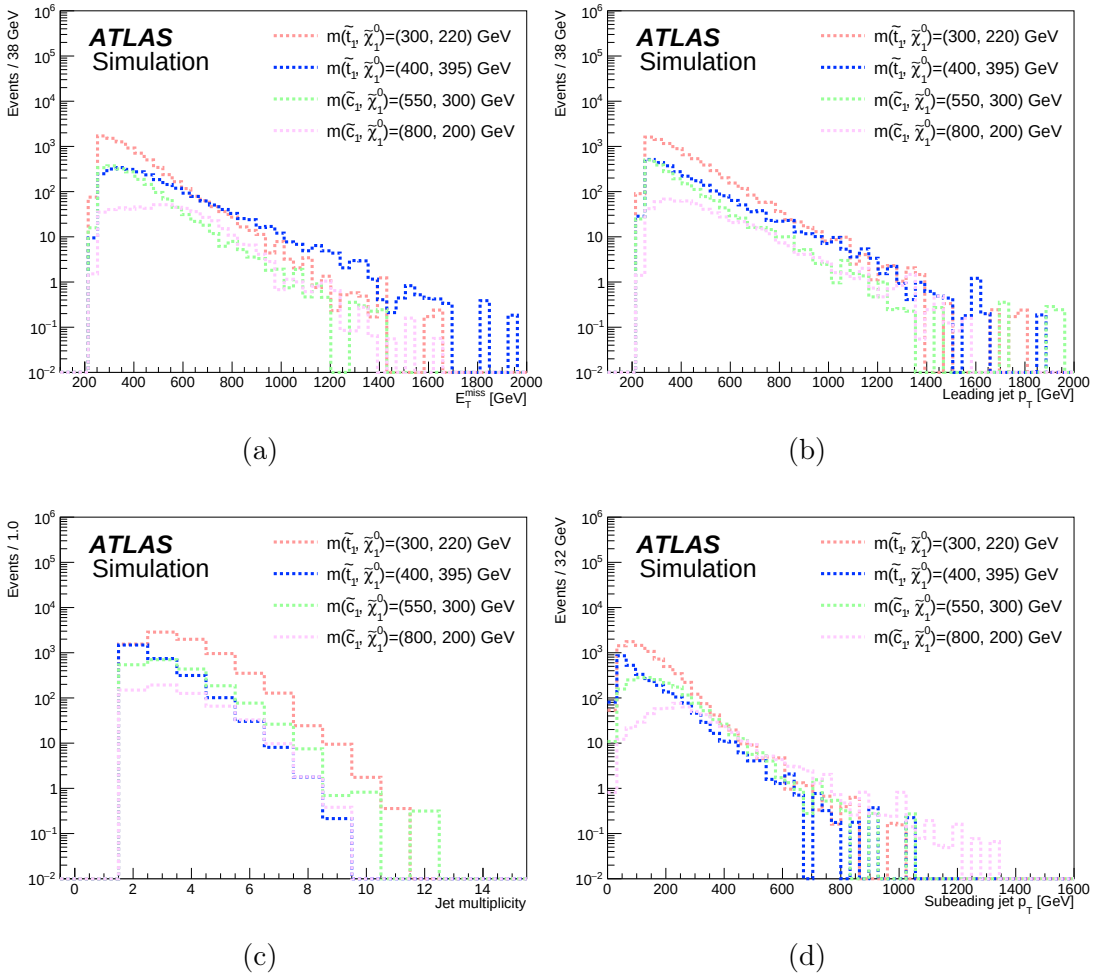

Figure 5.13: Signal distributions for different values of Δm. All signal samples are generated with a truth filter of $E_{\mathrm{T}}^{\mathrm{miss}} > 100$ GeV applied.

in the most compressed cases, lower multiplicity of reconstructed jets. This can be seen in figure 5.13. For the reconstructed $E_{\mathrm{T}}^{\mathrm{miss}}$ and p_{T} distributions for the leading and subleading jets in figures 5.13a, 5.13b and 5.13d, the peak is shifted toward higher values for models with a higher Δm. In figure 5.13c the $\Delta m = 5$ GeV signal has lower jet multiplicity due to the charm quark being too soft to be reconstructed.

More compressed scenarios can be targeted by requiring the presence of a hard ISR jet recoiling against the $\tilde{t}/\tilde{c}$ pair system, illustrated for the $\tilde{t}_1 \rightarrow c\tilde{\chi}_1^0$ signal in figure 5.14. This reduces the signal acceptance, but selects events with higher $E_{\mathrm{T}}^{\mathrm{miss}}$ and jet p_{T} . The dependence of the average $E_{\mathrm{T}}^{\mathrm{miss}}$ on the mass difference for different boosts to the squark system is shown in figure 5.15a for a squark of mass 800 GeV. For a system that is not boosted, a Δm of ~ 250 GeV is required before the average event survives the trigger selection. Applying a threshold of $p_{\mathrm{T}} > 250$ GeV on the leading jet sufficiently boosts the system such that the average $E_{\mathrm{T}}^{\mathrm{miss}}$ meets the trigger requirement. As Δm approaches the mass of the squark, the fraction of energy carried by the LSP approaches exactly half. At the same time the charm jet becomes harder (see figure 5.15b), leading to more energetic jets from the squark pair system.

Due to highly variable signal topologies, a single SR selection is unsuitable for

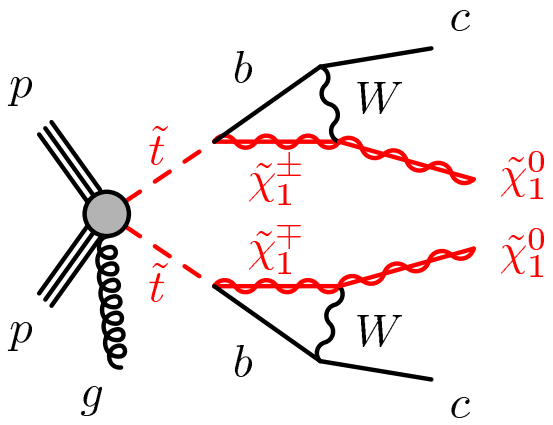

Figure 5.14: Diagram for the pair production of top squarks with subsequent decay to charm quarks. The presence of an ISR jet is indicated for illustrative purposes.

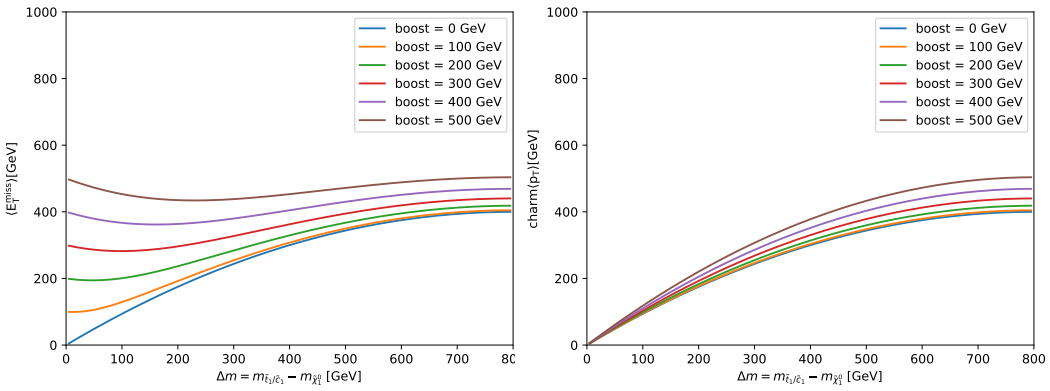

(a) (b)

Figure 5.15: Dependence of (a) average $E_{\mathrm{T}}^{\mathrm{miss}}$ and (b) charm p_{T} on the mass difference between the squark and the LSP for different boosts to the system. The squark mass is set to 800 GeV in each case.

targeting the whole grid of signal models. Instead, five SRs, targeting progressively higher Δm, were optimised. These SRs are labelled 1-5, with the label increasing for a higher targeted Δm range. A number of kinematic variables were investigated for the SR optimisation; the variables used in the final selection that are extra to the preselection are described below:

- ***c*-tagged jet multiplicity:** as described in section 5.6.1, a number of charm-tagging approaches were investigated. The most favourable S/B ratio is found in the two charm-tagged jet bin. This selection is challenging however since it becomes difficult to design any CR with sufficient statistics to estimate the dominant background processes. The chosen approach was to require at least one c-tagged jet using the tight working point shown in figure 5.8.

- **Leading jet *c*-tag veto:** in compressed models and models with intermediate Δm the hard leading jet selection preferentially selects an ISR jet. SM events with heavy flavour ISR may then enter the SR through a c-tagged leading jet. It can therefore be favourable for SRs targeting these models to veto any event where the leading jet is c-tagged.

- **Leading *c*-tagged jet p_{T}:** this is useful variable for targeting models in a specific range of Δm as it allows the p_{T} of the jet from the squark decay to be targeted. As Δm increases the energy share of the charm quark is increased and a tighter selection can be applied to the c-tagged jet p_{T}. For compressed scenarios the c-tagged jet is low in momentum and an upper threshold on its p_{T} can be favourable. Figure 5.16a demonstrates the dependence of the leading c-tagged jet p_{T} on the signal model, with a strong peak at low p_{T} for the $\Delta m = 80$ GeV signal. The double peak structure, particularly visible in the backgrounds, originates from the leading jet p_{T} requirement. The peak at 250 GeV is from events where the leading jet was tagged, whilst the peak at low momentum is from events where one of the subleading jets is tagged.

- **p_{T} of subleading jets:** the subleading and sub-subleading jet p_{T} are left free in the optimisation, along with the leading jet p_{T}. The optimisation tends to favour higher jet momenta, progressively decreasing for the softer jets in the event. This is expected; if the leading jet is an ISR jet the two subleading jets are from squark decays, taking higher shares of the energy of the parent.

- **Minimum transverse mass:** this variable was designed to suppress the contribution from $W \to \tau\nu$ events where the τ is mis-tagged as a c-jet. It is defined as the minimum transverse mass reconstructed from $\boldsymbol{p}_{\mathrm{T}}^{\mathrm{miss}}$ and a c-tagged jet p_{T}:

$$m_{\mathrm{T}}^{c} = \min_{c-\mathrm{jets}} \sqrt{2 \cdot E_{\mathrm{T}}^{\mathrm{miss}} p_{\mathrm{T}}^{c} \cdot (1 - \Delta\phi(\boldsymbol{p}_{\mathrm{T}}^{\mathrm{miss}}, \vec{p}_{\mathrm{T}}^{c}))}. \tag{5.3}$$

  The sum runs over all c-jets in the event. Since the transverse projection of the p_{T} is less than or equal to momentum, for an on-shell decay, this quantity is bounded from above by the mass of the parent of the invisible particle and the c-jet. In events with a mis-tagged hadronically decaying τ-lepton, the m_{T}^{c} distribution (see figure 5.16b) falls sharply beyond the W mass at around 80 GeV. A threshold of $m_{\mathrm{T}}^{c} > 120$ GeV dramatically suppresses this

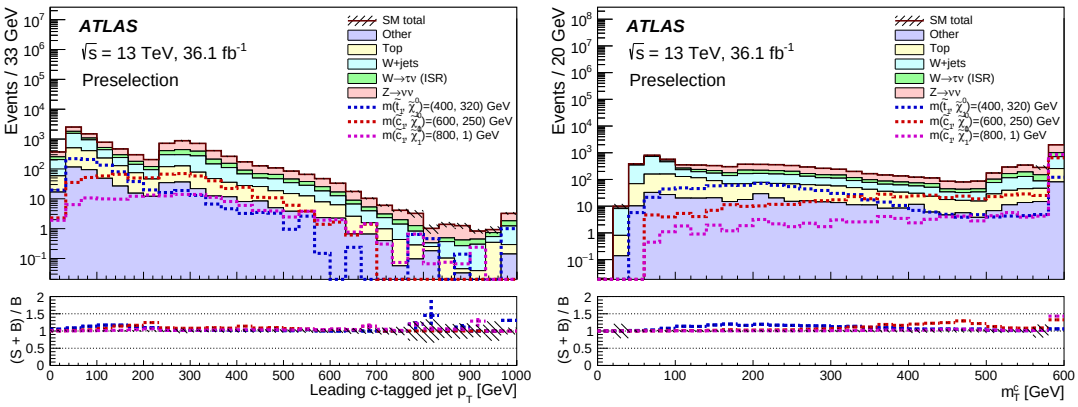

(a) (b)

Figure 5.16: MC distributions after the preselection and c-tagging has been applied. The leading c-jet p_{T} is shown in figure (a) and the m_{T}^{c} distribution is shown in figure (b). The dominant background processes are shown, with backgrounds contributing less than 5% combined into the "other" category. In the lower panel the ratio of the sum of the signal and background to the background, $(S+B)/B$ is shown for each signal model. Only statistical uncertainties are shown.

background. In $W \to \tau\nu$ events where the leading c-tagged jet is from ISR, the τ lepton from the W decay is not included in the m_{T}^{c} calculation and no W peak is visible.

The transverse mass was left free to vary in the optimisation with both a lower and upper threshold. It was found that the lower threshold at 120 GeV is always favourable as expected from the discussion above. The optimisation also favours a moving m_{T}^{c} window, varying from lower values to higher values as Δm increases. This is in part due to the mass of the squark tending to increase with Δm; as the mass of the parent of the c-jet and LSP increases, so the peak of the m_{T}^{c} distribution increases.

These variables and those used to define the preselection are sufficient to define the SRs. Once the final set of kinematic variables was chosen, the SRs were optimised by performing a scan over different configurations of selections based on the chosen variables. The figure of merit was the expected exclusion significance (defined in section 5.10) of the selection based on the MC prediction. This was an iterative process, the initial SRs were defined in this way and the procedure repeated with initial estimates of the normalisations for individual background processes, following the methodology described in section 5.8. The resulting SRs are described separately below:

- **SR1:** this was designed to target the most compressed signal models with $\Delta m < 50$ GeV. In these models, the decay products are soft enough that the c-jets often fail to meet reconstructed thresholds. As a result, at least two signal jets are required, the harder of these is expected to be an ISR jet. Events where the leading jet is c-tagged are vetoed and an upper threshold is applied on the leading c-tagged jet p_{T}. A m_{T}^{c} window is used to veto mis-

	SR1	SR2	SR3	SR4	SR5
Trigger	$E_{\mathrm{T}}^{\mathrm{miss}}$ triggers				
Leptons	0 e AND 0 μ				
$E_{\mathrm{T}}^{\mathrm{miss}}$ [GeV]	> 500				
$\Delta\phi_{\mathrm{min}}(\mathrm{jets}, \boldsymbol{p}_{\mathrm{T}}^{\mathrm{miss}})$[rad]	> 0.4				
$N_{c-\mathrm{jets}}$	≥ 1				
N_{jets}	≥ 2	≥ 3	≥ 3	≥ 3	≥ 3
Leading jet c-tag veto	yes	yes	yes	yes	no
p_{T}^{j1} [GeV]	> 250	> 250	> 250	> 250	> 300
p_{T}^{j2} [GeV]	–	–	> 100	> 140	> 200
p_{T}^{j3} [GeV]	–	–	> 80	> 120	> 150
p_{T}^{c1} [GeV]	< 100	> 60	> 80	> 100	> 150
m_{T}^{c} [GeV]	$\in (120, 250)$	$\in (120, 250)$	$\in (175, 400)$	> 200	> 400

Table 5.3: Overview of the SR selection criteria. N_{jets} and $N_{c-\mathrm{jets}}$ indicate the total number of jets and c-jets, respectively; p_{T}^{j1} , p_{T}^{j2} and p_{T}^{j3} indicate the transverse momentum of the leading, sub-leading and sub-sub-leading jet; and p_{T}^{c1} is the transverse momentum of the c-jet with the highest p_{T} .

tagged τ-leptons and reject higher mass systems with a c-jet and an invisible particle.

- **SR2:** targets less compressed scenarios, with Δm in the range 50-100 GeV. The jet multiplicity is increased in this region since the c-jets are unlikely to fall below the 30 GeV signal jet threshold, but an ISR is still required to boost the system for sufficient $E_{\mathrm{T}}^{\mathrm{miss}}$ to survive the trigger selection. The leading c-tagged p_{T} requirement is changed to a lower threshold to reflect the increased energy share of the c-jet in the squark system.

- **SR3:** this region targets intermediate mass differences between 100-450 GeV. The selection is similar to **SR2** but with additional selections on the subleading jets and a tightened leading c-jet p_{T} threshold. The m_{T}^{c} window is also increased.

- **SR4:** sensitive to a similar Δm range, but targeting a more boosted system, with tighter requirements on the subleading jets and the c-tagged jet, and replacing the m_{T}^{c} window by a tightened lower threshold.

- **SR5:** targets signal models with $\Delta m > 450$ GeV. For these higher mass differences it becomes likely that the leading two jets are both of the c-jets from the squark system, so the veto on events where the leading jet is charm-tagged is removed. All of the jet p_{T} thresholds and the m_{T}^{c} threshold are tightened relative to **SR4**.

For all SRs the $E_{\mathrm{T}}^{\mathrm{miss}}$ requirement was also tightened from the preselection to 500 GeV. All the SR selections are summarised in table 5.3.

Once a SR has been optimised, it is instructive to inspect the $N-1$ plot for each of the discriminating variables applied in the selection. An $N-1$ plot for a discriminating variable x is the distribution of x in the SR with the threshold on x removed. This allows the effectiveness of the threshold on x for separating signal

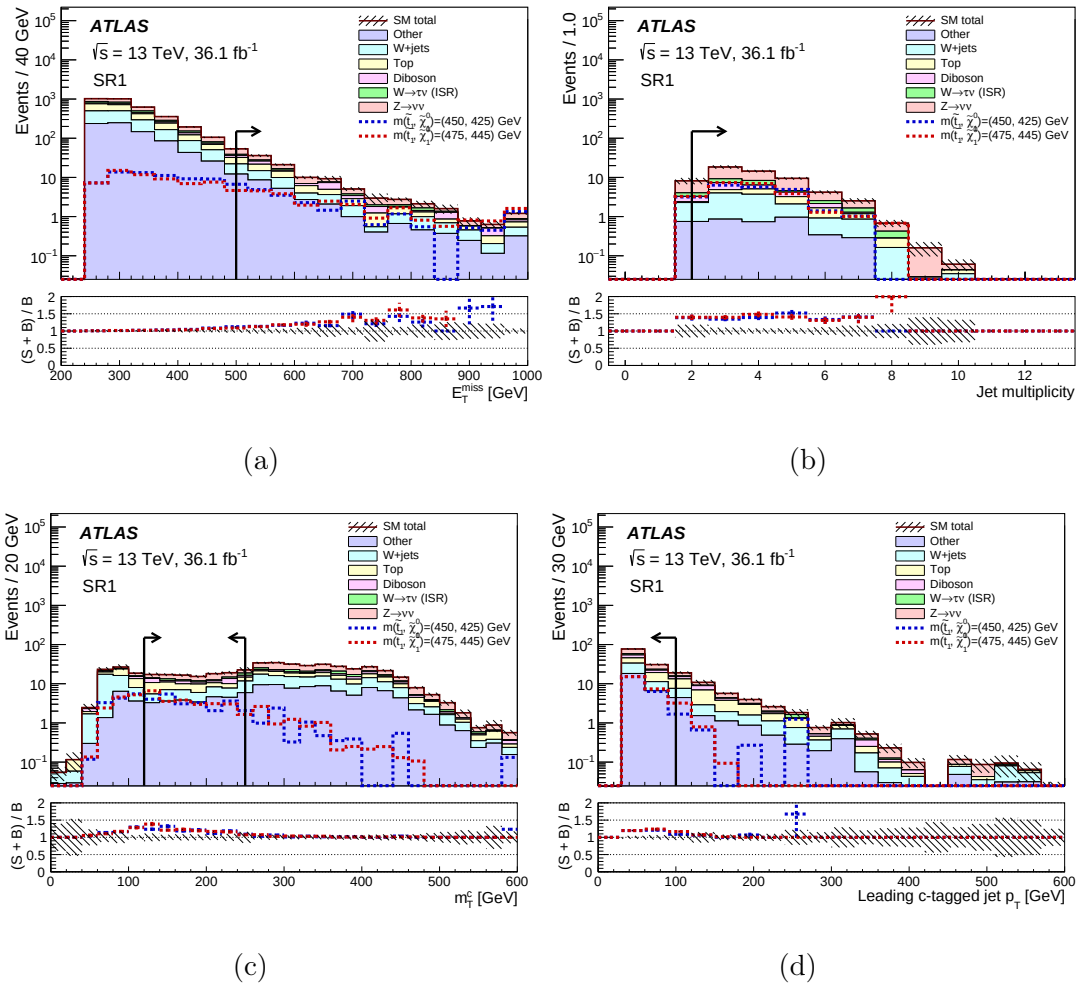

Figure 5.17: N-1 plots for **SR1**. Distributions for kinematic variables with the selection on that variable removed. An arrow is painted over each distribution to show the threshold applied. In the lower panel the ratio of the sum of the signal and background to the background, $(S+B)/B$ is shown for each signal model. Only statistical uncertainties are shown.

and background events to be evaluated. Figure 5.17 shows N-1 plots for **SR1**, with the $(S+B)/B$ ratio in each bin shown in the lower panel. The complete set of N-1 plots, for all regions, is included in appendix B.1. These plots demonstrate the effectiveness of each of the individual selections applied to target an enhanced $(S+B)/B$, and therefore exclusion power for the null hypothesis or the significance for discovery, for a given SR. Before the SRs can be unblinded, the remaining background contributions and uncertainties must be carefully estimated.

5.8 Background Estimation

Figure 5.18 shows the breakdown of SM contributions to **SR1** yields. The compositions are similar in the other SRs; the complete set of charts is therefore relegated to appendix B.2. The dominant contribution is from $Z \to \nu\nu$, with significant contributions from W+jets processes and $t\bar{t}$. The design of the CRs and VRs for each of these processes are described in the following sections.

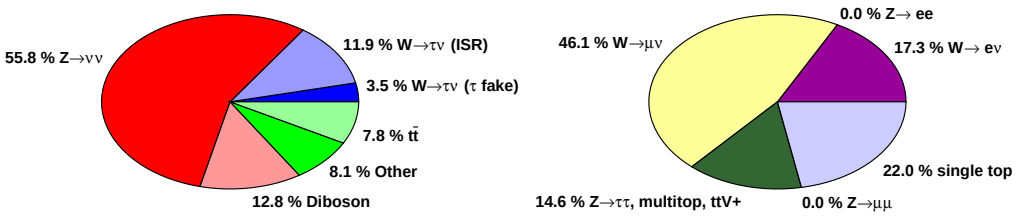

(a) (b)

Figure 5.18: (a) Breakdown of SM contributions to the total background after the **SR1** selection. The "other" category includes backgrounds that make up less than 5% of the total. (b) The composition of the "other" category, where $ttV+$ refers to top quark pair production in association with one or more weak bosons.

Diboson processes also make a significant contribution to the SR yields, however it is difficult to design appropriate CRs for these processes. They were therefore estimated purely based on MC. The same is true for smaller backgrounds: $Z \to \tau\tau$, $Z \to \mu\mu$, $Z \to ee$, single top and multitop, and top pair production in association with one or more weak bosons. The multijet background was estimated to be negligible in the SRs; the methodology for this estimate is described in section 5.8.3.

5.8.1 Z+jets Control Region

$Z \to \nu\nu$ is the dominant background in all SRs, contributing around $50-60\%$ of the total. This process enters the SRs primarily due to the presence of a tagged c-jet in the event, with a significant contribution from mis-tagged l-jets and a less significant contribution from mis-tagged b-jets. The relative contribution of each of these jet categories to **SR1** is shown in figure 5.19d. To estimate this background a CR is used, designed to be orthogonal to its corresponding SR, rich in events with similar kinematic properties to the $Z \to \nu\nu$ background and low in signal contamination. To recreate events with a two-body Z decay resulting in approximately massless daughters that are invisible to the detector, $Z \to ee$ and $Z \to \mu\mu$ were chosen, hereafter referred to collectively as $Z \to ll$, with the lepton p_{T} removed from the calculation of $E_{\mathrm{T}}^{\mathrm{miss}}$. The following kinematic variables are used (in addition to the standard cleaning criteria described in section 5.7.1) to target $Z \to ll$ events:

- **Trigger selection:** all events in the Z+jets CR are required to be triggered by either the $E_{\mathrm{T}}^{\mathrm{miss}}$ trigger used for the preselection or the primary electron trigger. The $E_{\mathrm{T}}^{\mathrm{miss}}$ trigger targets $Z \to \mu\mu$. As described in section 4.2.4, the online $E_{\mathrm{T}}^{\mathrm{miss}}$ calculation is based on calorimetric information only and therefore muons are not included. As a result, energetic dimuon Z decays are effectively invisible to the online $E_{\mathrm{T}}^{\mathrm{miss}}$. The primary electron trigger targets $Z \to ee$ decays.

- **Dilepton requirement:** all events are required to contain exactly two signal leptons of the same flavour and opposite sign (SFOS), muons are required for a $E_{\mathrm{T}}^{\mathrm{miss}}$ triggered event and electrons for an electron triggered event. To suppress dilepton events from non-Z events the reconstructed invariant mass of the dilepton system m_{ll} is required to fall within 15 GeV of the Z mass.

- **Lepton corrected $\boldsymbol{E}_{\mathbf{T}}^{\mathbf{miss}}$:** As described above, the leptons are treated as invisible to mimic the neutrinos from $Z \to \nu\nu$. This is achieved by vectorially adding the p_{T} of the leptons to $\boldsymbol{p}_{\mathrm{T}}^{\mathrm{miss}}$, equivalent to omitting the leptons from the $E_{\mathrm{T}}^{\mathrm{miss}}$ calculation. The value of m_{T}^{c} is recalculated using the lepton corrected $E_{\mathrm{T}}^{\mathrm{miss}}$, $E_{\mathrm{T}}^{\mathrm{miss,corr}}$. The $\Delta\phi_{\mathrm{min}}(\mathrm{jets}, \boldsymbol{p}_{\mathrm{T}}^{\mathrm{miss}})$ variable used to suppress multijet events is also recalculated.

- **Original $\boldsymbol{E}_{\mathbf{T}}^{\mathbf{miss}}$:** fully leptonic $t\bar{t}$ events can enter the CR by virtue of the $E_{\mathrm{T}}^{\mathrm{miss}}$ from the accompanying neutrinos. Such events are expected to have genuinely high $E_{\mathrm{T}}^{\mathrm{miss}}$ before correction. They are suppressed by requiring the original $E_{\mathrm{T}}^{\mathrm{miss}}$ to be low, which is expected to be the case for $Z \to ll$ events.

All other kinematic variables are unchanged from the definitions given in section 5.7.1. All selections are kept as close as possible to the SRs to minimise the extrapolation uncertainty from the CRs to the SRs. However, in order to maintain a sufficient number of events for the background estimation, the $E_{\mathrm{T}}^{\mathrm{miss,corr}}$ and jet p_{T} thresholds must be relaxed. The full event selection used for the $Z \to ll$ CR is given in table 5.4.

	Z CR1	Z CR2	Z CR3	Z CR4	Z CR5
Trigger	$E_{\mathrm{T}}^{\mathrm{miss}}$ OR single lepton				
Leptons	2 SF OS e OR μ				
$m_{\ell\ell}$ [GeV]	$\in (76, 106)$				
$\Delta\phi_{\mathrm{min}}(\mathrm{jet}, \boldsymbol{p}_{\mathrm{T}}^{\mathrm{miss,corr}})$ [rad]	> 0.4				
$N_{c-\mathrm{jets}}$	≥ 1				
$E_{\mathrm{T}}^{\mathrm{miss}}$ [GeV]	< 75				
$E_{\mathrm{T}}^{\mathrm{miss,corr}}$ [GeV]	> 250				
p_{T}^{j1} [GeV]	> 250				
N_{jets}	≥ 2	≥ 3	≥ 3	≥ 3	≥ 3
Leading jet c-tag veto	yes	yes	yes	yes	no
p_{T}^{j2} [GeV]	–	–	> 100	> 100	> 100
p_{T}^{j3} [GeV]	–	–	> 80	> 100	–
p_{T}^{c1} [GeV]	< 100	> 60	> 80	> 100	> 100
$m_{\mathrm{T}}^{c,\mathrm{corr}}$ [GeV]	$\in (120, 250)$	$\in (120, 250)$	$\in (175, 400)$	> 200	> 400

Table 5.4: Overview of the Z CR selection criteria. N_{jets} and $N_{c-\mathrm{jets}}$ indicate the total number of jets and c-jets, respectively; p_{T}^{j1}, p_{T}^{j2} and p_{T}^{j3} indicate the transverse momentum of the leading, sub-leading and sub-sub-leading jet; and p_{T}^{c1} is the transverse momentum of the c-jet with the highest p_{T}. Variables with the superscript "corr" refer to variables corrected as described in the text.

The background compositions for **CR1 Z** and **CR5 Z** are shown in figures 5.19a and 5.19b, respectively. A complete set of compositions is included in appendix B.3. These CRs are similarly composed: highly pure in $Z \to ll$ events, with a minor contribution from diboson events. The signal contamination in these regions is negligible. The $t\bar{t}$ contribution is small, demonstrating the effectiveness of the threshold on $E_{\mathrm{T}}^{\mathrm{miss,original}}$. The modelling of the jet flavour composition should be similar between the CRs and SRs to correctly emulate charm tagging. Figures 5.19c and 5.19d show the flavour composition of jets in **CR1 Z** and for $Z \to \nu\nu$ events in **SR1**, respectively. Close agreement is observed, validating the replacement

procedure. Also important is the agreement in flavour composition of the charm-tagged jet between **CR1 Z** and for $Z \to \nu\nu$ **SR1** since it used for kinematic variables used in the event selection. The comparison can be made by comparing figures 5.19e and 5.19f. Again, the agreement is good, with similar compositions for all jet configurations. The complete set of comparisons for all SRs is included in appendix B.4.

Figure 5.20 compares kinematic distributions for key variables in the preselection with lepton replacement for $Z \to ll$ and requiring at least one charm-tagged jet. The jet multiplicity agrees closely for all three processes as shown in figure 5.20a. $E_{\mathrm{T}}^{\mathrm{miss}}$, shown in figure 5.20b, and jet p_{T} for the leading and subleading jets, shown in figures 5.20c and 5.20d, respectively, show good shape agreement. The close agreement for all three processes demonstrates that $Z \to ll$ processes with lepton replacement make a good proxy for $Z \to \nu\nu$, probing a very similar region of phase space.

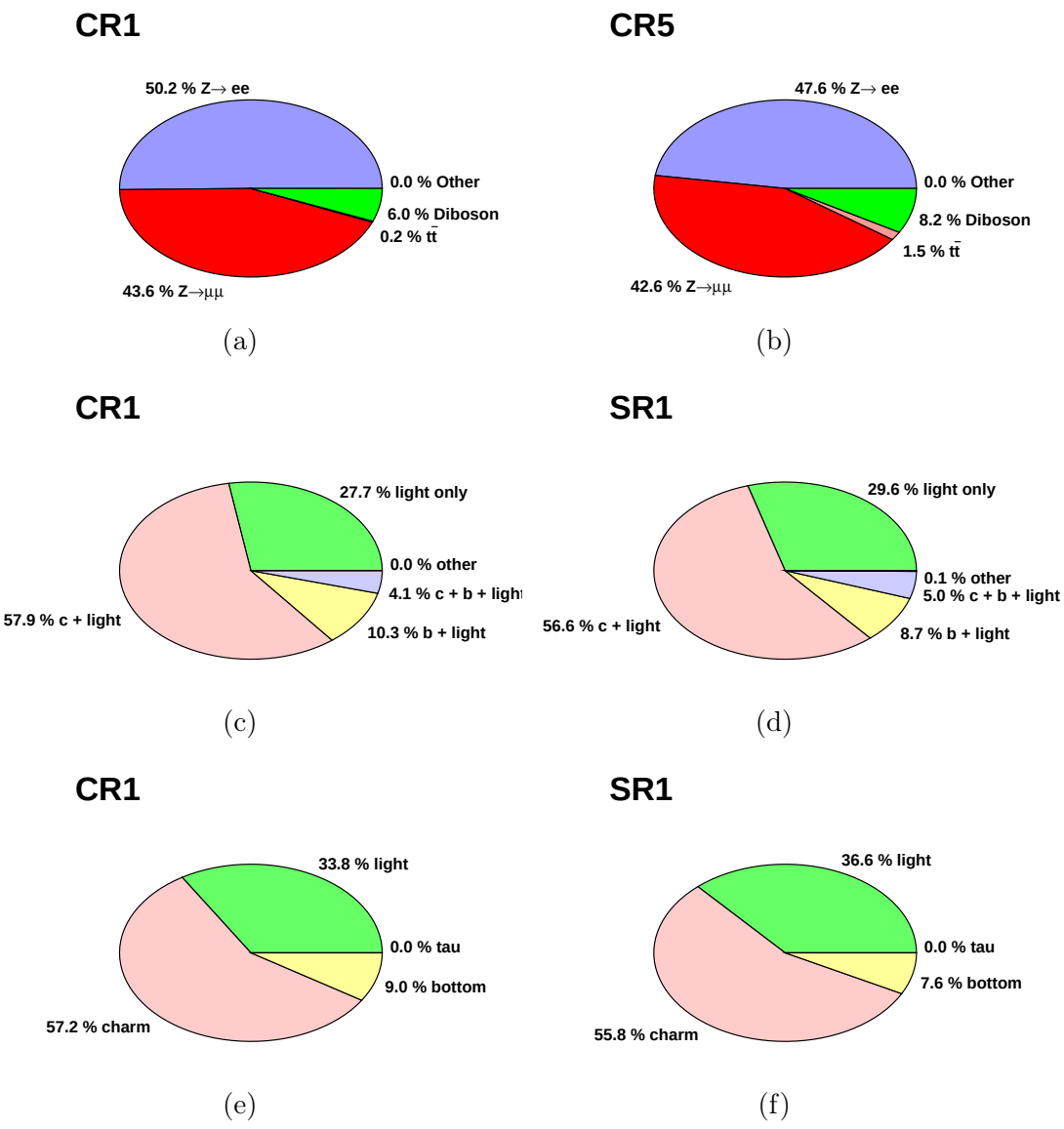

Figure 5.19: (a) Background composition in **CR1 Z** and (b) **CR5 Z**. The "other" category includes backgrounds that make up less than 5% of the total. (c) Flavour composition for **CR1 Z** and (d) $Z \to \nu\nu$ in **SR1**. Flavour origin of the leading charm tagged jet for (e) **CR1 Z** and (f) $Z \to \nu\nu$ in **SR1**.

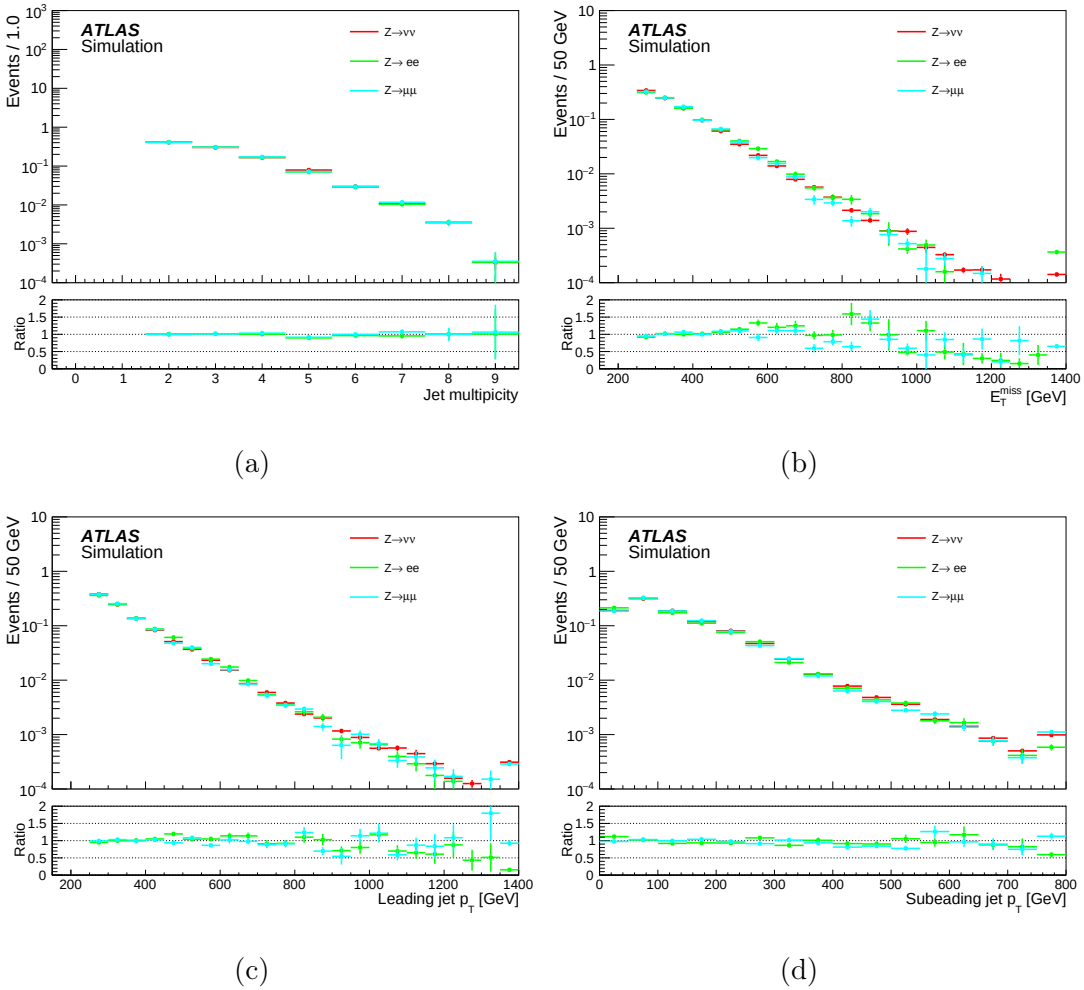

Figure 5.20: Comparison of (a) jet multiplicity, (b) $E_{\mathrm{T}}^{\mathrm{miss}}$, (c) leading jet p_{T} and (d) subleading jet p_{T} for $Z \to ll$ with lepton treatment and $Z \to \nu\nu$. $Z \to \nu\nu$ events are required to satisfy the preselection plus at least one c-tagged jet. $Z \to ll$ events must satisfy the preselection with lepton treatment and at least one c-tagged jet. The histograms are normalised to unit area.

5.8.2 W+jets and $t\bar{t}$ Control Regions

W+jets events make up $\sim 20\%$ of the SM background in the SRs, with the dominant component coming from $W \to \tau\nu$ events where the c-tag comes from an ISR so that the m_{T}^{c} requirement fails to veto the event. Another significant component is $t\bar{t}$ events which make up approximately $5 - 10\%$ of the SM background. Both are normalised in dedicated CRs, targeting single lepton events. The treatment of the lepton in the CRs should reproduce as closely as possible the behaviour of the W+jets and $t\bar{t}$ events that enter the zero lepton signal regions. The are two main mechanisms by which electrons and muons can fail to be identified by the baseline identification criteria:

- **Out of acceptance:** in some cases electrons and muons may be missed in the event reconstruction by failing to satisfy the $p_{\mathrm{T}} < 7$ GeV or $|\eta| < 2.5$ thresholds for baseline leptons. This can also occur with lower probability for leptons with $p_{\mathrm{T}} > 7$ GeV, where the p_{T} is under-measured due to resolution effects.

- **Misidentified as jets:** electrons and muons may be falsely identified as jets. This can be the result of the overlap removal procedure, where angular separation between the jet and the lepton is greater than 0.2 but less than the upper threshold for the jet to remove the lepton. The baseline identification criteria are loose, but still have some inefficiency. If the lepton fails to meet the baseline requirements but still meets the p_{T} threshold, for example rare cases where an electron "punches through" to the hadronic system, it may be reconstructed as a jet from deposits in the calorimeter. This is much more likely to happen for electrons as muons deposit little energy in the calorimeter system. They may also be incorporated into jets in a small fraction of cases.

Figures 5.21a and 5.21b show the distribution for the minimum angular separation between a truth electron and muon and jets, respectively, in lepton vetoed $t\bar{t}$ simulated data, where the electron or muon is required to originate from the $t\bar{t}$ decay. A sharp peak at low $\Delta R_{\mathrm{min}}(\mathrm{lepton}, \mathrm{jets}) < 0.4$ can be seen for leptons that meet the reconstruction threshold, representing the fraction that are identified as jets. The distribution is broad for very low p_{T} leptons which tend to be missed altogether. Figures 5.21c and 5.21d show the same distributions at low $\Delta R_{\mathrm{min}}(\mathrm{lepton}, \mathrm{jets})$. The primary peak for electrons shows the cases where the electron has failed the baseline requirements and is collinear with the jet reconstructed from its energy deposit. The secondary peak shows electrons lying between $0.2 < \Delta R < 0.4$ removed by jets during the overlap removal procedure. The broader distribution at low $\Delta R_{\mathrm{min}}(\mathrm{lepton}, \mathrm{jets})$ for muons is consistent with the p_{T} dependent upper threshold for the angular separation.

The behaviour of τ-leptons in the SRs depends on the mode of decay. Figure 5.22 shows the breakdown for τ-leptons entering the preselection and **SR1** as a result of the $W \to \tau\nu$ background. In the hadronic case, the τ-jet is reconstructed as a jet if its calibrated p_{T} satisfies the signal jet threshold and missed otherwise. In the leptonic case, whether the electron or muon is reconstructed or missed is dependent on its p_{T} as described above.

W+jets events can produce the $E_{\mathrm{T}}^{\mathrm{miss}}$ required in the preselection and SRs through two competing mechanisms:

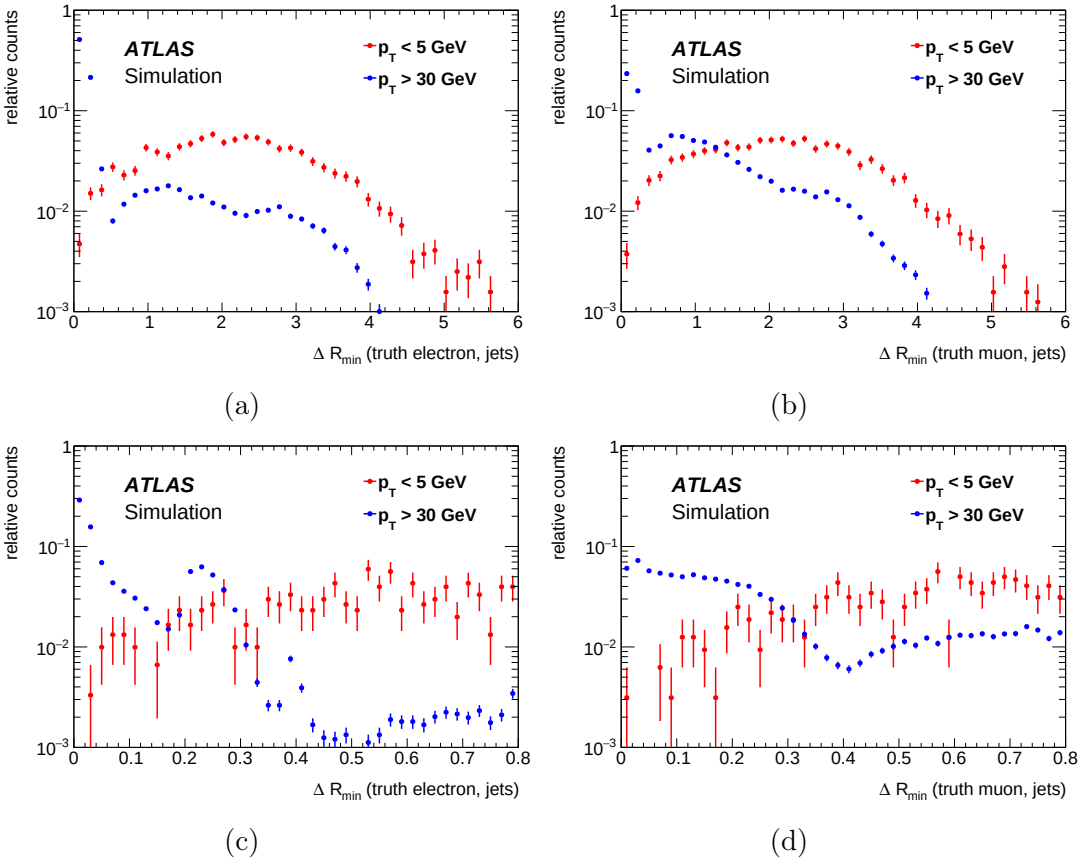

Figure 5.21: Minimum ΔR between (a) truth electrons and (b) truth muons and signal jets in $t\bar{t}$ simulated events, with a veto on (a) baseline electrons or (b) baseline muons. The distribution is compared for a truth-level lepton p_{T} threshold of < 5 GeV and > 30 GeV. The same distribution is shown, zoomed in the ΔR range, for (c) electrons and (d) muons. Only electrons and muons originating from the $t\bar{t}$ decay are considered.

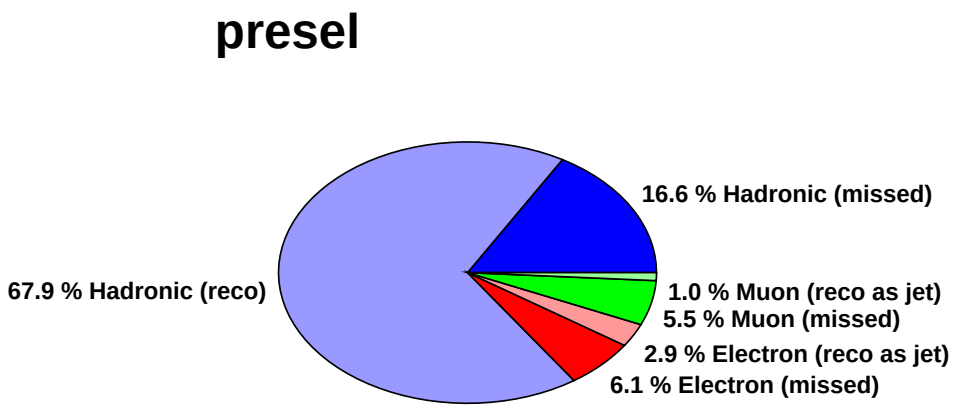

(a)

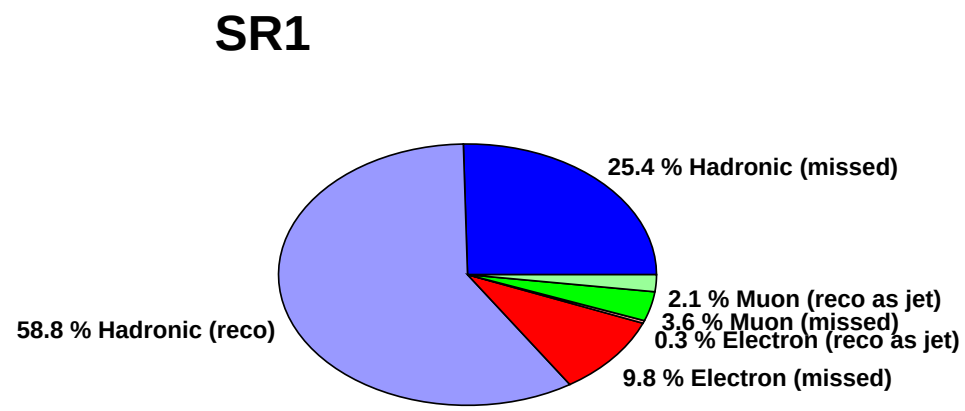

(b)

Figure 5.22: Breakdown of τ-lepton decays in (a) the preselection and (b) **SR1**, categorised according to the decay of the τ and whether the daughter was reconstructed or missed. Truth objects are considered matched to a reconstructed jet if they satisfy $\Delta R_{\text{min}}(\text{object}, \text{jets}) < 0.4$ and missed otherwise.

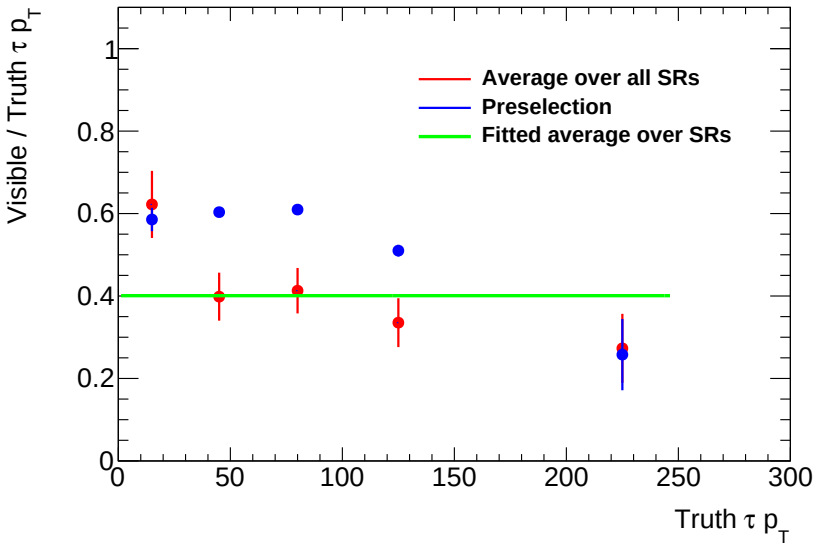

Figure 5.23: Fraction of visible p_{T}^{τ} in preselection and SRs, with the fitted average over all p_{T} bins shown for the SRs. The truth p_{T}^{τ} is retrieved from the MC truth record, with the visible portion taken from the total four-vector of the visible daughters.

1. A boost to the W system resulting in a high energy neutrino and large $E_{\mathrm{T}}^{\mathrm{miss}}$. Due to the small mass of the leptons compared to the W, the neutrino and lepton receive almost equal shares of the energy of the W, such that reconstructed energy difference between the neutrino and lepton is Gaussian, centred at zero. If this is the only mechanism by which $E_{\mathrm{T}}^{\mathrm{miss}}$ is produced the boost must be greater than the $E_{\mathrm{T}}^{\mathrm{miss}}$ requirement of the region (approximately 65% higher).

2. In highly asymmetric decays, in the tail of the Gaussian distribution of the energy difference between the neutrino and the lepton, the neutrino carries a high fraction of the energy of the parent W. Such highly asymmetric events are unlikely, but asymmetric events with a smaller boost are favoured in the SRs since the cross section for boosted events falls exponentially.

Since case (2) is favoured, leptons from W-decays in the preselection and SRs tend to be low in p_{T}. As a result, a significant fraction of electrons and muons from $W \to e\nu$ and $W \to \mu\nu$ are missed, with a significant fraction also reconstructed as jets. In the case of $W \to \tau\nu$, the τ decay will result in at least one neutrino, such that a fraction of the energy is always missed in all cases. For cases where a lepton has been reconstructed as a jet, the suitable treatment in the CR is to replace the lepton by the jet that removed it during overlap removal. This will give a similar detector response, namely a jet object with mis-calibrated energy. For the cases where the lepton is missed by the event reconstruction, the correct procedure is to treat the lepton in the CR as invisible, as in the $Z \to ll$ CRs.

Since the dominant process is $W \to \tau\nu$, where the energy of the τ-lepton is partially reconstructed, the visible fraction of the τ-lepton p_{T}, $p_{\mathrm{T,vis}}^{\tau}$ was calculated to determine the treatment of leptons in the CR. Figure 5.23 shows the ratio of the

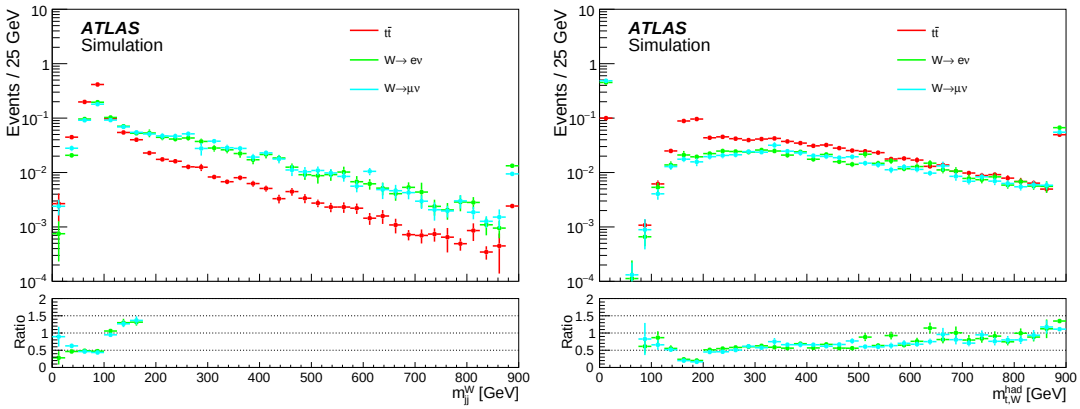

(a) (b)

Figure 5.24: Jet mass variables in the single lepton CR, with the preselection applied, in MC simulated data. Figure (a) shows the $m_{\mathrm{jj}}^{\mathrm{W}}$ and figure (b) $m_{t,W}^{\mathrm{had}}$.

visible p_{T} to the truth τ-lepton p_{T}:

$$R_{\mathrm{vis}} = \frac{p_{\mathrm{T,vis}}^{\tau}}{p_{\mathrm{T}}^{\tau}}, \tag{5.4}$$

as a function of the truth τ-lepton p_{T} , in simulated $W \to \tau\nu$ events. The low average R_{vis} in the SRs is due to the higher $E_{\mathrm{T}}^{\mathrm{miss}}$ threshold biasing the sample to more asymmetric τ-lepton decays where most of the energy goes to the associated neutrinos. The lowest p_{T} bin is consistent between the preselection and the SRs since here τ-lepton will often fail to meet reconstruction thresholds. A flat 40% value for R_{vis} was taken for all single lepton CRs. The CR lepton is removed from the event and the jet it removed during overlap removal is added, with its p_{T} rescaled by 40%, if it meets the acceptance requirements. The lepton p_{T} is then added vectorially to the $\boldsymbol{p}_{\mathrm{T}}^{\mathrm{miss}}$ with the magnitude of its momentum rescaled by the remaining 60%. All of the appropriate variables used in the kinematic variables for selection are recalculated using the lepton corrected objects. The following selection criteria are used to target W+jets and $t\bar{t}$ events in the single lepton SRs:

- **Trigger selection:** all events are required to pass the primary single electron or muon trigger.

- $\boldsymbol{\Delta\phi_{\mathrm{min}}(\mathrm{jets}, p_{\mathrm{T}}^{\mathrm{miss}})}$ **selection:** since the lepton p_{T} is added vectorially in significant portions to both the $\boldsymbol{p}_{\mathrm{T}}^{\mathrm{miss}}$ and an additional jet, the additional jet is likely to be close in ϕ to $\boldsymbol{p}_{\mathrm{T}}^{\mathrm{miss}}$. If this is the case the event is likely to fail to satisfy $\Delta\phi_{\mathrm{min}}(\mathrm{jet}, \boldsymbol{p}_{\mathrm{T}}^{\mathrm{miss,corr}}) > 0.4$. Instead, events in the single lepton CRs are required to satisfy:

$$\Delta\phi_{\mathrm{min}}(\mathrm{jets}, \boldsymbol{p}_{\mathrm{T}}^{\mathrm{miss}}) > 0.4 \quad \mathrm{OR} \quad \Delta\phi_{\mathrm{min}}(\mathrm{jet}, \boldsymbol{p}_{\mathrm{T}}^{\mathrm{miss,corr}}) > 0.4. \tag{5.5}$$

  This condition suppresses multijet background events without vetoing targeted events.

- **Single lepton requirement:** all events must have exactly one reconstructed signal muon or electron. The signal lepton is required to be matched to the

object that produced the trigger accept decision, using a simple ΔR requirement. The lepton is also required to have a p_{T} of at least 1 GeV greater than the trigger threshold, to ensure a constant trigger efficiency with respect to the offline electron definition. A further requirement is placed on the lepton, based on the transverse mass of the lepton and $\boldsymbol{p}_{\mathrm{T}}^{\mathrm{miss}}$ system:

$$m_{\mathrm{T}} = \sqrt{2 \cdot E_{\mathrm{T}}^{\mathrm{miss}} p_{\mathrm{T}}^{\mathrm{lep}} \cdot (1 - \cos \Delta\phi(\boldsymbol{p}_{\mathrm{T}}^{\mathrm{miss}}, \boldsymbol{p}_{\mathrm{T}}{}^{\mathrm{lep}}))} \tag{5.6}$$

calculated using the original, uncorrected $\boldsymbol{p}_{\mathrm{T}}^{\mathrm{miss}}$. For multijet background events entering the single lepton region, the invariant mass of the system should be small since the lepton is a fake from a jet originating from a light particle. For a true $W \to l\nu$ system, the invariant mass of the system should be much greater due to the high mass of the W. The multijet background is suppressed by placing a lower threshold on m_{T}.

- **Jet mass variables:** the single lepton requirement and lepton replacement scheme applied for the preselection give a sample enriched with $W \to e\nu$, $W \to \mu\nu$ and $t\bar{t}$ events, in approximately equal proportions. In order to further separate W+jets and $t\bar{t}$ events, the following variables are defined:

  1. $m_{\mathrm{jj}}^{\mathrm{W}}$: the jet pair with mass closest to the W. This is calculated by considering all possible dijet masses in the event. To avoid dijet pairs containing a mis-tagged b-jet from a top decay, c-tagged jets are considered for pairs only in events where exactly one non-tagged jet is present. Jets added by the replacement procedure are not considered. This variable targets $t\bar{t}$ which should be semileptonic due to the single lepton requirement. It searches for the jet pair from the hadronic W decay which peaks at the W mass (see figure 5.24a). In W+jets there is no jet pair from the W due to the single lepton requirement.
  2. $m_{t,W}^{\mathrm{had}}$: the jet pair with mass closest to the W is selected, and then a third jet is chosen from the remaining jets such that the three-jet system is closest to the top mass. One of the three jets in the system must be c-tagged. This variable targets the top quark system in cases where a jet from the hadronic W is tagged or the b-jet from the top decay is mis-tagged. Figure 5.24b shows the peak in $t\bar{t}$ at the mass of the top quark.

As for the Z CRs, the kinematic variables are kept as close as possible to the SRs, but relaxed to improve the number of events in the single lepton regions. They are defined identically and then separated using the jet mass variables. The full set of region definitions is given in table 5.5.

Figures 5.25a and 5.25b show the breakdown of the backgrounds that enter **CR1 W** and **CR5 W**, respectively. These regions are rich in W+jets with some $t\bar{t}$ contamination remaining after the selection on the jet mass variables described above. The flavour compositions for all backgrounds in **CR1 W** and for W+jets in **SR1** are compared in figures 5.25c and 5.25d. There is reasonable agreement for the number of events containing a truth c- and l-jet, and for events with only light flavour jets. The "other" category includes events with τ-leptons, which are suppressed in the CRs due to the lepton requirement. The lepton treatment is

	W/Top CR1	W/Top CR2	W/Top CR3	W/Top CR4	W/Top CR5
Trigger	$E_{\mathrm{T}}^{\mathrm{miss}}$ OR single lepton				
Lepton	1 e OR 1 μ				
$p_{\mathrm{T}}^{\mathrm{lep}}$ [GeV]	> 27				
$\Delta\phi_{\mathrm{min}}(\mathrm{jet}, \boldsymbol{E}_{\mathrm{T}}^{\mathrm{miss}})$ [rad]	$\Delta\phi_{\mathrm{min}}(\mathrm{jet}, \boldsymbol{E}_{\mathrm{T}}^{\mathrm{miss}}) > 0.4$ OR $\Delta\phi_{\mathrm{min}}(\mathrm{jet}, \boldsymbol{p}_{\mathrm{T}}^{\mathrm{miss,corr}}) > 0.4$				
m_{T} [GeV]	> 60				
$E_{\mathrm{T}}^{\mathrm{miss,corr}}$ [GeV]	> 250				
$p_{\mathrm{T}}^{j_1,\mathrm{corr}}$ [GeV]	> 250				
$N_{c-\mathrm{jets}}$	≥ 1				
$N_{\mathrm{jets}}^{\mathrm{corr}}$	≥ 2	≥ 3	≥ 3	≥ 3	≥ 3
Leading jet c-tag veto	yes	yes	yes	yes	no
$p_{\mathrm{T}}^{j_2,\mathrm{corr}}$ [GeV]	–	–	> 100	> 100	> 100
$p_{\mathrm{T}}^{j_3,\mathrm{corr}}$ [GeV]	–	–	> 80	> 100	–
p_{T}^{c1} [GeV]	< 100	> 60	> 80	> 100	> 100
$m_{\mathrm{T}}^{c,\mathrm{corr}}$ [GeV]	$\in (120, 250)$	$\in (120, 250)$	$\in (175, 400)$	> 200	> 400
$m_{t,W}^{\mathrm{had}}$ [GeV]	For W: < 50 OR > 220 For Top: $\in (50, 220)$				
m_{jj}^{W} [GeV]	For W: > 175 For Top: no requirement				

Table 5.5: Overview of the W and Top CR selection criteria. N_{jets} and $N_{c-\mathrm{jets}}$ indicate the total number of jets and c-jets, respectively; p_{T}^{j1} , p_{T}^{j2} and p_{T}^{j3} indicate the transverse momentum of the leading, sub-leading and sub-sub-leading jet; and p_{T}^{c1} is the transverse momentum of the c-jet with the highest p_{T} and $p_{\mathrm{T}}^{\mathrm{lep}}$ is the lepton p_{T} . Variables with the superscript "corr" refer to variables corrected as described in the text.

intended to simulate the behaviour of τ-leptons that are not found in the CRs. There is a larger component from b-jets in the CRs, due to $t\bar{t}$ contamination. The agreement is similar for the leading c-tagged jets, as shown in figures 5.25e and 5.25f. The complete set of compositions for the W+jets CRs is included in appendix B.6.

Distributions for W+jets after the preselection and at least one c-tagged jet, and for $W \to e\nu$ and $W \to \mu\nu$ after the preselection with single lepton treatment and at least one c-tagged jet, are shown in figure 5.26. In the preselection, W+jets events may enter the signal region through missed objects or through objects faking jets. In the lepton treatment *every* event has one jet added, biasing the jet multiplicity to higher values. This impacts the kinematic distributions, since the additional jet is drawn from a distribution of leptons that is biased to higher values by the $E_{\mathrm{T}}^{\mathrm{miss}}$ requirement.

The background compositions for the $t\bar{t}$ CRs 1 and 5 are shown in figures 5.27a and 5.27b. These regions are approximately 55% $t\bar{t}$ with significant contamination from W+jets. The flavour compositions, shown in figures 5.27c and 5.27d, show that again the τ-lepton component is lost, and is modelled by the lepton replacement. The contamination from W+jets events results in a disagreement between the c- and b-jet flavour compositions; the case for the leading charm-tagged jet is similar, as can be seen from figures 5.27e and 5.27f.

The distributions for $t\bar{t}$ events in the preselection with at least one c-jet and with lepton replacement are shown in figure 5.28. The jet multiplicity, $E_{\mathrm{T}}^{\mathrm{miss}}$ and leading jet p_{T} are all biased toward higher values in the single lepton region, compared with the preselection. This behaviour is similar to that observed for W+jets, however for $t\bar{t}$ the jet multiplicity is higher than for W+jets so that the single lepton region suffers less at low p_{T} for the subleading jet, which is less likely to be due to an additional energetic lepton.

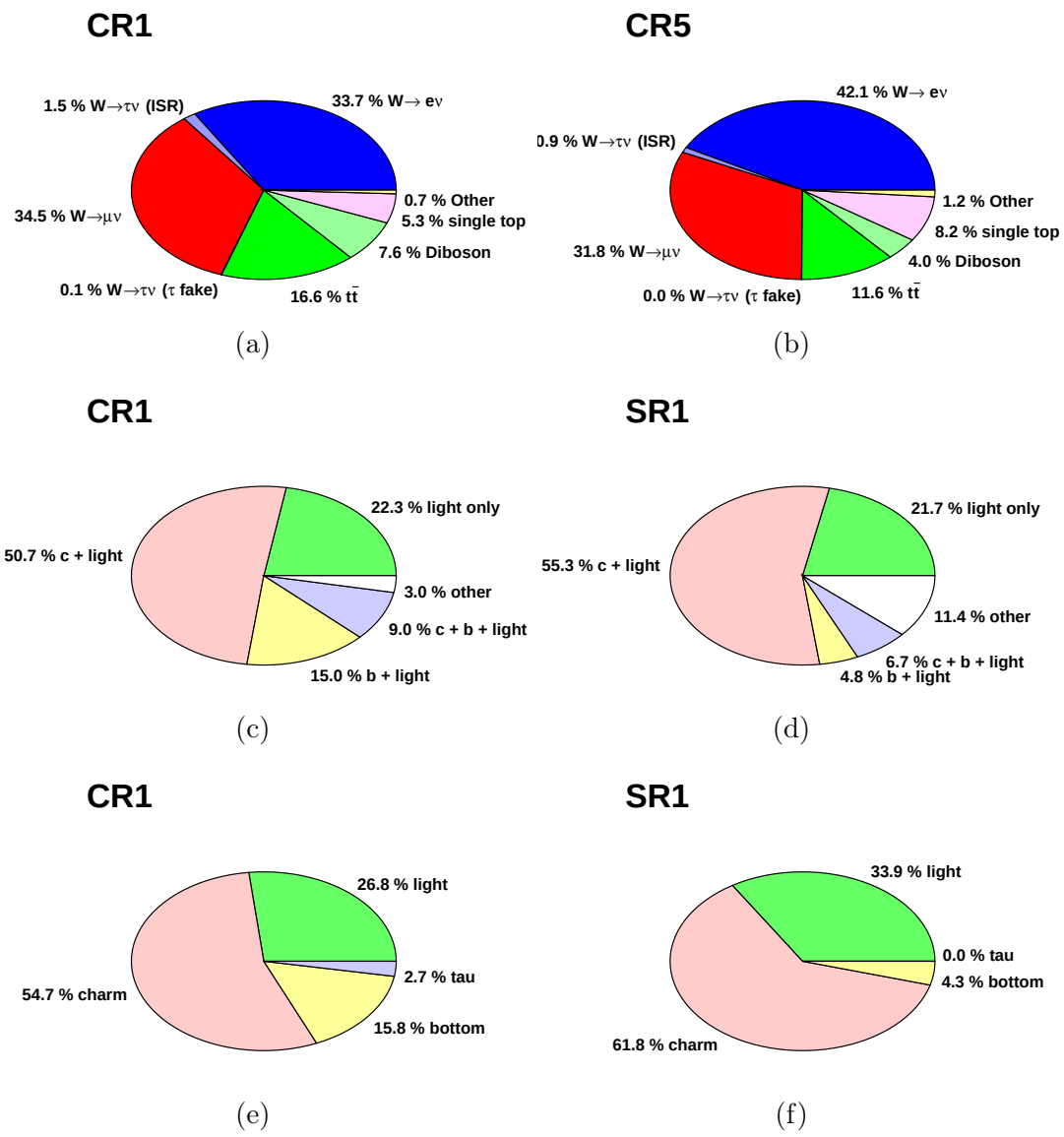

Figure 5.25: Background compositions in (a) **CR1 W** and (b) **CR5 W**. The "other" category includes backgrounds that make up less than 5% of the total. (c) Flavour composition for **CR1 W** and (d) W+jets in **SR1**. Flavour origin of the leading charm tagged jet for (e) **CR1 W** and (f) W+jets in **SR1**.

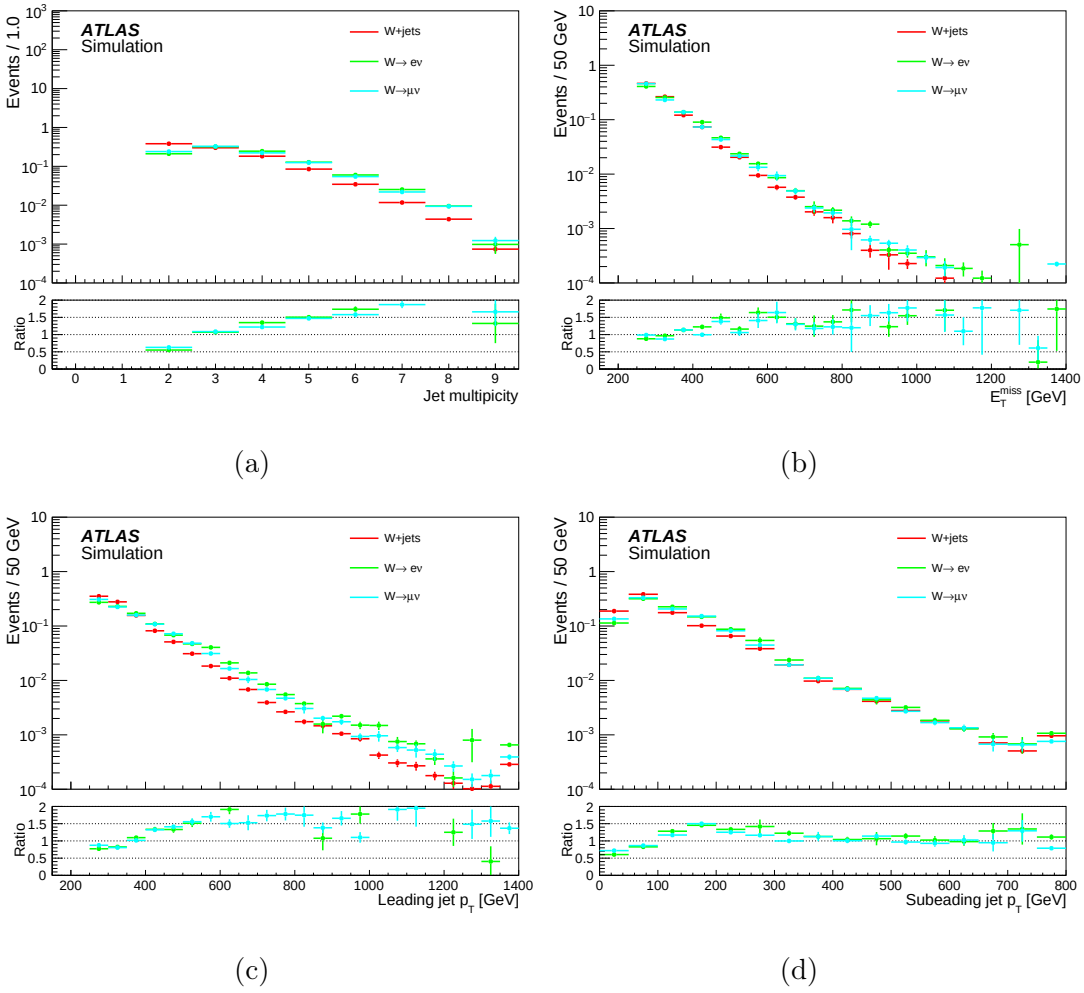

Figure 5.26: Comparison of kinematic variables in W+jets and $W \to l\nu$ with lepton treatment. W+jets events are required to satisfy the preselection plus at least one c-tagged jet. $W \to l\nu$ events must satisfy the preselection with lepton treatment and at least one c-tagged jet. The histograms are normalised to unity.

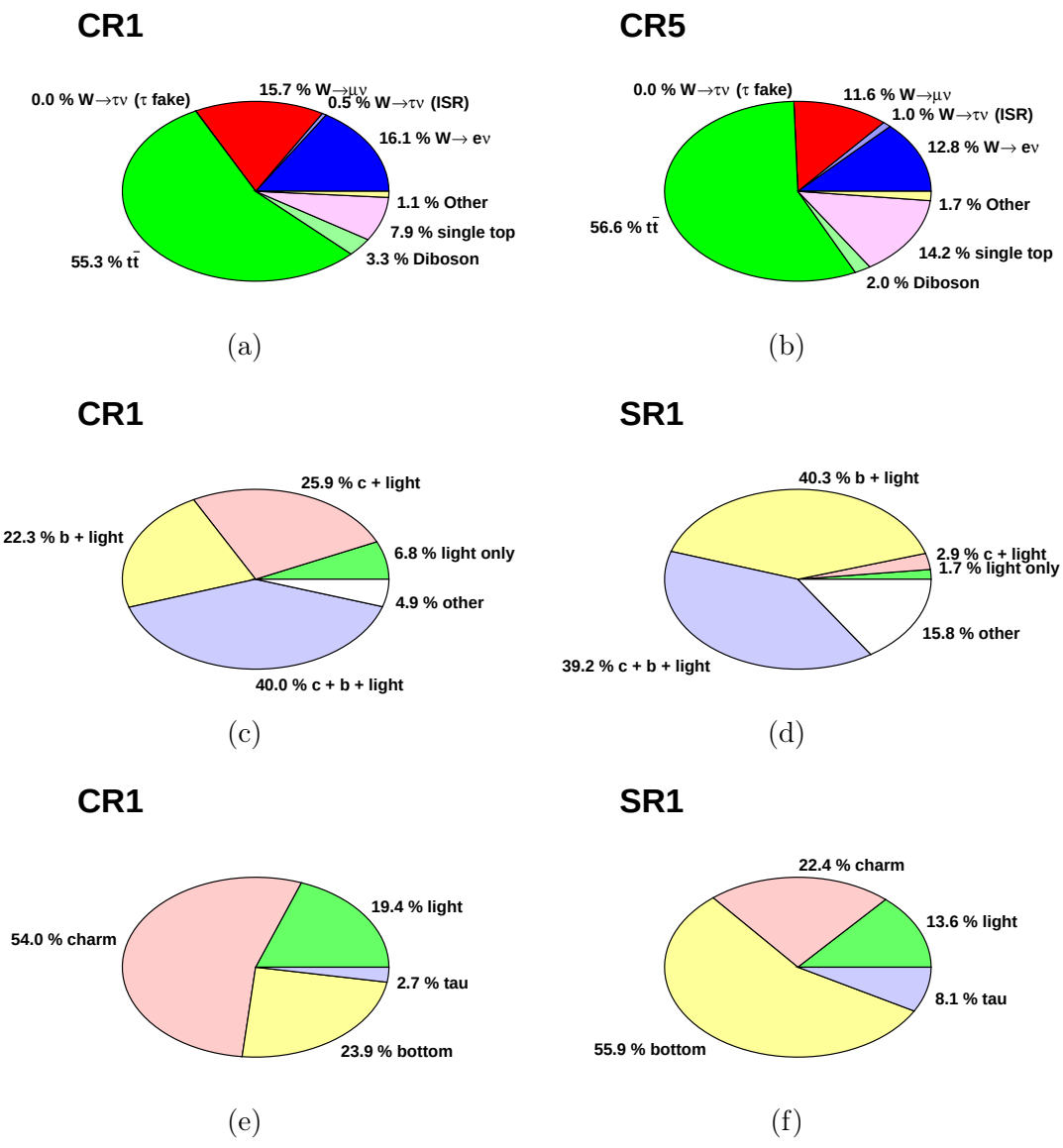

Figure 5.27: Background compositions in (a) **CR1** $t\bar{t}$ and (b) **CR5** $t\bar{t}$. The "other" category includes backgrounds that make up less than 5% of the total. Flavour composition for (c) **CR1** $t\bar{t}$ and (d) $t\bar{t}$ in **SR1**. Flavour composition of the leading charm tagged jet for (e) **CR1** $t\bar{t}$ and (f) $t\bar{t}$ in **SR1**.

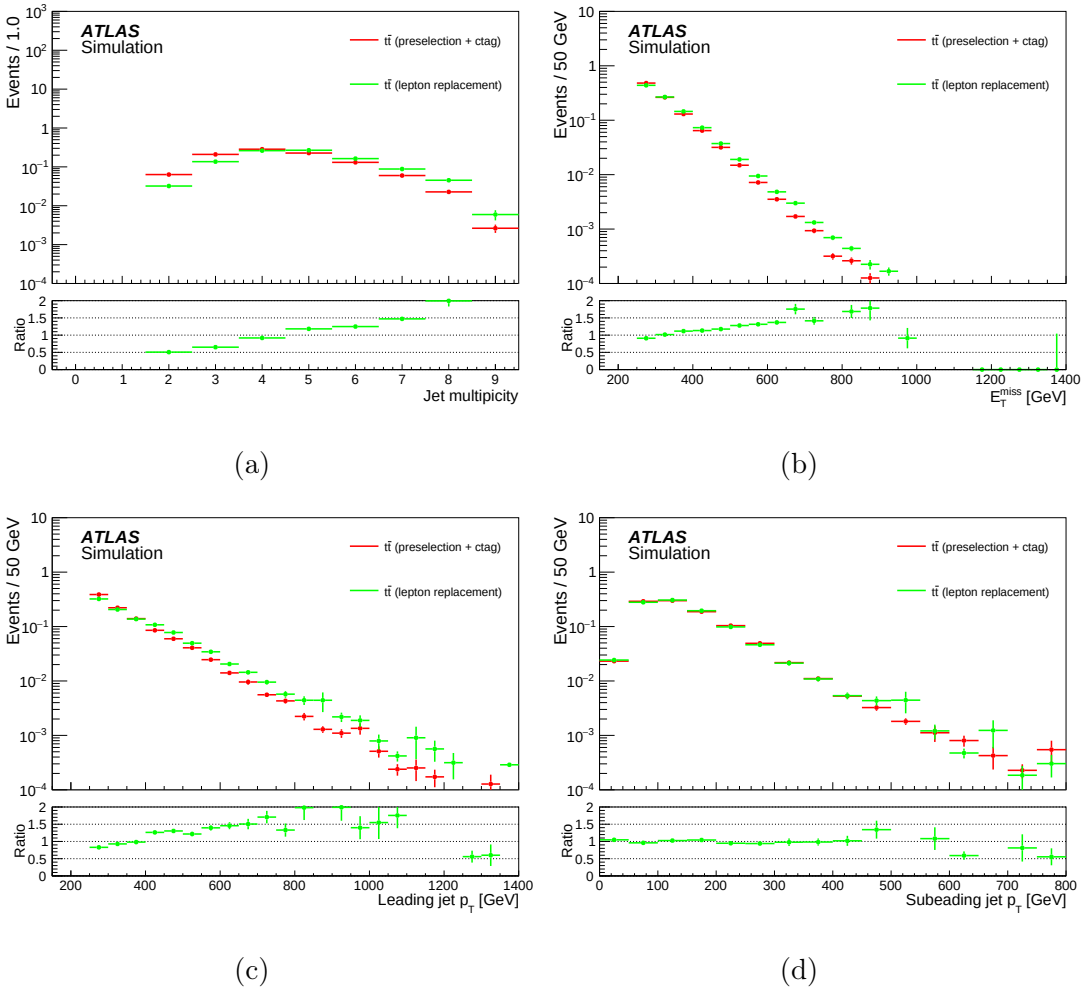

Figure 5.28: Comparison of kinematic variables in $t\bar{t}$ events in the preselection plus one c-jet and with lepton treatment. The histograms are normalised to unity.

5.8.3 Multijet Background Estimate by Jet Smearing

The close agreement between data and MC in the preselection suggests that the multijet contribution following the $\Delta\phi_{\min}(\text{jets}, \boldsymbol{p}_{\mathrm{T}}^{\mathrm{miss}})$ requirement is small. Since it is impractical to simulate this background in the high $E_{\mathrm{T}}^{\mathrm{miss}}$ tail with sufficient statistics, it is necessary to estimate precisely its contribution to the preselection and SRs using a data-driven approach. The estimate is performed using the *jet smearing* method [212]. A sample of "seed" events with well measured $E_{\mathrm{T}}^{\mathrm{miss}}$ are selected from the data. These events are then "smeared" by randomly fluctuating the momentum magnitude of jets in the event according to the detector response function, measured from MC simulated events and corrected for by comparison with data. The resulting sample of "pesudo-data" is used for the multijet estimation. Each of these components is described in more detail below:

- **Seed selection:** this is intended to collect a sample of well measured events with no large fluctuations in the jet energy measurement. They are chosen by applying a threshold on the $E_{\mathrm{T}}^{\mathrm{miss}}$ significance, defined as:

$$S = \frac{E_{\mathrm{T}}^{\mathrm{miss}} - M}{\sqrt{\sum E_{\mathrm{T}}}} \tag{5.7}$$

  where $\sum E_{\mathrm{T}}$ is the scalar sum of measured energy in the event. In principle an upper threshold on $E_{\mathrm{T}}^{\mathrm{miss}}$ would ensure the event is well reconstructed, however this would introduce a bias toward selecting events with lower p_{T} jets, since the $E_{\mathrm{T}}^{\mathrm{miss}}$ resolution scales like $\sum E_{\mathrm{T}}$. The M term in the numerator of S is a signal versus background *separation scale* [213]. A value of $M = 8$ GeV was found to remove bias in the leading jet p_{T} distribution. The following requirement on the $E_{\mathrm{T}}^{\mathrm{miss}}$ significance:

$$S < 0.5 + 0.1 \times N_{\mathrm{bjets}} \tag{5.8}$$

  is applied. The additional b-jet multiplicity term uses jets tagged using the MV2c20 tagger with fixed 77% efficiency. This in part takes into account the different detector response to light and heavy flavour jets.

  Seed events are also required to fire a single jet trigger. The requirement is a logical OR between triggers with thresholds ranging from 15 GeV to 400 GeV. As a consequence of the high multijet cross section, these triggers have increasing prescale factors applied as the trigger threshold is lowered. The trigger prescale factors also vary as a function of the LB in response to the varying instantaneous luminosity. The average trigger prescale factors range from 1.0 for `HLT_j400` to $\mathcal{O}(10000)$ for `HLT_j15`. Weights are applied according to the prescale factor of the lowest threshold trigger that accepted the event, with events rejected if the trigger-matched jet does not meet the p_{T} threshold to be in the efficiency plateau of the corresponding trigger.

- **Response function:** the jet response in MC is defined as:

$$R_{\mathrm{MC}} = \frac{p_{\mathrm{T}}^{\mathrm{reco}}}{p_{\mathrm{T}}^{\mathrm{truth}}}. \tag{5.9}$$

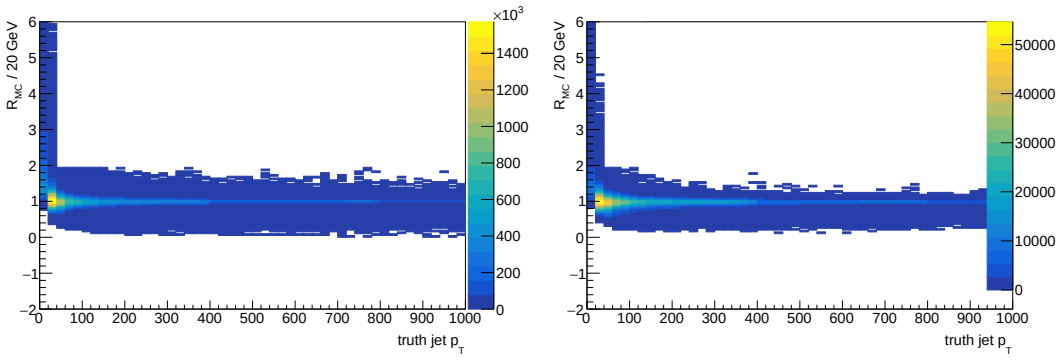

(a) (b)

Figure 5.29: Jet response maps used for jet smearing. The maps are measured for (a) non b-tagged jets and (b) b-tagged jets.

The jet response function is a map binned in truth p_{T} and the response derived from MC simulated multijet events. Reconstructed jets are required to be isolated, with a minimum of $\Delta R > 0.4$ in separation from other reconstructed physics objects. These jets must also be matched to within $\Delta R < 1.0$ of a *truth jet*, formed by performing jet clustering on stable final state particles from the MC truth record. Stable particles are defined as those with a lifetime greater than 30 ps. The closest truth jet in ΔR is considered to be matched to the reconstructed jet. Any neutrinos that fall within the cone of the truth jet are added vectorially to $p_{\mathrm{T}}^{\mathrm{truth}}$ to take into account true and fake sources of $E_{\mathrm{T}}^{\mathrm{miss}}$ for the response function. Separate response functions are derived for b-tagged jets and non b-tagged jets. Figures 5.29a and 5.29b show the measured response functions for b-tagged and non b-tagged jets, respectively. There is a long tail for positive R_{MC} in the lowest p_{T} bins. This originates from truth jets that do not meet the threshold for reconstruction and can only be reconstructed if the response is positive.

The jet response in MC is applied to seed events in data to produce pseudo-data for comparison with data. The response map is then corrected to obtain agreement between data and MC. Two corrections are applied:

1. First, to correct the Gaussian response, events with exactly two anti-aligned jets are selected from the data and pseudo-data. These events are parameterised in terms of the jet asymmetry, defined

$$A(p_{\mathrm{T},1}, p_{\mathrm{T},2}) = \frac{p_{\mathrm{T},1} - p_{\mathrm{T},2}}{p_{\mathrm{T},1} + p_{\mathrm{T},2}}, \tag{5.10}$$

where $p_{\mathrm{T},1}$ and $p_{\mathrm{T},2}$ are the momenta of the leading and subleading jet, respectively. The asymmetry is useful since, for jets with similar pseudorapidity, its Gaussian width σ_A is related to that of the jet p_{T} by

$$\sigma_A \sim \frac{\sigma(p_{\mathrm{T}})}{\sqrt{2}p_{\mathrm{T}}}. \tag{5.11}$$

The asymmetry is fitted in bins of jet p_{T} in order to derive corrections to the Gaussian width of the jet response. It is found that the MC systematically underestimates the width by a few per cent. The corrections then

amount to a widening of the Gaussian response such that the pseudo-data matches the data.

2. The non-Gaussian tail in the jet response is corrected for by selecting events with a single energetic jet and two low momentum jets. A $E_{\mathrm{T}}^{\mathrm{miss}}$ threshold is applied and the leading jet is required to be either aligned or anti-aligned with the $\boldsymbol{p}_{\mathrm{T}}^{\mathrm{miss}}$, with the subleading jets required to be isolated from the $\boldsymbol{p}_{\mathrm{T}}^{\mathrm{miss}}$ direction. This allows the $E_{\mathrm{T}}^{\mathrm{miss}}$ to be matched to the energetic jet, allowing the high and low tails of the jet response to be distinguished. If the $E_{\mathrm{T}}^{\mathrm{miss}}$ is assumed to be dominated by the fluctuation of the energetic jet its true momentum $\boldsymbol{p}_{\mathrm{T}}(\mathrm{true})$ may be recovered according to

$$\boldsymbol{p}_{\mathrm{T}}(\mathrm{true}) \sim \boldsymbol{p}_{\mathrm{T}}(\mathrm{reco}) + \boldsymbol{p}_{\mathrm{T}}^{\mathrm{miss}} \,. \tag{5.12}$$

The jet response is then recovered from

$$R = \frac{\boldsymbol{p}_{\mathrm{T}}(\mathrm{reco}) \cdot \boldsymbol{p}_{\mathrm{T}}(\mathrm{true})}{|\boldsymbol{p}_{\mathrm{T}}(\mathrm{true})|^2}. \tag{5.13}$$

Corrections to the jet response are derived by fitting the pseudo-data to the data in the R distribution.

- **Smearing procedure:** each jet in a seed event is smeared by multiplying the components of its four-vector by random numbers drawn from the jet response map. Thus a new, pseudo-event is formed, using the seed as a template. All variables are recalculated in the smeared event. This procedure is repeated 10000 times for each seed to produce a data-driven simulated sample of multijet events with sufficient statistics in the high $E_{\mathrm{T}}^{\mathrm{miss}}$ tail to estimate yields in the SRs.

- **Normalisation:** the pseudo-data sample may be of arbitrary size, depending on the chosen S threshold and the number of smears per seed event. The normalisation is constrained in a CR, identical to the preselection but with the $\Delta\phi_{\mathrm{min}}(\mathrm{jets}, \boldsymbol{p}_{\mathrm{T}}^{\mathrm{miss}})$ selection adjusted to target multijet events. First, only the leading three jets are considered for the minimum angular separation, rather than all jets in the event. Second, the threshold is inverted. The normalisation is evaluated in the region $\Delta\phi_{\mathrm{min}}(\mathrm{jets}_{1,2,3}, \boldsymbol{p}_{\mathrm{T}}^{\mathrm{miss}}) < 0.2$. This normalisation is then validated by removing the $\Delta\phi_{\mathrm{min}}(\mathrm{jets}, \boldsymbol{p}_{\mathrm{T}}^{\mathrm{miss}})$ requirement altogether and comparing data and MC. Figure 5.30 shows data / MC comparisons in the VR after applying the normalisation determined from the CR. The overall agreement is good, with the multijet events primarily occupying the low $\Delta\phi_{\mathrm{min}}(\mathrm{jets}, \boldsymbol{p}_{\mathrm{T}}^{\mathrm{miss}})$ bin, as expected.

The resulting pseudo-data sample is used for estimating the multijet contribution in the SRs. The multijet contribution was estimated for the case where no charm tagging is applied to derive an upper bound. The upper bound for each SR is shown in table 5.6. The contribution is expected to be less than 2.5% in any region, under the conservative assumption that every event survives the charm tagging requirements. It was found that around 10% of smeared events in a SR-like selection without c-tagging variables contained a b-tagged jet, using a 77% efficiency working point with a c-jet fake rate of around 15%. The relative purity of the b-tagged

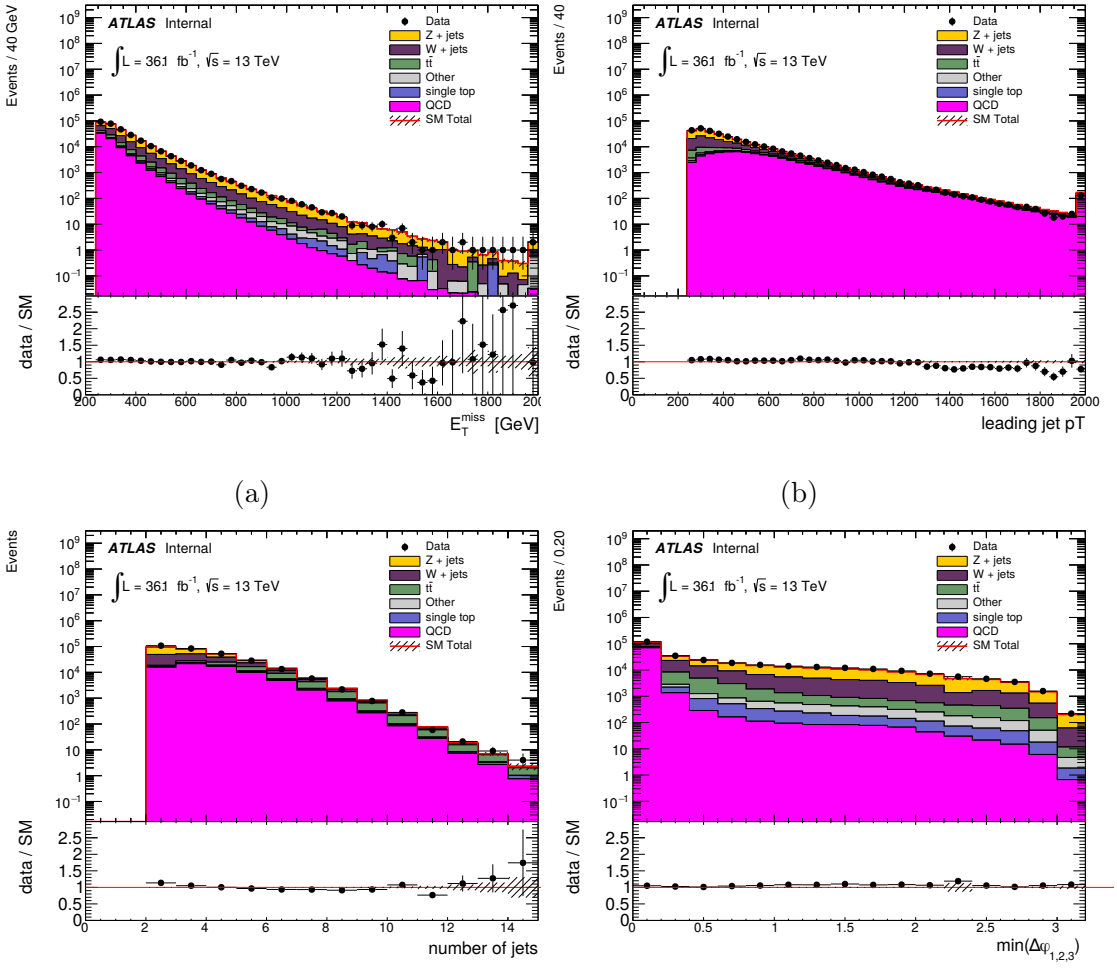

Figure 5.30: Data / MC comparisons in the jet smearing VRs for selected kinematic distributions.

jets in these events is roughly 95% b-jets and 5% c-jets, assuming the contribution from light jets, with fake rate 0.01%, is small. Neglecting light jets completely, the fraction of events likely to contain a c-tagged jet is roughly given by:

$$\frac{N_{c-\text{jets}}}{N_{\text{total}}} = \frac{k}{N_{\text{total}}} \cdot \frac{p}{\epsilon} \tag{5.14}$$

where k is the number of events with one or more b-tagged jets, p is the c-jet purity of the selected events and ϵ is the fake rate. This corresponds to approximately 3.33% of the multijet events in the SR likely to survive the c-tagging stage of the selection. This estimate is approximate, but demonstrates that the multijet contribution to the SRs is expected to be small after c-tagging is applied.

Region	QCD Estimate (no tagging applied)	Total SR BG (tagging applied)	Relative QCD amount upper bound estimate
SR1	0.87 ± 0.02	48.4	1.8%
SR2	0.62 ± 0.02	25.6	2.4%
SR3	0.62 ± 0.02	24.6	2.5%
SR4	0.61 ± 0.02	46.7	1.3%
SR5	0.86 ± 0.02	53.3	1.6%

Table 5.6: Expected multijet background events for each signal region. The first column gives the raw estimate for the number of multijet events in the region, with no c-tagging applied. The second column shows the number of background events with c-tagging applied. The final column shows the upper bound estimate, assuming all of the multijet events survive the c-tagging.

5.8.4 Validation Regions

The VRs are used to validate the extrapolation from the CRs to the SRs. They are designed to occupy the phase space region between the CRs and the SRs, with kinematics and flavour tagged jet compositions as close as possible to the SRs. To suppress signal contamination, the m_{T}^{c} is adjusted, and kinematic selections on $E_{\text{T}}^{\text{miss}}$ and jet momenta are inverted. A new VR is introduced for each inverted kinematic variable. For example in **SR1** two regions are defined, one with $E_{\text{T}}^{\text{miss}}$ inverted, where the leading jet p_{T} distribution can be fully inspected in the appropriate regime, and another, with the leading jet p_{T} inverted, such that the data / MC over the full $E_{\text{T}}^{\text{miss}}$ distribution can be validated. For regions 2-4 three inverted selections are required to sufficiently suppress signal, so three regions are required to validate each of the inverted thresholds. Signal contamination is further suppressed by applying a lower threshold on m_{jj}^{W}, since in signal the dijet system not including the c-tagged jet is expected to either include an ISR jet or to originate from a low mass squark. An overview of the VR definitions is given in table 5.7.

The background composition is compared for **SR3** and **VR3 A-C** in figure 5.31, and the corresponding flavour compositions for the leading charm-tagged jet in figure 5.32. The complete set can be found in appendix B.9. The change in the kinematic

	VR1	VR2	VR3	VR4	VR5
Trigger	$E_{\mathrm{T}}^{\mathrm{miss}}$ triggers				
Leptons	0 e AND 0 μ				
$E_{\mathrm{T}}^{\mathrm{miss}}$ [GeV]	> 500				
$\Delta\phi_{\mathrm{min}}(\mathrm{jet}, \boldsymbol{E}_{\mathrm{T}}^{\mathrm{miss}})$ [rad]	> 0.4				
$N_{c-\mathrm{jets}}$	≥ 1				
m_{jj}^{W} [GeV]	> 125				
N_{jets}	≥ 2	≥ 3	≥ 3	≥ 3	≥ 3
Leading jet c-tag veto	yes	yes	yes	yes	no
p_{T}^{j1} [GeV]	> 250	> 250	> 250	> 250	> 300
p_{T}^{c1} [GeV]	< 100	> 60	> 80	> 100	> 200
m_{T}^{c} [GeV]	> 250	$\in (300, 450)$	$\in (300, 400)$	$\in (300, 500)$	> 400
A $E_{\mathrm{T}}^{\mathrm{miss}}$ [GeV]	< 350	< 350	< 350	< 350	< 350
A p_{T}^{j2} [GeV]	–	< 175	< 200	< 200	–
B p_{T}^{j1} [GeV]	< 350	< 350	< 350	< 350	–
B p_{T}^{j2} [GeV]	–	< 175	< 200	< 200	< 175
C $E_{\mathrm{T}}^{\mathrm{miss}}$ [GeV]	–	< 350	< 350	< 350	–
C p_{T}^{j1} [GeV]	–	< 350	< 350	< 350	–

Table 5.7: Overview of the VR selection criteria. N_{jets} and $N_{c-\mathrm{jets}}$ indicate the total number of jets and c-jets, respectively; p_{T}^{j1} and p_{T}^{j2} indicate the transverse momentum of the leading and sub-leading jet; and p_{T}^{c1} is the transverse momentum of the c-jet with the highest p_{T} .

thresholds results in different background compositions between the VRs and **SR3**. The m_{T}^{c} requirement is increased for all VRs which reduces the contribution from $W \to \tau\nu$ events where the τ-lepton is mis-tagged. Inverting the $E_{\mathrm{T}}^{\mathrm{miss}}$ threshold increases the relative contribution from $t\bar{t}$ events which then leads to an increased fraction of b-jets. The level of agreement in the flavour composition of the leading charm-tagged jet between the VRs and **SR3** is considered sufficient, with roughly similar fractions for each flavour and a consistent ranking of the most important flavour contributions across each of the regions.

The VRs are not included in the statistical fit to the data. Instead, the normalisations derived from the background-only fit described in section 5.11 are applied in the VRs. The same normalisations are applied to the SRs, so that if the modelling in the VRs is satisfactory, the extrapolation from the CRs to the SRs is validated.

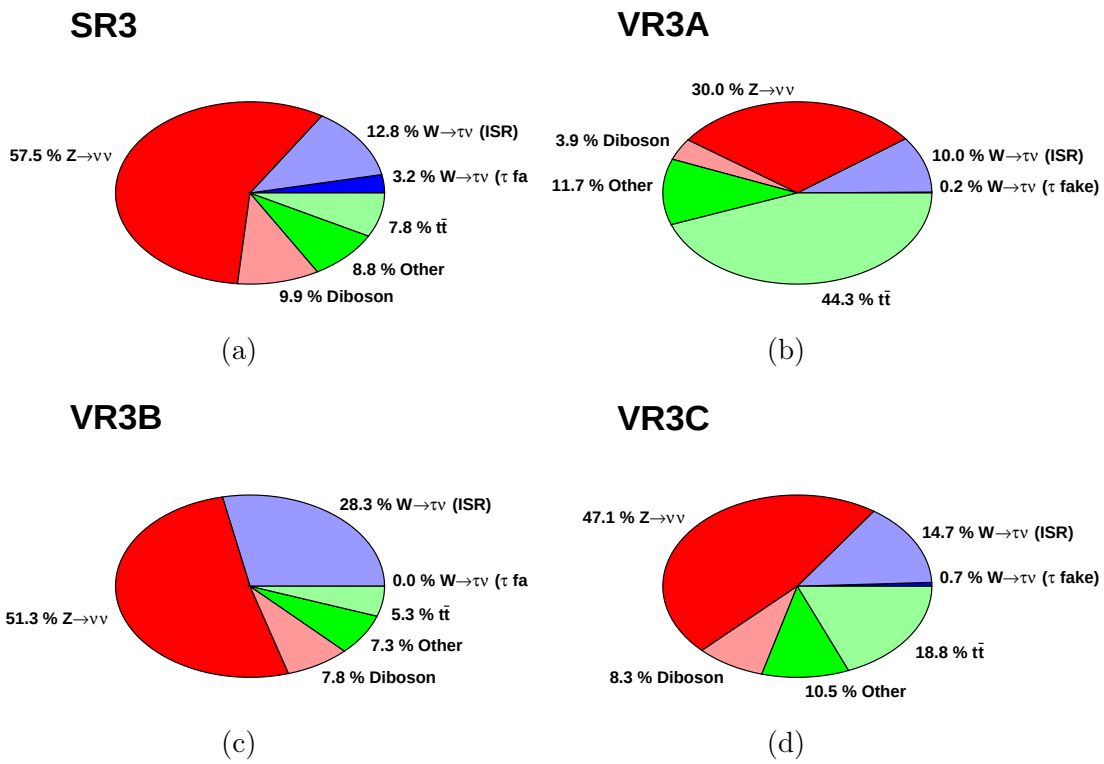

Figure 5.31: Background compositions in **SR3** and its corresponding VRs. (a) **SR3** and its corresponding validations regions (b) A, (c) B and (d) C.

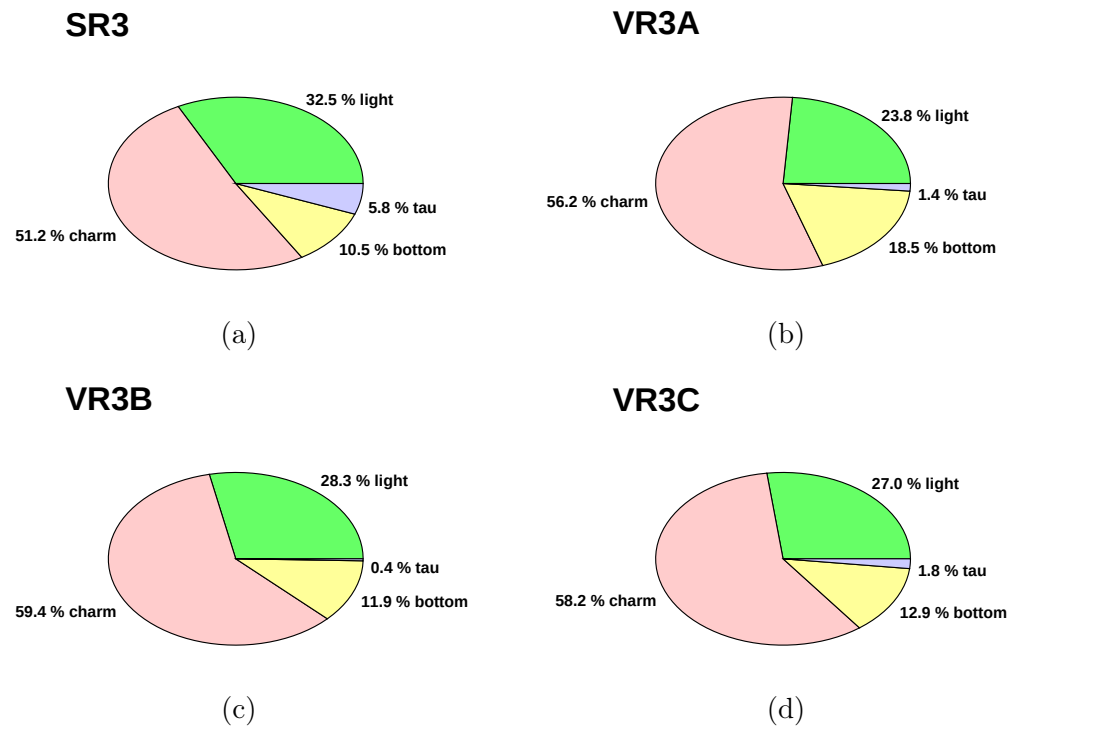

Figure 5.32: Flavour compositions for the leading charm-tagged jet in **SR3** and its corresponding VRs. (a) **SR3** and its corresponding validations regions (b) A, (c) B and (d) C.

5.9 Systematic Uncertainties

Systematic uncertainties must be included for any input parameters that affect the estimate of the predicted yields in the SRs. These uncertainties can be organised into two broad categories: experimental uncertainties and theory uncertainties. Experimental uncertainties result from the finite precision of the detector response and calibration procedures. Theory uncertainties are related to the imperfect modelling of physics processes. Each of these systematic uncertainties is evaluated by applying variations according to the measured uncertainty and assessing the impact on the region yields. Each is then treated by including an associated nuisance parameter (NP) in the likelihood fits as described in the following sections. The full list of experimental uncertainties is given below:

- **Jet energy scale JES:** uncertainties related to the calibration of the JES as described in section 4.4.4. A total of 80 systematic uncertainties are associated with the calibration process. Such a large list of additional uncertainties would be cumbersome to evaluate, instead a reduced set of four systematics is used. These sets aim to reproduce the uncertainty correlations across jet p_{T} and η. The reduction, described in Ref. [174], is performed by adding uncertainties of smaller magnitude in quadrature to reduce the list, then grouping the dominant sources into regions of p_{T} and η where they are most relevant. A number of grouping procedures were compared in $Z \to \nu\nu$ events, with similar results.

- **Jet energy resolution JER:** the jet energy is smeared within its uncertainties, determined in dedicated studies according to Ref. [214].

- **Jet vertex tagger JVT:** the scale factors associated to the JVT tagger used for pileup suppression are varied according to the measured uncertainty.

- **Charm tagging:** an NP is included for the tagging efficiency of $b-$, $c-$ and $l-$jets. Additional uncertainties are included for the extrapolation to high p_{T} from the efficiency at low p_{T}.

- **Missing transverse energy:** the variations applied to physics objects are propagated to the $E_{\mathrm{T}}^{\mathrm{miss}}$ calculation. Additional variations are applied to account for uncertainties in the resolution and scale of the soft term.

- **Lepton resolution, reconstruction and identification:** NPs are included to account for energy scale and resolution, separately for electrons and muons. Additional uncertainties associated to the scale factor corrections for lepton identification efficiencies are evaluated.

- **Pileup reweighting:** pileup-dependent weights are applied to MC events to ensure that the pileup distribution matches the data. An additional scale factor is applied to the value of $< \mu >$ to calibrate the MC to the pileup distribution observed in data. This scale factor is varied up and down according to its measured uncertainty.

- **Luminosity:** the uncertainty on the total integrated luminosity is determined to be 3.2% [215], which is taken into account as an additional systematic.

The dominant experimental uncertainties are those originating from the JES and the c-tagging efficiency. They are found to be $7-9\%$ and $5-8\%$ respectively across all of the regions.

Theory uncertainties are estimated by applying systematic variations of the input parameters for the MC. These variations are applied for SR-like, CR-like and VR-like selections. The theory uncertainties are derived separately for V+jets, $t\bar{t}$ and diboson processes.

Apart from the selections, theoretical uncertainties in the modelling of W+jets and Z+jets are treated identically and treated as fully correlated among all regions. The merging scale, which divides particles into sets that are treated by either the ME or parton shower calculation, is varied from a nominal value of 20 GeV by ± 10 GeV. The resummation scale used for the resummation of soft gluon emissions is varied by a factor of $\sqrt{2}$ and $1/\sqrt{2}$ and the factorisation and renormalisation scales are both varied by factors of 0.5 and 1.5. The input PDF set is also varied using adjusted `NNPDF3.0NNLO` replicas: `MMHT2014NNLO` [216] and `CT14NNLO` [217]. An additional uncertainty is included for 100 internal variations of the nominal PDF set using the `LAPDF` [218] tool. The renormalisation scale and PDF uncertainties are dominant, ranging from $6-11\%$ and $7-15\%$ respectively across the SRs.

For $t\bar{t}$, hadronisation and parton showering uncertainties are evaluated using alternative samples generated with `POWHEG-BOX` v2 [219] and showered using `Herwig++` v2.7.1, using the `UEEE5` [220] underlying event tune. ISR and final-state radiation modelling uncertainties, as well as those associated to the resummation scale and parton shower tune are estimated by varying the settings of `POWHEG-BOX` v2 for the event generation. Generator level uncertainties are estimated with samples generated using `Sherpa` 2.2.1.

For diboson theory uncertainties, alternative samples are used with the resummation, normalisation and factorisation scales varied. To account for the specific choice of electroweak parameters an additional 15% normalisation uncertainty is applied. Other backgrounds with small contributions to the SRs are simply attached an uncertainty of 100% to save processing time. Due to low contributions this has little impact on the results of the analysis.

Heavy flavour modelling uncertainties are mitigated by the MC normalisation to the yields in the CRs. Additional uncertainties arising from the extrapolation from the CRs to the SRs are considered. The case of V+jets and $t\bar{t}$ are studied separately:

- ***V*+jets:** all jets in these processes arise from initial- and final-state radiation. The normalisation for the SR is derived by fitting the CRs to the data, effectively correcting the heavy flavour production cross section. However, if the relative contributions from different flavours are mis-modelled, the relative cross section for heavy flavour production will not be fully correct. This is the case in some W+jets regions (see appendix B.6). For these regions an additional systematic is derived by varying the yield of the heavy flavour component in the CR up and down by $\pm\sigma$, where σ is taken to be the uncertainty on the cross section as measured in Ref. [221].

- ***tt̄* :** in $t\bar{t}$ events heavy flavour jets can arise either from initial/final-state radiation or from hadronic $t\bar{t}$ decay. In the case of hadronic $t\bar{t}$ decay no additional uncertainty needs to be introduced. The relative fraction of $t\bar{t}$ events in the CRs and SRs in which the heavy flavour jet is from ISR is relatively small,

between 4% and 12% across all regions. No additional uncertainty is introduced for the heavy flavour cross section in $t\bar{t}$ regions.

Uncertainties on the SUSY signal simulation are also considered. Experimental uncertainties are included in the same way as for the backgrounds. The total experimental uncertainty in the signal yields was found to be 11-24% across the $\tilde{t}_1/\tilde{t}_1 - \tilde{\chi}_1^0$ mass plane. The dominant uncertainty in all SRs is that associated to the c-tagging efficiency, which is largely dependent on the squark mass, varying between 10-20% in the mass range 300-1000 GeV. Additional uncertainties in the acceptance and efficiency of the SUSY signal MC samples are considered, due to the variation of the QCD coupling constant α_S, the renormalisation and factorisation scales, the CKKW scale used to match the parton shower and matrix element descriptions, and the parton shower tunes. The total magnitude of these uncertainties ranges up to about 13%, depending on the signal region and sparticle masses considered.

5.10 Statistical Procedure

This section provides details of the statistical treatment used to assess whether there is evidence of a significant excess of data in the SRs and, if no excess is observed, to determine the region of the stop and LSP mass plane that can be disfavoured at the 95% confidence level.

5.10.1 Likelihood Construction

The predicted yield in a given region is:

$$N = \mu_s n_s (1 + \sum_j \theta_s^j \sigma_s^j) + \sum_i \mu_b^i n_b^i (1 + \sum_j \theta_b^j \sigma_b^{ij}) \tag{5.15}$$

where μ_s is the *signal strength*, corresponding to zero for the background-only hypothesis, and n_s is the expected signal yield. μ_b^i is the normalisation for background process i and n_b^i its expected yield, where the index i runs over each of the simulated backgrounds and $\mu_b^i = 1$ for processes estimated using MC only. The θ^js are the NPs associated with each of the systematic uncertainties, with the index j running over the complete set, and σ^{ij} is the corresponding standard deviation for the jth uncertainty for process i.

The number of events observed in a given region is Poisson distributed with mean N determined by the predicted yield in equation 5.15. For single-bin regions, the likelihood function L is constructed from the product of the individual probability density functions as follows:

$$\begin{aligned} L(\mathbf{n}^{\text{obs}}, \boldsymbol{\theta}^0 | \mu_s\,, \boldsymbol{\mu}_b, \boldsymbol{\theta}) &= P_{\text{SR}} \times P_{\text{CR}} \times C_{\text{syst}} \\ &= P(n_{SR}^{\text{obs}} | N_{SR}(\mu_s, \boldsymbol{\mu}_b, \boldsymbol{\theta})) \times \prod_{i \in \text{CR}} P(n_i^{\text{obs}}, N_i(\mu_s, \boldsymbol{\mu}_b, \boldsymbol{\theta})) \times C_{\text{syst}}(\boldsymbol{\theta}^0, \boldsymbol{\theta}) \end{aligned} \tag{5.16}$$

where n^{obs} is the observed yield for a given region. The $C_{\text{syst}}(\boldsymbol{\theta}^0, \boldsymbol{\theta})$ term is added to take into account the probability of a given systematic fluctuating by amount θ^i,

to reproduce the variations observed according to equation 5.15. If the systematics are assumed to be subject to Gaussian fluctuations the term will take the form:

$$C_{\text{syst}}(\boldsymbol{\theta}^0, \boldsymbol{\theta}) = \prod_{j \in S} G(\theta_j^0 - \theta_j) \tag{5.17}$$

where S denotes the full set of included systematics. The $\boldsymbol{\theta}^0$ are auxiliary measurements, which are set to zero for the fitting procedure, but can be varied when generating pseudo-experiments for the profile likelihood ratio. The μ_s, $\boldsymbol{\mu_b}$ and $\boldsymbol{\theta}$ parameters are estimated by maximising the likelihood, which is done numerically. The likelihood construction and minimisation is implemented using HistFitter [193] interfaced with the HistFactory [222] package.

5.10.2 Hypothesis Testing

It is customary to quote the probability of an observation in terms of the significance Z, given by

$$Z = \Phi^{-1}(1 - p) \tag{5.18}$$

where Φ^{-1} is the inverse of the cumulative Gaussian distribution and p is the probability, or p-value, of the observation under the null hypothesis. In this sense Z is a measure of the number of Gaussian σ that an observation deviates from the null hypothesis. For this analysis the following tests are performed:

1. First, the compatibility of the observed yields in the SRs with the background-only hypothesis. A rejection of the background-only hypothesis with a confidence of $> 5\sigma$ is the target for declaring a significant excess of data against the SM prediction.

2. If no such excess is observed, the objective is to set limits in the squark / LSP mass plane by excluding the signal hypothesis. A signal is considered excluded if the signal plus background hypothesis is rejected with a confidence of $Z > 3\sigma$.

The probability for the hypothesised signal strength μ_s is determined using the profile likelihood ratio $\lambda(\mu_s)$, defined as

$$\lambda(\mu_s) = \frac{L(\mu_s, \hat{\hat{\boldsymbol{\mu}}}_{\boldsymbol{b}}, \hat{\hat{\boldsymbol{\theta}}})}{L(\hat{\mu}_s, \hat{\boldsymbol{\mu}}_{\boldsymbol{b}}, \hat{\boldsymbol{\theta}})}. \tag{5.19}$$

The likelihood L is defined as in equation 5.16. In the numerator, $\hat{\hat{\boldsymbol{\mu}}}_{\boldsymbol{b}}$ and $\hat{\hat{\boldsymbol{\theta}}}$ are the vectors of parameters that maximise L for a fixed μ_s hypothesis. In the denominator, $\hat{\mu}_s$, $\hat{\boldsymbol{\mu}}_{\boldsymbol{b}}$ and $\hat{\boldsymbol{\theta}}$ are the signal strength and set of background normalisations and NPs that maximise the likelihood with the signal strength allowed to vary in the fit. Thus the statistic $\lambda(\mu_s)$ is a function of the hypothesised signal strength, and satisfies the inequality $0 \leq \lambda(\mu_s) \leq 1$. If $\lambda(\mu_s) = 1$, the hypothesised value of μ_s corresponds to the best possible description of the data, given the model.

The profile likelihood ratio is used to define the test statistic t_{μ_s}:

$$t_{\mu_s} = -2 \ln \lambda(\mu_s). \tag{5.20}$$

Higher values of t_{μ_s} indicate a greater degree of incompatibility between the data and the hypothesised μ_s. The p-value is determined from the probability distribution function associated to the test statistic:

$$p_{\mu_s} = \int_{t_{\mu_s}}^{\infty} f(t_{\mu_s}|\mu_s) dt_{\mu_s}. \tag{5.21}$$

The integrand $f(t_{\mu_s}|\mu_s)$ is approximated according to Ref. [223], and its evaluation is performed using HistFitter interfaced to the RooStats [224] software tool.

The test statistic is adjusted according to whether the test is for discovery, case (1) above, or exclusion, case (2) above. In case (1) the test statistic q_0 is used, defined by

$$q_0 = \begin{cases} -2\ln\lambda(0) & \hat{\mu}_s \geq 0, \\ 0 & \hat{\mu}_s \leq 0. \end{cases} \tag{5.22}$$

This definition encodes the assumption that the presence of a signal should only increase the expectation value of the event rate. Thus in the case of an under-fluctuation in the observed data, the background-only hypothesis is automatically accepted. For case (2), t_{μ_s} is instead adjusted in the following way:

$$q_{\mu_s} = \begin{cases} -2\ln\lambda(\mu_s) & \hat{\mu}_s \leq \mu_s, \\ 0 & \hat{\mu}_s > \mu_s. \end{cases} \tag{5.23}$$

In this definition the signal model will not be excluded if the observed data suggests that $\hat{\mu}_s > \mu_s$.

The test statistics q_0 and q_{μ_s} can be used to place a confidence limit CL on the possible signal models, representing a bound on the set of models that are excluded with a minimum probability α, namely:

$$1 - CL \geq \alpha = p_{\mu_s}. \tag{5.24}$$

This definition of the CL may however produce spurious results in some cases. For example, if the observed data represents a large under-fluctuation compared with the expected background, signal models that predict no events in the region may be excluded at 95% confidence. Thus the analysis may exclude signals to which it is not sensitive. To counter this effect, the CL_s method [225] is adopted, where the p-value for the signal is normalised to the confidence limit in the background-only hypothesis to define CL as follows:

$$1 - CL \geq CL_s = \frac{p_{\mu_s}}{1 - p_b}. \tag{5.25}$$

The CL_s method is a conservative approach, bounded by the definition given in equation 5.24. It is penalised in the case that the confidence in the background-only hypothesis is low, increasing CL_s such that the model is no longer excluded according to the condition in equation 5.25.

5.11 Background-only Fit

The background-only fit is implemented according to section 5.10.1, with the signal strength set to zero, fitting only the CRs to determine $\boldsymbol{\mu_b}$ and $\boldsymbol{\theta}$. From the covariance matrix of the fitted parameters, total error on the background extrapolation is

Fit parameter	SR1	SR2	SR3	SR4	SR5
μ_W	$1.13^{+0.20}_{-0.43}$	$1.20^{+0.44}_{-0.45}$	$1.70^{+0.45}_{-0.42}$	$1.49^{+0.37}_{-0.32}$	$1.28^{+0.33}_{-0.26}$
μ_Z	$1.35^{+0.27}_{-0.40}$	$1.34^{+0.26}_{-0.22}$	$1.22^{+0.28}_{-0.23}$	$1.29^{+0.29}_{-0.22}$	$1.30^{+0.32}_{-0.23}$
μ_{Top}	$1.15^{+0.38}_{-0.28}$	$1.28^{+0.54}_{-0.48}$	$0.86^{+0.33}_{-0.35}$	$0.80^{+0.34}_{-0.30}$	$1.01^{+0.45}_{-0.30}$

Table 5.8: Normalisation factors after the background-only fit. The central values with the detector-related systematic uncertainties, corresponding to one standard deviation, are reported.

estimated according to:

$$\sigma^2_{b,\text{tot}} = \sum_i^n \left(\frac{\partial b}{\partial \eta_i}\right)^2 \sigma^2_{\eta i} + \sum_i^n \sum_{j\neq i}^n \rho_{ij} \left(\frac{\partial b}{\partial \eta_i}\right)\left(\frac{\partial b}{\partial \eta_j}\right) \sigma_{\eta_i}\sigma_{\eta_j} \tag{5.26}$$

where η_i are the fit parameters, with the index i running over the NPs θ_i and background normalisations μ_b^i. The ρ_{ij} are the correlation coefficients between parameters η_i and η_j, and σ_{η_i} is the standard deviation for the ith parameter. In total there are five fit configurations: one for each SR. The normalisation for each fitted background in each of the SRs is summarised in table 5.8. The central values for μ_{Top} are anti-correlated μ_W (see figure 5.33), with large uncertainties. This is due to the mutual contamination in the single lepton CRs; for regions where the $t\bar{t}$ component has a high normalisation, the fitted μ_W is squeezed to lower values in the fit, and vice versa. The $t\bar{t}$ contribution in the SRs is relatively low and the effect on the results is not too severe.

Figure 5.34 shows comparisons between data and MC in selected distributions in the CRs, after rescaling by the normalisations derived in the background-only fit. Good agreement between data and prediction is seen in each of the regions. Figure 5.35 shows the comparison between the observed and predicted yield in each of the VRs after applying the background normalisations. The number for each VR indicates which CRs were used to derive the normalisations. For example, regions **VR1A** and **VR1B** share normalisations derived from CRs corresponding to **SR1**. The ratio of data to prediction fluctuates as expected, with no evidence of significant mis-modelling of the background observed. Thus the extrapolation of the normalisation factors from the CRs is validated.

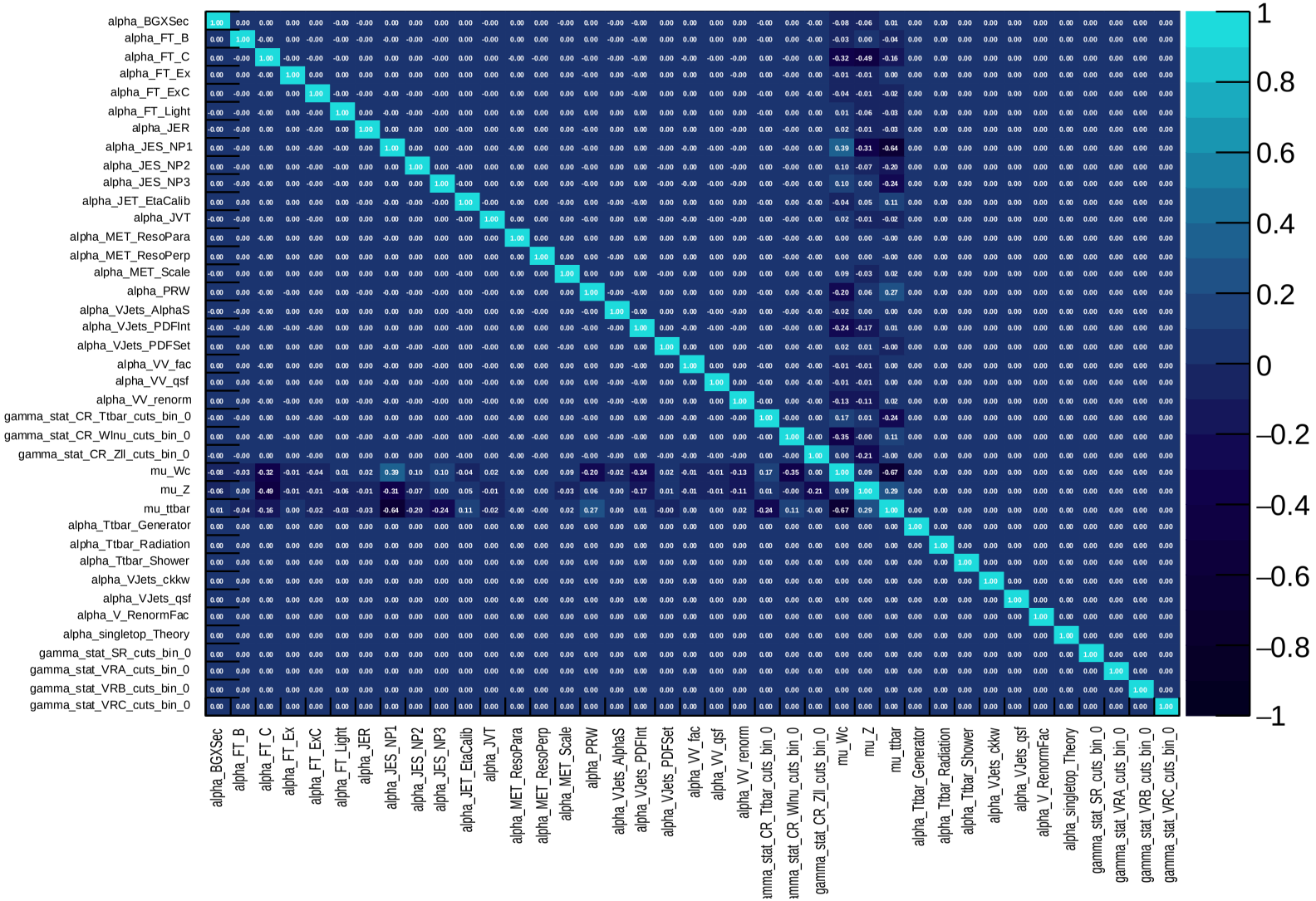

Figure 5.33: Correlation matrix for the background-only fit parameters for **SR2**. The names used for the parameters are expanded in appendix C.1.

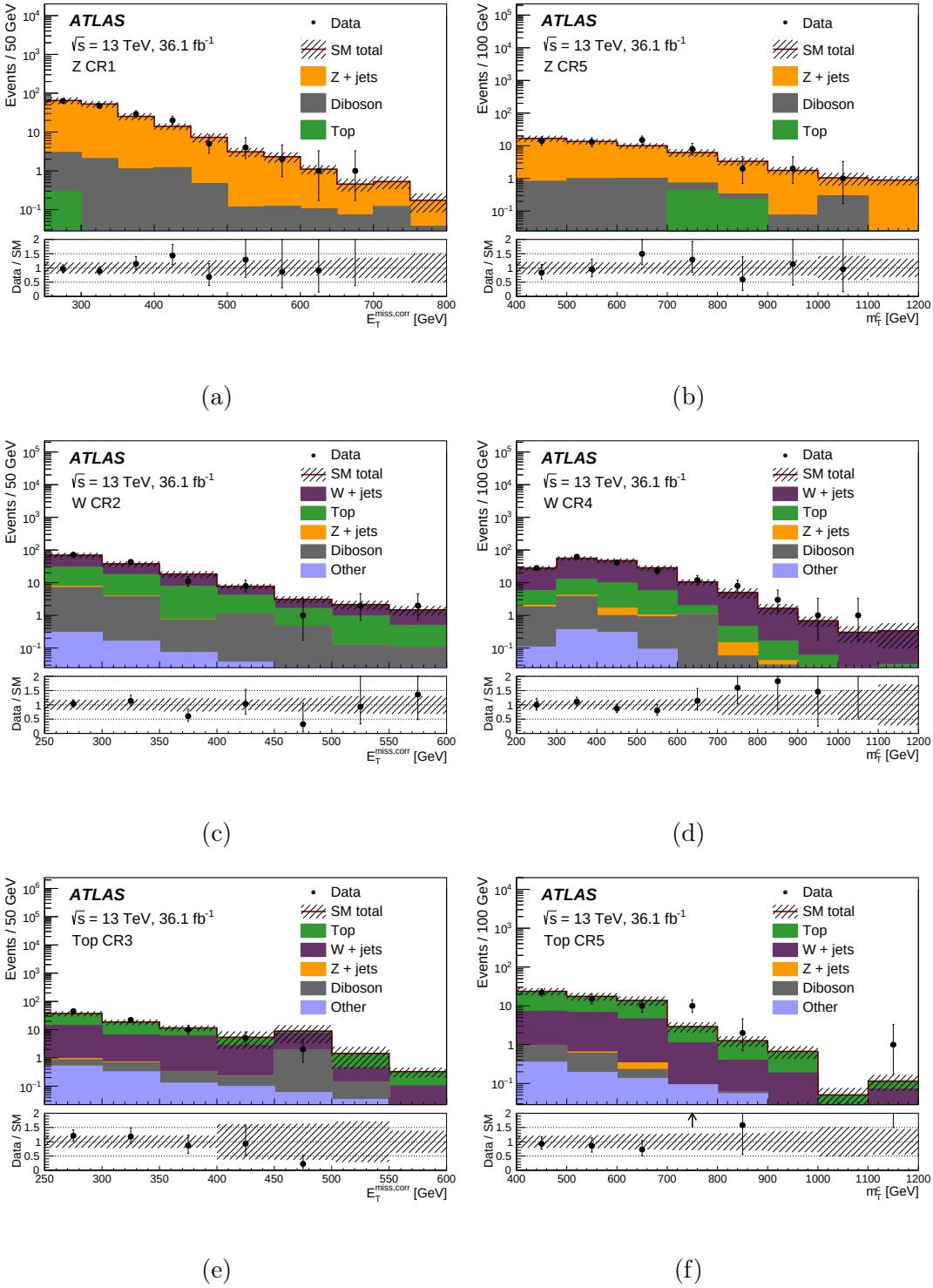

Figure 5.34: Selected comparisons between data and expectation after the background-only fit for the $E_{\mathrm{T}}^{\mathrm{miss,corr}}$ distribution in (a) Z CR1, (c) W CR2 and (e) Top CR3, and for the m_{T}^{c} distribution in (b) Z CR5, (d) W CR4 and (f) Top CR5 . The contributions from all SM backgrounds are shown as a histogram stack. The shaded band indicates the detector-related systematic uncertainties and the statistical uncertainties of the MC samples. The error bars on the data points indicate the data's statistical uncertainty. The lower panel shows the ratio of the data to the SM prediction after the background-only fit.

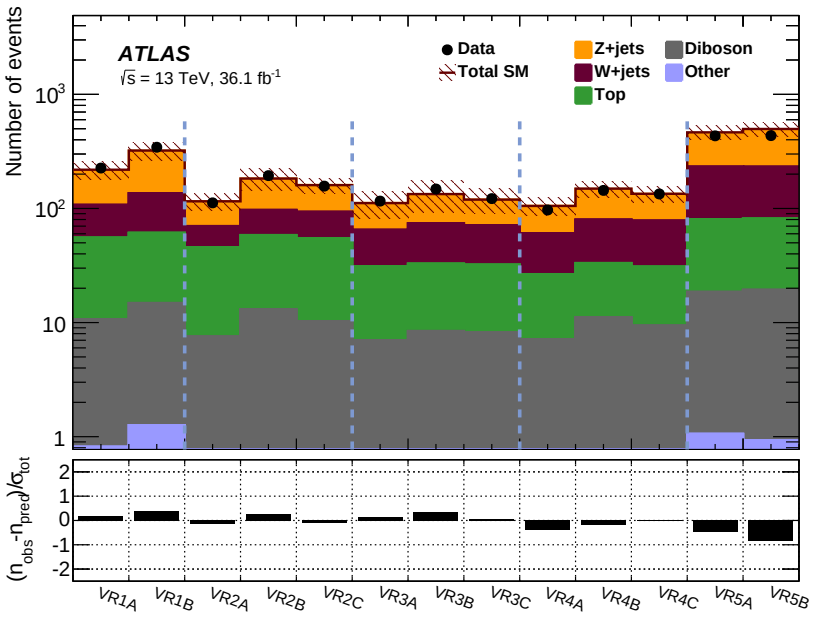

Figure 5.35: Comparison of the number of data events and predicted SM yield in each VR. The normalisation of the backgrounds is obtained from the fit to the CRs. The shaded band indicates the total background uncertainty. The lower panel shows the pulls, estimated as the difference between the observed number of events (n_{obs}) and the predicted background yields (n_{pred}) divided by the total uncertainty (σ_{tot}).

5.12 Results

After the validation of the extrapolation procedure, the data yields in the SRs can be compared to the prediction. The observed event yields and expected signal yields in each SR are summarised in table 5.9 and illustrated in figure 5.36. Table 5.9 also shows upper limits on the visible cross section at the 95% confidence level, $\langle\sigma_{\text{vis}}\rangle^{95}_{\text{obs}}$, for non-SM processes in each SR, as well as the derived upper limit on the number of signal events, S^{95}_{obs}. Finally, the table shows the p-value for the background to fluctuate to the observed yield if no signal is present, $p(s = 0)$. The upper limit at the 95% confidence level is also shown for the expected background in each region, S^{95}_{exp}. These upper limits are derived in a model independent way using the test statistic given in 5.22, under the background-only hypothesis, and with the SRs included in the fit. The uncertainty on the $Z \to \nu\nu$ background is the dominant uncertainty in each SR. The total uncertainty on the background prediction ranges from 15-20% for the SRs. No significant excess was seen in any of SRs, with a slight over-fluctuation seen in **SR2** and under-fluctuations observed in all other SRs, less than 1σ in each case. The smallest p-value for a fluctuation of the background to the observed data is 0.41 in **SR2**, with the p-value defaulting to 0.5 in the case of an under-fluctuation. The post background-only fit $E_{\text{T}}^{\text{miss}}$ distributions comparing data and MC are shown in figure 5.37, with benchmark signals for each region overlaid. Each of these distributions shows good agreement between data and MC.

The statistic given in 5.23 is used to derive 95% confidence limits under the signal plus background hypothesis in the squark / LSP mass plane, with a signal model excluded if the CL_s is less than 0.05. The limits are shown in figure 5.38, and for the mass difference versus the squark mass in figure 5.39. The contours are built using the most sensitive SR for each signal model, with the transitions between signal regions visible in figure 5.38 at approximately (480, 400) GeV for **SR2** to **SR3** and (500, 300) GeV for **SR3** to **SR4**. Superimposed are the limits obtained from the Run 1 analyses and the 13 TeV ATLAS monojet analysis [226], targeting events with $E_{\text{T}}^{\text{miss}}$ and an energetic jet, which has sensitivity in the compressed region of the parameter space. The monojet analysis improves on the sensitivity achieved by this analysis in models where the c-quarks are too low in p_{T} to meet the jet reconstruction threshold, and therefore cannot be tagged.

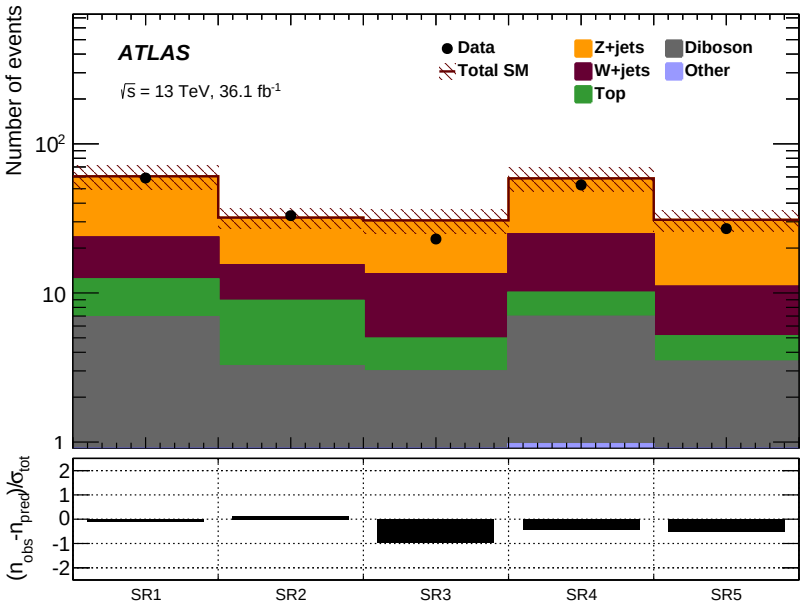

Figure 5.36: Comparison of the numbers of data events and predicted SM yields in each signal region. The normalisation of the backgrounds is obtained from the fit to the CRs. The shaded band indicates the total background uncertainty. The lower panel shows the pulls, estimated as the difference between the observed number of events (n_{obs}) and the predicted background yields (n_{pred}) divided by the total uncertainty (σ_{tot}).

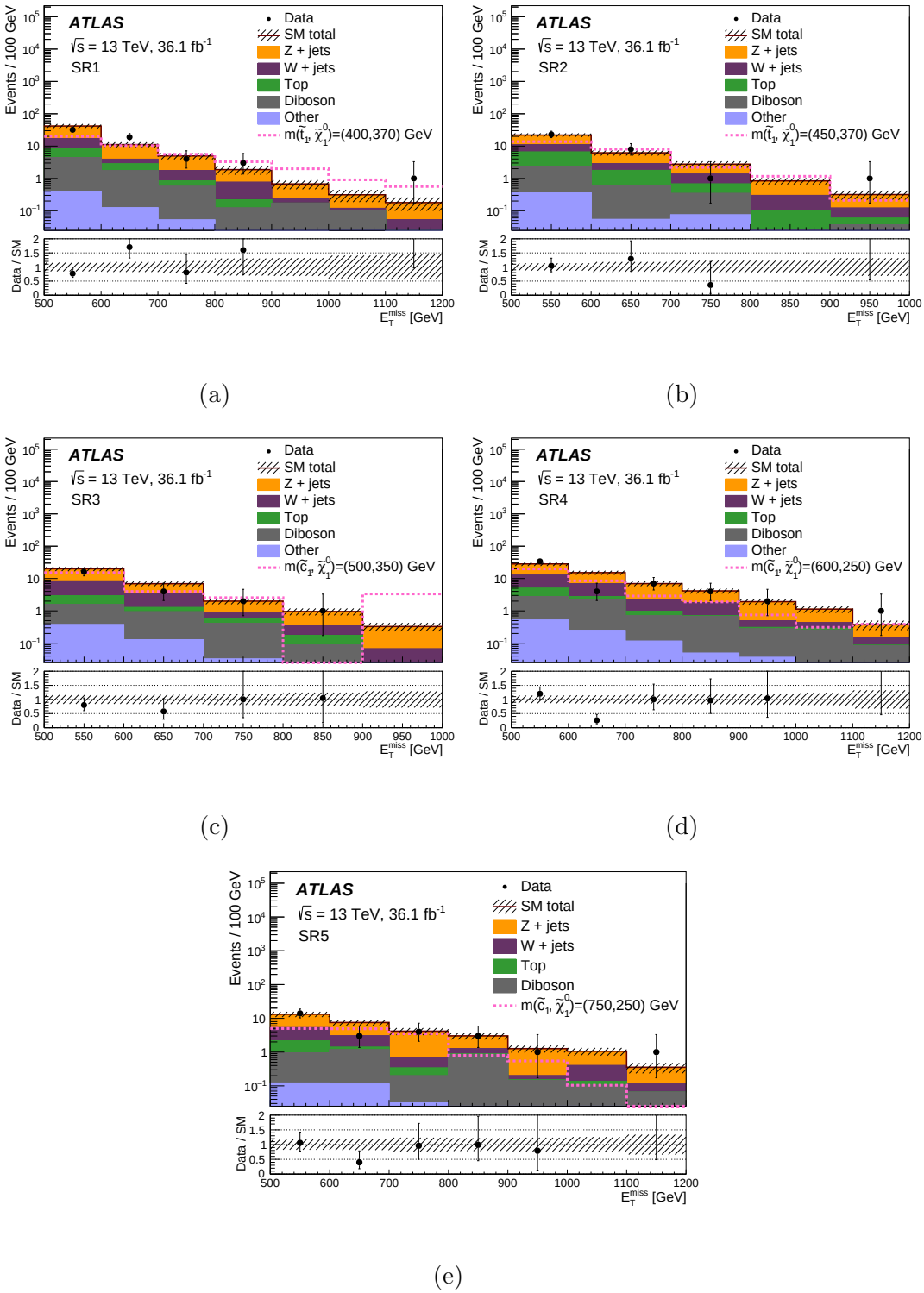

Figure 5.37: Comparison between data and expectation after the background-only fit for the $E_{\mathrm{T}}^{\mathrm{miss}}$ distribution (a) in SR1, (b) in SR2, (c) in SR3, (d) in SR4, and (e) in SR5. The shaded band indicates the detector-related systematic uncertainties and the statistical uncertainties of the MC samples, while the error bars on the data points indicate the data's statistical uncertainty. The final bin in each histogram includes the overflow. The lower panel shows the ratio of the data to the SM prediction after the background-only fit. In each plot, the distribution is also shown for a representative signal point.

Yields	SR1	SR2	SR3	SR4	SR5
Observed	59	33	23	53	27
Total SM	61 ± 11	32 ± 5	31 ± 6	59 ± 11	31 ± 5
Z+jets	37.1 ± 7.8	16.7 ± 3.2	17 ± 5	34 ± 8	20 ± 4
W+jets	11.2 ± 5.1	6.5 ± 2.3	8.4 ± 2.0	15 ± 4	5.9 ± 1.5
Top	5.4 ± 2.0	5.6 ± 2.6	2.0 ± 2.0	3.1 ± 1.8	1.7 ± 0.7
Diboson	6.3 ± 2.1	2.7 ± 1.7	2.4 ± 0.7	5.9 ± 2.3	3.2 ± 1.6
Other	0.6 ± 0.1	0.5 ± 0.1	0.5 ± 0.1	1.0 ± 0.1	0.3 ± 0.1
Signal benchmarks					
$(m_{\tilde{t}_1}, m_{\tilde{\chi}_1^0}) = (450, 425)$ GeV	22.7 ± 4.0	9.1 ± 2.6	1.6 ± 1.0	1.84 ± 0.71	0.45 ± 0.27
$(m_{\tilde{t}_1}, m_{\tilde{\chi}_1^0}) = (500, 420)$ GeV	18.3 ± 3.4	19.7 ± 4.9	15.2 ± 4.1	8.0 ± 2.2	1.26 ± 0.64
$(m_{\tilde{t}_1}, m_{\tilde{\chi}_1^0}) = (500, 350)$ GeV	5.4 ± 2.0	11.6 ± 3.3	26.1 ± 6.7	18.7 ± 5.4	3.0 ± 1.1
$(m_{\tilde{t}_1}, m_{\tilde{\chi}_1^0}) = (600, 350)$ GeV	1.91 ± 0.87	3.2 ± 1.3	10.5 ± 3.0	24.0 ± 5.9	7.0 ± 2.2
$(m_{\tilde{t}_1}, m_{\tilde{\chi}_1^0}) = (900, 1)$ GeV	0.67 ± 0.19	0.61 ± 0.21	1.61 ± 0.50	11.7 ± 2.0	10.2 ± 1.8
$\langle\sigma_{\text{vis}}\rangle^{95}_{\text{obs}}$ [fb]	0.67	0.46	0.33	0.59	0.40
S^{95}_{obs}	24.2	16.6	11.9	21.3	14.3
S^{95}_{exp}	$24.4^{+13.2}_{-7.6}$	$16.0^{+5.6}_{-4.4}$	$15.0^{+5.2}_{-3.1}$	$24.9^{+9.6}_{-7.1}$	$15.3^{+6.8}_{-2.2}$
$p(s = 0)$	0.5	0.41	0.5	0.5	0.5

Table 5.9: Observed and expected yields for all the SRs considered in the analysis. The uncertainties include experimental, theoretical, and MC statistical uncertainties. Benchmark signal model yields are also given for each SR. The lower part of the table reports the 95% confidence level upper limits on the visible cross section, $\langle\sigma_{\text{vis}}\rangle^{95}_{\text{obs}}$, on the number of signal events, S^{95}_{obs}, and on the number of signal events given the expected number (and $\pm 1\sigma$ excursions of the expectation) of background events, S^{95}_{exp}. The discovery p-value, $p(s = 0)$, where s is the number of signal events, is also reported. The value of 0.5 is assigned in the case of a downward data fluctuation where the number of observed events is less than the expected number of events.

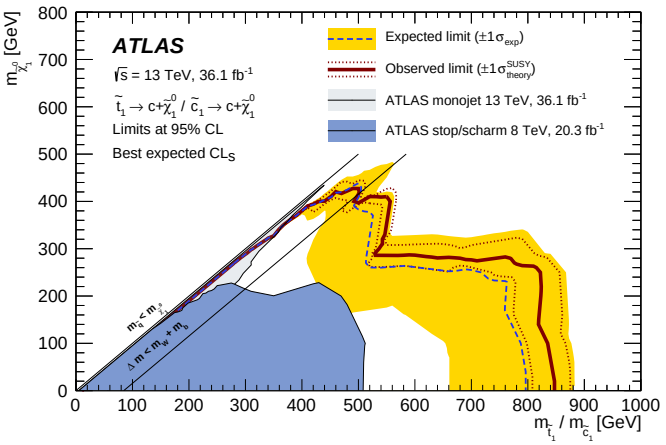

Figure 5.38: Observed and expected exclusion contours at the 95% confidence limit, as well as $\pm 1\sigma$ variation of the expected limit, in the $\tilde{t}_1, \tilde{c}_1$–$\tilde{\chi}_1^0$ mass plane. The SR with the best expected sensitivity is adopted for each point of the parameter space. The solid band around the expected limit (dashed line) shows the impact of the experimental and SM background theoretical uncertainties. The dotted lines show the impact on the observed limit of the variation of the nominal signal cross section by $\pm 1\sigma$ of its theoretical uncertainties. The observed limit from the monojet search at $\sqrt{s} = 13$ TeV [226] and from the Run-1 analysis at $\sqrt{s} = 8$ TeV are also overlaid. Δm denotes $m_{\tilde{t}_1,\tilde{c}_1} - m_{\tilde{\chi}_1^0}$.

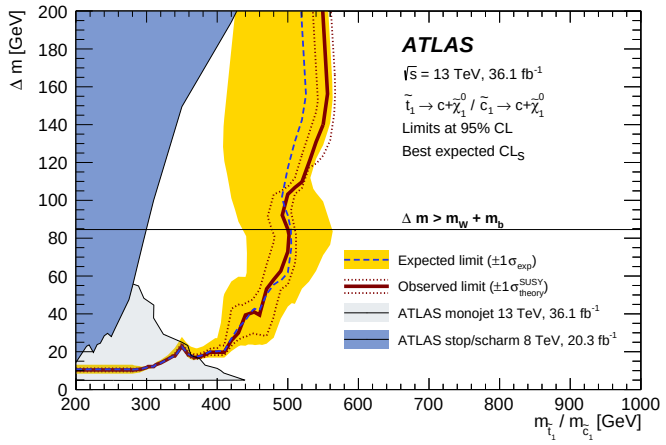

Figure 5.39: Observed and expected exclusion contours at the 95% confidence limit, as well as $\pm 1\sigma$ variation of the expected limit, in the $m_{\tilde{t}_1,\tilde{c}_1}$–$\Delta m$ plane, where Δm denotes $m_{\tilde{t}_1,\tilde{c}_1} - m_{\tilde{\chi}_1^0}$. The SR with the best expected sensitivity is adopted for each point of the parameter space. The solid band around the expected limit (dashed line) shows the impact of the experimental and SM background theoretical uncertainties. The dotted lines show the impact on the observed limit of the variation of the nominal signal cross section by $\pm 1\sigma$ of its theoretical uncertainties. The observed limit from the monojet search at $\sqrt{s} = 13$ TeV [226] and from the Run-1 analysis at $\sqrt{s} = 8$ TeV are also overlaid.

5.12.1 Summary

A selection has been designed to target SUSY signal models with $E_{\mathrm{T}}^{\mathrm{miss}}$, c-jets and zero leptons in the final state. This chapter has provided a recap of the theoretical motivations for such models first given in chapter 2 followed by a detailed description of the SR development and the procedures for estimating the background contributions and systematic uncertainties. The statistical treatment used to interpret the results was also presented.

No significant excess above SM predictions was observed by this analysis, and stringent limits were placed in the squark and LSP mass parameter space, with a stop decaying to charm quarks disfavoured up to a mass of 500 GeV for a corresponding LSP mass of 420 GeV. The limits on the mass of the stop quark are similar to those obtained in a related search performed by CMS in Ref. [227], with less reach in the highly compressed limit by around 50 GeV. Scharms are disfavoured up to a mass of 850 GeV in the case of a LSP in the approximate mass range 0-300 GeV.

The results of the analysis significantly extend previous limits shown in figure 5.1. These results are based on pp collisions collected by the ATLAS detector in 2015 and 2016. These data represent only a quarter of the total integrated luminosity delivered by the LHC by the end of Run 2; with the SR yield estimates dominated by statistical uncertainties, extending this analysis to the total Run 2 dataset will improve its sensitivity further. The LHC is currently being upgraded, and will operate at a centre-of-mass energy of 14 TeV following its current shutdown. The resulting increase in cross-section for high mass squarks will allow them to be targeted by re-optimised SRs. This analysis was designed for sensitivity to a broad class of SUSY models with c-jets and $E_{\mathrm{T}}^{\mathrm{miss}}$ in the final state, over a large range of masses in the squark-LSP parameter space. Further adaptions may be made in the future to target more specific models, for example dedicated MVA models trained for individual pairs of squark-neutralino masses, directly extending sensitivity to high mass squarks and neutralinos.

6 | Soft b-tagging in Compressed SUSY Scenarios

This analysis was the second major strand of the author's PhD research and makes up a key component of the work published in Ref. [2]. The objective for this analysis was to develop a tagging algorithm for the identification of low momentum b-hadrons with the ATLAS detector. This was successful and the soft b-tagging reconstruction software developed by the author is now integrated into `Athena`, the ATLAS software framework. At the time of writing the calibration of this tagger is underway, and it is finding use in the optimisation of new SRs targeting compressed SUSY models.

6.1 Compressed SUSY Scenarios

As discussed in sections 2.3.3 and 5.7.2, compressed SUSY models are both theoretically appealing and challenging to target. A small mass difference $\Delta m = m_{\tilde{t}_1/\tilde{b}_1} - m_{\tilde{\chi}_1^0}$ between the squark and the LSP can result in decay products that are too low in p_{T} to be reconstructed by the calorimeter system and therefore beyond the reach of conventional flavour tagging methods. Current ATLAS searches targeting direct stop and sbottom production make use of b-tagged jets and their sensitivity to models in the compressed regime is limited. Figures 6.1a and 6.1b show the exclusion limits set by stop and sbottom searches using 36.1 fb^{-1} of data collected by ATLAS in Run 2 [228, 229]. Both searches lose sensitivity as the mass difference between the squark and the LSP approaches zero. The same effect can be seen in the $\tilde{t}_1 \to c\tilde{\chi}_1^0$ search presented in the previous chapter; figure 5.39 shows a clear gap in sensitivity for low Δm.

Figure 6.2a shows the p_{T} spectrum for b-hadrons resulting from stop four-body and sbottom decays with $\Delta m = 20$ GeV. The p_{T} spectrum peaks at a lower value for the stop decay due to the higher multiplicity of decay products. Figure 6.2b shows the b-tagged jet multiplicity again comparing stop four-body and sbottom signals. For both signals the $b-$hadrons have $p_{\mathrm{T}} < 30$ GeV in most cases, often yielding calorimeter clusters below the threshold of standard jet reconstruction. These b-hadrons are therefore beyond the reach of conventional b-tagging methods. This is shown by the low multiplicity of b-tagged jets. In some cases very soft b-hadrons may still be tagged with low probability, for example if they are incorporated into a nearby calorimeter jet by the anti-k_t algorithm.

The defining characteristic of compressed stop and sbottom signals is the presence of low momentum b-hadron that cannot be identified by flavour tagging based on calorimeter jets. The method of *soft-tagging* is an innovation that circumvents this difficulty by aiming to reconstruct the SV from the b-hadron decay independently of calorimeter jet reconstruction. By tagging soft b-hadrons, sensitivity to compressed signals may be recovered. The objective for the analysis presented in this chapter was to develop soft-tagging for use in third-generation SUSY searches with the ATLAS detector. Two main approaches were investigated: one approach

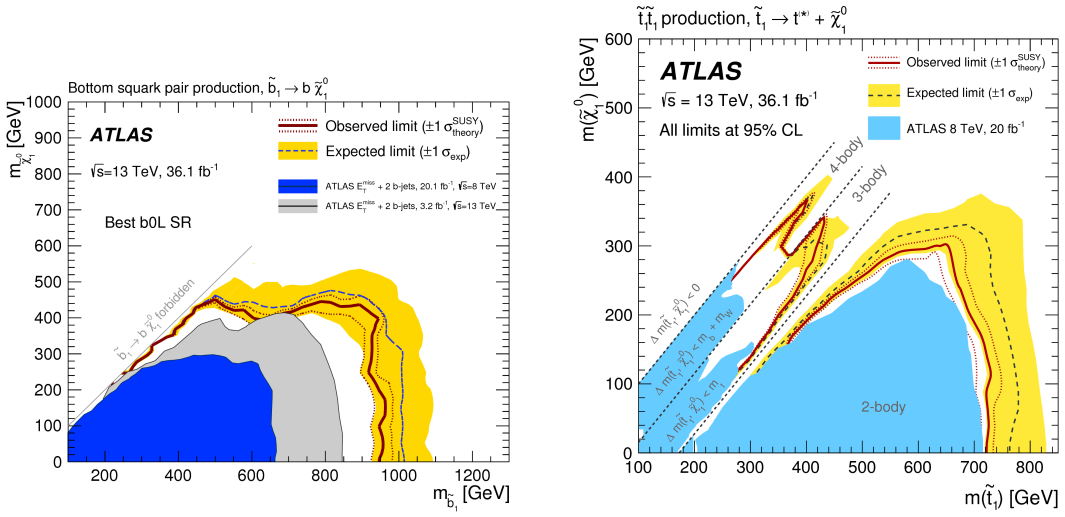

(a) (b)

Figure 6.1: Sensitivity in the squark and LSP mass plane for (a) Run 2 sbottom and (b) stop analyses by ATLAS. The contours show the expected and observed exclusion limits at 95% confidence. Superimposed are the limits obtained by previous ATLAS analyses. Taken from Refs. [228, 229].

attempts to reconstruct SVs from collections of tracks, the other applies the tagging algorithms described in section 4.4.5 to anti-k_t jets reconstructed from tracks only. The former approach was the main contribution of the author to the soft-tagging efforts at ATLAS and the algorithm development, tagging performance and calibration strategy are described in section 6.2. In section 6.2.7 soft tagging in low momentum track jets is briefly described and the performance of the two methods is compared.

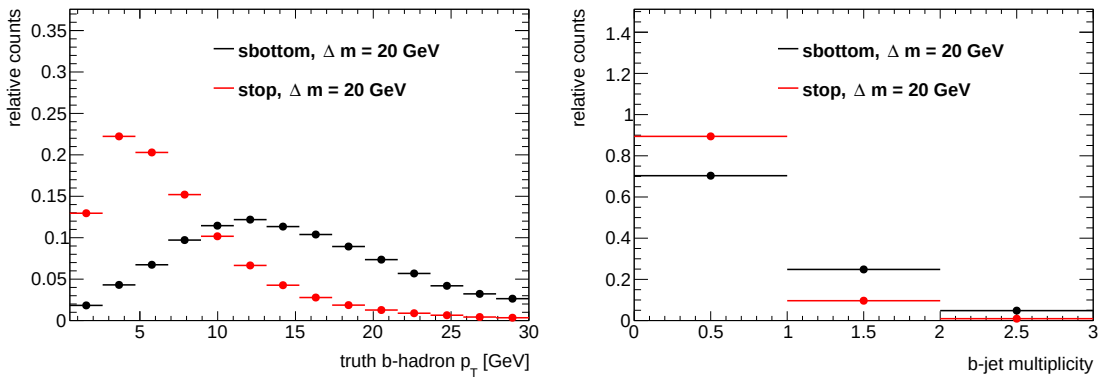

(a) (b)

Figure 6.2: (a) p_{T} spectrum and (b) b-tagged jet multiplicity in compressed stop and sbottom signals. The mass splitting for each signal is $\Delta m = 20$ GeV and the b-tagging algorithm is MV2c10 with a fixed 77% efficiency OP, applied to anti-k_t calorimeter jets.

6.2 Soft b-tagging by Track Clustering

In a typical pp collision event, hundreds of tracks are reconstructed in the ID, arising primarily from PVs. On the other hand, a typical b-hadron decay will result in a handful of reconstructed tracks. Soft b-tagging by track clustering aims to identify the SV that results from the decay of low momentum b-hadrons based on tracking information. Clusters of tracks are formed from regions of the detector with a high density of displaced tracks in close proximity. These form candidate SVs which may then be reconstructed using vertexing algorithms. A similar approach was used for a $B\bar{B}$ angular correlation measurements [230] and for compressed stop searches [231] by CMS.

This soft b-tagging algorithm takes all reconstructed tracks in an event as input and outputs a container of reconstructed SVs. The main steps of the algorithm are outlined below:

- **Common track selection:** the algorithm performs a first pass through the container of reconstructed tracks in the event, applying a preselection to filter out poor quality tracks or tracks that are likely to originate from pileup. Tracks are required to satisfy the following preselection criteria:

  1. fall within $|\eta| < 2.5$, the region of the detector covered by the ID.
  2. have at least seven hits in the silicon detectors.
  3. have no more than one hit in a module shared by another track.
  4. have no more than two holes in the silicon detectors.
  5. have no more than one hole in the pixel detector.
  6. if a module is shared, the requirement on the number of pixel detector hits is increased to ten.
  7. for pileup rejection, any track is rejected if it was used in the fit of a reconstructed PV that is not the hard-scatter vertex.

8. tracks are removed if they are associated to a calorimeter jet using ghost association (see section 4.4.4). This requirement serves two purposes: first, it reduces the overlap between soft b-tagging and conventional b-tagging by removing the possibility to identify b-hadrons within jets. These b-hadrons can in most cases be tagged by an arbitrarily loose MV2 based tagger and are not the primary focus of this algorithm. Second, a large number of background tracks in the event can be associated to a jet in this way. Thus it also serves as useful discriminant for rejecting tracks that did not originate from a soft b-hadron.

- **Seed track selection:** a collection of *seed* tracks is selected during a first pass through the filtered track container. Seed tracks must satisfy strict selection criteria based on p_{T} and impact parameter significance, optimised to preferentially select tracks originating from a $b-$hadron decay.

- **Cluster track selection:** tracks are clustered to seeds based on a separate set of selection criteria, by performing a second pass through the filtered track container. These criteria are based on the 3D track-track distance, angular separation and requirements on the impact parameter significance. After the cluster track selection, a set of track clusters, one for each seed, is stored by the algorithm. Any seeds with no clustered tracks are removed.

- **Secondary vertex reconstruction:** the track clusters are supplied to a vertex reconstruction algorithm for the reconstruction of any SVs within the cluster. The final output of this algorithm is a collection of reconstructed vertices.

Each of the above steps is described in further detail in the following sections.

6.2.1 Seed Track Selection

The seed track selection is designed to identify tracks that are likely to have originated from a b-hadron. To optimise the selection, a sample of simulated "signal" tracks was obtained from $\tilde{b}_1 \to b\tilde{\chi}_1^0$ and $\tilde{t}_1 \to bff'\tilde{\chi}_1^0$ events generated using `MadGraph`, as for the signals used in chapter 5, with the inputs adapted according to the physics process. The mass of the sbottom was set to 600 GeV and the mass of the stop to 400 GeV, in both cases the mass difference was set to 20 GeV. A reconstructed track is associated to the b-hadron using a truth-matching probability score, calculated as the weighted fraction of hits in a track with a common origin according to the truth record. This score ranges from 0-1 and provides a measure of the probability that a reconstructed track originated from a given truth particle. For this analysis, the truth-match probability is required to be > 0.75.

A sample of simulated "background" tracks not originating from b-hadrons was obtained from $Z \to \nu\nu$ events, generated as in section 5.5, with a truth filter applied to veto any events with a truth $b-$ or $c-$hadron. The events were also filtered such that the maximum of the scalar sum of p_{T} of the visible objects in the event and the truth p_{T} of the Z, must fall in the range 280-500 GeV. This sample was chosen as representative of the main expected background for a soft-tagging based SR.

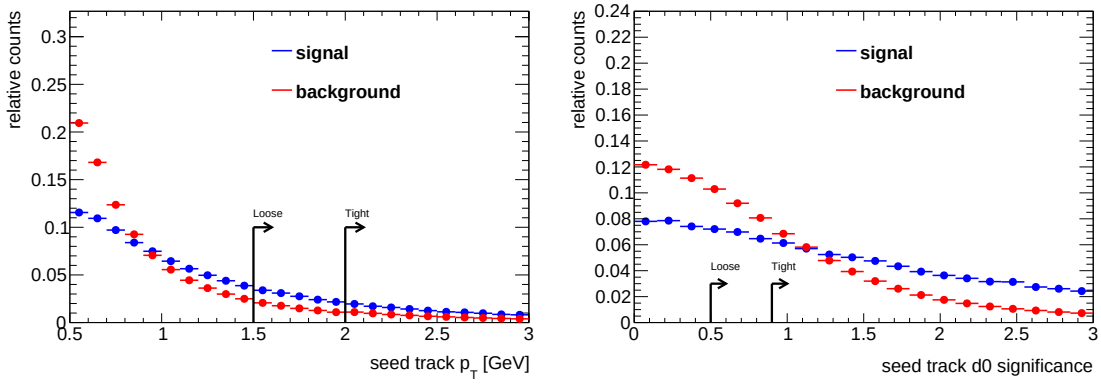

(a) (b)

Figure 6.3: (a) Track p_{T} and (b) d_0 significance in signal and background tracks. Example thresholds are shown for a loose and tight OP. The signal tracks are taken from tracks that are truth-matched to a b-hadron originating from a sbottom decay in simulated $\tilde{b}_1 \to b\tilde{\chi}_1^0$. The background tracks are taken from $Z \to \nu\nu$ simulated events with a truth veto on $b-$ and $c-$hadrons.

A number of variables were explored for the seed selection; the most effective were found to be the track p_{T} and the transverse impact parameter significance, defined as:

$$S_{d0} = \frac{d_0}{\sigma(d_0)}, \tag{6.1}$$

where $\sigma(d_0)$ is the uncertainty on d_0, taken from the covariance matrix associated to the track fit parameters. S_{d0} essentially measures the level of inconsistency between the track d_0 and the PV_0, measured in standard deviations. A lower threshold is applied for each of these variables, with the value depending on the OP chosen. Signal and background track distributions, along with example thresholds for a "tight" and "loose" OP are shown in figure 6.3. Track p_{T} is the most effective discriminant, with tracks from b-hadrons tending to higher p_{T}. A tight threshold is applied to select high p_{T} seeds. Signal tracks also tend to be displaced, tending to higher values of S_{d0}. The contribution from background tracks at higher displacement is due primarily to resolution effects, with a secondary contribution from other weakly decaying, long-lived, particles, for example K_S^0.

6.2.2 Cluster Track Selection

Following the seed selection, a list of displaced candidate tracks is prepared by applying a lower threshold on S_{d0}. The distribution of S_{d0} for truth-matched (to a b-hadron) and non-matched candidate cluster tracks is shown in 6.4a. Candidate tracks are then clustered to seeds based on geometric proximity to locate regions of the detector with high density of displaced tracks. Both the angular and spatial separation are considered, measured as follows:

- **Angular separation:** the angular separation between the four-vector of the seed track and the cluster track, measured at the perigee. This defines a cone surrounding the seed track; any candidate must fall within this cone to be included in the cluster. Figure 6.4b shows the ΔR between the seed and

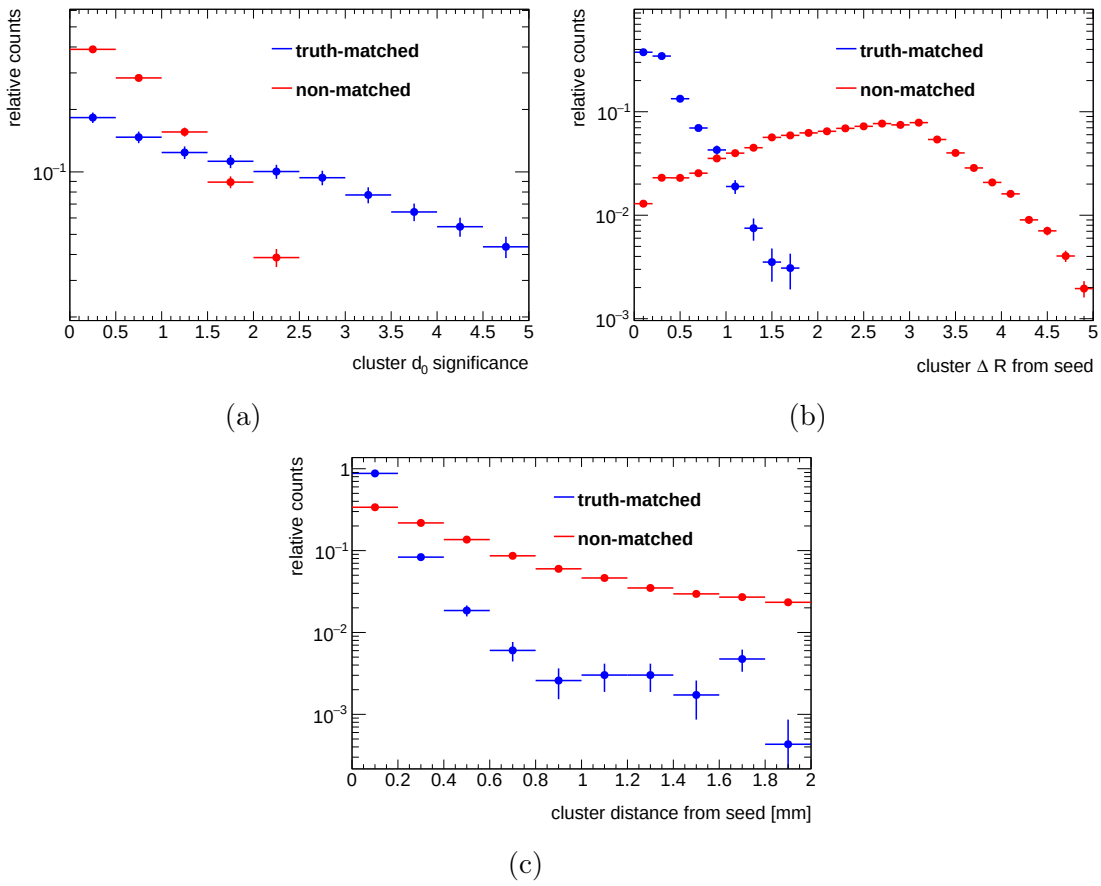

Figure 6.4: (a) Candidate cluster track impact parameter significance, (b) track-seed ΔR and (c) track-seed distance. In this figure, the seed is always required to be truth-matched to a b-hadron. The tracks labelled as truth-matched are matched to the same b-hadron as the seed. Non-matched tracks are considered to be any track that is not matched to the same b-hadron as the seed track in the event.

candidate tracks, where the seed is truth-matched. Tracks originating from the same b-hadron as that associated to the seed are shown in blue, unmatched tracks are shown in red. The angular separation between the seed and matched tracks is small in most cases. Starting from a narrow cone, as the cone size is expanded, the efficiency to tag b-hadrons increases, until the maximum separation of $\Delta R = 1.5$ is reached. After this point there is no increase in efficiency as the cone size is large enough to include all reconstructed tracks from the b-hadron in most cases. The distribution of non-matched tracks is very broad, consistent with random η and ϕ distributions. It is therefore favourable to narrow the cone to target the sharp peak at low ΔR, sacrificing efficiency for a large improvement to the rejection of non-matched tracks.

- **3D track-track distance:** defined as the distance of closest approach between the seed and the candidate track. There is no analytical solution for the distance between two helices, instead a numerical approximation scheme is used. This scheme applies Newton's method to identify the points on the track helices that minimise the distance between them. The position on the track helix can

be parameterised in terms of a single parameter ϕ_T:

$$\begin{aligned} x(\phi_T) &= x_0 - \rho\cos(\phi_0 + \phi_T), \\ y(\phi_T) &= y_0 - \rho\sin(\phi_0 + \phi_T), \\ z(\phi_T) &= z_0 - \rho(\cot\theta_0)\phi_T, \end{aligned} \tag{6.2}$$

where cartesian position at the perigee is $\vec{r}_0 = (x_0, y_0, z_0)$ and $\rho = p_{\mathrm{T}}/(0.3B)$ is the radius of curvature of the track as determined from the transverse momentum and magnetic field at the perigee. The magnetic field is taken from a magnetic field map of the ATLAS solenoid [232]. The total squared difference $\Delta\vec{r}^2$ in distance is minimised as a function of $\phi_{T,a/b}$ for tracks a and b, with the position on each track initialised to the perigee position. The precision is computed as:

$$\delta = \Delta\phi_{T,a}^2 + \Delta\phi_{T,b}^2, \tag{6.3}$$

where $\Delta\phi_T$ is the correction to ϕ_T between successive iterations. The test for convergence is $\delta < 10^{-8}$. The number of iterations is limited to 20, if convergence has not been reached the track is not clustered to the seed. If the determinant of the Hessian of $\Delta\vec{r}^2(\phi_{T,a}, \phi_{T,b})$ is negative-definite or semi-definite, the minimisation has found a saddle-point or maximum and the track is rejected.

Figure 6.4c shows the distance of candidate tracks to a truth-matched seed in an event, calculated according to the above procedure. Tracks that are truth-matched to the same b-hadron as the seed tend to have low separation by this measure, < 0.4 mm for most tracks. The distribution for non-matched tracks is much broader, with a large tail in higher values. A significant faction can still be found close to the truth-matched track.

6.2.3 Vertex Reconstruction

The above procedure returns a set of track clusters, which are then used as inputs to the SVF algorithm [181], described in section 4.4.5. The SVF algorithm takes as input the PV_0, selected tracks and a direction, in the form of a four-vector, around which a cone is defined, with the radius parameter left free in the optimisation. The SVF attempts to reconstruct a SV using only input tracks that fall within the defined cone. Figure 6.5a shows the fraction of b-hadrons from sbottom decays in the p_{T} range 10-20 GeV that get reconstructed by the SVF algorithm, given the direction of the b-hadron p_{T} according to the MC truth record. Due to the low momentum, the decay products of the b-hadron can have a wide angular distribution, which causes the efficiency of reconstruction to be sensitive to the size of the cone. For a narrow cone of radius 0.2, the efficiency is low since the number of tracks passed to the algorithm is typically insufficient to recover the SV. As the cone is expanded, the efficiency increases, approaching a constant value when the cone size is roughly 1.2, large enough to contain all tracks from the b-hadron almost 100% of the time. The corresponding efficiency to reconstruct a "fake" SV in a random cone is shown in figure 6.5b. The random direction is taken from the negative p_{T} sum of the two b-hadrons from a sbottom decay, a region where no genuine SV is expected. The fake rate increases with the cone size, as more tracks are considered in the

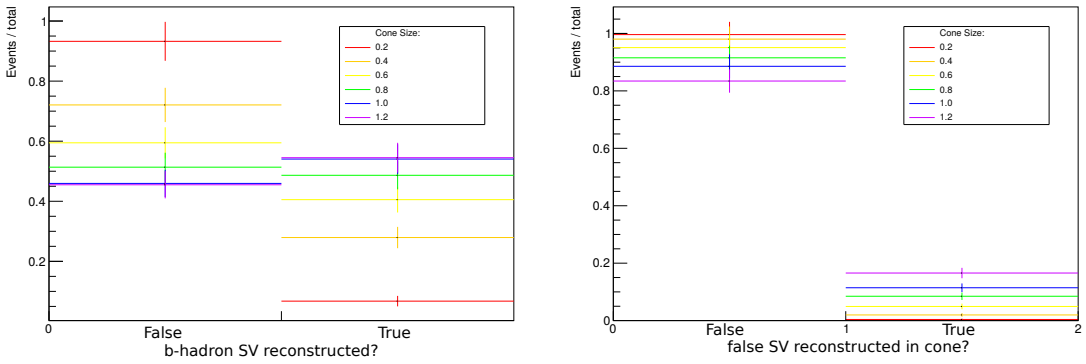

(a) (b)

Figure 6.5: (a) Efficiency of the SVF algorithm to reconstruct the secondary vertex from a b-hadron originating from sbottom decay in the p_{T} range 10-20 GeV, for different cone sizes. The cone is opened around the direction of the p_{T} of the b-hadron, taken from the truth record. (b) Rate at which fakes are reconstructed in a random cone centred around the direction resulting from taking the negative p_{T} sum of the two b-hadrons in sbottom events.

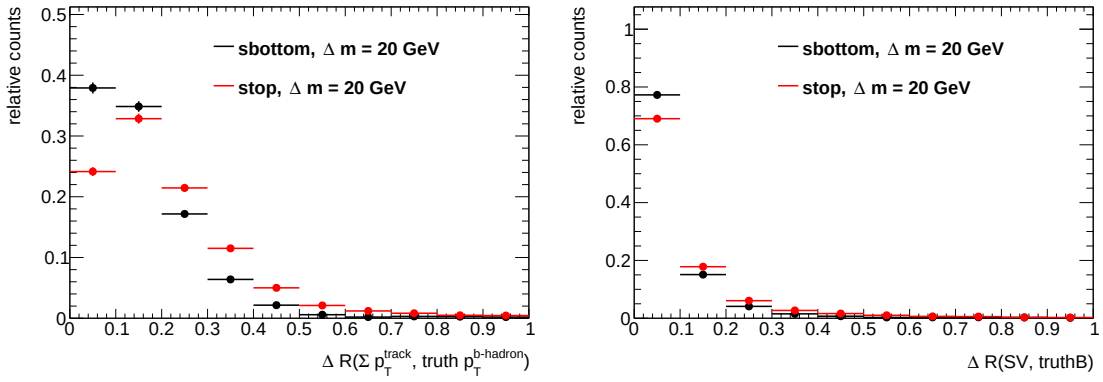

(a) (b)

Figure 6.6: (a) Angular separation between the sum of p_{T} of tracks within a cluster that is truth-matched to a b-hadron, and the truth p_{T} direction of the matching b-hadron. (b) Angular separation between the line connecting the PV_0 and the reconstructed SV, and the direction of the truth p_{T} of the matching b-hadron. The b-hadron is considered matched to the cluster if the cluster contains one or more tracks that are truth-match to it. The resolution is shown for sbottom and stop four-body decays with $\Delta m = 20$ GeV.

reconstruction procedure, increasing the likelihood of reconstructing a fake SV due to random crossings of tracks.

The efficiencies shown in figure 6.5a assume that the direction of the b-hadron can be recovered from the clustered tracks with perfect resolution. They represent an upper bound, with the efficiency diminished by the angular resolution with which the flight direction of the b-hadron can be reconstructed. The flight direction of the b-hadron is taken to be the direction of the vectorial p_{T} sum of all of the constituent tracks within the cluster, $p_{\mathrm{T}}^{\mathrm{cluster}}$. Figure 6.6a shows the angular resolution of $p_{\mathrm{T}}^{\mathrm{cluster}}$ for clusters matched to truth b-hadrons, measured as the angular separation between $p_{\mathrm{T}}^{\mathrm{cluster}}$ and the truth b-hadron p_{T}. The resolution worsens for the stop four-body decay sample due to the compressed p_{T} spectrum, which results in a wider angular distribution of decay products. Figure 6.6b shows the angular separation between the truth b-hadron flight direction and the line connecting the PV_0 and a reconstructed SV matched to the truth b-hadron. Reconstructed SVs display a sharp angular resolution with respect to the truth b-hadron, in cases where they are matched.

Figure 6.7 shows event displays of matched and non-matched tracks with $S_{d0} > 0.9$ in $\eta - \phi$ and $x - y$ space, in events where the b-hadron was successfully reconstructed. The x and y coordinates in the $x - y$ event display are taken from $\sin\phi$ and $\cos\phi$ projections of the magnitude of the distance of the track from the seed. The tracks that are truth-matched to the b-hadron tend to be close to the seed track both in ΔR and in distance of closest approach. The seed tracks are characterised by a high density of tracks in close proximity. These event displays demonstrate that the SVF is capable of reconstructing a SV_0 in the presence of many non-matched tracks. Figure 6.8 shows event displays where no SV matching a truth b-hadron decay vertex was reconstructed. Figures 6.8a and 6.8b show a case where a fake cluster not matching a b-hadron has been reconstructed. The truth b-hadron has a low p_{T} , and the reconstructed SV can be associated to a high density region of non-matched tracks. Figures 6.8c and 6.8d show a case where the cluster cannot be associated to a b-hadron, and no SV is reconstructed. The cluster is formed from an isolated seed, with a low density of tracks in close proximity.

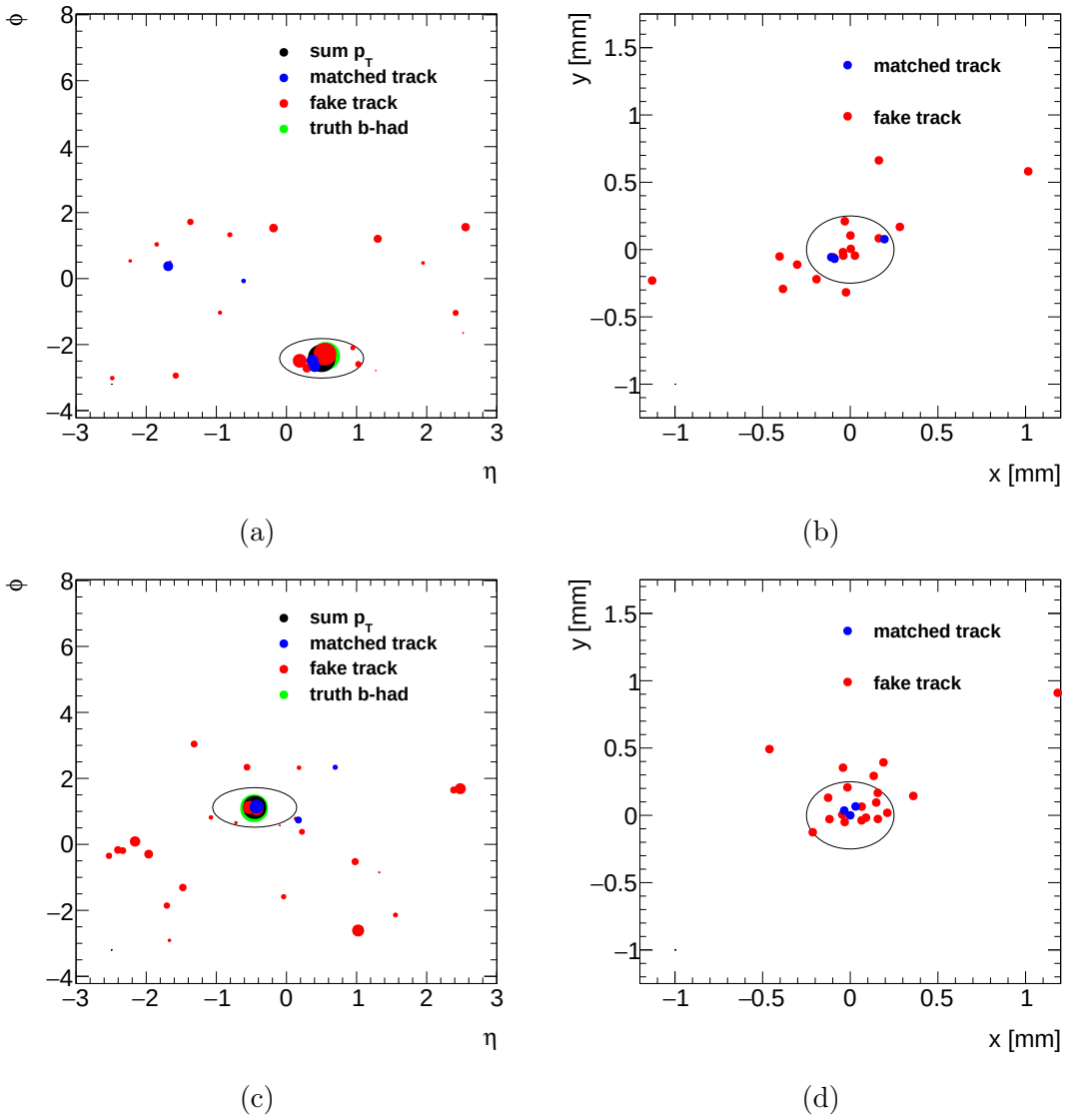

Figure 6.7: Event displays showing the tracks in simulated sbottom ($\Delta m = 20$ GeV) events in $\eta - \phi$ and $x - y$ space where the clusters contains tracks that are truth-matched to a b-hadron, and a vertex was correctly reconstructed from the cluster. Figures in the same row correspond to the same event. In the $\eta - \phi$ displays, each marker shows a track, with the size a nonlinear function of the track p_{T}. The marker is coloured black to indicate the sum of the track p_{T} for the cluster that was reconstructed from the tracks, blue to indicate a track matched to a b-hadron with probability $> 75\%$, red to indicate a track that does not satisfy the matching criterion and green to indicate the p_{T} of the b-hadron according to the truth record. The ellipse shows a cone of radius $R < 0.6$. The $x - y$ displays are centred on the seed track, showing the distance projected to x or y. All tracks shown are required to satisfy $S_{d0} > 0.9$.

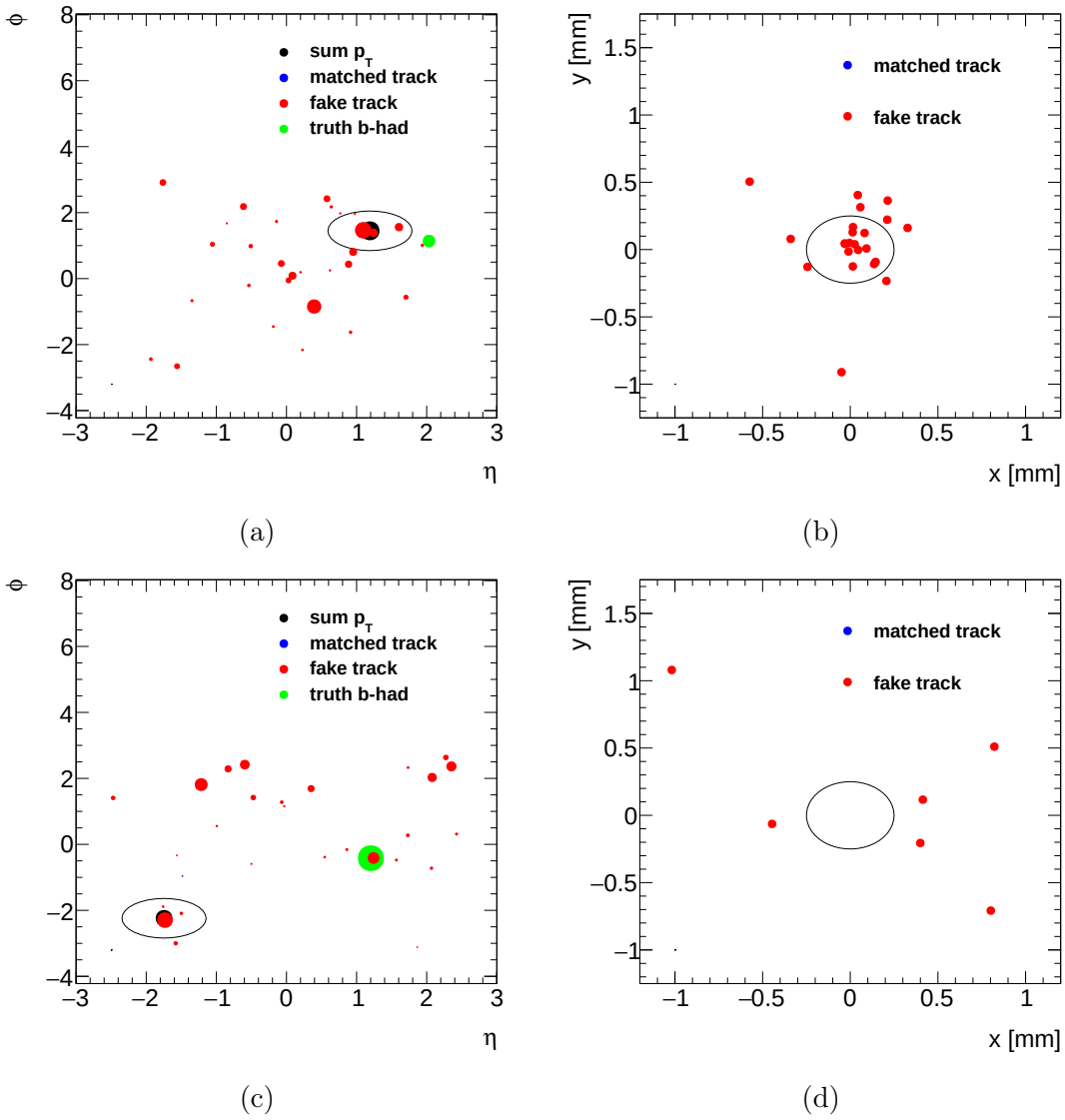

Figure 6.8: Event displays showing the tracks in simulated sbottom ($\Delta m = 20$ GeV) events in $\eta - \phi$ and $x - y$ space where the cluster contains no tracks that are truth-matched to a b-hadron, where a vertex was falsely reconstructed (top) or the cluster was correctly discarded (bottom). Figures in the same row correspond to the same event. In the $\eta - \phi$ displays, each marker shows a track, with the size a nonlinear function of the track p_{T}. The marker is coloured black to indicate the sum of the track p_{T} for the cluster that was reconstructed from the tracks, blue to indicate a track matched to a b-hadron with probability $> 75\%$, red to indicate a track that does not satisfy the matching criterion and green to indicate the p_{T} of the b-hadron according to the truth record. The ellipse shows a cone of radius $R < 0.6$. The $x - y$ displays are centred on the seed track, showing the distance projected to x or y. All tracks shown are required to satisfy $S_{d0} > 0.9$.

6.2.4 Optimisation

The algorithm outlined above consists of three main stages: the seed selection, track clustering and application of the SVF algorithm to the resulting list of track clusters. Optimising each stage separately is not possible since the optimal configuration of selection criteria for one stage is sensitive to the configuration of the other stages. Thus the full algorithm must be evaluated on sufficient signal and background events for any variation of the seed selection, clustering procedure or SVF configuration. As a consequence, performing a grid scan over discriminating variables quickly becomes very costly in terms of computing resources, even when considering a small subset of the potential track properties and SVF configuration parameters. The dimensionality of the optimisation was reduced using the following procedure:

1. A loose OP, with loose thresholds on track p_{T} and impact parameter significance and a wide cone for the SVF vertex reconstruction, was defined to represent a maximum efficiency.

2. Discriminating variables based on track properties and SVF configuration parameters were individually varied to obtain a set of OPs with decreasing efficiency and fake rate. The efficiency and fake rate are defined as follows:

   - The signal efficiency ϵ_{sig} is defined as fraction of b-hadrons in the range 10-20 GeV that can be matched to a track cluster for which a SV was successfully reconstructed. A cluster is considered matched to a b-hadron if it contains one or more tracks that are truth-matched to it. The efficiency is measured in a sample of events drawn from a sbottom sample with $\Delta m = 20$ GeV.
   - The fake efficiency ϵ_{fake} is determined from $Z \to \nu\nu$ simulation, where events containing a truth b- or c-hadron are vetoed. The fake efficiency is measured as the fraction of events containing a reconstructed SV.

3. The set of increasingly tight OPs for each potential discriminating variable are used to evaluate the area under the ROC curve, AUC. The AUC variable is then used to rank each of the potential discriminating variables, with the best performing five chosen for the final optimisation.

A grid of potential OPs was obtained by scanning over the five chosen discriminating variables. The efficiency to fake rate ratio $R_\epsilon = \epsilon_{\mathrm{sig}}/\epsilon_{\mathrm{fake}}$ was used as the figure-of-merit for this optimisation. To select optimal OPs, this figure-of-merit was evaluated for a set of OPs falling within an efficiency class, defined by an upper and lower threshold on the efficiency of OPs within the class. For example, in the efficiency class 0.26-0.29, only OPs with efficiency measured to be within this range were considered, and the OP with the highest R_ϵ chosen to be optimal for the class. The optimum R_ϵ for a number of efficiency classes is shown in figure 6.9: it diminishes as the efficiency class moves to higher values. This effect can be visualised by factorising the vertex reconstruction efficiency into two of its components: the average multiplicity of track clusters in the event, $\langle N_{\mathrm{clusters}} \rangle$ and the efficiency to reconstruct a SV given a cluster, $\epsilon_{\mathrm{cluster}}$. Both of these quantities can defined for matched clusters and fake clusters. Clusters are considered to be matched if they contain at least one track that is truth-matched to a b-hadron, and fake clusters

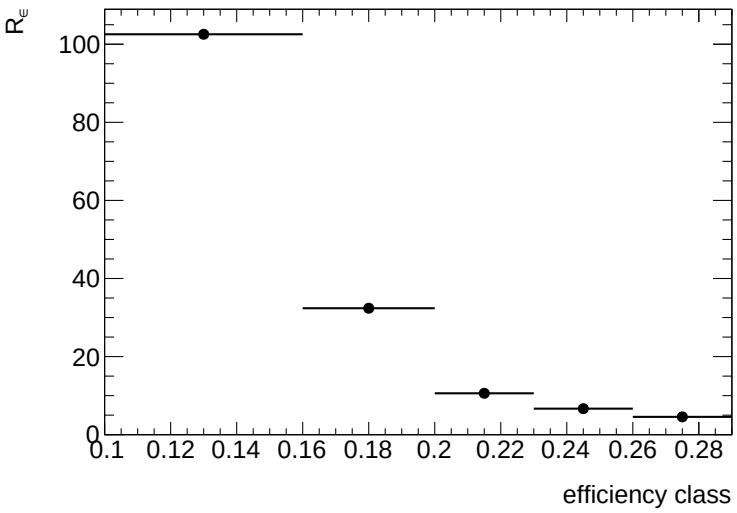

Figure 6.9: Optimal R_ϵ for different efficiency classes. For each efficiency class, the optimal OP is chosen from OPs with a measured efficiency that falls within the range of that class.

	Seed track		Cluster		
Working point	S_{d0}^{seed}	p_{T}	S_{d0}^{cluster}	$\Delta R_{\text{seed}}^{\text{track}}$	$\text{d}_{\text{seed}}^{\text{track}}$
`Loose`	0.5	1.5 GeV	1.5	0.75	0.25 mm
`Tight`	0.9	2 GeV	0.9	0.7	0.6 mm

Table 6.1: Selections applied for loose and tight OPs.

are any that are found in the background sample. Figure 6.10a shows $\langle N_{\text{clusters}} \rangle$ for signal events and $Z \to \nu\nu$ events with a c- or b-veto. As the window defining the efficiency class is moved to higher values, OPs with looser selections on seed and cluster tracks are favoured. This leads to a larger multiplicity of track clusters, with a larger increase for fake clusters. At the same time, as shown in figure 6.10b, the efficiency to reconstruct a SV is roughly constant for matched clusters and rising with the efficiency class for fake clusters. To achieve a higher efficiency requires admitting a large number of additional fake tracks, increasing the probability to reconstruct fake vertices from random crossing of tracks, degrading the performance as measured by R_ϵ. Two OPs were selected for performance studies and SR optimisation. Both are shown in table 6.1. The `Tight` OP falls in the efficiency class 0.20-0.23 and the `Tight` OP falls in the efficiency class 0.16-0.2. Both OPs represent different tradeoffs between efficiency and optimal R_ϵ.

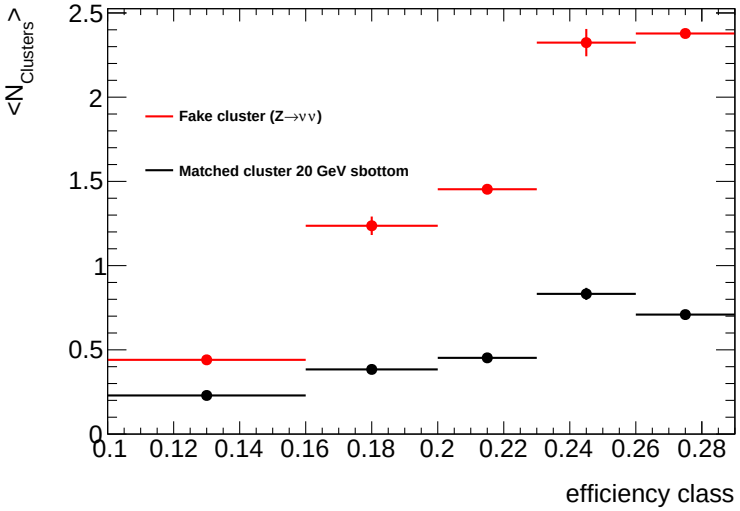

(a)

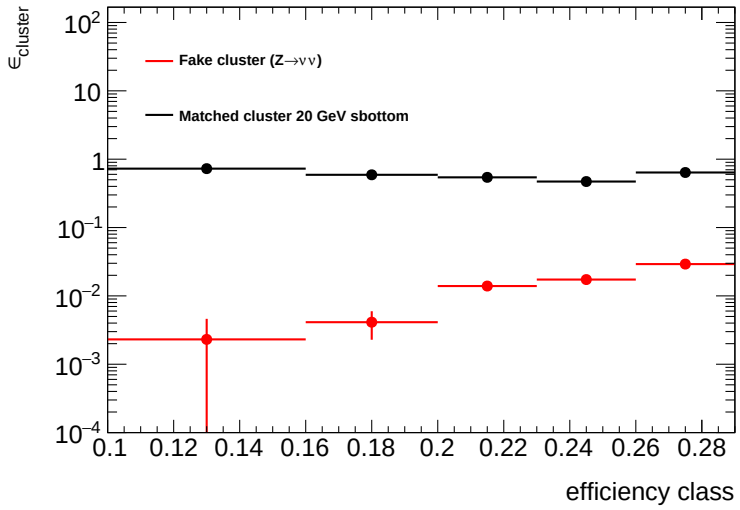

(b)

Figure 6.10: (a) Average cluster multiplicity $\langle N_{\text{clusters}} \rangle$ and (b) efficiency per cluster $\epsilon_{\text{cluster}}$ for different efficiency classes. For each efficiency class $\langle N_{\text{clusters}} \rangle$ and $\epsilon_{\text{cluster}}$ are shown for the OP with the optimal R_ϵ of all OPs with measured efficiency falling within that class.

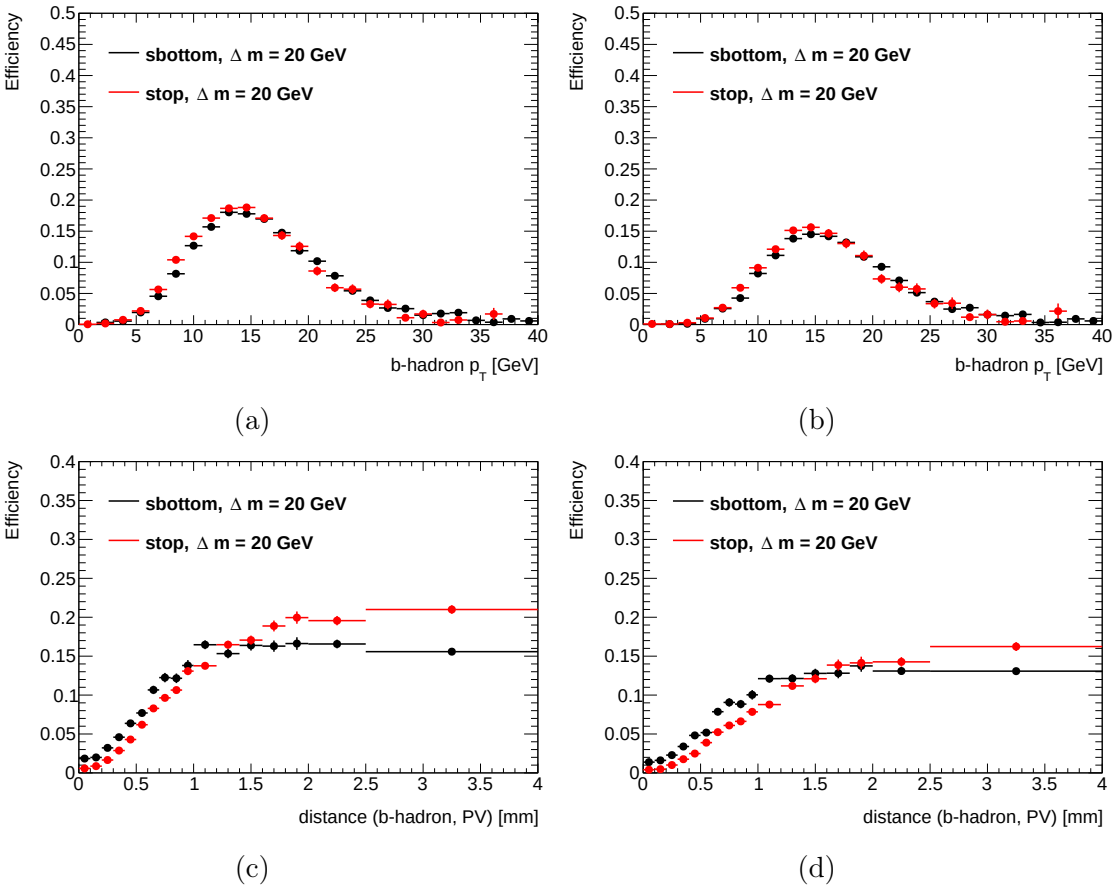

Figure 6.11: Secondary vertex reconstruction efficiency as a function of b-hadron p_{T} for the (a) `Loose` OP and (b) `Tight` OP. The efficiency is also shown as a function of the distance between the truth b-hadron decay vertex and the PV_0 for the (c) `Loose` and (d) `Tight` OPs.

6.2.5 Performance

For measuring the performance of soft b-tagging OPs, the efficiency definition for reconstructed SVs is unchanged, however the truth-matching condition is refined from that used in the optimisation. A b-hadron is considered matched if the angular separation between the line joining the PV_0 and the reconstructed SV and the direction of the truth b-hadron p_{T} is less than 0.3. Figure 6.11 shows the efficiency of the `Tight` and `Loose` working points measured in stop and sbottom decays and parameterised as a function of the b-hadron p_{T} and as a function of the distance from the truth b-hadron decay vertex and the PV_0. The efficiency increases with the truth b-hadron p_{T} until it reaches a maximum. It then starts to diminish as the b-hadron becomes more energetic and thus more likely to be reconstructed as a jet. This is the effect of the veto on tracks associated to jets; as the jet reconstruction threshold is approached, the efficiency deteriorates. The algorithm displays a strong dependence on the distance between the truth b-hadron decay vertex and the PV_0, demonstrating the difficulty of resolving SVs that decay in close proximity to the PV_0.

Figures 6.12a and 6.12b show the efficiency calculated with respect to the number of clusters. The efficiency in this case is defined as the fraction of clusters that

are truth-matched to a b-hadron from a stop or sbottom decay that produce a reconstructed SV after application of the SVF algorithm. As in the previous section, a cluster is defined as matched to a truth b-hadron if it contains one or more tracks that can be truth-matched to the b-hadron with a probability of greater than 0.75. The similarity of the efficiency distributions, which mainly differ only in the statistical uncertainties, demonstrates that gain in efficiency for the `Loose` OP in comparison with the `Tight` OP is due mainly to the multiplicity of clusters in the event, rather than providing higher quality clusters to the SVF algorithm. The fake rate for both OPs is shown in figures 6.12c and 6.12d, drawn from $Z \to \nu\nu$ events with a veto on truth b- and $c-$hadrons. The SVF has a low rate to reconstruct SVs in clusters where no $b-$ or $c-$hadrons are present. The main effect contributing to the fake rate is the multiplicity of clusters, which is mainly influenced by the seed selection, and to a lesser extent the cluster selection, which may in some cases remove tracks until there is only one remaining such that the cluster is removed from the event. The fake rate of the SVF is roughly normalised by the number of clusters in the event, with additional corrections from the track multiplicity within the clusters.

6.2.6 Data / Monte Carlo Comparisons

The algorithm described thus far is capable of identifying low momentum b-hadrons in the p_{T} range 10-20 GeV with efficiency $\sim 15\%$ in simulation, corresponding to a fake rate of $\sim 1.5\%$ for the `Tight` OP. The calibration effort for this OP is ongoing. The intention for this section is to give an outline of the calibration strategy that has been considered so far, which allows a first look at how the soft b-tagging performs in data collected by ATLAS. The objective for this calibration is to determine the efficiency to identify b-hadrons in data, and the rate at which fake SVs are reconstructed. This requires the preparation of a sample rich in b-hadrons that fall within the acceptance of the soft b-tagging algorithm, namely 10-20 GeV b-hadrons that are sufficiently isolated from calorimeter jets. Such a sample can be obtained by applying a selection targeting fully leptonic $t\bar{t}$ events where exactly one b-hadron has been tagged by conventional tagging. The remaining b-hadron is then accessible to soft b-tagging provided it lies in the p_{T} range 10-20 GeV. According to MC simulated $t\bar{t}$ events, this is the case in 20% of $t\bar{t}$ events that pass the selection criteria. The selection criteria used to target fully leptonic $t\bar{t}$ events are shown in table 6.2. After applying this selection, the ratio of the total event yield in data to that predicted by $t\bar{t}$ simulation, using 44.3 fb^{-1} of integrated luminosity, is 1.15. For the purpose of this study, only $t\bar{t}$ simulation is considered and the `Tight` OP defined in table 6.1 is used. Figure 6.13 shows comparisons between data and $t\bar{t}$ simulated events after applying the selection defined in table 6.2 and requiring exactly one `Tight` reconstructed SV. The $t\bar{t}$ is divided into the following categories, based on the angular separation between the line joining the PV_0 to the SV and the truth hadron p_{T}, $\Delta R(\mathrm{SV}, p_{\mathrm{T}})$:

- ***b*-matched:** any SV for which a b-hadron satisfying $\Delta R(\mathrm{SV}, p^b_{\mathrm{T}}) < 0.3$ can be found.
- ***c*-matched:** any SV for which no b-hadron satisfying $\Delta R(\mathrm{SV}, p^b_{\mathrm{T}}) < 0.3$ can be found and at least one c-hadron satisfying $\Delta R(\mathrm{SV}, p^c_{\mathrm{T}}) < 0.3$ can be found.
- **fake:** no $b-$ or $c-$hadron can be found satisfying $\Delta R(\mathrm{SV}, p_{\mathrm{T}}) < 0.3$.

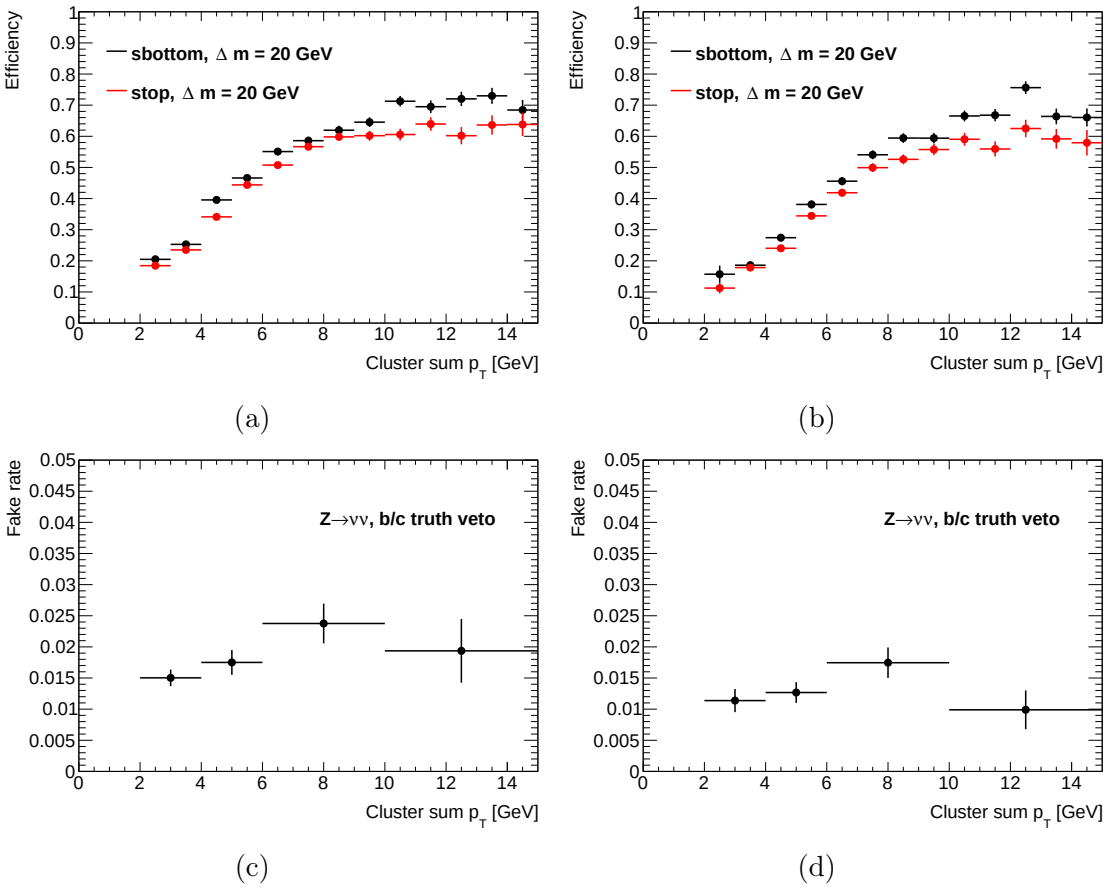

Figure 6.12: Secondary vertex reconstruction efficiency and fake rates measured with respect to track clusters. The efficiency is measured with respect to clusters that contain tracks that can be matched to a truth b-hadron for (a) `Loose` and (b) `Tight` OPs. The fake rate is measured in $Z \to \nu\nu$ simulated events with a veto on any events containing a truth b- or c-hadron. The fake efficiency is the fraction of track clusters that produce a reconstructed SV. The fake rate is shown for (c) `Loose` and (d) `Tight` OPs. In each case the efficiency is shown as a function of the cluster p_{T}, taken to be the p_{T} sum of all tracks in the cluster.

Cut	Selection
Trigger	17 GeV electron + 14 GeV muon
$E_{\mathrm{T}}^{\mathrm{miss}}$ [GeV]	> 30
Jet multiplicity	≥ 2
b-jet multiplicity	1
Electron multiplicity	1
Muon multiplicity	1

Table 6.2: Summary of kinematic selection targeting fully leptonic $t\bar{t}$ events. The leptons are required to have opposite sign.

The contribution from c-hadrons should be small according to the $t\bar{t}$ simulation, with fake SVs tending to lower track multiplicity, p_{T} and mass. The comparison between data and MC clearly suggests that the simulation is underestimating the number of fake SVs, with the disagreement more pronounced in regions of the distributions occupied by fakes in the MC.

Figure 6.14a shows the fraction of reconstructed SVs in $t\bar{t}$ simulation, with the following truth-matching categories, where a truth particle is considered matched if it satisfies $\Delta R(\mathrm{SV}, p_{\mathrm{T}}^{\mathrm{particle}}) < 0.3$:

- ***D*:** any SV for a which no matching b-hadron can be found and at least one matching c-hadron can be found.
- **τ:** any SV for a which no matching $b-$ or c-hadron can be found and at least one matching τ-lepton can be found.
- **K_S^0:** any SV for a which no matching b-, $c-$ or τ is matched, and a matching K_S^0 is found.
- ***K* other:** any SV for a which no matching b-, $c-$ or τ is matched, and a matching K other than a K_S^0 is found.
- **No match:** no truth particle can be found within $\Delta R(\mathrm{SV}, p_{\mathrm{T}}^{\mathrm{particle}}) < 0.3$.

The majority of reconstructed vertices are matched to b-hadrons, with a small contribution from vertices matched to $c-$hadrons and hadronically decaying τ-leptons. The contribution from strange hadrons is also small, demonstrating the effectiveness of the SVF veto on two-track vertices with invariant mass consistent with V_0 decays (see section 4.4.5). The contribution of vertices matched to light flavour hadrons is negligible. The remaining vertices cannot be matched to a truth particle within $\Delta R < 0.3$ and make up the dominant source of non b-matched fakes. Figures 6.14b, 6.14c and 6.14d show the rate at which events are found to contain a fake reconstructed vertex as a function of the multiplicity of tracks satisfying the seed selection criteria, for the `Tight` OP. Figure 6.14b shows the fake rates in $t\bar{t}$ simulation: the efficiency to reconstruct $c-$hadrons and hadronically decaying τ-leptons is roughly independent of the track multiplicity, while the rate to reconstruct non-matched vertices increases with the seed track multiplicity. Figures 6.14c and 6.14d show the fake rates for $Z \to \nu\nu$ with a veto on events containing truth $c-$ or $b-$hadrons, for different p_{T} systems. The non-matched vertex rate in $Z \to \nu\nu$ is approximately linear as a function of the seed track multiplicity. This is consistent with non-matched

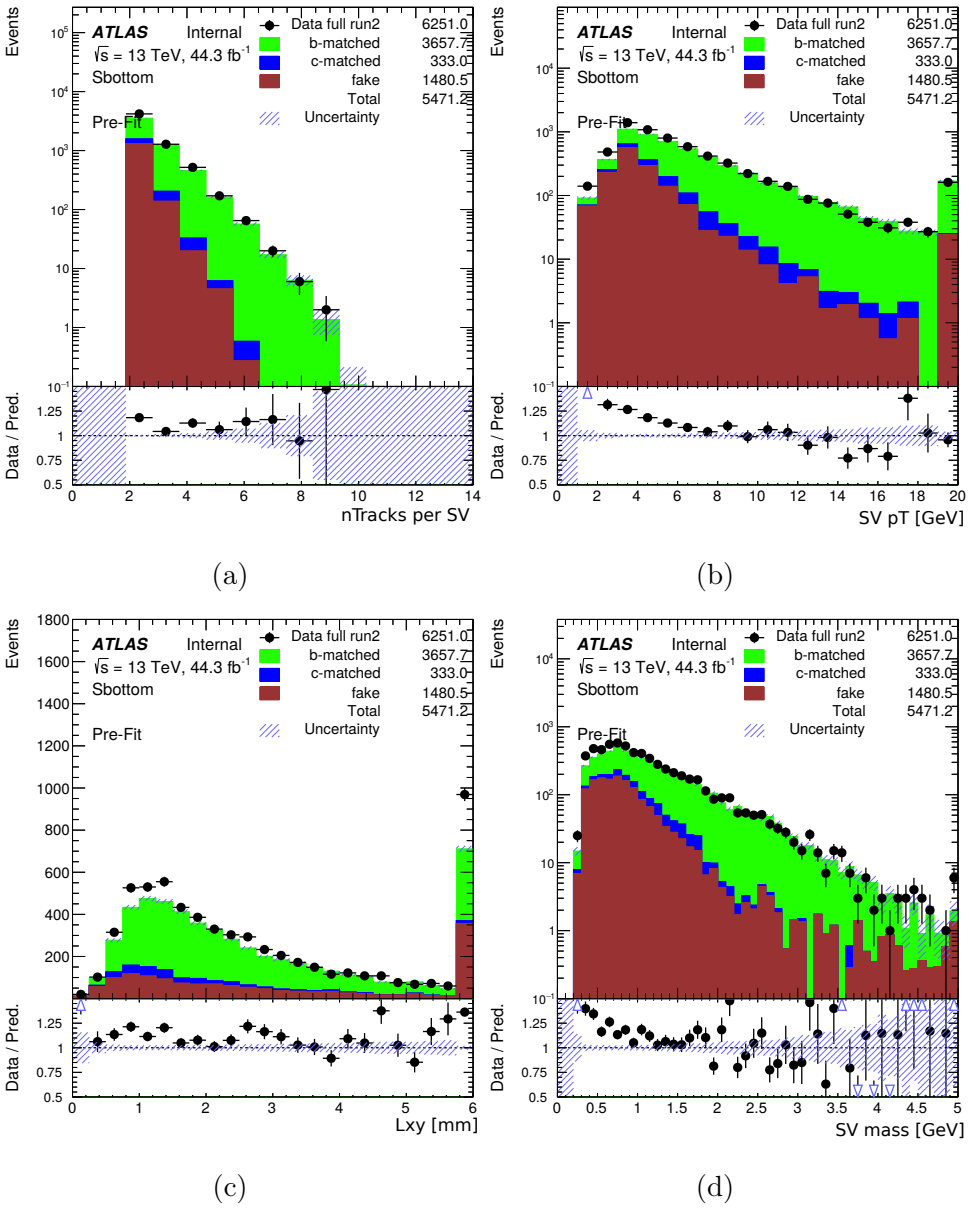

Figure 6.13: Comparison between data and $t\bar{t}$ simulation with one Tight reconstructed SV. The distributions shown are (a) the number of tracks associated to the SV, (b) the p_{T} of the SV, reconstructed from the sum of all its constituent tracks, (c) the distance between the PV_0 and the reconstructed SV, referred to as L_{xy} and (d) the mass of the reconstructed SV, taken from the four-vector sum of the constituent tracks. The $t\bar{t}$ sample is divided into the following categories based on the nature of the reconstructed SV: b-matched, c-matched and fake. The SV is considered matched to a hadron if the line joining the PV_0 and the reconstructed SV and the direction of the truth hadron p_{T} is less than 0.3. The SV is considered to be a fake if it does not match any hadron.

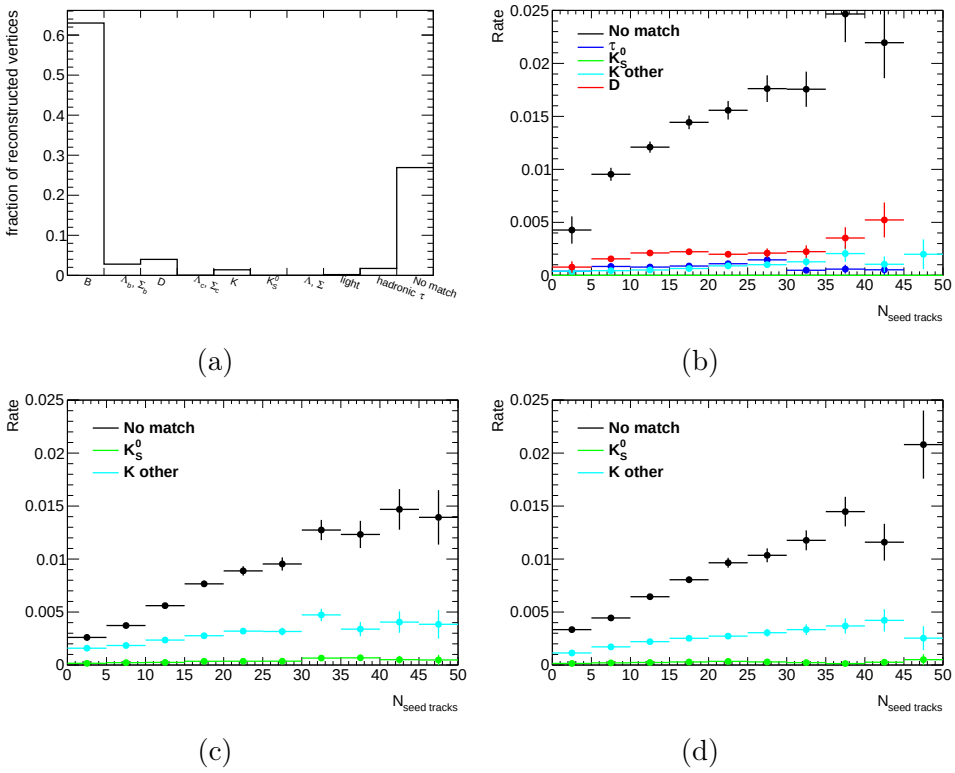

Figure 6.14: (a) Multiplicity for truth-matched SV categories in $t\bar{t}$ simulation. (b) Per event fake rate vs. multiplicity of tracks satisfying the `Tight` OP seed selection for $t\bar{t}$. Per event fake rate in $Z \to \nu\nu$ events with a truth $b-$ and $c-$hadron veto and a requirement of $\max(\sum_i |p_{\mathrm{T}}{}^{\mathrm{truth}}|, p_{\mathrm{T}}{}^{Z,\mathrm{truth}})$, where i runs over all visible objects in the event, to be between (c) 140-280 GeV and (d) 280-500 GeV.

vertices resulting primarily from random crossings of tracks, with an increased rate in $t\bar{t}$ due to contamination from vertices resulting $b-$ and $c-$hadrons that lie further than $\Delta R = 0.3$.

Distributions comparing the properties of vertices are shown for a variety of truth-matching categories in $t\bar{t}$ simulated events in figure 6.15. The only selection applied for these events is a requirement that at least one W decayed leptonically, whilst in figure 6.13, fully leptonic events are selected. The figure shows that combinatoric fakes tend toward a low reconstructed p_{T} and invariant mass, low track multiplicity and low transverse distance from the hard-scatter vertex, with a long tail for the latter. The properties of combinatoric fakes are consistent with the properties of the reconstructed SVs in excess events in data compared to MC simulation in figure 6.13. Taken together, figures 6.13, 6.14 and 6.15 suggest that MC simulation underestimates the multiplicity of combinatoric fakes. This is possibly a result of poor modelling of track multiplicity and S_{d0} in the MC.

6.2.7 Soft b-tagging in Track Jets

The algorithm described thus far represents a novel approach to tagging soft b-hadrons, completely independently of calorimeter jets. The development of this algorithm should be considered as part of a wider soft b-tagging effort at ATLAS, with a variety of methods investigated. The main alternative to soft b-tagging

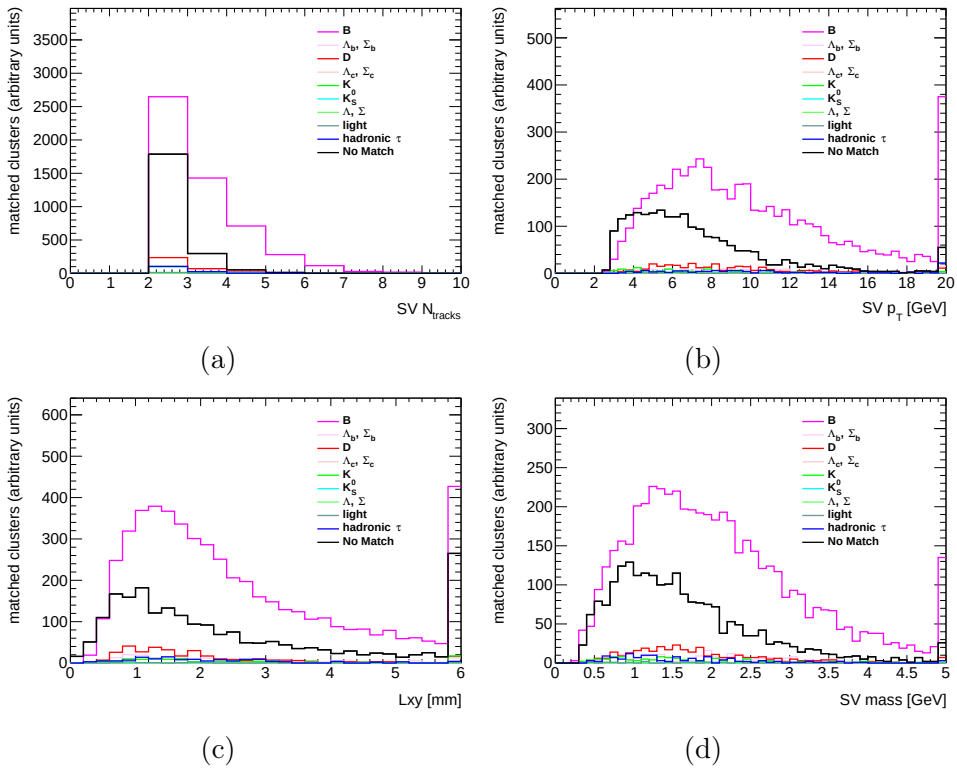

Figure 6.15: (a) Track multiplicity, (b) reconstructed p_{T}, (c) distance between the PV_0 and the SV in mm and (d) the reconstructed mass distributions for truth-matched and non-matched reconstructed vertices in $t\bar{t}$ simulation.

independently of calorimeter jets is to extend to a p_{T} range below the calorimeter jet threshold by instead applying conventional b-tagging to jets reconstructed only from reconstructed tracks in the ID. The performance of soft b-tagging in low momentum track jets is competitive with the clustering approach developed in this chapter. Figure 6.16 shows a comparison of the reconstruction efficiency as a function of truth b-hadron p_{T} for both approaches, using OPs with equivalent fake rates. The two methods display a complementarity, with the vertexing approach effective at targeting b-hadrons in a lower p_{T} range.

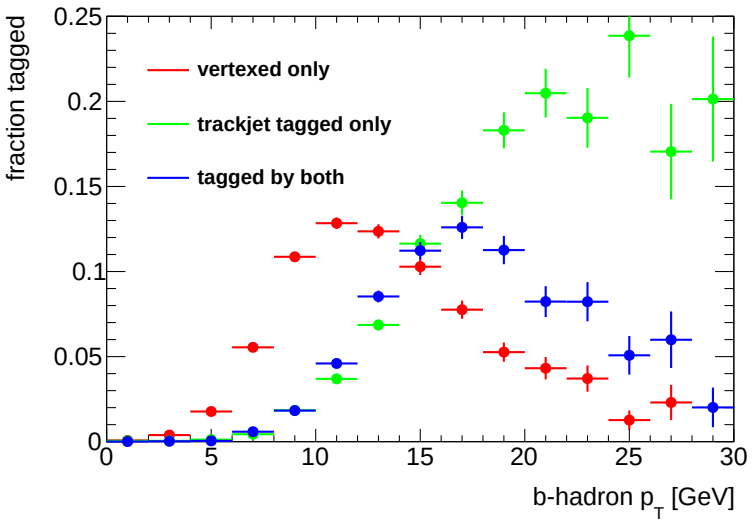

Figure 6.16: Complementarity of soft b-tagging by track clustering and b-tagging in low momentum track jets. Three categories are considered: b-hadrons that are truth-matched to a reconstructed SV only (red), b-hadrons that are truth-matched to a b-tagged track jet only (green) and b-hadrons that are truth-matched to both a reconstructed SV and b-tagged track jet. For each of these categories the fraction of b-hadrons that satisfy the categorised criterion is shown. The OPs are chosen such that the fake rate is roughly equivalent, corresponding to a per event fake rate of 2% in $Z \to \nu\nu$ events with a veto on $b-$ and $c-$hadrons.

6.3 Summary and Outlook

Soft b-tagging by track clustering represents a new approach to tagging b-hadrons, previously not used by ATLAS. The algorithm has evolved, from research and development to full deployment within the ATLAS software framework. As demonstrated in figure 6.16, this method allows b-hadrons to be recovered that were previously inaccessible to conventional b-tagging methods. At the time of writing, the calibration effort for this tagger is ongoing, with the key aim to derive scale factors to correct for mis-modelling of the b-hadron tagging efficiency and combinatorial fake rate.

Parallel to this effort, new SRs are being developed, making use of soft b-tagging to target compressed sbottom and stop four-body models in zero- and one-b-tagged jet bins. Table 6.3 shows preliminary results for SRs designed to target compressed sbottom signals with $\Delta m = 20$ GeV. The table shows the expected sensitivity, based on simulation, for the current SRs used by ATLAS to target compressed sbottom signals [228], based on a 2 b-tagged jet requirement. The table also shows the expected sensitivity of SRs requiring 1 or 0 b-tagged jets, with an additional requirement of at least one reconstructed SV. These additional SRs are constructed by scanning over the same kinematic variables used for the 2 b-tagged jet analysis to find the optimal configuration in 0 or 1 b-tagged jet cases. Using soft b-tagging, one can easily design SRs with sensitivity equivalent to those that are restricted to conventional b-tagging.

The potential utility of soft b-tagging is not restricted to compressed SUSY models; any signal that results in very low momentum b-hadrons could benefit.

	2 b-jets	1 b-jet, > 0 SV	0 b-jets, > 0 SV	Combined
$m(\tilde{b}_1, \tilde{\chi}_1^0) = (400, 380)$	8.32	4.32	1.79	9.54
$m(\tilde{b}_1, \tilde{\chi}_1^0) = (500, 480)$	3.34	2.16	0.76	4.05
$m(\tilde{b}_1, \tilde{\chi}_1^0) = (600, 580)$	1.85	1.86	0.43	2.66

Table 6.3: Expected sensitivity for soft b-tagging SRs. The sensitivity is quoted in terms of the significance Z, described in section 5.10.2. The expected sensitivity is given for three benchmark compressed sbottom signal models, each with $\Delta m = 20$ GeV. The combined sensitivity is calculated as the sum in quadrature of each of the contributing SRs.

The performance may improve with further optimisation, and it may be possible to target low momentum c-hadrons and distinguish them from b-hadrons, expanding the reach of the search presented in chapter 5. To conclude, the analysis presented in this chapter outlines a novel technique that enables events with b-hadrons that would previously have been lost, to be identified.

7 | Conclusion

This thesis has presented a search for direct production of SUSY in final states with $E_{\mathrm{T}}^{\mathrm{miss}}$, zero leptons and c-jets. No significant excess of events above the SM expectation was observed, so exclusion limits were placed on the mass of the squark and LSP, significantly extending those placed by Run 1 searches. This analysis is sensitive to both stop and scharm production in the context of R-parity conserving SUSY. The limits placed in the $(\tilde{t}_1, \tilde{\chi}_1^0)$ mass plane provide important coverage in the mass region $\Delta m < m_W + m_b$ as part of the wider ATLAS third generation SUSY search effort. The search for direct scharm production is the only dedicated ATLAS search for this signal, with stringent limits placed in the $(\tilde{c}_1, \tilde{\chi}_1^0)$ mass plane. This thesis has emphasised the importance of considering these searches in the context of the wider ATLAS and CMS SUSY search effort, as well as indirect SUSY limits. The results of this analysis represent one further null result amongst dozens. As TeV-level SUSY becomes increasingly disfavoured by LHC data, its tantalising promise as a solution to the Hierarchy problem (and others) of particle physics moves further into the distance. Two main possibilities remain for SUSY to be a realistic description of nature; either it is a symmetry too broken to solve the problems that motivate searches for it, or it lies in regions of the parameter space that are difficult to probe, inaccessible to LHC detectors or that so far no-one has thought to look.

The possibility remains that SUSY is a true description of nature, with evidence for a signal in ATLAS data missed due to limitations in reconstruction algorithms. It is therefore important to squeeze as much coverage from existing data as possible. This motivates the second main analysis of this thesis, the development a new algorithm for identifying low p_{T} b-hadrons. This algorithm successfully reconstructs b-hadrons with competitive performance. It has been developed to target by compressed SUSY models, with promising projected sensitivity gains for benchmark signal models. It also has potential applications in any search for, or measurement of, processes with soft b-hadrons in the final state. This algorithm has further potential to be optimised to target low momentum c-hadrons, potentially extending the coverage of SUSY searches to final states with $E_{\mathrm{T}}^{\mathrm{miss}}$ and charm quarks into more compressed regions of the parameter space.

The end of Run 2 of the LHC is an interesting time for particle physics. On the one hand, it has confirmed the SM as a complete theoretical framework to describe particles and their interactions up the TeV scale. On the other hand it leaves many experimental observations unexplained, and, for those to whom aesthetics are important, it has an unsatisfying requirement for the fine tuning of parameters. This points to "new physics" beyond the SM at a higher energy scale. It was hoped that the LHC would reveal new physics beyond the SM. Unfortunately this appears not to be so. Perhaps Run 3 of the LHC will provide the hint of new physics that many had hoped for, perhaps this hint lies at a higher scale, requiring an even larger Collider than the LHC. Whichever is the case, the particle physics community will find a way to keep looking.

A | Electron Trigger Efficiency Measurements

The author of this thesis made a significant contribution to the ATLAS electron and photon (e/γ) trigger group between 2015 and 2018. The primary contribution, described in this appendix, was the measurement of electron trigger efficiencies in data and MC simulation, for ongoing validation of the trigger performance during data taking and to derive scale factors to correct for mis-modelling of electron trigger efficiencies in simulation. The measurements that result from this work were used by most contemporaneous ATLAS analyses, and contribute directly to Refs. [3, 4].

A.1 Electron Trigger Menu in Run 2

The ATLAS electron trigger sequence is described in section 4.2.1, along with the evolution of the lowest unprescaled single electron trigger from 2015 to 2016, when the data was collected for the main analysis presented in chapter 5. The work detailed in this appendix concerns the single electron trigger and also the di-electron, multi-electron and combined electron triggers for data taking in 2015, 2016 and 2017. Table A.1 shows the unprescaled electron triggers used by ATLAS for data in 2015-2017, using the following nomenclature:

- **HLT_NeX:** indicates a high-level-trigger chain, followed by the number N of electrons required by the chain, satisfying a lower threshold on the transverse energy of X GeV. For combined triggers e may be replaced by mu to indicate that a muon is required.
- **lhvloose, lhloose, lhmedium, lhtight:** the *lh* indicates that a likelihood-based identification was used (a cut-based selection was used for Run 1 electron triggers). This is followed by a description of the cut on the *lh* discriminant, for example *vloose*, or "very" loose, is the loosest requirement, with each tighter category selecting a subset of the sample of the previous category.
- **nod0:** indicates that no cut was applied on the transverse impact parameter. This is the baseline for all triggers post-2015.
- **ivarloose:** indicates that track-based isolation requirements are applied for the chain.
- **Combined triggers:** joined by an underscore _ for a logical AND requirement and joined by OR to indicate a logical OR requirement between the chains.

The time evolution of the electron trigger menu reflects the need to tighten trigger selections in response to higher instantaneous luminosity and harsher pileup conditions, whilst introducing modifications to the selection criteria to improve background rejection. In 2016, transverse impact parameter based requirements were

2015	
single electron	HLT_e24_lhmedium_OR_HLT_e60_lhmedium_OR_e120_lhloose
di-electron	HLT_2e12_lhloose
multi-electron	HLT_e17_lhloose_2e9_lhloose
combined trigger	HLT_e17_lhloose_mu14 HLT_e7_lhloose_mu24 HLT_2e12_lhloose_mu10 HLT_e12_lhloose_2mu10
2016	
single electron	HLT_e26_lhtight_nod0_ivarloose_OR_ HLT_e60_lhmedium_nod0_OR_e140_lhloose_nod0
di-electron	HLT_2e17_lhvloose_nod0
multi-electron	HLT_e17_lhloose_nod0_2e9_lhloose_nod0
combined trigger	HLT_e17_lhloose_nod0_mu14 HLT_e24_lhmedium_nod0_mu8 HLT_e12_lhloose_nod0_2mu10 HLT_2e12_lhloose_nod0_mu10
2017	
single electron	HLT_e26_lhtight_nod0_ivarloose_OR_ HLT_e60_lhmedium_nod0_OR_e140_lhloose_nod0
di-electron	HLT_2e17_lhvloose_nod0 HLT_2e24_lhvloose_nod0
multi-electron	HLT_e24_lhvloose_nod0_2e12_lhvloose_nod0
combined trigger	HLT_e26_lhmedium_nod0_mu8 HLT_e7_lhmedium_nod0_mu24 HLT_e12_lhloose_nod0_2mu10 HLT_2e12_lhloose_nod0_mu10 HLT_e17_lhloose_mu14

Table A.1: Electron trigger menu for data taking in 2015-2017.

removed. These variables are found to improve the offline selection, but were found to introduce inefficiencies in the online selection due to poor resolution. Another change post-2015 was the introduction of isolation requirements at L1 and HLT for improved background rejection and rate reduction.

In 2017, an upgrade was introduced for the fast calorimeter selection, the *ringer* algorithm [233]. The ringer algorithm explores the conic geometry of the electron shower shape, building successive rings in the calorimeter. These are used to build a vector of discriminating variables, which are fed into a neural network classifier. The ringer algorithm performs electron identification with a significant reduction to the number of calls to the tracking system, which is typically expensive in terms of computing time. The ringer algorithm also improves background rejection for an equivalent efficiency by a factor of two, allowing the trigger thresholds to be kept as low as possible.

A.2 Electron Efficiency Measurements

The main objective for this work was to measure the efficiency ϵ_{trig} for each of the electron trigger chains shown in table A.1 with respect to offline electron identification and isolation OPs. The electron trigger efficiency is important for any SM measurement or new physics search that requires electrons in a SR or CR since it contributes to the total electron efficiency needed to determine the predicted yield. The total electron efficiency ϵ_{total} can be factorised as

$$\begin{aligned}\epsilon_{\text{total}} &= \epsilon_{\text{EMclus}} \times \epsilon_{\text{reco}} \times \epsilon_{\text{ID}} \times \epsilon_{\text{iso}} \times \epsilon_{\text{trig}} \\ &= \left(\frac{N_{\text{cluster}}}{N_{\text{all}}}\right) \times \left(\frac{N_{\text{reco}}}{N_{\text{cluster}}}\right) \times \left(\frac{N_{\text{id}}}{N_{\text{reco}}}\right) \times \left(\frac{N_{\text{iso}}}{N_{\text{id}}}\right) \times \left(\frac{N_{\text{trig}}}{N_{\text{iso}}}\right).\end{aligned} \tag{A.1}$$

The first factor ϵ_{EMclus} is the fraction of prompt electrons that produce candidate EM clusters in the calorimeter system, given by the ratio of the total number of electrons N_{all} to the number of EM clusters N_{cluster}. This factor is determined purely from MC by matching reconstructed clusters to electrons produced at generator level. The second factor ϵ_{reco} is the efficiency to reconstruct an electron candidate, given an EM cluster. The third factor ϵ_{id} is the fraction of electron candidates associated to true electrons that then satisfy the identification criteria. The fourth factor is the efficiency with which identified electrons pass the isolation requirements. Finally, the fifth factor is the electron trigger efficiency with respect to this requirement, the subject of this study. It is given by the ratio of the number of electrons that satisfy the isolation requirements N_{iso} to the number of electrons satisfying the online trigger selection N_{trig}. In some cases, no isolation requirement is applied, and the electron trigger efficiency is instead measured as $\frac{N_{\text{trig}}}{N_{\text{id}}}$.

To measure the electron trigger efficiency in data, a clean, unbiased sample of electrons must first be obtained. This is achieved by using the *tag-and-probe* method to select electrons from $Z \to ee$ decays. The data sample is selected by the lowest unprescaled electron trigger corresponding to the year of data taking, as shown in table A.1. $Z \to ee$ events are selected by requiring two electrons with opposite sign. The first electron, the *tag*, is required to pass strict selection criteria, enumerated below:

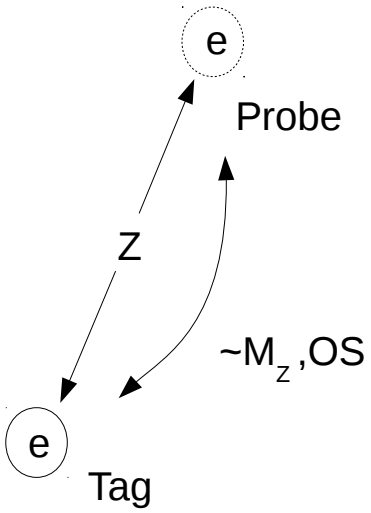

Figure A.1: Illustration of the tag-and-probe method using $Z \to ee$ electrons. The probe electron is matched to the tag electron if the invariant mass of the di-electron system is close to the Z mass, M_Z, and if it has opposite sign (OS).

- **Trigger-matching:** the tag must be matched to the online object that fired the single electron trigger, based on angular separation.
- **Transverse energy:** the tag must meet the minimum E_{T} threshold of 25 GeV in 2015 data and 27 GeV in 2016 and 2017 data. This ensures a constant trigger efficiency with respect to the offline electron identification OP.
- **Offline identification:** the tag is required to satisfy offline selection criteria. The analysis is repeated for three different offline OPs for the tag identification: `Tight`, `Tight` with isolation and `Medium` with isolation. These systematic variations for this analysis choice are later used to determine systematic uncertainties on the efficiency.

If a tag can be identified in the event, the second electron is identified as the probe electron if the invariant mass of the di-electron system is sufficiently close to the mass of the Z, M_Z. The analysis is repeated for three Z mass windows: $[80, 100]$ GeV, $[75, 105]$ GeV and $[70, 110]$ GeV, for the evaluation of the systematic uncertainty on the efficiency measurement. The tag-and-probe method is illustrated in figure A.1. The probe electron is then required to have $E_{\mathrm{T}} > 4$ GeV and to satisfy an offline identification and isolation OP combination. The quantity ϵ_{trig} can then be evaluated as:

$$\epsilon_{\mathrm{trig}} = \left(\frac{N_{\mathrm{trig}}}{N_{\mathrm{iso}}} \right). \tag{A.2}$$

The denominator is simply all probes passing the offline identification + isolation OP and the numerator has the additional requirement to have fired the electron trigger to be measured. The efficiency is measured for all trigger + offline identification +

isolation combinations. In total, this amounts to approximately 500 combinations for each year to be measured.

For multi-object triggers, the efficiency for each of the individual triggers that make up the combined trigger is measured separately. Multi-object triggers tend to have lower acquisition rates than single-object triggers and as a result can often be operated at lower thresholds. The single-object components of these triggers cannot be unprescaled due to the cost in terms of rate increase. The efficiency for prescaled triggers is computed by running the trigger algorithm for all events during data taking, but not allowing the trigger to record an event. The data can then be reprocessed to obtain the trigger decision in events selected by other triggers.

The efficiency measurements for an unprescaled single electron trigger and the double electron trigger in 2017 data are shown in figure A.2. The agreement between data and MC simulation is good, with the largest discrepancies in the trigger turn-on curve and in the crack region ($1.37 < |\eta| < 1.5$) and end-caps. The efficiency suffers in the crack region, where there is a significant amount of material servicing the detector. The crack region is typically vetoed at analysis-level. The efficiency is robust as a function of pileup, with a slightly increased dependence for the isolated trigger, as expected.

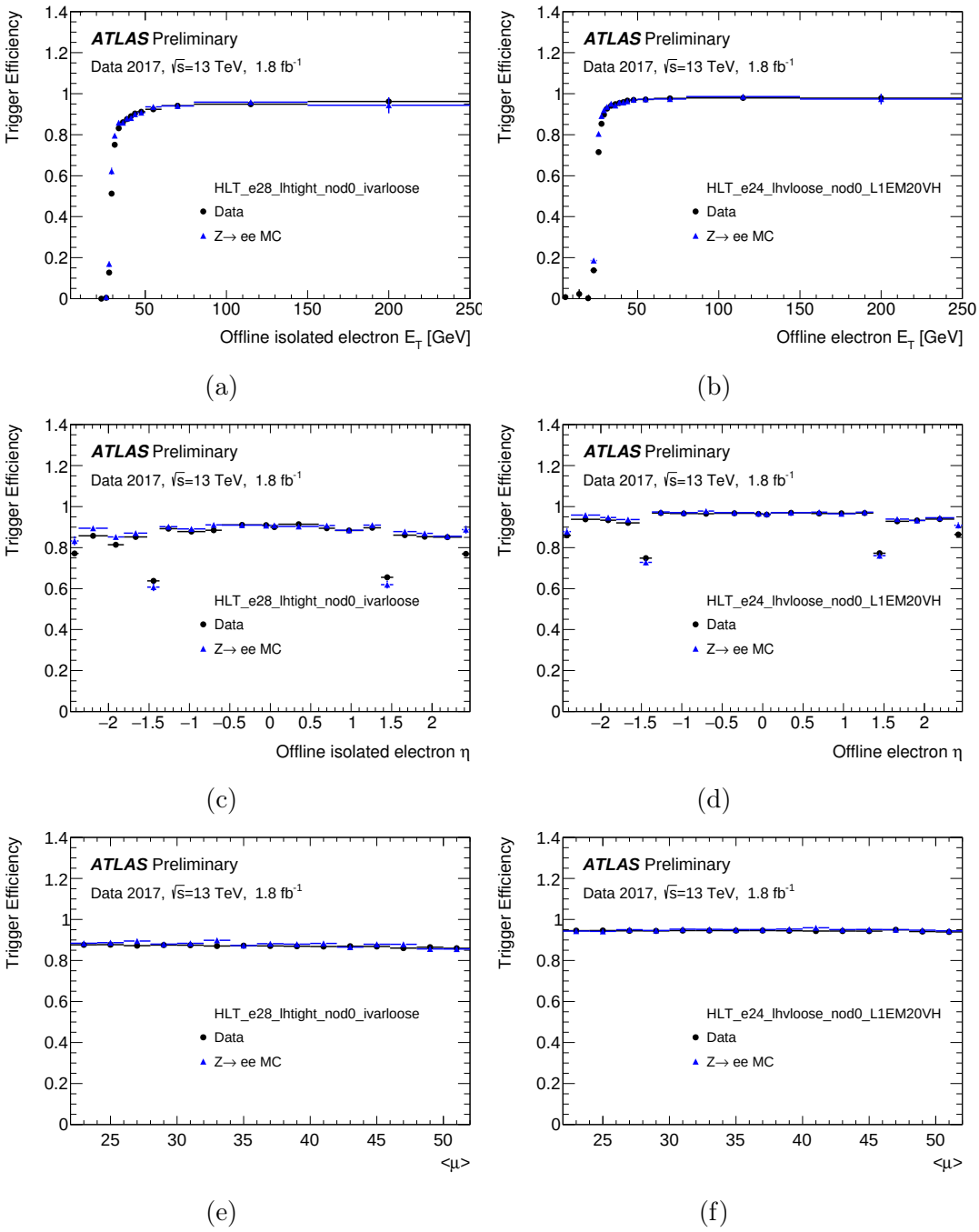

Figure A.2: Electron efficiencies in 2017 data. The left-hand plots show the trigger efficiency for HLT_e28_lhtight_nod0_ivarloose and the right-hand plots show the trigger efficiency for HLT_e24_lhvloose_nod0. In the top row, the efficiency is shown as a function of E_{T}. In the middle row, the efficiency is shown as a function of η, requiring E_{T} to be greater than the trigger threshold plus 1 GeV. In the bottom row, the efficiency is shown as a function of the number of interactions per bunch crossing, with the same requirement on E_{T} as for the plots in the middle row. The efficiency for each plot is measured with respect to the same offline identification level and isolation requirement as the trigger shown. No background subtraction is applied for these plots. The error bars show binomial uncertainties.

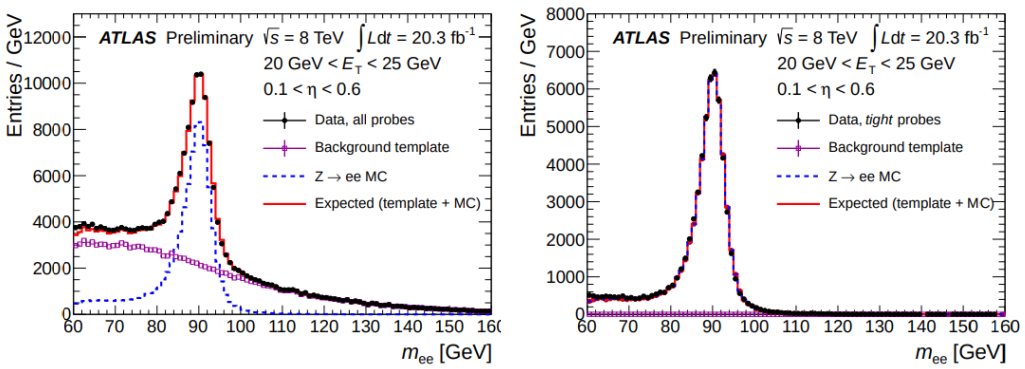

(a) (b)

Figure A.3: Invariant mass distribution for di-electron system in data. The distribution is shown in the 20 GeV $< E_{\mathrm{T}} <$ 25 GeV, $0.1 < \eta < 0.6$ bin, (a) for EM clusters reconstructed as electrons with a matching track and (b) satisfying the `Tight` offline OP. The $Z \to ee$ simulation is scaled to match the total estimated in the Z mass window. Images taken from Ref. [234].

A.2.1 Background Estimation

The background contribution is subtracted from the efficiency measurement using a background template. Probes for the background template are chosen by selecting EM clusters reconstructed as electrons with matching tracks and inverting the offline identification and isolation requirements. The probe selection for the template was optimised to minimise biases due to inversion of the selection and contamination from signal electrons. The contribution of signal electrons was estimated from MC simulation.

The background is normalised using the sideband region $m_{ee} \in [120, 250]$ GeV. The same template is used for the shape estimate in the numerator and denominator, but for the numerator, where contamination from signal electrons is important, the normalisation is determined using same-sign electrons. The invariant mass distribution for the probes is shown in data in figure A.3. The template used for the background subtraction is varied in order to determine the associated systematic uncertainty.

A.2.2 Scale Factor Corrections

The efficiencies are calculated in $Z \to ee$ simulation and in data, with the background subtracted. The ratio of the efficiency in data to the efficiency in MC is used to obtain scale factors, which are the applied to correct for the mis-modelling of the efficiency in MC simulation. The scale factors are calculated for $E_{\mathrm{T}} \times \eta$ bins, using the central value of the efficiency in data and MC, taken as the arithmetic mean of all of the systematic variations in the background template, tag identification OP and Z mass window. The statistical uncertainty is taken as the arithmetic mean of the statistical uncertainty for each systematic variation. The correlation in the statistical uncertainty for each variation is expected to be large, so each is treated as fully correlated. The systematic uncertainty on the efficiency is taken as the standard deviation of the variations with respect to the arithmetic mean. Figure A.4 shows the scale factors derived for the single electron trigger and the di-electron

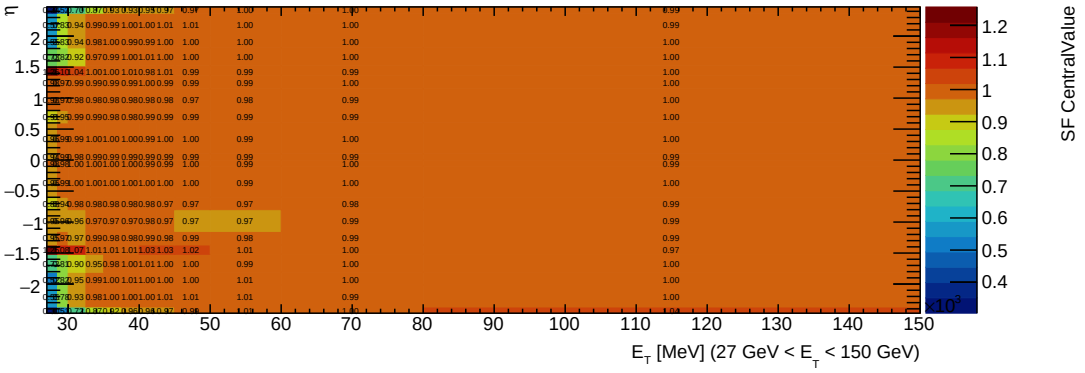

(a)

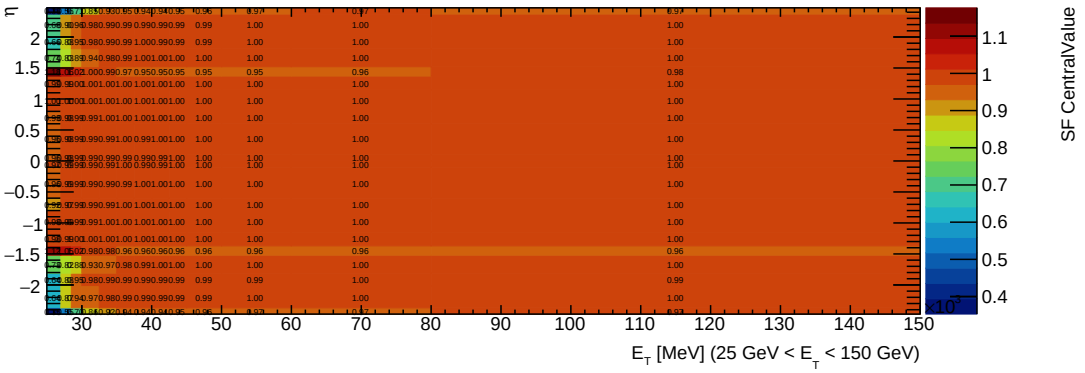

(b)

Figure A.4: 2D scale factor map showing scale factor corrections binned by E_{T} and η for (a) the primary single electron trigger and (b) the single object component of the di-electron trigger, measured in 2017 data. The total uncertainty on the scale factor for each bin is < 0.01 except in the crack region and end-caps, where it is < 0.03. Background subtraction is applied for all plots. The efficiencies used in the derivation of the scale factors are measured with respect to the offline identification and isolation OP that correspond to the measured trigger.

trigger measured in 2017 data. Excluding the crack region and the end-caps, the scale factors are close to unity in most bins, with a total relative uncertainty of $< 1\%$ of the measured value.

A.3 Summary

In this appendix the methodology for electron trigger measurements has been outlined. These measurements represent a significant portion of the author's contribution to the ATLAS collaboration. The scale factor corrections derived in this work were distributed throughout the collaboration for application at analysis level for any measurement or search that makes use of electrons. The measurement of electron trigger efficiencies is also an important part of the ongoing validation of the detector operation and new software releases.

B | Additional Plots

B.1 N-1 Plots

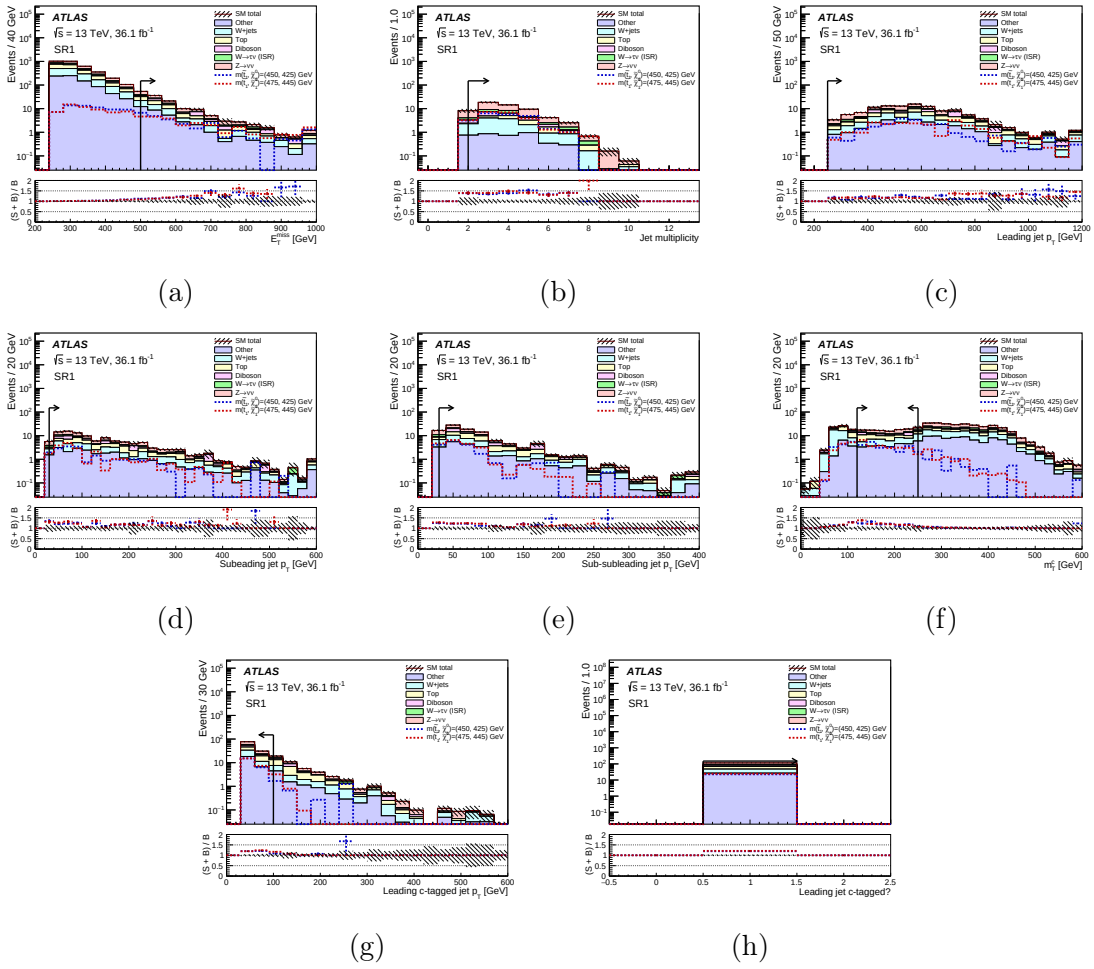

(a) (b) (c)

(d) (e) (f)

(g) (h)

Figure B.1: N-1 plots for **SR1**. Distributions for kinematic variables with the applied cut on that variable removed. An arrow is painted over each distribution to show the value of the cut. In the lower panel the ratio of the sum of the signal and background to the background, $(S + B)/B$ is shown for each signal model. Only statistical uncertainties are shown.

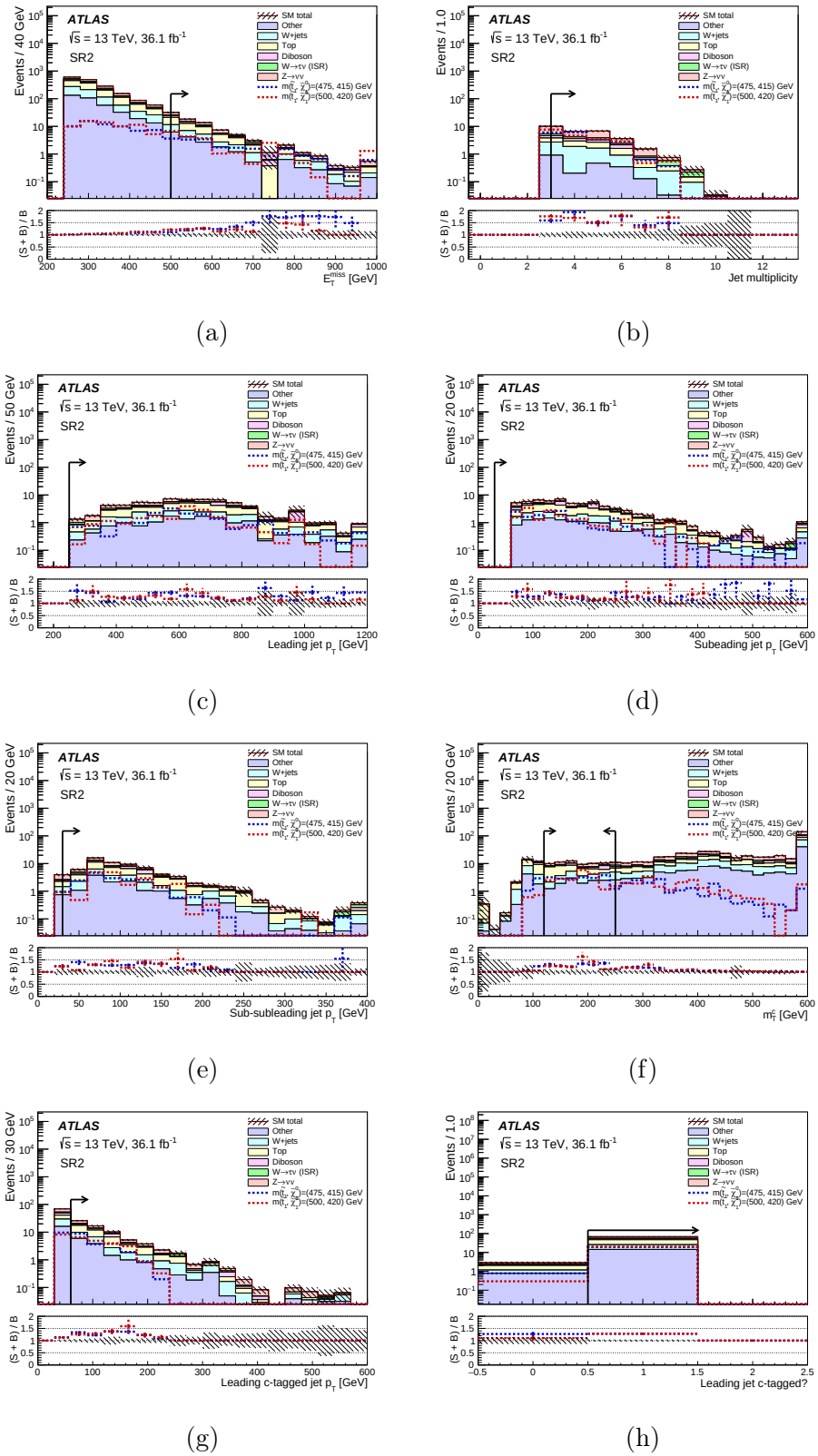

Figure B.2: N-1 plots for **SR2**. Distributions for kinematic variables with the applied cut on that variable removed. An arrow is painted over each distribution to show the value of the cut. In the lower panel the ratio of the sum of the signal and background to the background, $(S + B)/B$ is shown for each signal model. Only statistical uncertainties are shown.

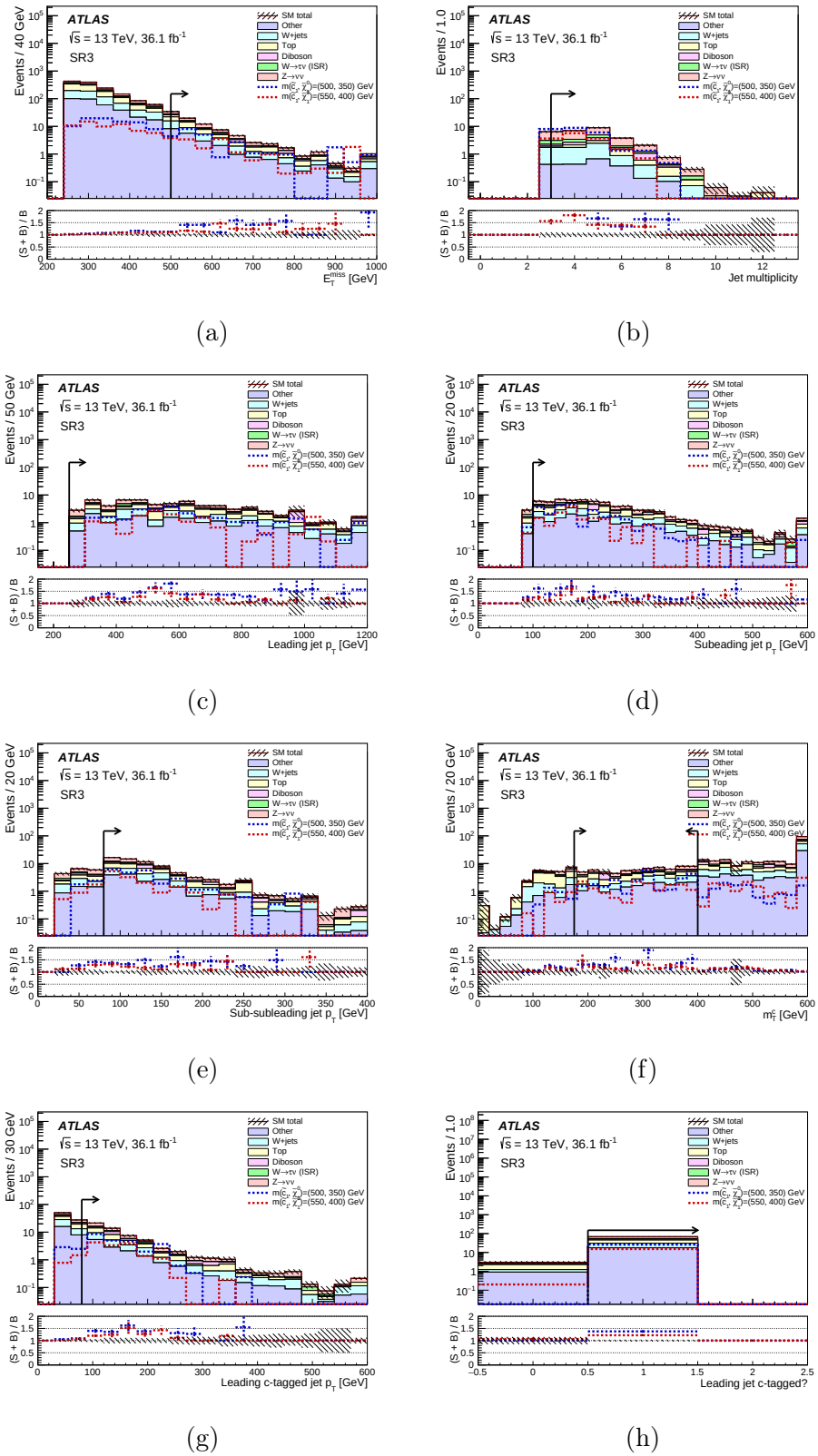

Figure B.3: N-1 plots for **SR3**. Distributions for kinematic variables with the applied cut on that variable removed. An arrow is painted over each distribution to show the value of the cut. In the lower panel the ratio of the sum of the signal and background to the background, $(S + B)/B$ is shown for each signal model. Only statistical uncertainties are shown.

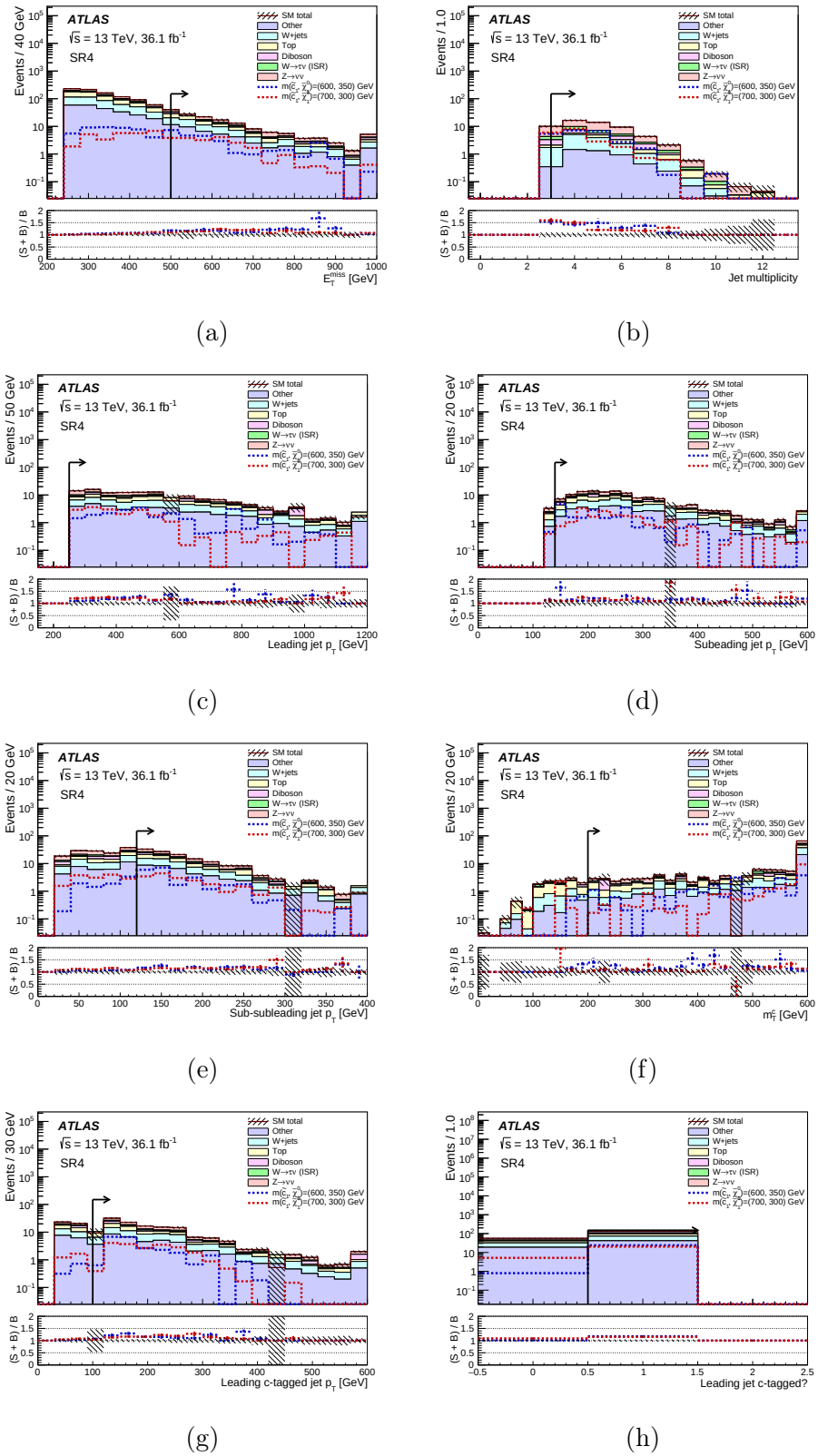

Figure B.4: N-1 plots for **SR4**. Distributions for kinematic variables with the applied cut on that variable removed. An arrow is painted over each distribution to show the value of the cut. In the lower panel the ratio of the sum of the signal and background to the background, $(S + B)/B$ is shown for each signal model. Only statistical uncertainties are shown.

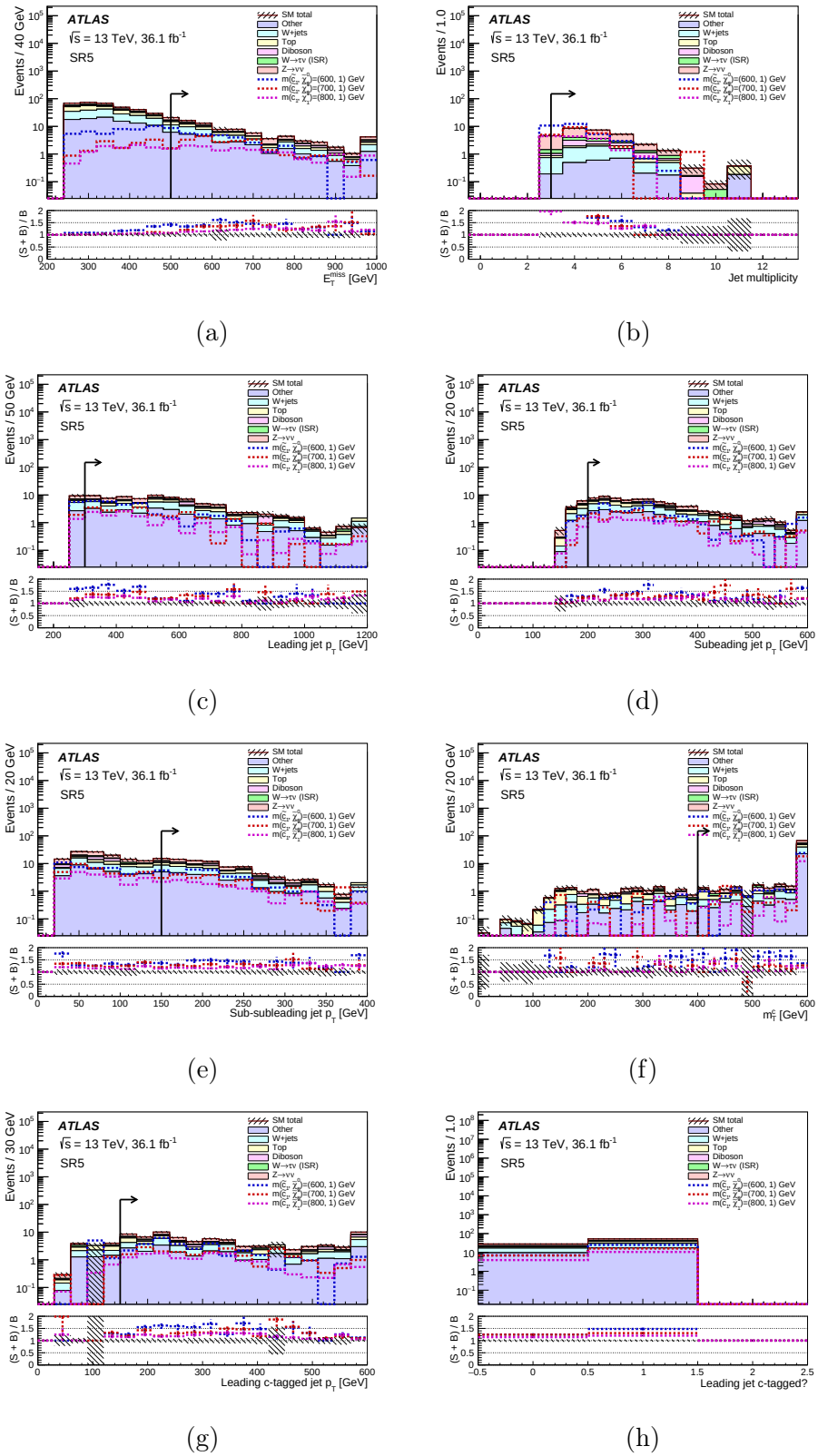

Figure B.5: N-1 plots for **SR5**. Distributions for kinematic variables with the applied cut on that variable removed. An arrow is painted over each distribution to show the value of the cut. In the lower panel the ratio of the sum of the signal and background to the background, $(S + B)/B$ is shown for each signal model. Only statistical uncertainties are shown.

B.2 Signal Region Compositions

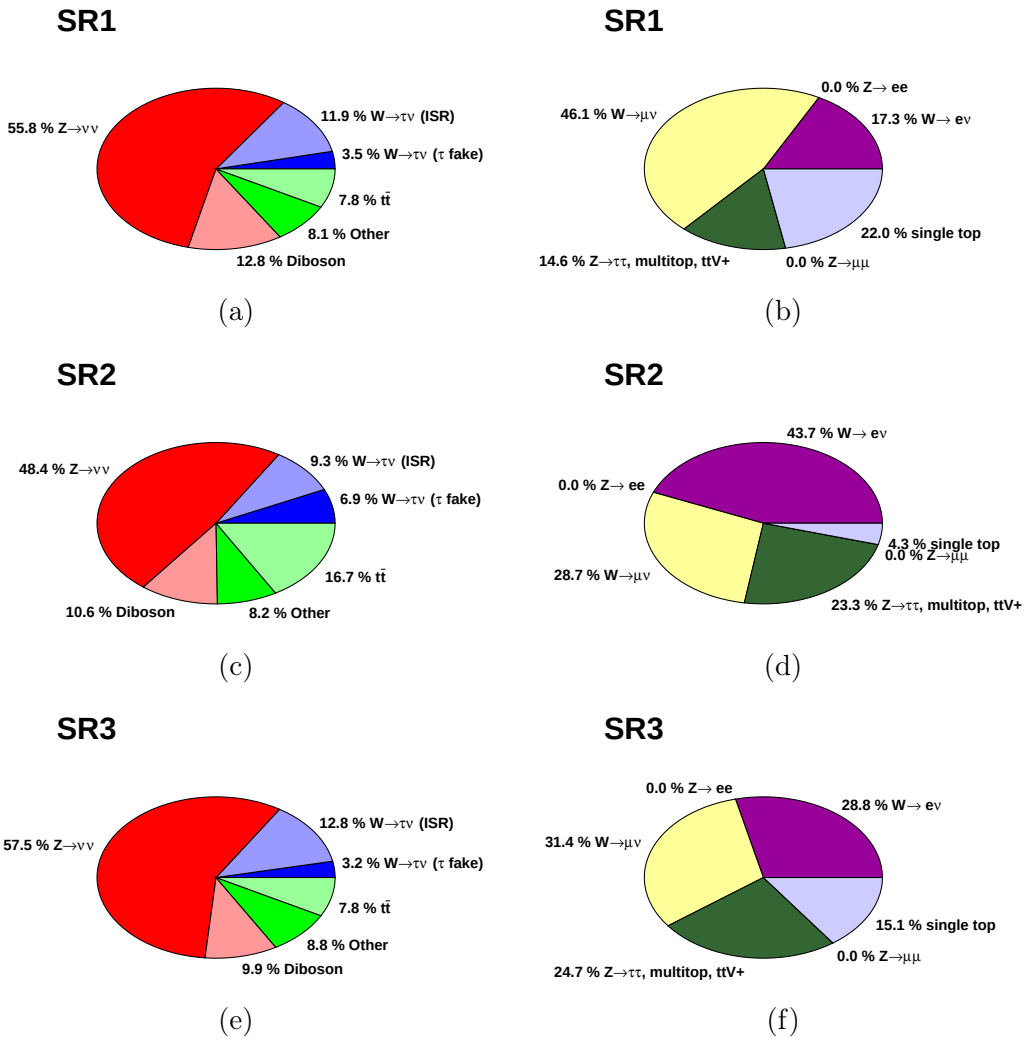

Figure B.6: Breakdown of SM contributions to the total background after the **SR** selections (left). The "other" category includes backgrounds that make up less than 5% of the total. The remaining components are shown in the right-hand plots, where $ttV+$ refers to top quark pair production in association with one or more weak bosons.

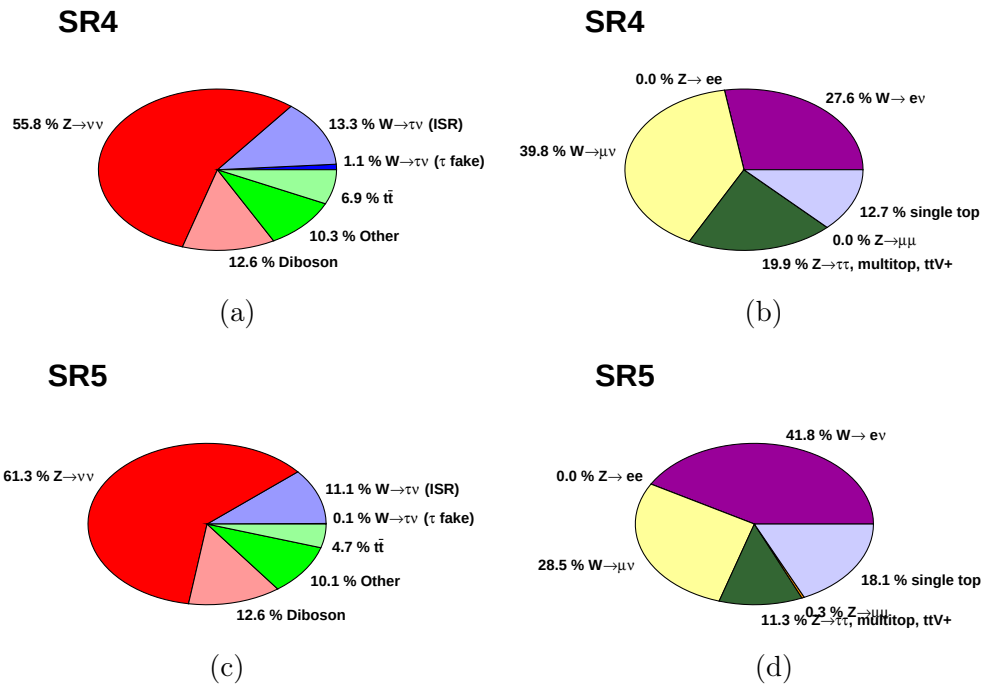

Figure B.7: Breakdown of SM contributions to the total background after the **SR** selections (left). The "other" category includes backgrounds that make up less than 5% of the total. The remaining components are shown in the right-hand plots, where $ttV+$ refers to top quark pair production in association with one or more weak bosons.

B.3 Z+jets Control Region Compositions

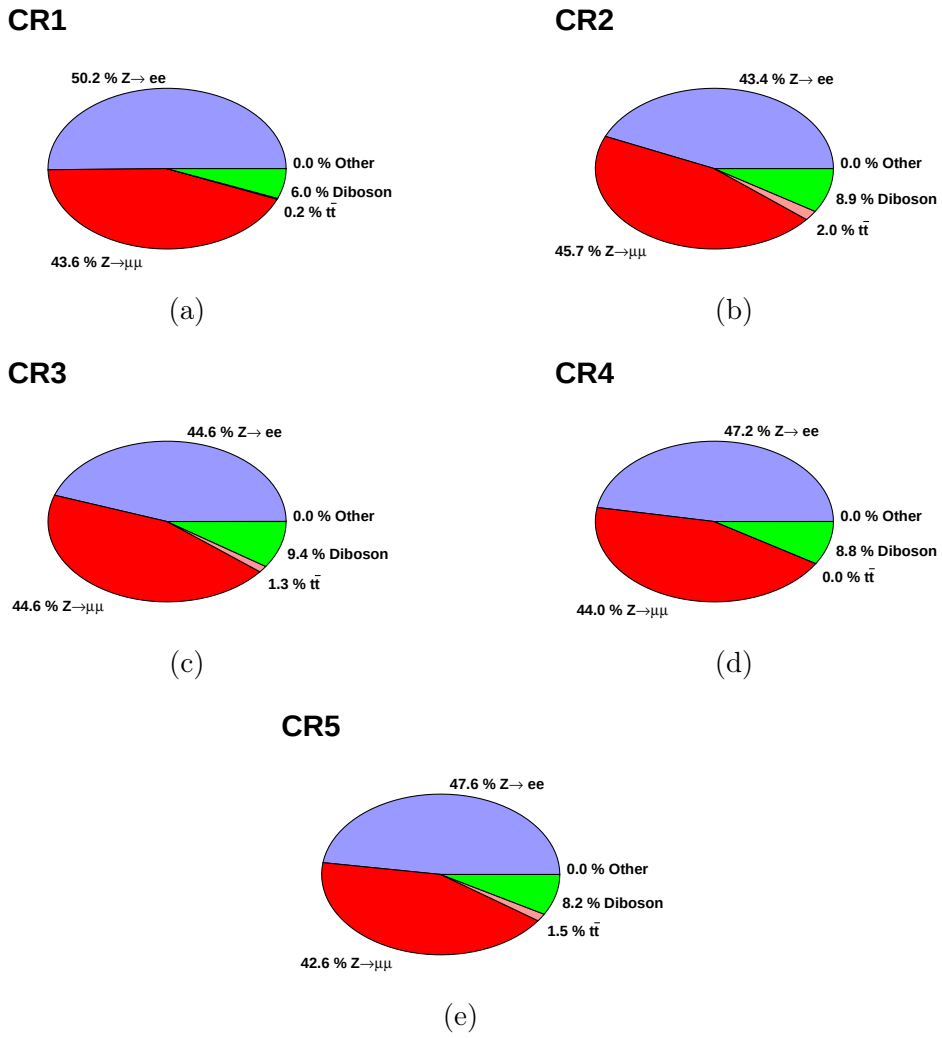

Figure B.8: Breakdown of SM contributions to the total background after the **CR** selections (left). The "other" category includes backgrounds that make up less than 5% of the total.

B.4 Z+jets Control Region and Signal Region Comparisons

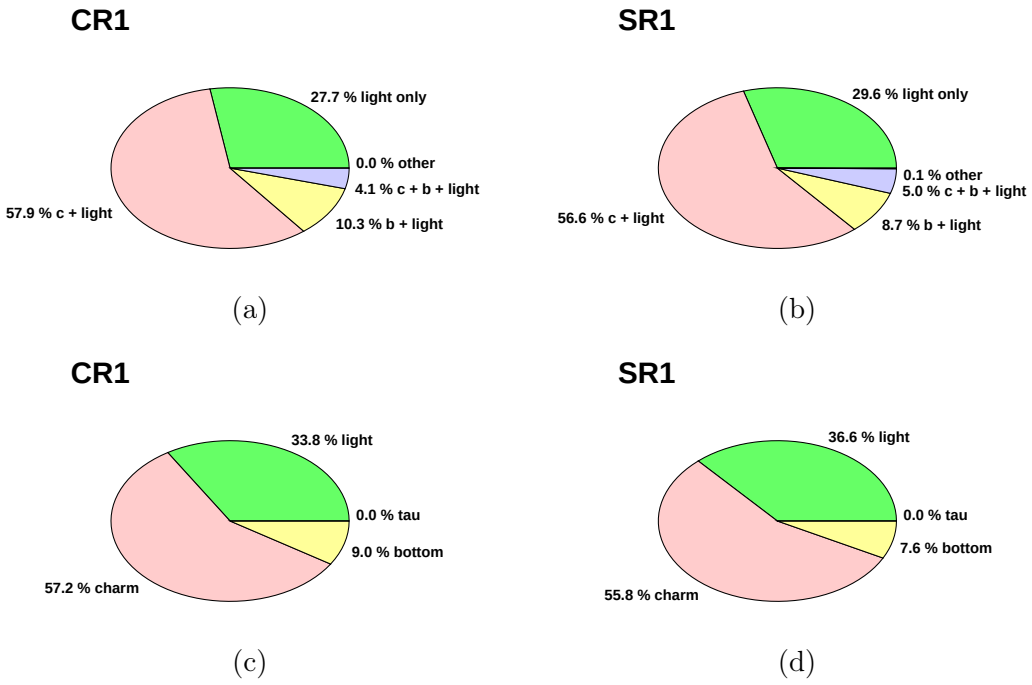

(a) (b)

(c) (d)

Figure B.9: (a) Flavour composition for **CR1 Z** and (b) $Z \to \nu\nu$ in its corresponding SR. (c) Flavour composition of the leading charm tagged jet for **CR1 Z** and (d) for $Z \to \nu\nu$ in its corresponding SR.

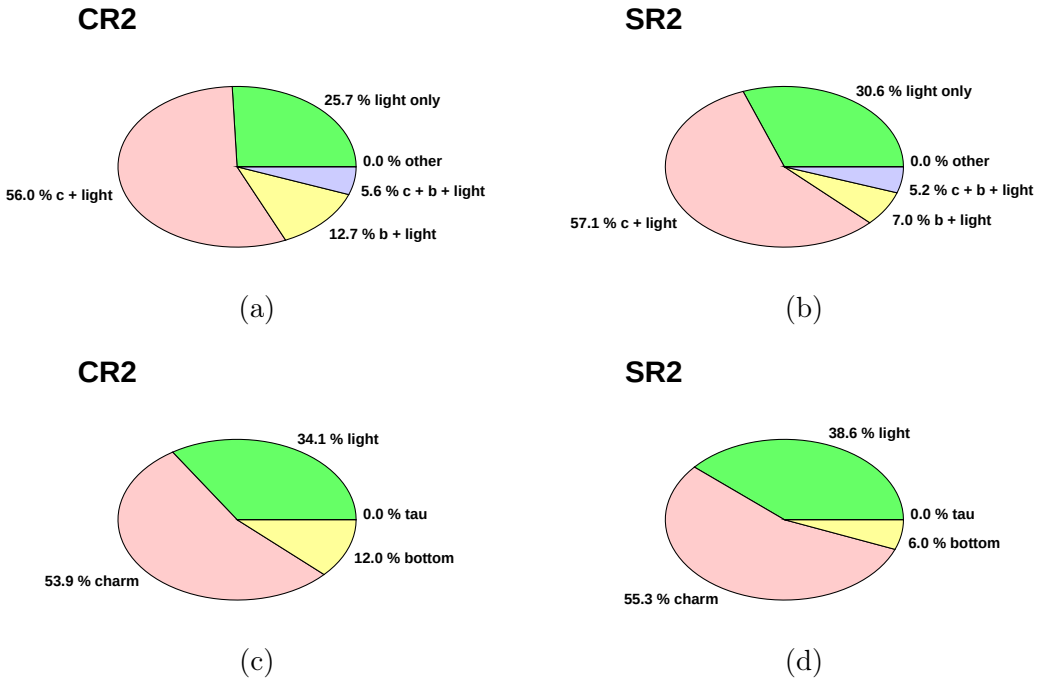

Figure B.10: (a) Flavour composition for **CR2 Z** and (b) $Z \to \nu\nu$ in its corresponding SR. (c) Flavour composition of the leading charm tagged jet for **CR2 Z** and (d) for $Z \to \nu\nu$ in its corresponding SR.

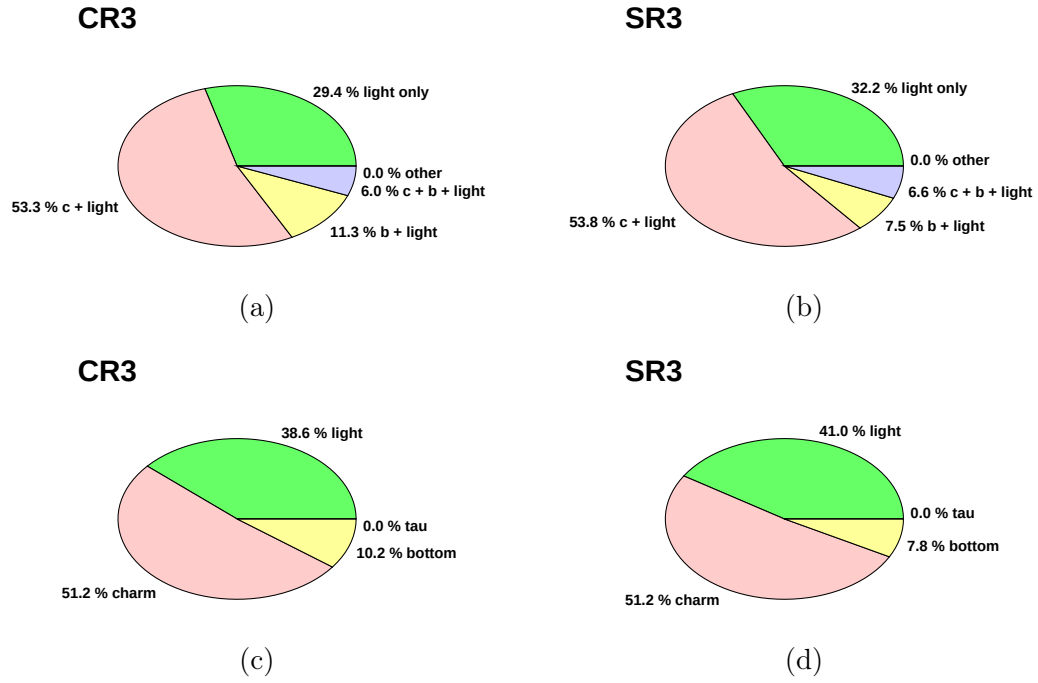

Figure B.11: (a) Flavour composition for **CR3 Z** and (b) $Z \to \nu\nu$ in its corresponding SR. (c) Flavour composition of the leading charm tagged jet for **CR3 Z** and (d) for $Z \to \nu\nu$ in its corresponding SR.

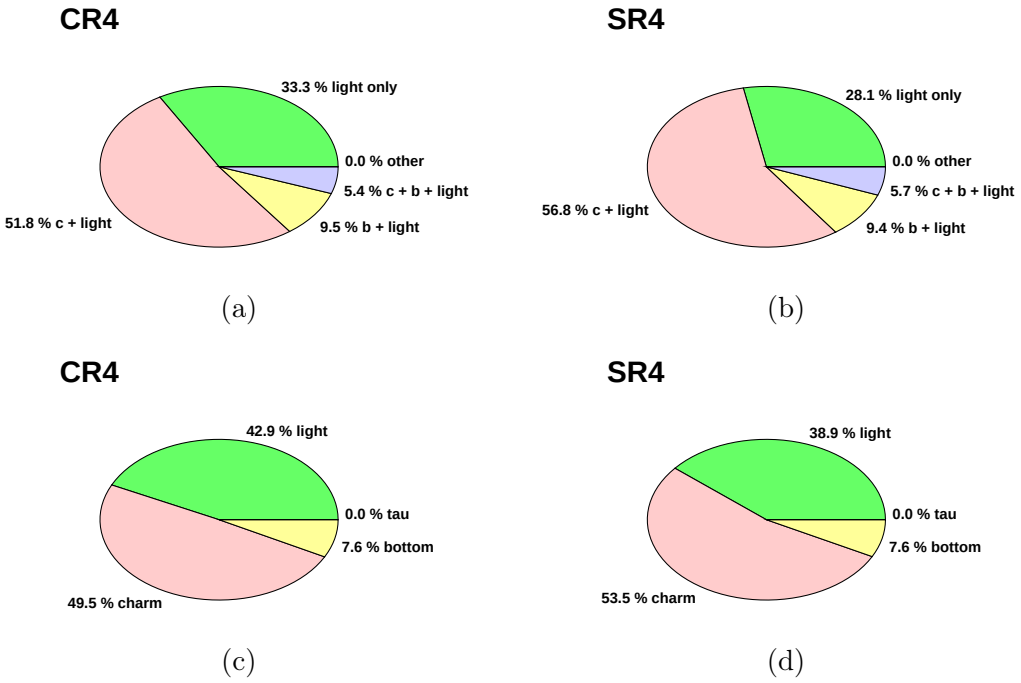

(a) (b)

(c) (d)

Figure B.12: (a) Flavour composition for **CR4 Z** and (b) $Z \to \nu\nu$ in its corresponding SR. (c) Flavour composition of the leading charm tagged jet for **CR4 Z** and (d) for $Z \to \nu\nu$ in its corresponding SR.

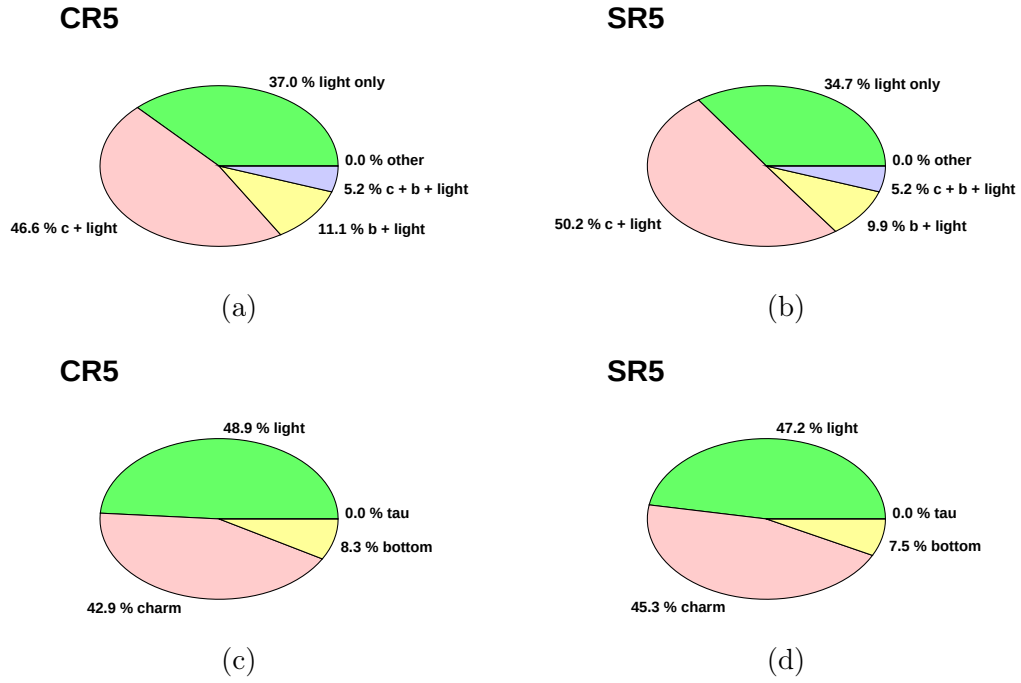

(a) (b)

(c) (d)

Figure B.13: (a) Flavour composition for **CR5 Z** and (b) $Z \to \nu\nu$ in its corresponding SR. (c) Flavour composition of the leading charm tagged jet for **CR5 Z** and (d) for $Z \to \nu\nu$ in its corresponding SR.

B.5 W+jets Control Region Compositions

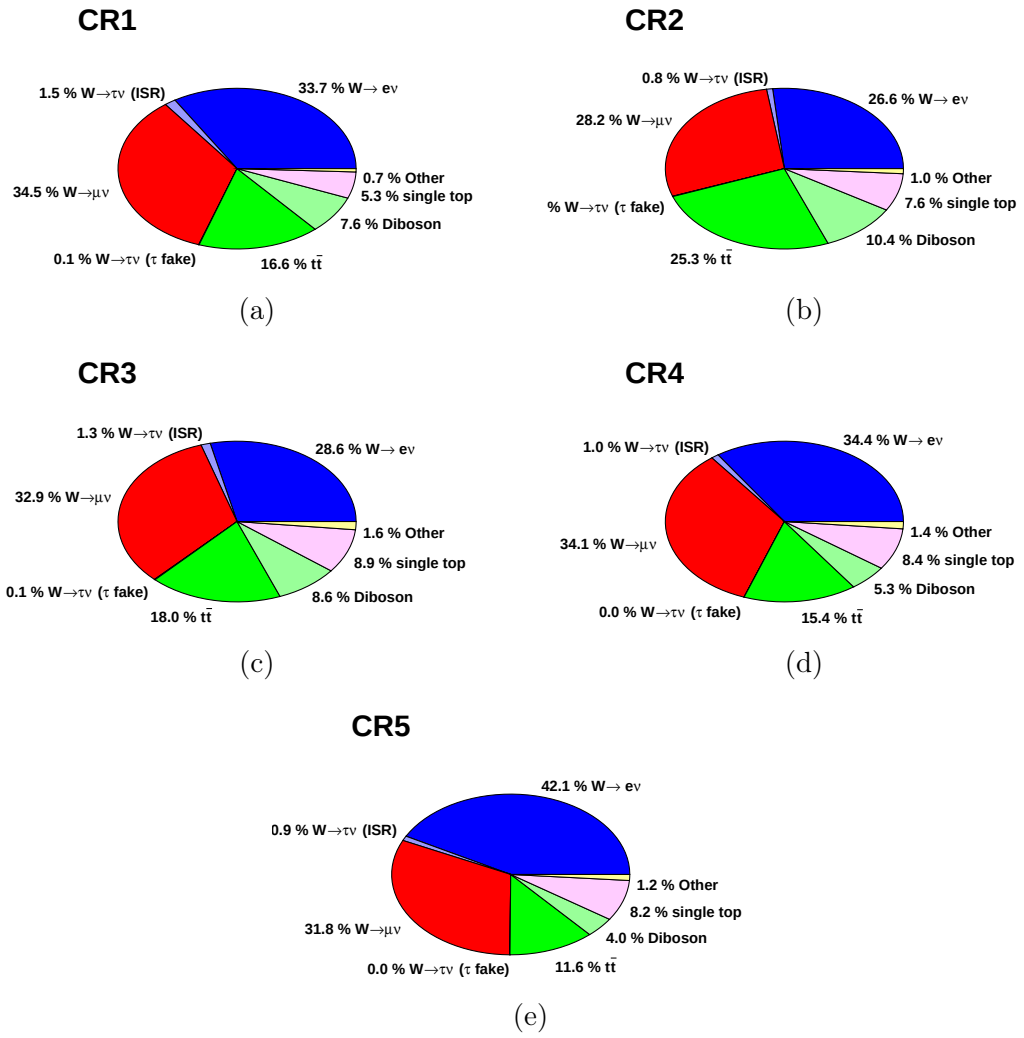

Figure B.14: Breakdown of SM contributions to the total background after the **CR** selections (left). The "other" category includes backgrounds that make up less than 5% of the total.

B.6 W+jets Control Region and Signal Region Comparisons

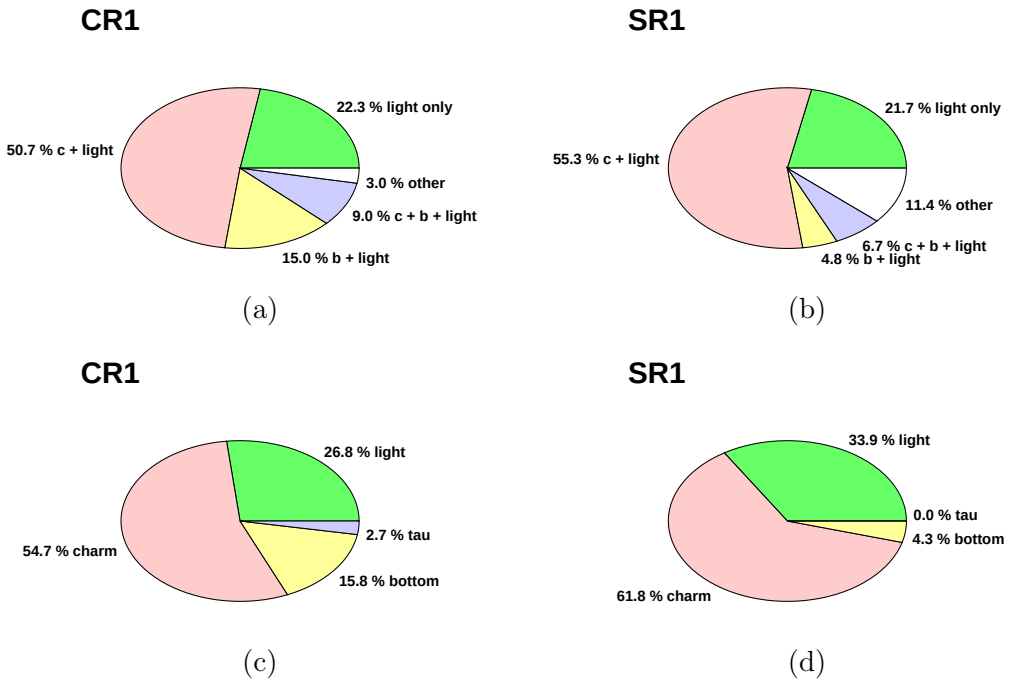

(a) (b)

(c) (d)

Figure B.15: (a) Flavour composition for **CR1 W** and (b) W+jets in its corresponding SR. (c) Flavour composition of the leading charm tagged jet for **CR1 W** and (d) for W+jets in its corresponding SR.

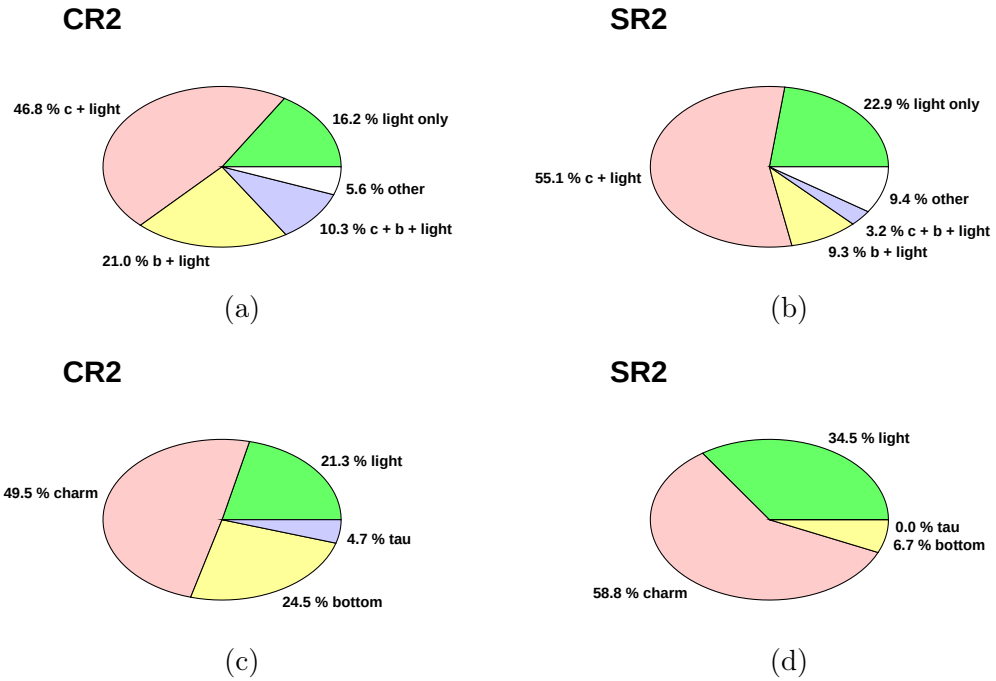

Figure B.16: (a) Flavour composition for **CR2 W** and (b) W+jets in its corresponding SR. (c) Flavour composition of the leading charm tagged jet for **CR2 W** and (d) for W+jets in its corresponding SR.

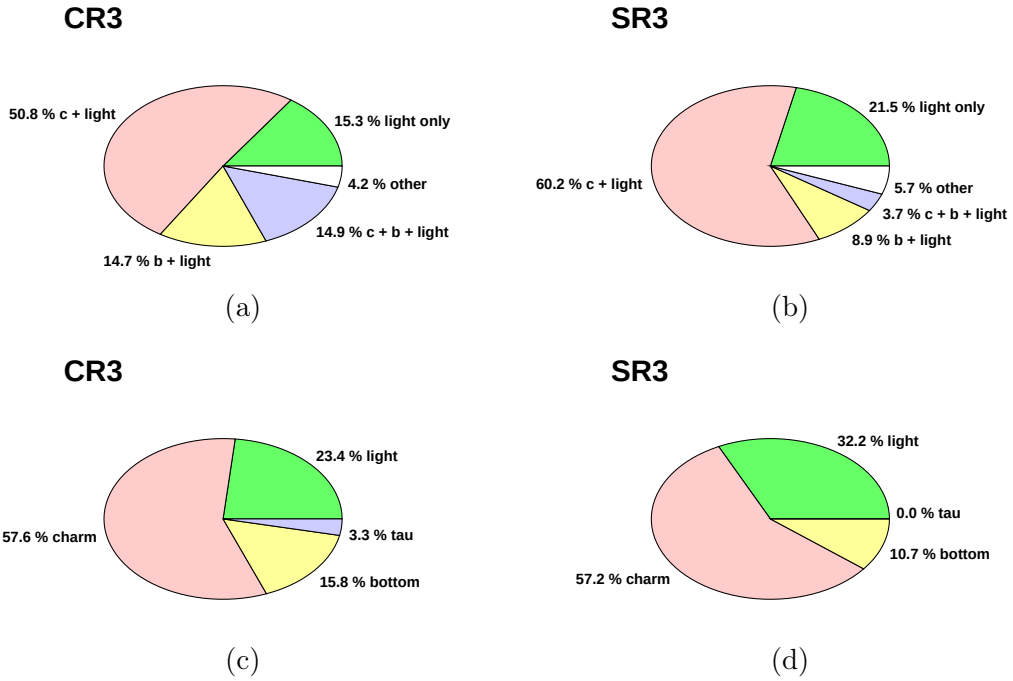

Figure B.17: (a) Flavour composition for **CR3 W** and (b) W+jets in its corresponding SR. (c) Flavour composition of the leading charm tagged jet for **CR3 W** and (d) for W+jets in its corresponding SR.

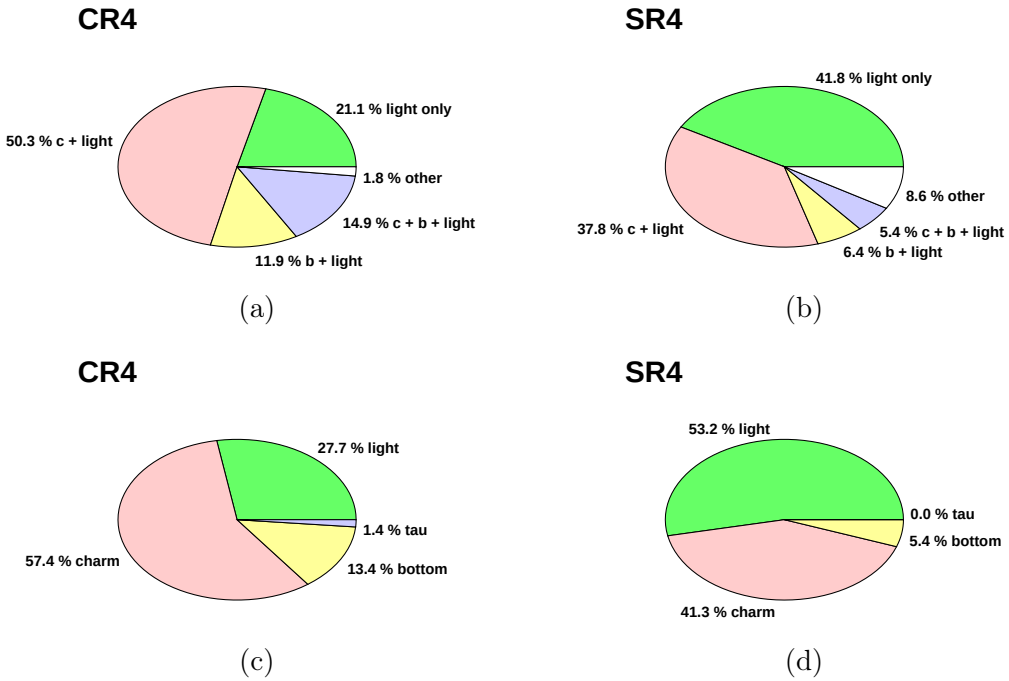

Figure B.18: (a) Flavour composition for **CR4 W** and (b) W+jets in its corresponding SR. (c) Flavour composition of the leading charm tagged jet for **CR4 W** and (d) for W+jets in its corresponding SR.

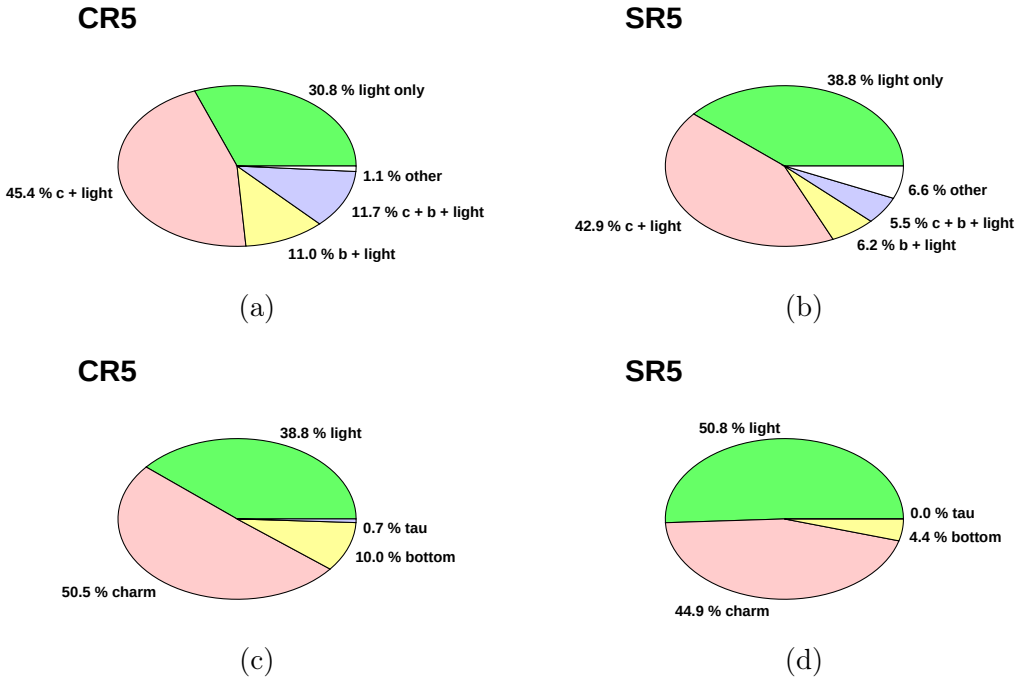

Figure B.19: (a) Flavour composition for **CR5 W** and (b) W+jets in its corresponding SR. (c) Flavour composition of the leading charm tagged jet for **CR5 W** and (d) for W+jets in its corresponding SR.

B.7 $t\bar{t}$ Control Region Compositions

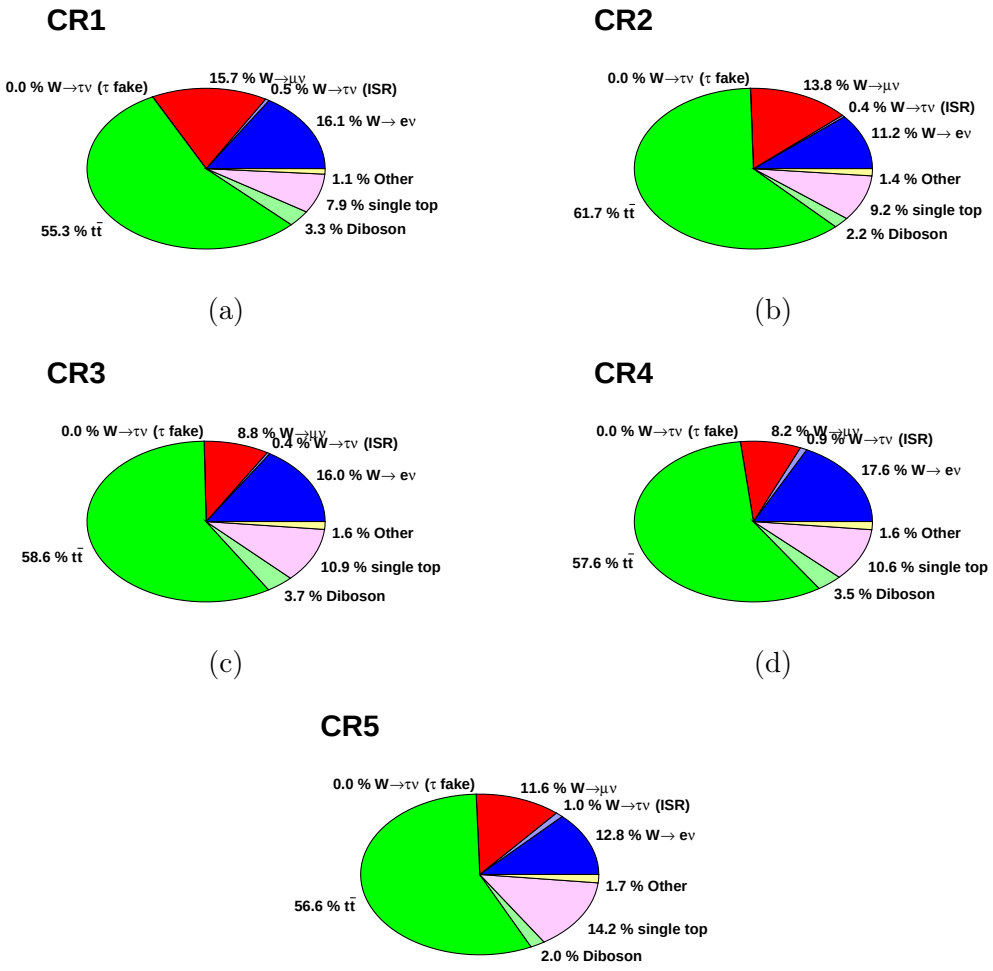

Figure B.20: Breakdown of SM contributions to the total background after the **CR** selections (left). The "other" category includes backgrounds that make up less than 5% of the total.

B.8 $t\bar{t}$ Control Region and Signal Region Comparisons

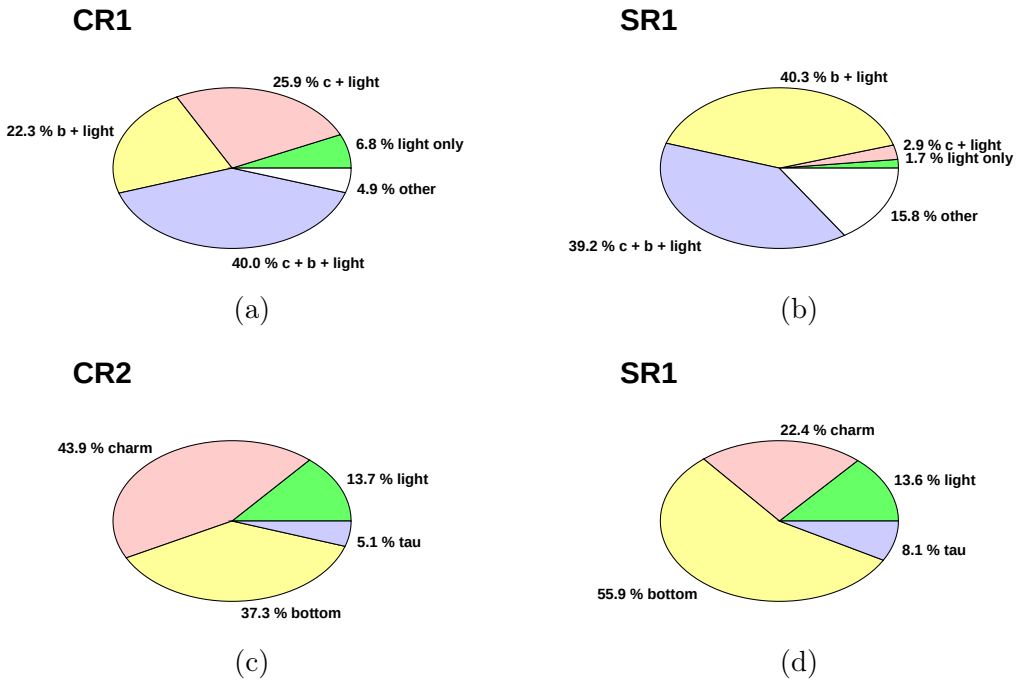

Figure B.21: (a) Flavour composition for **CR1** $t\bar{t}$ and (b) $t\bar{t}$ in its corresponding SR. (c) Flavour composition of the leading charm tagged jet for **CR1** $t\bar{t}$ and (d) for $t\bar{t}$ in its corresponding SR.

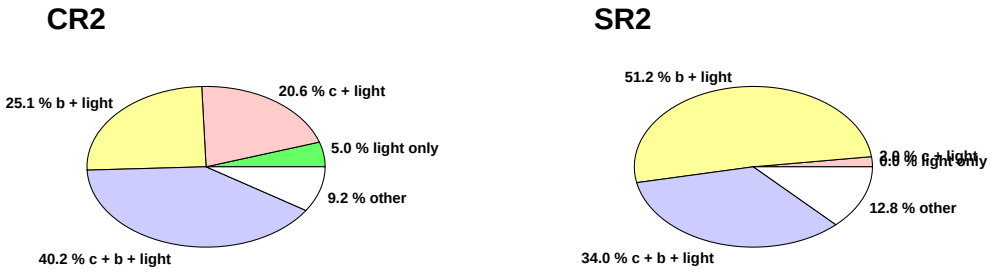

(a) (b)

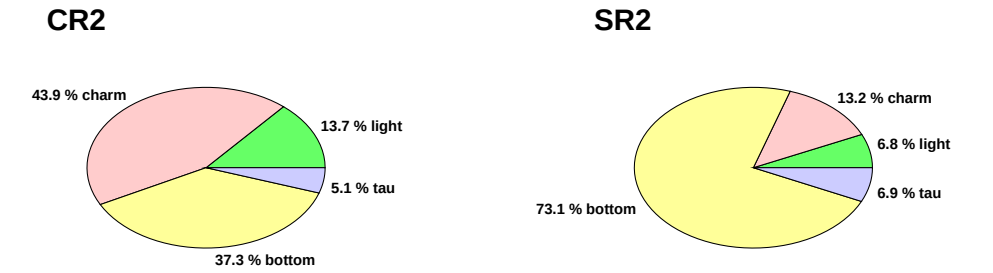

(c) (d)

Figure B.22: (a) Flavour composition for **CR2** $t\bar{t}$ and (b) $t\bar{t}$ in its corresponding SR. (c) Flavour composition of the leading charm tagged jet for **CR2** $t\bar{t}$ and (d) for $t\bar{t}$ in its corresponding SR.

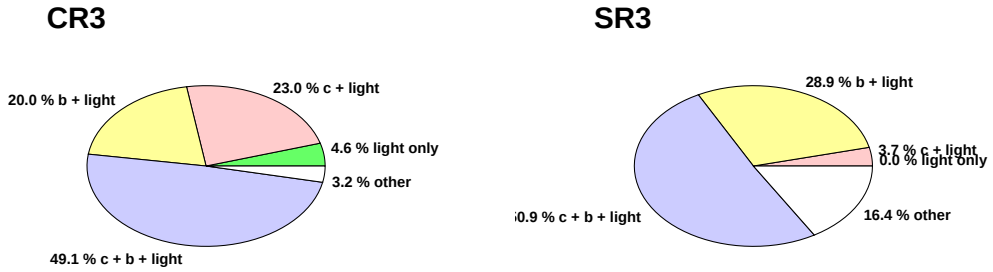

(a) (b)

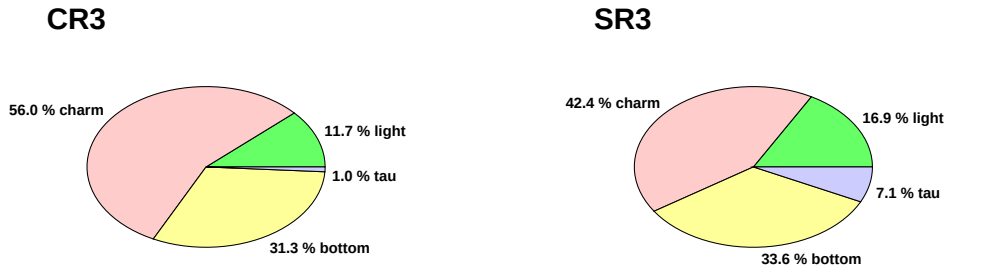

(c) (d)

Figure B.23: (a) Flavour composition for **CR3** $t\bar{t}$ and (b) $t\bar{t}$ in its corresponding SR. (c) Flavour composition of the leading charm tagged jet for **CR3** $t\bar{t}$ and (d) for $t\bar{t}$ in its corresponding SR.

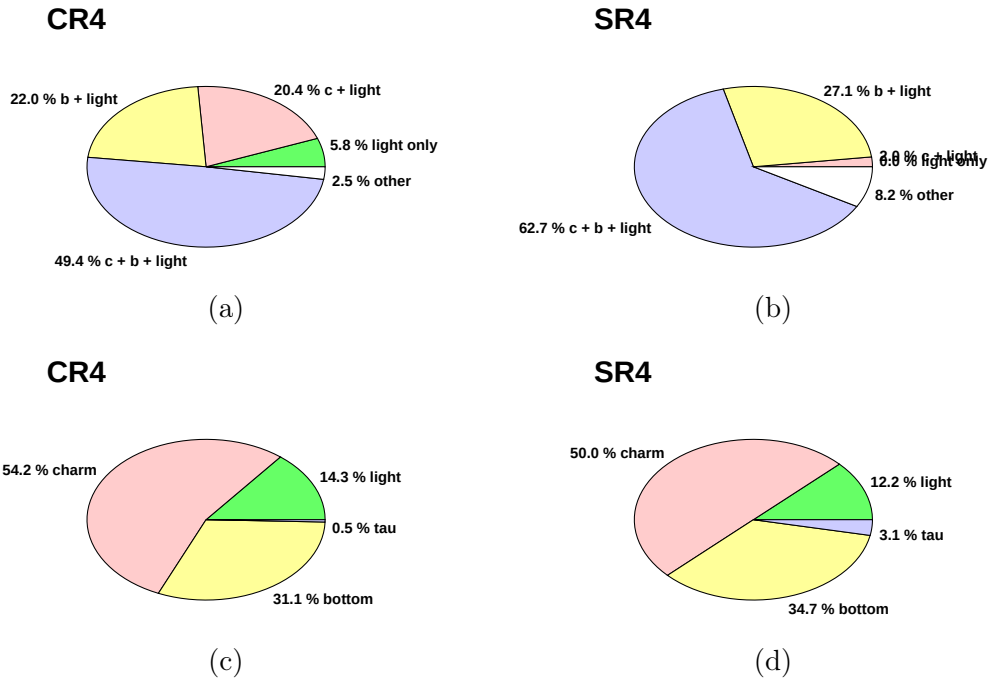

Figure B.24: (a) Flavour composition for **CR4** $t\bar{t}$ and (b) $t\bar{t}$ in its corresponding SR. (c) Flavour composition of the leading charm tagged jet for **CR4** $t\bar{t}$ and (d) for $t\bar{t}$ in its corresponding SR.

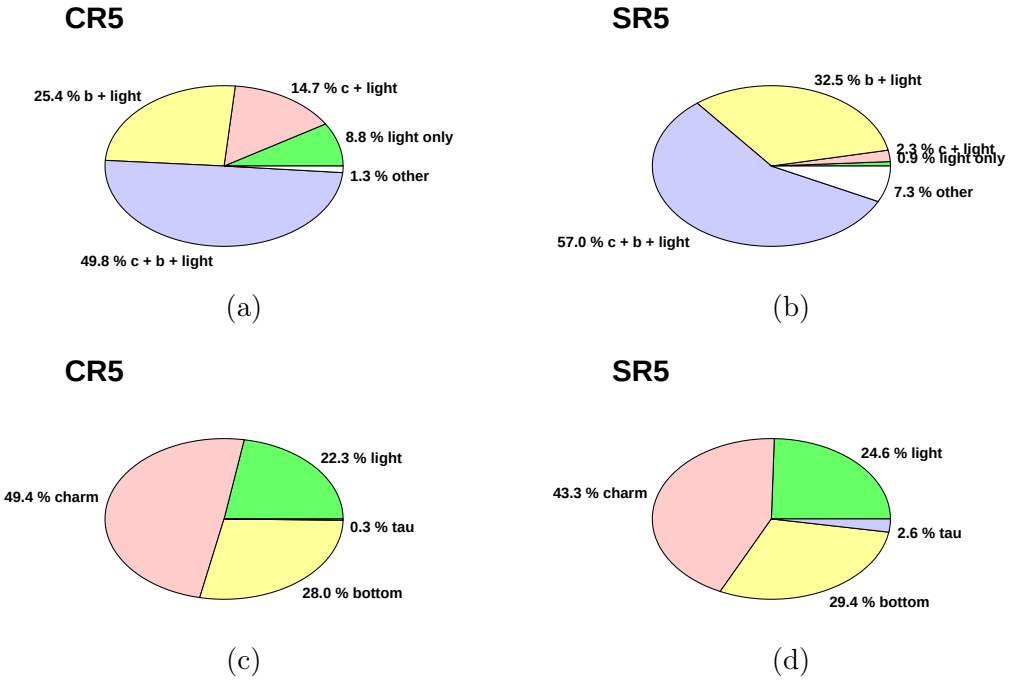

Figure B.25: (a) Flavour composition for **CR5** $t\bar{t}$ and (b) $t\bar{t}$ in its corresponding SR. (c) Flavour composition of the leading charm tagged jet for **CR5** $t\bar{t}$ and (d) for $t\bar{t}$ in its corresponding SR.

B.9 Signal and Validation Region Compositions

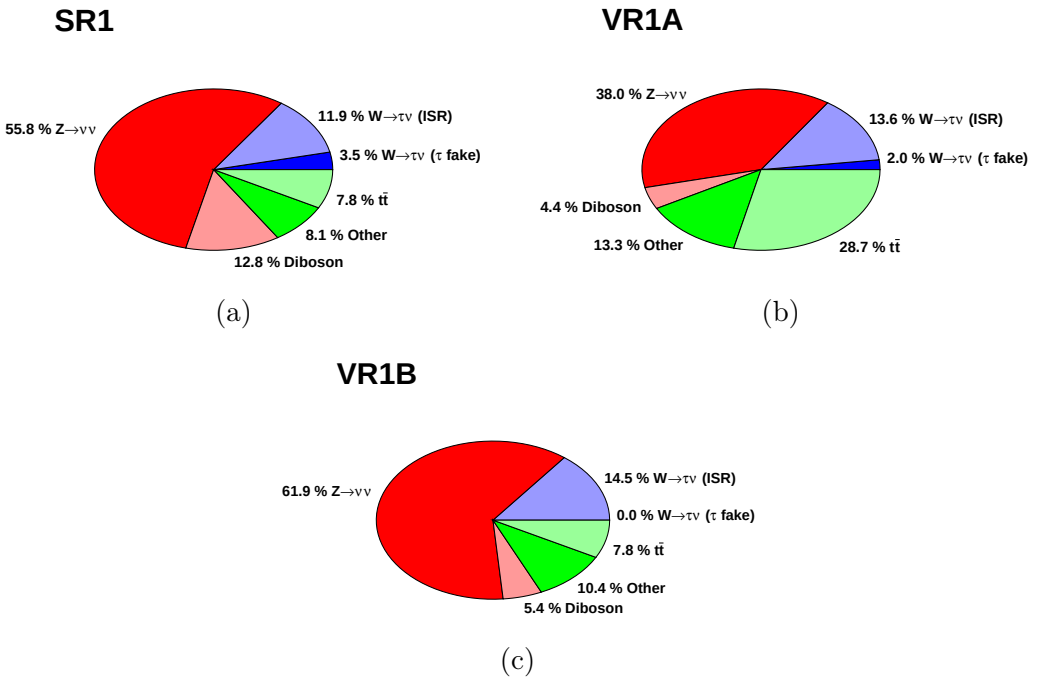

Figure B.26: Background compositions in **SR1** and its corresponding validation regions. (a) **SR1** and its corresponding validations regions (b) A and (c) B.

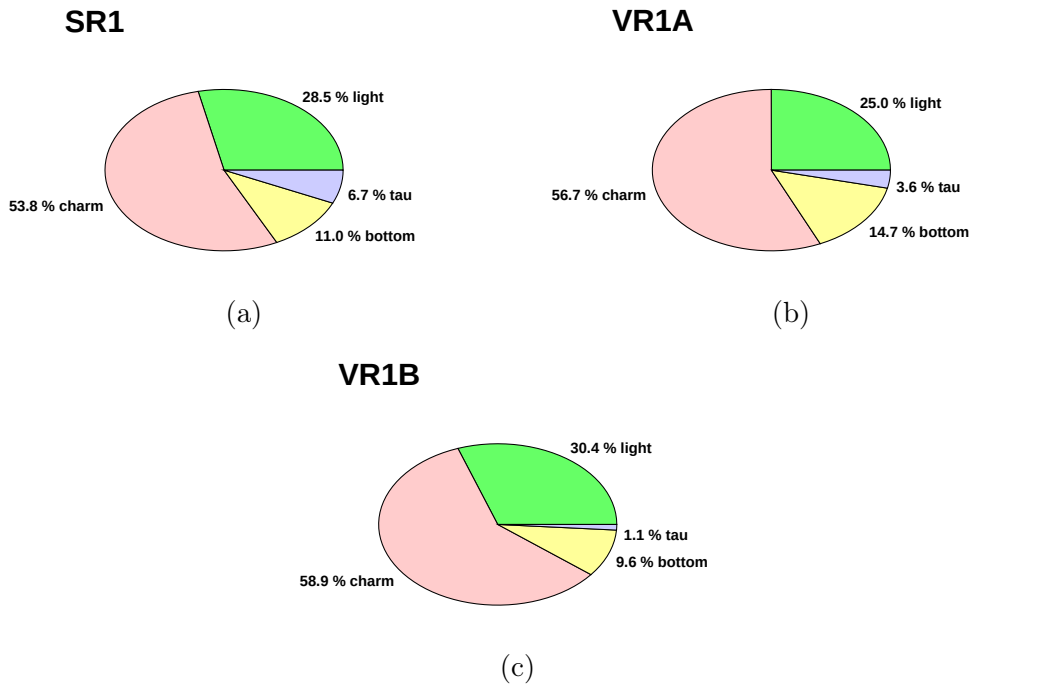

Figure B.27: Flavour compositions for the leading charm-tagged jet in **SR1** and its corresponding validation regions. (a) **SR1** and its corresponding validations regions (b) A and (c) B.

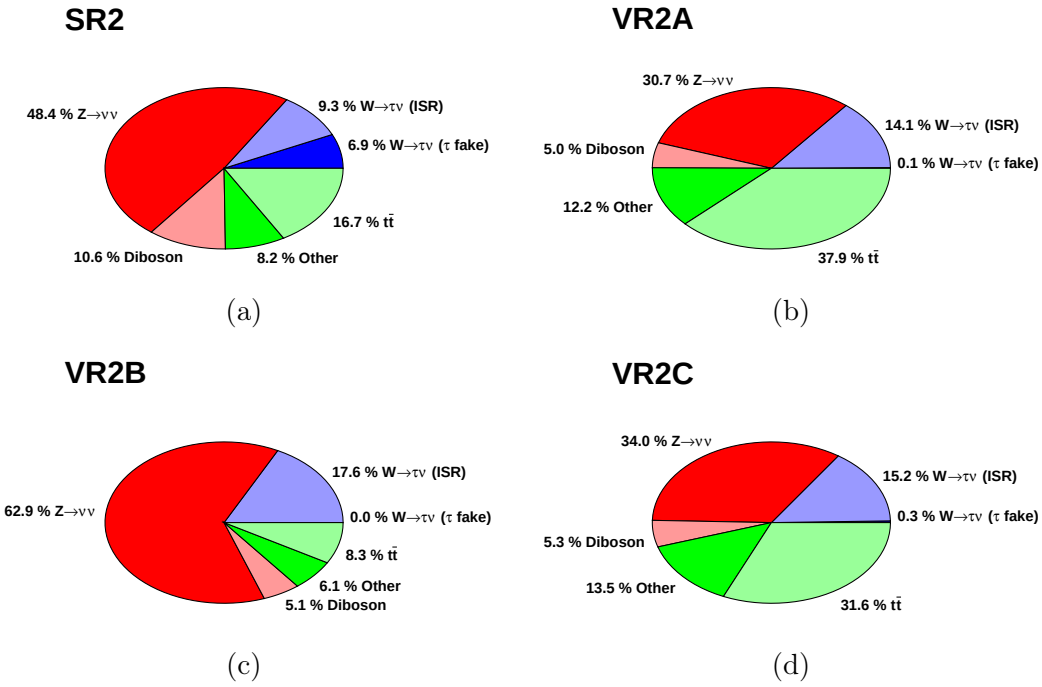

Figure B.28: Background compositions in **SR2** and its corresponding validation regions. (a) **SR2** and its corresponding validations regions (b) A, (c) B and (d) C.

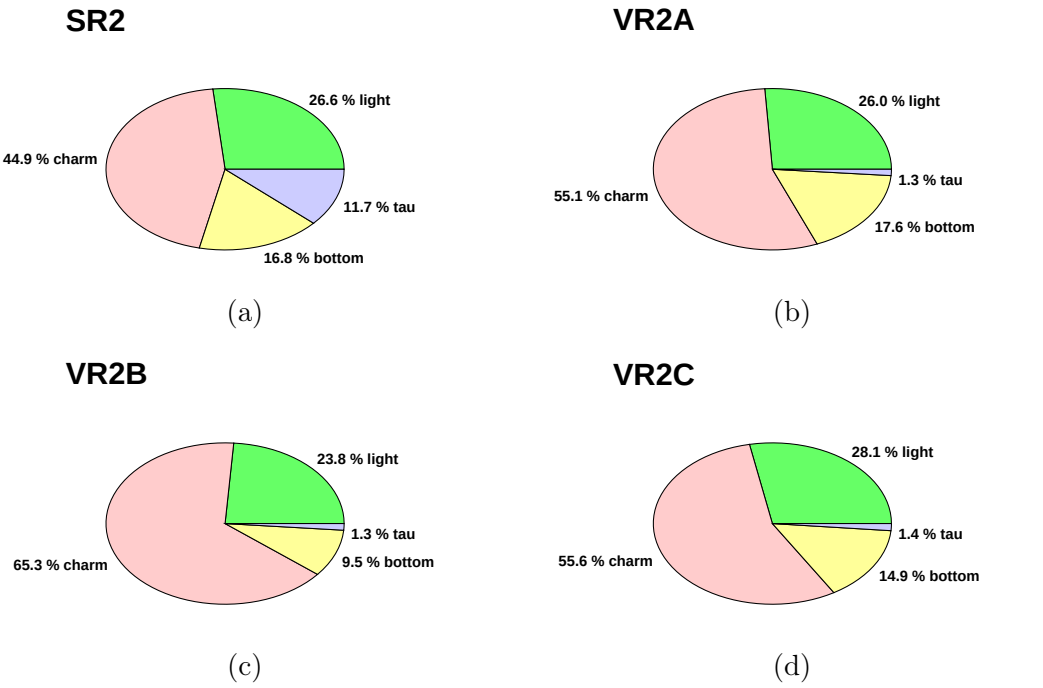

Figure B.29: Flavour compositions for the leading charm-tagged jet in **SR2** and its corresponding validation regions. (a) **SR2** and its corresponding validations regions (b) A, (c) B and (d) C.

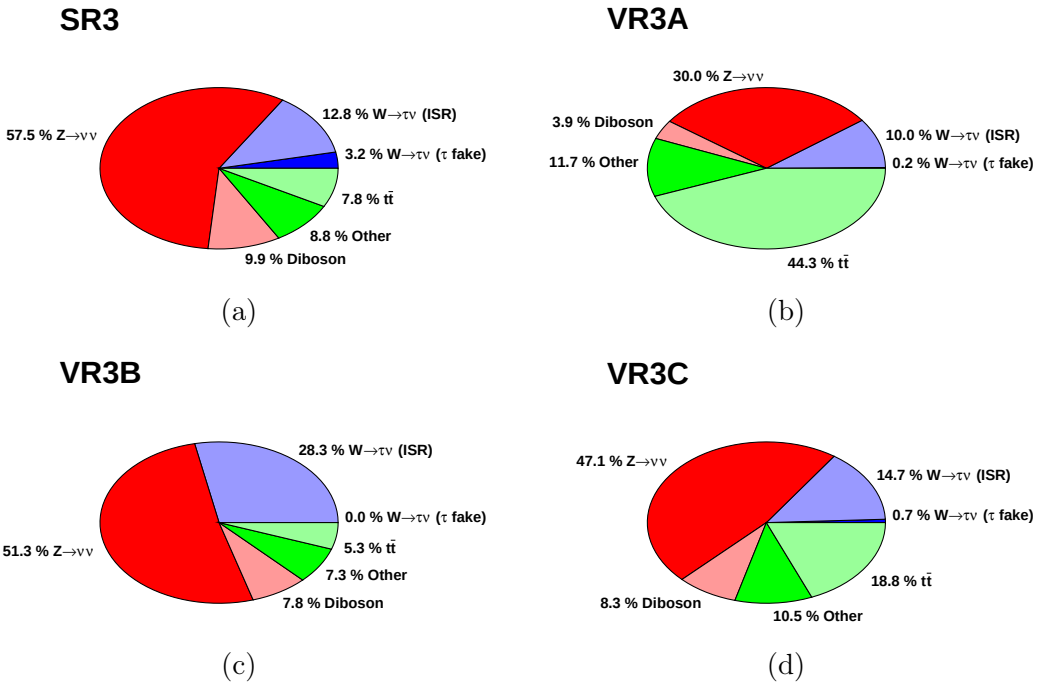

Figure B.30: Background compositions in **SR3** and its corresponding validation regions. (a) **SR3** and its corresponding validations regions (b) A, (c) B and (d) C.

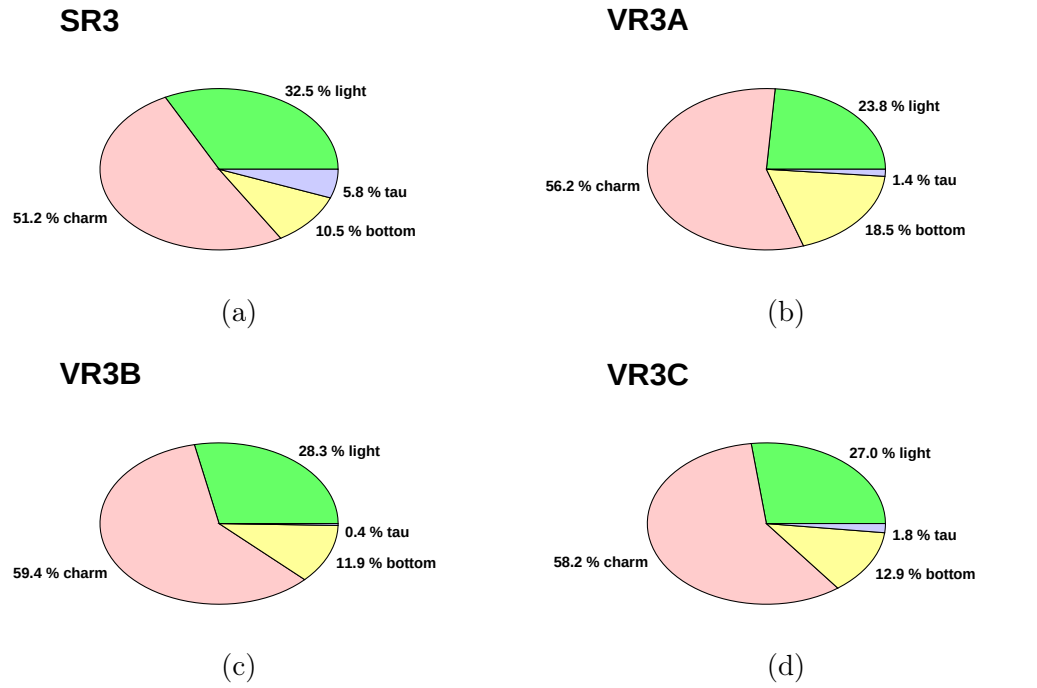

Figure B.31: Flavour compositions for the leading charm-tagged jet in **SR3** and its corresponding validation regions. (a) **SR3** and its corresponding validations regions (b) A, (c) B and (d) C.

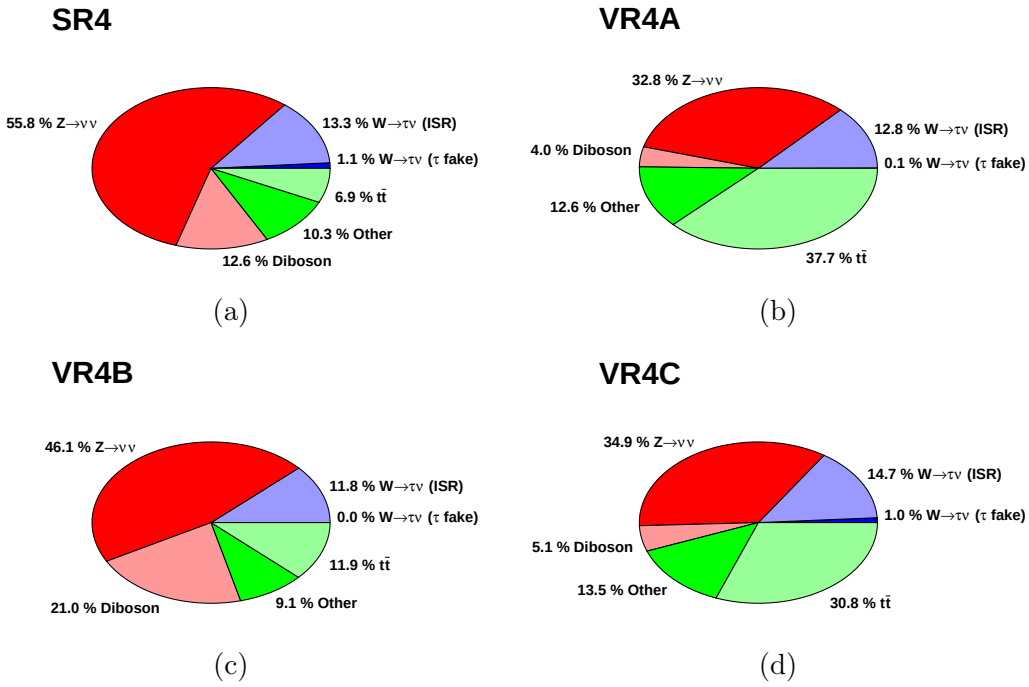

Figure B.32: Background compositions in **SR4** and its corresponding validation regions. (a) **SR4** and its corresponding validations regions (b) A, (c) B and (d) C.

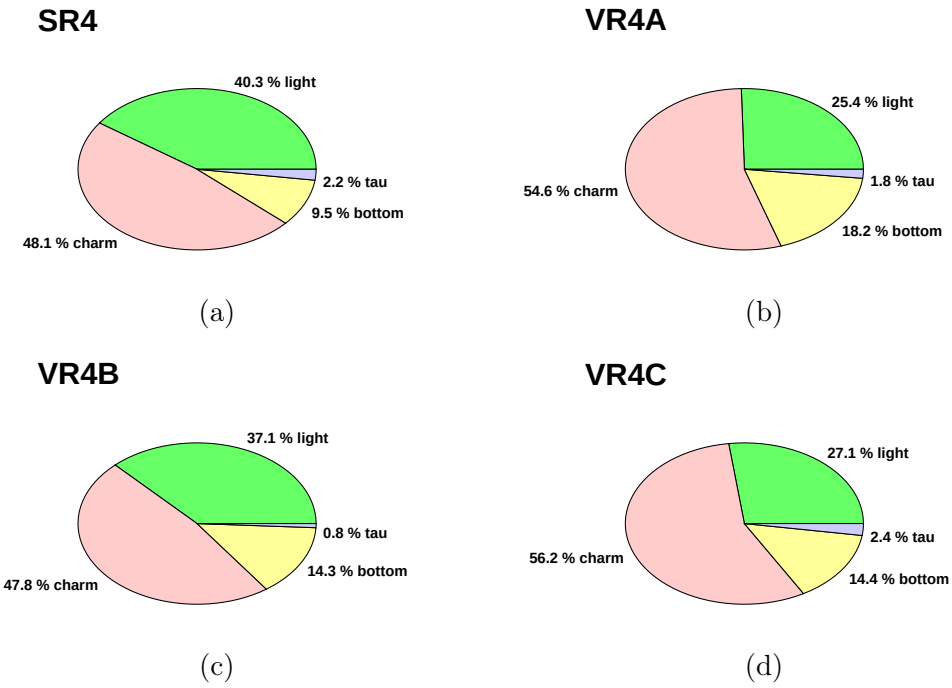

Figure B.33: Flavour compositions for the leading charm-tagged jet in **SR4** and its corresponding validation regions. (a) **SR4** and its corresponding validations regions (b) A, (c) B and (d) C.

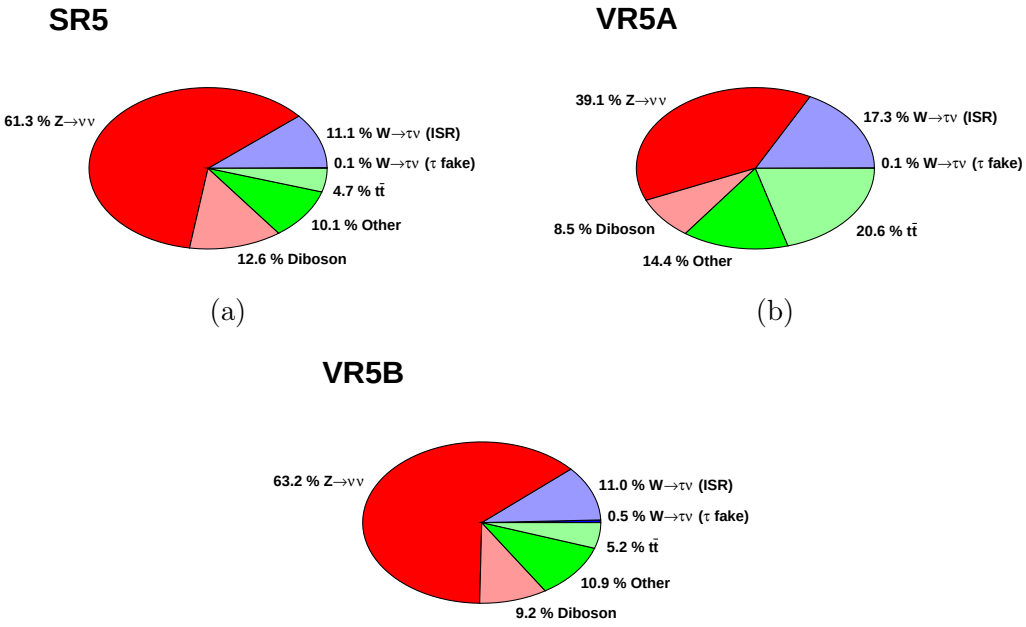

(a) (b) (c)

Figure B.34: Background compositions in **SR5** and its corresponding validation regions. (a) **SR5** and its corresponding validations regions (b) A and (c) B.

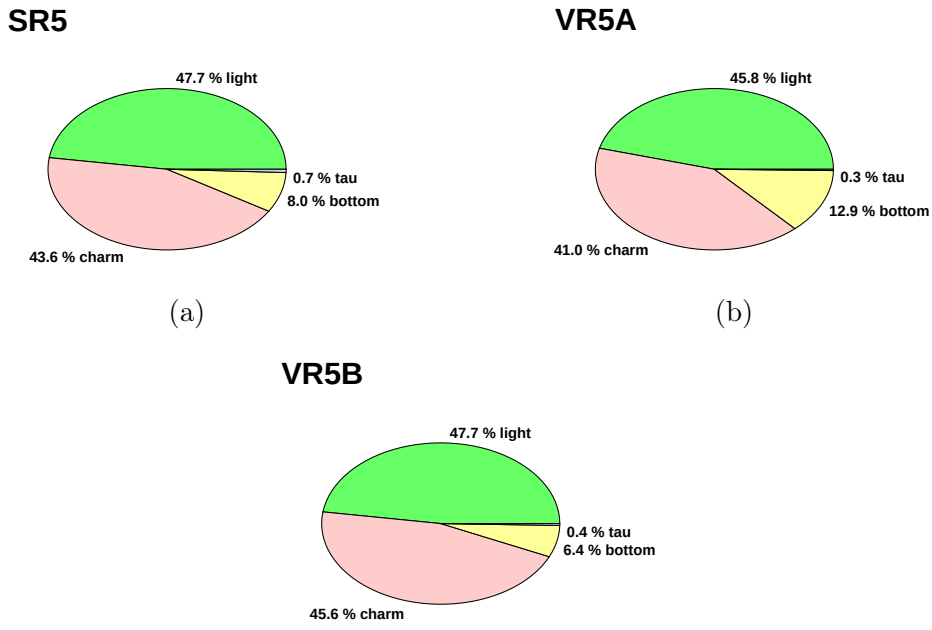

(a) (b) (c)

Figure B.35: Flavour compositions for the leading charm-tagged jet in **SR5** and its corresponding validation regions. (a) **SR5** and its corresponding validations regions (b) A and (c) B.

C | Fit Parameters and Correlations

C.1 Glossary of Fit Parameters

This section lists each of the parameters included in the background-only fit with the name expanded. In general, **alpha** precedes a nuisance parameter, **gamma** a statistical uncertainty associated to the yield in a given region and **mu** a background normalisation. The parameters are listed in the same order as they appear in the correlation matrix.

- **alpha_BGXSec:** background cross section
- **alpha_FT_B:** b flavour tagging uncertainty
- **alpha_FT_C:** c flavour tagging uncertainty
- **alpha_FT_Ex:** flavour tagging extrapolation uncertainty
- **alpha_FT_ExC:** c flavour tagging extrapolation uncertainty
- **alpha_FT_Light:** light flavour tagging uncertainty
- **alpha_JER:** JER uncertainty
- **alpha_JES_NP1:** JES, nuisance parameter set 1
- **alpha_JES_NP2:** JES, nuisance parameter set 2
- **alpha_JES_NP3:** JES, nuisance parameter set 3
- **alpha_JET_EtaCalib:** jet eta calibration uncertainty
- **alpha_JVT:** JVT uncertainty
- **alpha_MET_ResoPara:** $E_{\mathrm{T}}^{\mathrm{miss}}$ resolution uncertainty, parallel component
- **alpha_MET_ResoPerp:** $E_{\mathrm{T}}^{\mathrm{miss}}$ resolution uncertainty, perpendicular component
- **alpha_MET_Scale:** $E_{\mathrm{T}}^{\mathrm{miss}}$ scale uncertainty
- **alpha_PRW:** pileup re-weighting scale factor uncertainty
- **alpha_VJets_AlphaS:** strong coupling constant uncertainty for V+jets
- **alpha_VJets_PDFInt:** PDF internal variations for V+jets
- **alpha_VJets_PDFSet:** PDF comparisons for V+jets
- **alpha_VV_fac:** factorisation scale uncertainty for diboson
- **alpha_VV_qsf:** resummation scale uncertainty for diboson

- **gamma_stat_CR_Ttbar_cuts_bin_0:** statistical uncertainty for $t\bar{t}$ CR yield
- **gamma_stat_CR_Wlnu_cuts_bin_0:** statistical uncertainty for $W \to l\nu$ CR yield
- **gamma_stat_CR_Zll_cuts_bin_0:** statistical uncertainty for $Z \to ll$ CR yield
- **mu_Wc:** normalisation for W+jets background
- **mu_Z:** normalisation for $Z \to \nu\nu$ background
- **mu_ttbar:** normalisation for $t\bar{t}$ background
- **alpha_Ttbar_Generator:** $t\bar{t}$ hard scattering uncertainty
- **alpha_Ttbar_Radiation:** $t\bar{t}$ radiation uncertainty
- **alpha_Ttbar_Shower:** $t\bar{t}$ shower uncertainty
- **alpha_VJets_ckkw:** ME to parton shower merging variation for V+jets
- **alpha_VJets_qsf:** ME resummation scale uncertainty for V+jets
- **alpha_V_RenormFac:** renormalisation and factorisation scale for single boson
- **alpha_singletop_Theory:** total theory uncertainty for single top
- **gamma_stat_SR_cuts_bin_0:** statistical uncertainty for SR yield
- **gamma_stat_VRA_cuts_bin_0:** statistical uncertainty for VRA yield
- **gamma_stat_VRB_cuts_bin_0:** statistical uncertainty for VRB yield
- **gamma_stat_VRC_cuts_bin_0:** statistical uncertainty for VRC yield

C.2 Background-Only Fit Correlations

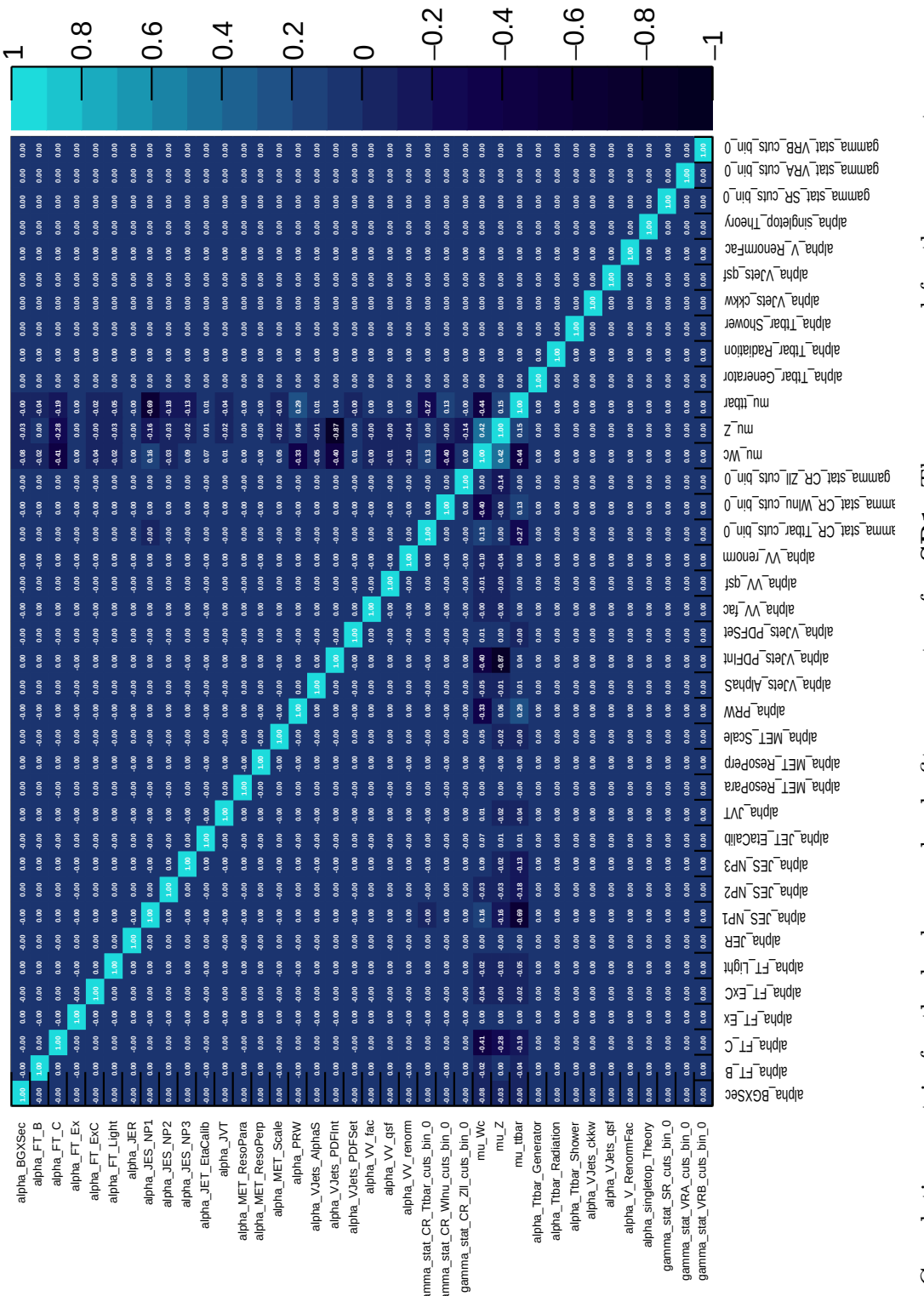

Figure C.1: Correlation matrix for the background-only fit parameters for **SR1**. The names used for the parameters are expanded in appendix C.1.

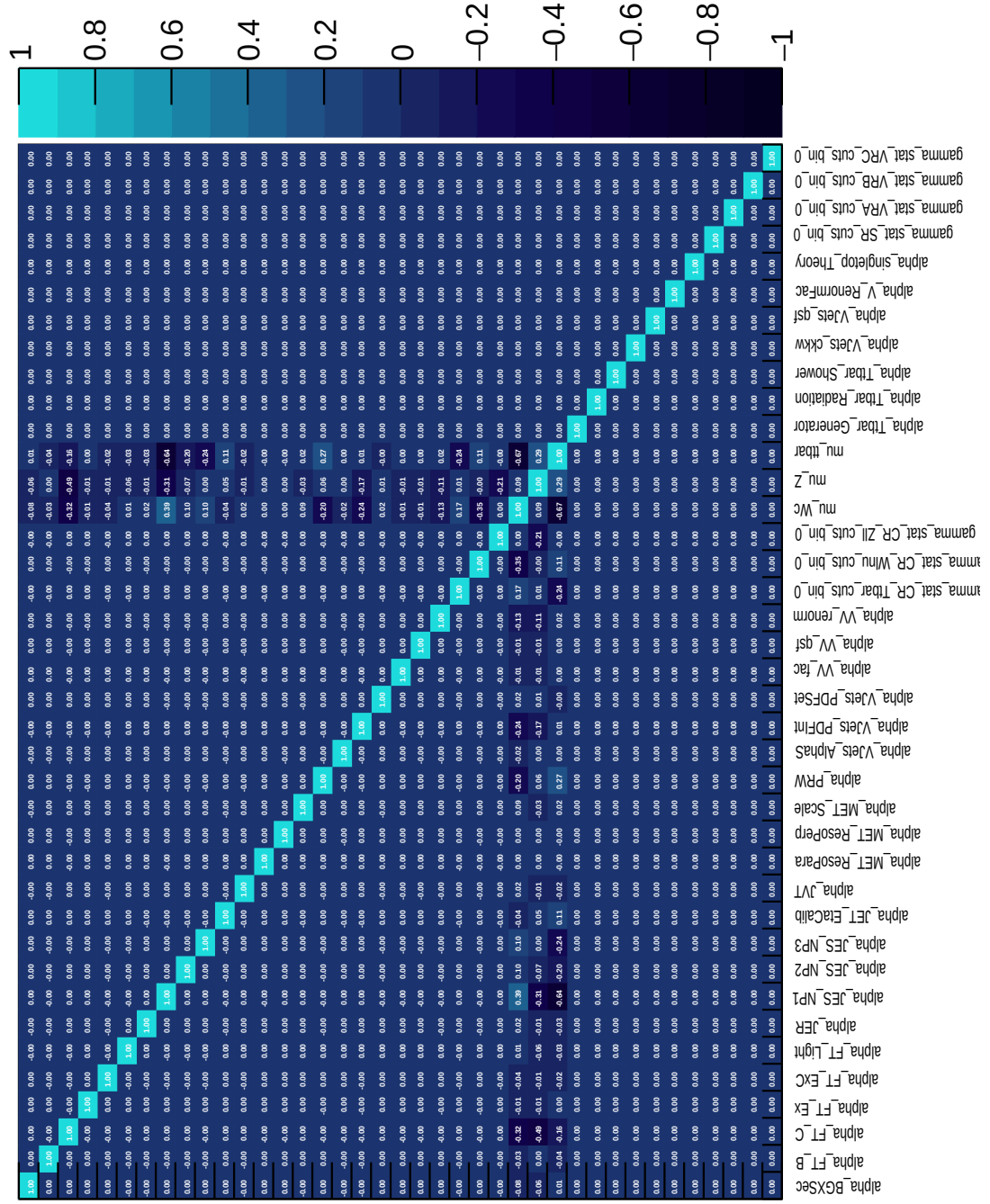

Figure C.2: Correlation matrix for the background-only fit parameters for **SR2**. The names used for the parameters are expanded in appendix C.1.

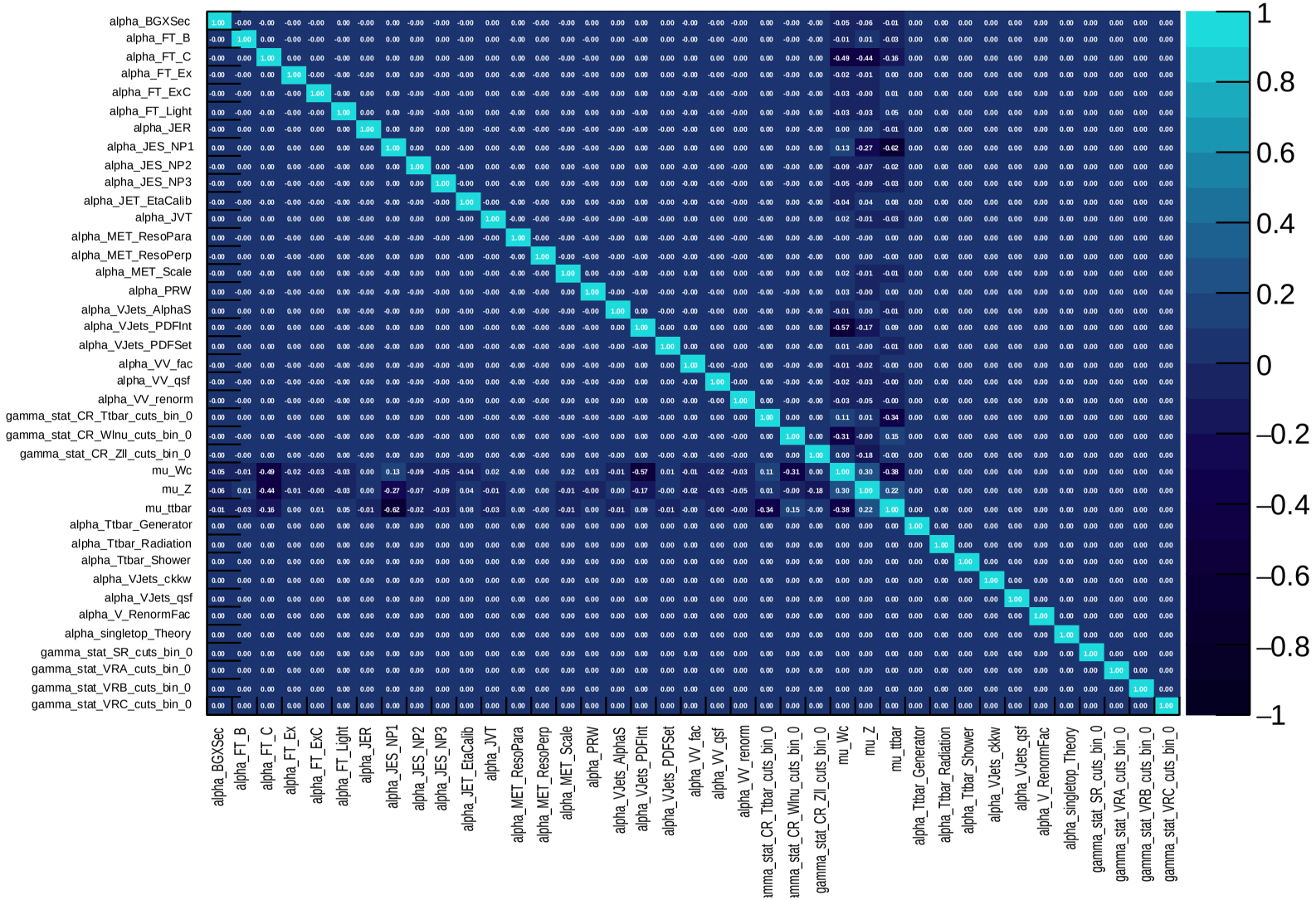

Figure C.3: Correlation matrix for the background-only fit parameters for **SR3**. The names used for the parameters are expanded in appendix C.1.

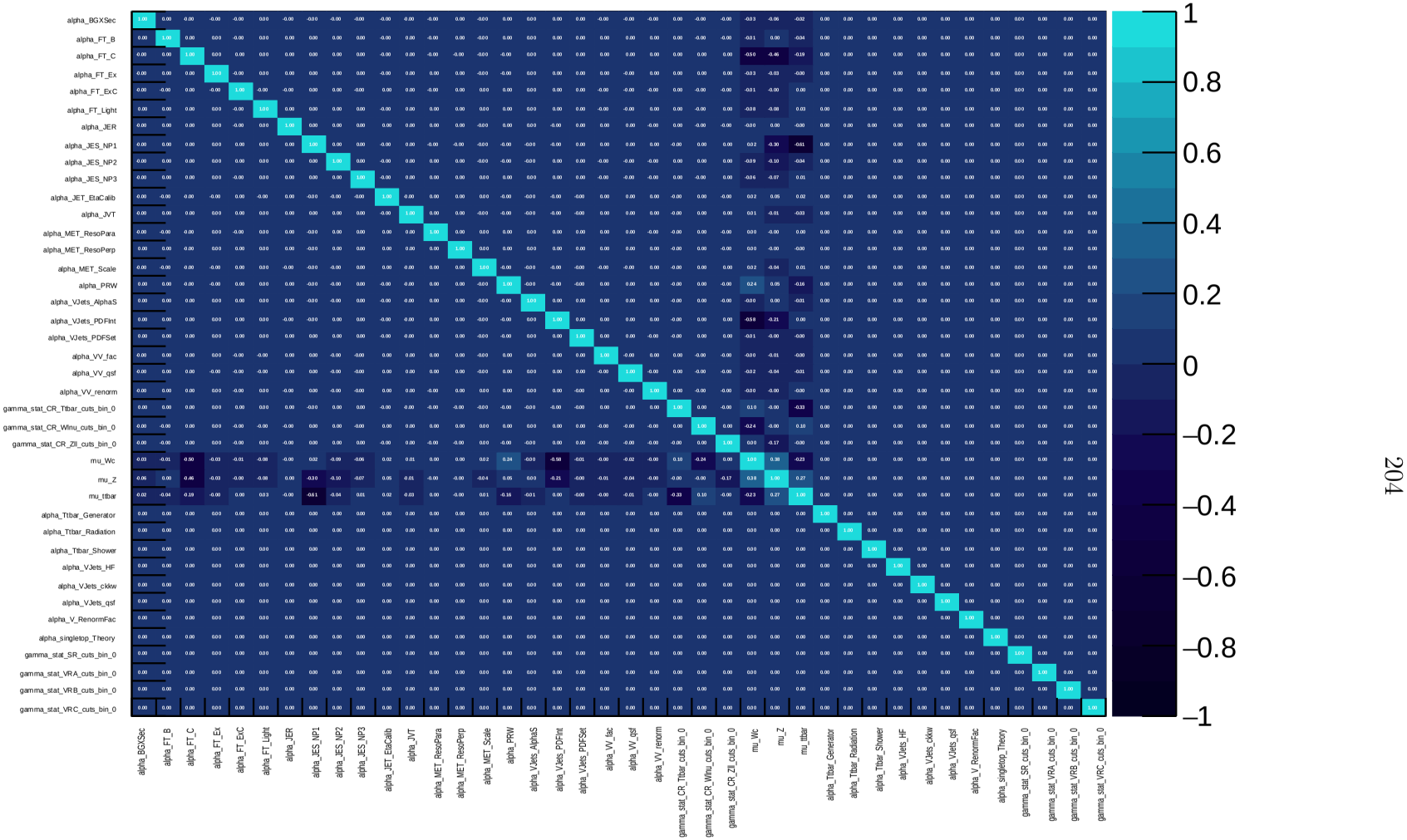

Figure C.4: Correlation matrix for the background-only fit parameters for **SR4**. The names used for the parameters are expanded in appendix C.1.

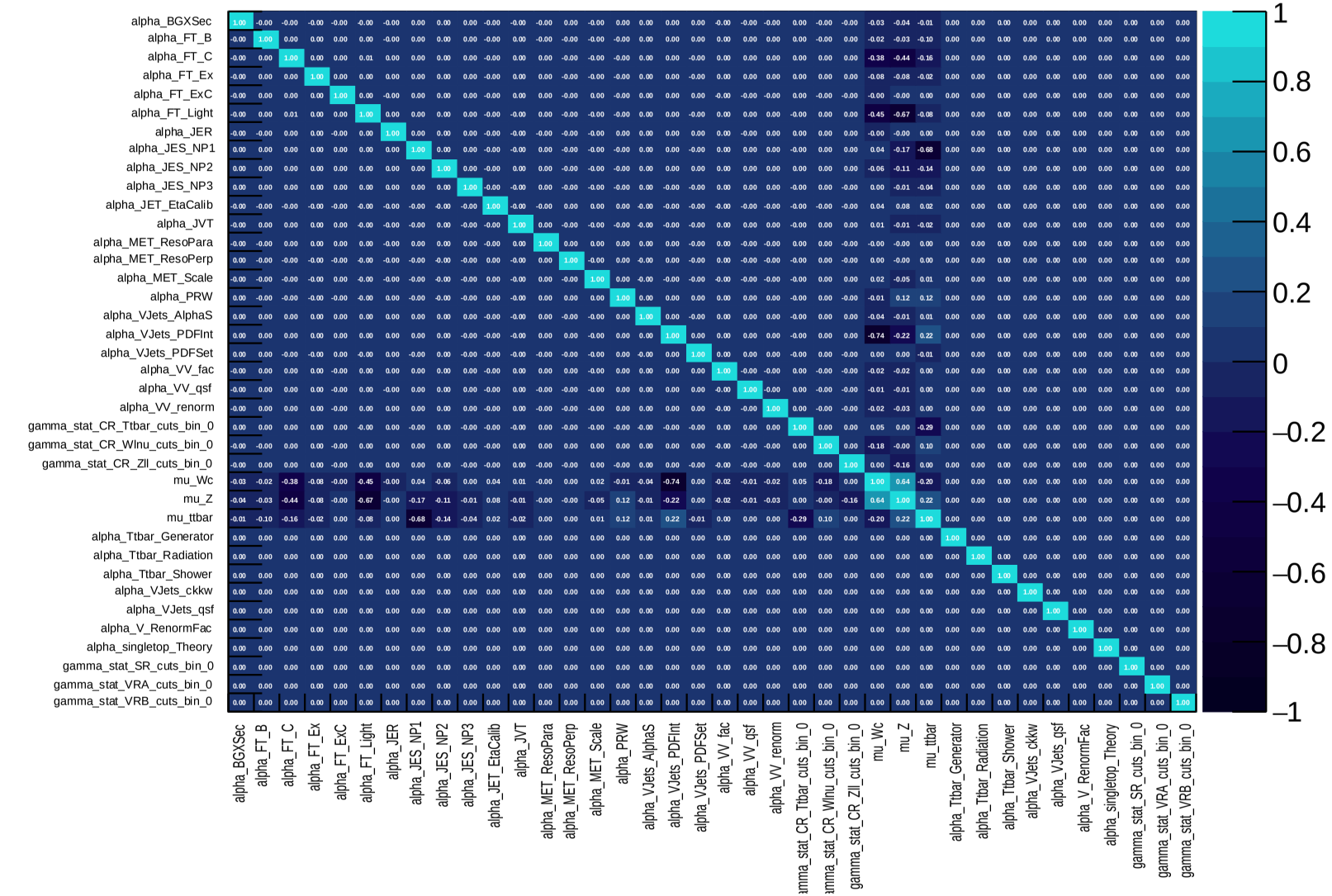

Figure C.5: Correlation matrix for the background-only fit parameters for **SR5**. The names used for the parameters are expanded in appendix C.1.

Bibliography

[1] The ATLAS Collaboration *Search for supersymmetry in final states with charm jets and missing transverse momentum in 13 TeV pp collisions with the ATLAS detector* JHEP **09** (2018) 050
https://doi.org/10.1007/JHEP09(2018)050 2, 78

[2] The ATLAS Collaboration *Soft b-hadron tagging for compressed SUSY scenarios* ATLAS-COM-CONF-2019-027 (2019)
https://cds.cern.ch/record/2682131 2, 142

[3] The ATLAS Collaboration *Electron reconstruction and identification in the ATLAS experiment using the 2015 and 2016 LHC proton-proton collision data at* $\sqrt{s} = 13$ *TeV* Eur. Phys. J. C **79** (2019) 639
https://doi.org/10.1140/epjc/s10052-019-7140-6 2, 166

[4] The ATLAS Collaboration *Performance of electron and photon triggers in ATLAS during LHC Run 2* Submitted to Eur. Phys. J. C
https://arxiv.org/abs/1909.00761 2, 166

[5] M. E. Peskin and D. V. Schroeder *An Introduction to Quantum Field Theory* Perseus Books Publishing, L.L.C. (1995) 4, 6, 11

[6] S. Weinberg *The Quantum Theory of Fields Volume I* Cambridge Univ. Press, Cambridge 4, 6

[7] E. Noether *Invariant variation problems* Transport Theory and Statistical Physics **1** (1971) 186-207
https://doi.org/10.1080/00411457108231446 5

[8] A. Salam and J. C. Ward *On a gauge theory of elementary interactions* Nuovo Cim. **19** (1961) 165-170
https://doi.org/10.1007/BF02812723 6

[9] S. L. Glashow *Partial Symmetries of Weak Interactions* Nucl. Phys. **22** (1961) 579-588
https://doi.org/10.1016/0029-5582(61)90469-2 6

[10] C. S. Wu *et al Experimental Test of Parity Conservation in Beta Decay* Phys. Rev. **105** (1957) 1413
https://doi.org/10.1103/PhysRev.105.1413 6

[11] F. J. Hasert *et al Observation of Neutrino Like Interactions Without Muon Or Electron in the Gargamelle Neutrino Experiment* Phys. Lett. B **46** (1973) 138-140
https://doi.org/10.1016/0370-2693(73)90499-1 6

[12] T. Nakano and K. Nishijima *Charge Independence for V-particles* Progress of Theoretical Physics **10** (1953) 581-582
https://doi.org/10.1143/PTP.10.581 6

[13] M. Gell-Mann *The interpretation of the new particles as displaced charge multiplets* Nuovo Cim. **4** (1956) 848-866
https://doi.org/10.1007/BF02748000 6

[14] P. W. Higgs *Spontaneous Symmetry Breakdown without Massless Bosons* Phys. Rev. **145** (1966) 1156
https://doi.org/10.1103/PhysRev.145.1156 7

[15] T. W. B. Kibble *Symmetry Breaking in Non-Abelian Gauge Theories* Phys. Rev. **155** (1967) 1554
https://doi.org/10.1103/PhysRev.155.1554

[16] F. Englert and R. Brout *Broken Symmetry and the Mass of Gauge Vector Mesons* Phys. Rev. Lett. **13** (1964) 321
https://doi.org/10.1103/PhysRevLett.13.321 7

[17] J. Ellis *Higgs Physics* European School of High-Energy Physics (ESHEP) (2013) 117-168
https://doi.org/10.5170/CERN-2015-004.117 8

[18] N. Cabibbo *Unitary Symmetry and Leptonic Decays* Phys. Rev. Lett. **10** (1963) 531
https://doi.org/10.1103/PhysRevLett.10.531 9

[19] M. Kobayashi and T. Maskawa *CP Violation in the Renormalizable Theory of Weak Interaction* Prog. Theor. Phys. **49** (1973) 652-657
https://doi.org/10.1143/PTP.49.652 9

[20] The ATLAS Collaboration *Observation of a new particle in the search for the Standard Model Higgs boson with the ATLAS detector at the LHC* Phys. Lett. **716** (2012) 1-29
https://doi.org/10.1016/j.physletb.2012.08.020 9

[21] The CMS Collaboration *Observation of a new boson at a mass of 125 GeV with the CMS experiment at the LHC* Phys. Lett. **716** (2012) 30-61
https://doi.org/10.1016/j.physletb.2012.08.021 9

[22] The ATLAS Collaboration and the CMS Collaboration *Measurement of the Higgs boson mass in the $H \to ZZ^* \to 4l$ and $H \to \gamma\gamma$ channels with $\sqrt{s} = 13$ TeV pp collisions using the ATLAS detector* Phys. Lett. **784** (2018) 345-366
https://doi.org/10.1016/j.physletb.2018.07.050 10

[23] The ATLAS Collaboration and the CMS Collaboration *Combined Measurements of the Higgs Boson Mass in pp Collisions at $\sqrt{s} = 7$ and 8 TeV with ATLAS and CMS Experiments* Phys. Rev. Lett. **114** (2015)
https://doi.org/10.1103/PhysRevLett.114.191803 10

[24] The ATLAS Collaboration *Combined measurements of Higgs boson production and decay using up to 80 fb^{-1} of proton–proton collision data at $\sqrt{s} = 13$ TeV collected with the ATLAS experiment* ATLAS-CONF-2018-031 (2018)
https://atlas.web.cern.ch/Atlas/GROUPS/PHYSICS/CONFNOTES/ATLAS-CONF-2018-031/ 10

[25] M. Tanabashi *et al.* (Particle Data Group) *2018 Review of Particle Physics* Phys. Rev. D **98** (2018) 030001
https://doi.org/10.1103/PhysRevD.98.030001 11, 12, 15, 19, 20

[26] J. W. F. Valle *Neutrino masses: evidences and implications* Rev. Mod. Phys. **75** (2014) 345-402
https://doi.org/10.1103/RevModPhys.75.345 11

[27] Y. A. Golfand and E. P. Likhtman *Extension of the Algebra of Poincare Group Generators and Violation of p Invariance* JETP Lett. **13** (1971) 323-326
http://inspirehep.net/record/68412 12

[28] D. V. Volkov and V. P. Akulov *Is the Neutrino a Goldstone Particle?* Phys. Lett. B **46** (1973) 109-110
https://doi.org/10.1016/0370-2693(73)90490-5

[29] J. Wess and B Zumino *Supergauge Transformations in Four-Dimensions* Nucl. Phys. B **70** (1974) 39-50
https://doi.org/10.1016/0550-3213(74)90355-1

[30] J. Wess and B. Zumino *Supergauge Invariant Extension of Quantum Electrodynamics* Nucl. Phys. B **78** (1974) 1-13
https://doi.org/10.1016/0550-3213(74)90112-6

[31] S. Ferrara and B. Zumino *Supergauge Invariant Yang-Mills Theories* Nucl. Phys. B **79** (1974) 413-421
https://doi.org/10.1016/0550-3213(74)90559-8

[32] A. Salam and J. A. Strathdee *Super-symmetry and non-Abelian gauges* Phys. Lett. B **51** (1974) 353-355
https://doi.org/10.1016/0370-2693(74)90226-3 12

[33] A. D. Sakharov *Violation of CP Invariance, C asymmetry, and baryon asymmetry of the universe* Pisma Zh. Eksp. Teor. Fiz. **5** (1967) 32-35
https://doi.org/10.1070/PU1991v034n05ABEH002497 12

[34] N. Jarosik *et al.* *Seven-Year Wilkinson Microwave Anisotropy Probe (WMAP1) Observations: Sky Maps, Systematic Errors, and Basic Results* Astrophysical Journal Supplement **192** (2011) 14
https://doi.org/10.1088/0067-0049/192/2/14 13, 15

[35] G. 't Hooft *Symmetry Breaking Through Bell-Jackiw Anomalies* Phys. Rev. Lett. **37** (1976) 8-11
https://doi.org/10.1103/PhysRevLett.37.8 13

[36] M. Carena, J. M Moreno, M. Quiros, M. Seco, and C. E. M. Wagner *Supersymmetric CP violating currents and electroweak baryogenesis* Nucl. Phys. B **599** (2001) 158-184
https://doi.org/10.1016/S0550-3213(01)00032-3 13

[37] H. Georgi, H. R. Quinn, and S. Weinberg *Hierarchy of Interactions in Unified Gauge Theories* Phys. Rev. Lett **33** (1974) 451
https://doi.org/10.1103/PhysRevLett.33.451 13

[38] L. Susskind *Dynamics of spontaneous symmetry breaking in the Weinberg-Salam theory* Phys. Rev. D **20** (1979) 2619
https://doi.org/10.1103/PhysRevD.20.2619 13

[39] S. Troitsky *Unsolved problems in particle physics* Phys. Usp. **55** (2012) 72-95
https://doi.org/10.3367/UFNe.0182.201201d.0077 13

[40] A. Djouadi *The Anatomy of Electro-Weak Symmetry Breaking. II: The Higgs bosons in the Minimal Supersymmetric Model* Phys. Rept. **459** (2008) 1-241
https://doi.org/10.1016/j.physrep.2007.10.005 13, 17

[41] K. Garrett and G. Duda *Dark Matter: A Primer* Adv. Astron. **2011** (2011) 968283
https://doi.org/10.1155/2011/968283 14

[42] K. G. Begeman, A. H. Broeils, and R. H. Sanders *Extended rotation curves of spiral galaxies - Dark haloes and modified dynamics* Monthly Notices of the Royal Astronomical Society **249** (1991) 523-537
https://doi.org/10.1093/mnras/249.3.523 15

[43] A. G. Bergmann, V. Petrosian, and R. Lynds *Gravitational lens models of arcs in clusters* Astrophys. J. **350** (1990) 23-35
https://doi.org/10.1086/168359 14

[44] C. Alcock *et al. The MACHO Project: Microlensing Results from 5.7 Years of Large Magellanic Cloud Observations* Astrophys. J. **542** (2000) 281-307
https://doi.org/10.1086/309512 14

[45] P. Tisserand *et al. Limits on the Macho Content of the Galactic Halo from the EROS-2 Survey of the Magellanic Clouds* Astron. Astrophys. **469** (2007) 387-404
https://doi.org/10.1051/0004-6361:20066017 14

[46] R. H. Cyburt *Primordial nucleosynthesis for the new cosmology: Determining uncertainties and examining concordance* Phys. Rev. D **70** (2004) 023505
https://doi.org/10.1103/PhysRevD.70.023505 15

[47] Planck Collaboration *Planck 2018 results. VI. Cosmological parameters* (2018)
http://arxiv.org/abs/arXiv:1807.06209 15, 24

[48] D. Fargion and R. Mignani *Massive Neutrinos In Particle Physics And Their Astrophysical And Cosmological Implications* Hadronic J. **6** (1983) 1170
http://inspirehep.net/record/195215 16

[49] J. Ellis, J. S. Hagelin, D. V. Nanopoulos, K. A. Olive, and M. Srednecki *Supersymmetric Relics from the Big Bang* Nucl. Phys. B **238** (1984) 453-476
https://doi.org/10.1016/0550-3213(84)90461-9 16

[50] H. Goldberg *Constraint on the Photino Mass from Cosmology* Phys. Rev. Lett. **50** (1983) 1419
https://doi.org/10.1103/PhysRevLett.103.099905 16

[51] L. Girardello and M. T. Grisaru *Soft Breaking of Supersymmetry* Nucl. Phys. B **194** (1982) 65-76
https://doi.org/10.1016/0550-3213(82)90512-0 17

[52] S. P. Martin *A Supersymmetry Primer* Adv. Ser. Dir. High Energy Phys. **21** (2010) 1-153
https://doi.org/10.1142/9789814307505_0001 17

[53] A. H. Chamseddine, R. L. Arnowitt, and P. Nath *Locally Supersymmetric Grand Unification* Phys. Rev. Lett. **49** (1982) 970
https://doi.org/10.1103/PhysRevLett.49.970 17

[54] R. Barbieri, S. Ferrara, and C. A. Savoy *Gauge Models with Spontaneously Broken Local Supersymmetry* Phys. Lett. B **119** (1982) 343-347
https://doi.org/10.1016/0370-2693(82)90685-2

[55] G. L. Kane, C. F. Kolda, L. Roszkowski, and J. D. Wells *Study of constrained minimal supersymmetry* Phys. Rev. D **49** (1994) 6173-6210
https://doi.org/10.1103/PhysRevD.49.6173 17

[56] M. Bona *et al. Model-independent constraints on* $\Delta F = 2$ *operators and the scale of new physics* JHEP **03** (2008) 049
https://doi.org/10.1088/1126-6708/2008/03/049 18

[57] G. Isidori, Y. Nir, and G. Perez *Flavor Physics Constraints for Physics Beyond the Standard Model* Ann. Rev. Nucl. Part. Sci. **60** (2010) 355-380
https://doi.org/10.1146/annurev.nucl.012809.104534 18

[58] K. Hidaka and A. Bartl *Impact of bosonic decays on the search for the lighter stop and sbottom squarks* Phys. Lett. B **501** (2001) 78-85
https://doi.org/10.1016/S0370-2693(01)00108-3 20

[59] R. Barbieri and G. F. Giudice *Upper bounds on supersymmetric particle masses* Nucl. Phys. B **306** (1988) 63-76
https://doi.org/10.1016/0550-3213(88)90171-X 20

[60] B. de Carlos and J. A. Casas *One-loop analysis of the electroweak breaking in supersymmetric models and the fine-tuning problem* Physics Letters B **309** (1993) 320-328
https://doi.org/10.1016/0370-2693(93)90940-J 20

[61] M. Carena, M. Quiros, and C. E. M. Wagner *Opening the Window for Electroweak Baryogenesis* Phys. Lett. B **380** (1996) 81-91
https://doi.org/10.1016/0370-2693(96)00475-3 20

[62] The ATLAS Collaboration *ATLAS Run 1 searches for direct pair production of third-generation squarks at the Large Hadron Collider* Eur. Phys. J. C **76** (2016) 153
https://doi.org/10.1140/epjc/s10052-016-3935-x 20, 21

[63] R. Gröber, M. Mühlleitner, E. Popenda, and A. Wlotzka *Light stop decays into* $Wb\tilde{\chi}_1^0$ *near the kinematic threshold* Phys. Lett. B **747** (2015) 144-151
https://doi.org/10.1016/j.physletb.2015.05.060 20

[64] C. Boehm, A. Djouadi, and M. Drees *Light Scalar Top Quarks and Supersymmetric Dark Matter* Phys. Rev. D **62** (1999) 035012
https://doi.org/10.1103/PhysRevD.62.035012 21

[65] The ATLAS Collaboration *Search for squarks and gluinos in final states with jets and missing transverse momentum using 36 fb^{-1} of $\sqrt{s}$ = 13 TeV pp collision data with the ATLAS detector* Phys. Rev. D **97** (2018) 122001
https://doi.org/10.1103/PhysRevD.97.112001 21

[66] The CMS Collaboration *Search for supersymmetry in multijet events with missing transverse momentum in proton-proton collisions at 13 TeV* Phys. Rev. D **96** (2017) 032003
https://doi.org/10.1103/PhysRevD.96.032003 21

[67] Y. Nir and N. Seiberg *Should squarks be degenerate?* Phys. Lett. B **309** (1993) 337-343
https://doi.org/10.1016/0370-2693(93)90942-B 21

[68] R. Mahbubani, M. Papucci, G. Perez, J. T. Ruderman, and A. Weiler *Light non-degenerate squarks at the LHC* Phys. Rev. Lett. **110** (2013) 151804
https://doi.org/10.1103/PhysRevLett.110.151804 21

[69] J. Alwall, M. Le, M. Lisanti, and J. G. Wacker *Searching for Directly Decaying Gluinos at the Tevatron* Phys. Lett. B **666** (2008) 34-37
https://doi.org/10.1016/j.physletb.2008.06.065 23

[70] J. Alwall, P. Schuster, and N. Toro *Simplified Models for a First Characterization of New Physics at the LHC* Phys. Rev. D **79** (2009) 075020
https://doi.org/10.1103/PhysRevD.79.075020

[71] D. Alves *et al. Simplified Models for LHC New Physics Searches* J. Phys. G **39** (2012) 105005
https://doi.org/10.1088/0954-3899/39/10/105005 23

[72] C. Huang, W. Liao, and Q. Yan *The Promising process to distinguish supersymmetric models with large tan Beta from the standard model: B —> X(s) mu+ mu-* Phys. Rev. D **59** (1999) 011701
https://doi.org/10.1103/PhysRevD.59.011701 23

[73] C. Hamzaoui, M. Pospelov, and M. Toharia *Higgs mediated FCNC in supersymmetric models with large tan Beta* Phys. Rev. D **59** (1999) 095005
https://doi.org/10.1103/PhysRevD.59.095005

[74] S. R. Choudhury and N. Gaur *Dileptonic decay of B(s) meson in SUSY models with large tan Beta* Phys. Lett. B **451** (1999) 86-92
https://doi.org/10.1016/S0370-2693(99)00203-8

[75] K. S. Babu and C. F. Kolda *Higgs mediated $B^0 \to \mu^+\mu^-$ in minimal supersymmetry* Phys. Rev. Lett. **84** (2000) 228-231
https://doi.org/10.1103/PhysRevLett.84.228

[76] S. R. Choudhury, A. S. Cornell, N. Gaur, and G. C. Joshi *Signatures of new physics in dileptonic B-decays* Int. J. Mod. Phys. A **21** (2006) 2617-2634 https://doi.org/10.1142/S0217751X06029491 23

[77] The ATLAS Collaboration *Study of the rare decays of B_S^0 and B^0 mesons into muon pairs using data collected during 2015 and 2016 with the ATLAS detector* JHEP **1904** (2019) 098 https://doi.org/10.1007/JHEP04(2019)098 23

[78] LHCb Collaboration *Measurement of the $B_s^0 \to \mu^+\mu^-$ branching fraction and effective lifetime and search for $B^0 \to \mu^+\mu^-$ decays* Phys. Re. Lett. **118** (2017) 191801 https://doi.org/10.1103/PhysRevLett.118.191801 23

[79] J. Ellis, M. K. Gaillard, and D. V. Nanopoulos *A Phenomenological Profile of the Higgs Boson* Nucl. Phys. B **106** (1976) 292 https://doi.org/10.1016/0550-3213(76)90382-5 24

[80] A. Djouadi *Squark effects on Higgs boson production and decay at the LHC* Phys. Lett. B **435** (1998) 101-108 https://doi.org/10.1016/S0370-2693(98)00784-9 24

[81] J. R. Espinosa, C. Grojean, V. Sanz, and M. Trott *NSUSY Fits* JHEP **1212** (2012) 077 https://doi.org/10.1007/JHEP12(2012)077 24

[82] C. R. Nappi and B. A. Ovrut *Supersymmetric extension of the $SU(3) \times SU(2) \times U(1)$ model* Phys. Lett. **113** (1982) 175-179 https://doi.org/10.1016/0370-2693(82)90418-X 25

[83] M. Dine and W. Fischler *A phenomenological model of particle physics based on supersymmetry* Phys. Lett. **110** (1982) 227-231 https://doi.org/10.1016/0370-2693(82)91241-2

[84] L. Alvarez-Gaumé, M. Claudson, and M. B. Wise *Low-energy supersymmetry* Nucl. Phys. **207** (1982) 96-110 https://doi.org/10.1016/0550-3213(82)90138-9 25

[85] The ATLAS Collaboration *ATLAS Public Results - Supersymmetry* https://atlas.web.cern.ch/Atlas/GROUPS/PHYSICS/CombinedSummaryPlots/SUSY/ 25, 26, 27, 28

[86] The CMS Collaboration *CMS Public Results - Supersymmetry* https://twiki.cern.ch/twiki/bin/view/CMSPublic/PhysicsResultsSUS 26, 27

[87] G. F. Giudice and A. Romanino *Split supersymmetry* Nucl. Phys. B **699** (2004) 487 https://doi.org/10.1016/j.nuclphysb.2004.11.048 27

[88] N. Arkani-Hamed and S. Dimopoulos *Supersymmetric unification without low energy supersymmetry and signatures for fine-tuning at the LHC* JHEP **0506** (2004) 073 https://doi.org/10.1088/1126-6708/2005/06/073 27

[89] L. Randall and R. Sundrum *Out of this world supersymmetry breaking* Nucl.Phys. B **557** (1999) 79-118 https://doi.org/10.1016/S0550-3213(99)00359-4 27

[90] G. F. Giudice, M. A. Luty, H. Murayama, and R. Rattazzi *Gaugino mass without singlets* JHEP **9812** (1998) 027 https://doi.org/10.1088/1126-6708/1998/12/027 27

[91] The ATLAS Collaboration *Reinterpretation of searches for supersymmetry in models with variable R-parity-violating coupling strength and long-lived R-hadrons* (2018) http://inspirehep.net/record/1662545 29

[92] The ATLAS Collaboration *The ATLAS Experiment at the CERN Large Hadron Collider* JINST **3** (2008) S08003 https://doi.org/10.1088/1748-0221/3/08/S08003 31, 35, 36, 37, 40, 42, 43, 47

[93] L. Evans and P. Bryant *LHC Machine* JINST **3** (2008) S08001 https://doi.org/10.1088/1748-0221/3/08/S08001 31, 33

[94] R. Assmann, M. Lamont, and S. Myers *A brief history of the LEP collider* Nucl. Phys. Proc. Suppl. **109B** (2002) 17-31 https://doi.org/10.1016/S0920-5632(02)90005-8 31, 80

[95] The CMS Collaboration *The CMS Experiment at the CERN LHC* JINST **3** (2008) S08004 https://doi.org/10.1088/1748-0221/3/08/S08004 31

[96] ALICE Collaboration *The ALICE experiment at the CERN LHC* JINST **3** (2008) S08002 https://doi.org/10.1088/1748-0221/3/08/S08002 31

[97] LHCb Collaboration *The LHCb Detector at the LHC* JINST **3** (2008) S08005 https://doi.org/10.1088/1748-0221/3/08/S08005 31

[98] TOTEM Collaboration *The TOTEM Experiment at the CERN Large Hadron Collider* JINST **3** (2008) S08007 https://doi.org/10.1088/1748-0221/3/08/S08007 31

[99] LHCf Collaboration *The LHCf detector at the CERN Large Hadron Collider* JINST **3** (2008) S08006 https://doi.org/10.1088/1748-0221/3/08/S08006 31

[100] MoEDAL Collaboration *Technical Design Report of the MoEDAL Experiment* CERN-LHCC-2009-006, MoEDAL-TDR-001 (2009) http://inspirehep.net/record/1299494 31

[101] L. Di Lella and C. Rubbia *The Discovery of the W and Z Particles* Adv. Ser. Dir. High Energy Phys. **23** (2015) 137-163 http://dx.doi.org/10.1142/9789814644150_0006 31

[102] M. Esma *The CERN Accelerator Complex* (2016) OPEN-PHO-ACCEL-2016-009
https://cds.cern.ch/record/2197559 32

[103] C. Bernardini, G. F. Corazza, G. Di Giugno, G. Ghigo, J. Haissinski, P. Marin, R. Querzoli, and B. Touschek *Lifetime and Beam Size in Electron Storage Rings* Phys. Rev. Lett. **10** (1963) 407
http://inspirehep.net/record/918681/ 32

[104] The ATLAS Collaboration *Luminosity Public Results Run 2*
https://twiki.cern.ch/twiki/bin/view/AtlasPublic/LuminosityPublicResultsRun2 33, 34

[105] The ATLAS Collaboration *Luminosity determination in pp collisions at* $\sqrt{s} =$ 8 *TeV using the ATLAS detector at the LHC* Eur. Phys. J. C **76** (2016) 653
https://doi.org/10.1140/epjc/s10052-016-4466-1 34

[106] S. Van der Meer *Calibration of the effective beam height in the ISR* CERN-ISR-PO-68-31 (1968)
https://cds.cern.ch/record/296752/ 34

[107] The ATLAS Collaboration *ATLAS Insertable B-Layer Technical Design Report* CERN-LHCC-2010-013. ATLAS-TDR-19 (2010)
https://cds.cern.ch/record/1291633 37

[108] K. Potamianos *The upgraded Pixel detector and the commissioning of the Inner Detector tracking of the ATLAS experiment for Run-2 at the Large Hadron Collider* PoS EPS-HEP2015 (2015) 261
http://arxiv.org/abs/arXiv:1608.07850 38

[109] The ATLAS Collaboration *ATLAS Public Results - Tracking Performance*
https://atlas.web.cern.ch/Atlas/GROUPS/PHYSICS/PLOTS/IDTR-2015-007/ 39

[110] The ATLAS Collaboration *The Silicon Microstrip Sensors of the ATLAS SemiConductor Tracker* Nucl. Instrum. Methods Phys. Re. A **578** (2007) 98-118
http://dx.doi.org/10.1016/j.nima.2007.04.157 38

[111] The ATLAS Collaboration *The ATLAS Transition Radiation Tracker (TRT) proportional drift tube: Design and performance* JINST **3** (2008) P02013
https://doi.org/10.1088/1748-0221/3/02/P02013 39

[112] The ATLAS Collaboration *Measurement of the Inelastic Proton-Proton Cross Section at* $\sqrt{s} = 13$ *TeV with the ATLAS Detector at the LHC* Phys. Rev. Lett. **117** (2016) 182002
https://journals.aps.org/prl/abstract/10.1103/PhysRevLett.117.182002 45

[113] The ATLAS Collaboration *Performance of the ATLAS Trigger System in 2015* Eur. Phys. J. C **77** (2017) 317
https://doi.org/10.1140/epjc/s10052-017-4852-3 46, 57

[114] P. Calafiura, W. Lavrijsen, C. Leggett, M. Marino, and D. Quarrie *The Athena Control Framework in Production, New Developments and Lessons Learned* Computing in High Energy Physics and Nuclear Physics (2005) 456 https://cds.cern.ch/record/688747 49, 64

[115] P. J. Laycock *et al.* on behalf of the ATLAS Collaboration *ATLAS data preparation in run 2* J. Phys. **898** (2017) 042050 https://doi.org/10.1088/1742-6596/898/4/042050 50

[116] The ATLAS Collaboration *Electron efficiency measurements with the ATLAS detector using the 2015 LHC proton-proton collision data* ATLAS-CONF-2016-024 (2016) http://cdsweb.cern.ch/record/2157687 51

[117] S. Jones on behalf of the ATLAS Collaboration *The ATLAS Electron and Photon Trigger* J. Phys. Conf. Ser. **1162** (2018) 012037 doi:10.1088/1742-6596/1162/1/012037 51

[118] A. Hoecker *et al. TMVA - Toolkit for Multivariate Data Analysis* PoS ACAT **040** (2007) http://tmva.sourceforge.net/ 52, 72, 74

[119] The ATLAS Collaboration *Trigger Menu in 2015* ATL-DAQ-PUB-2016-001 (2016) https://cds.cern.ch/record/2136007 53, 54

[120] The ATLAS Collaboration *Trigger Menu in 2016* ATL-DAQ-PUB-2017-001 (2017) https://cds.cern.ch/record/2242069 53, 54

[121] The ATLAS Collaboration *Egamma Trigger Public Results Run 2* https://twiki.cern.ch/twiki/bin/view/AtlasPublic/EgammaTriggerPublicResults 53

[122] M.M. Morgenstern on behalf of the ATLAS Collaboration *Performance of the ATLAS Muon Trigger in Run 2* Proceedings of the XXVI International Symposium on Nuclear Electronics & Computing (2017) https://cds.cern.ch/record/2293044/ 54

[123] The ATLAS Collaboration *Muon Trigger Public Results Run 2* https://twiki.cern.ch/twiki/bin/view/AtlasPublic/MuonTriggerPublicResults 55

[124] W. Lampl *et al. Calorimeter Clustering Algorithms : Description and Performance* ATL-COM-LARG-2008-003 (2008) https://cds.cern.ch/record/1099735 56

[125] The ATLAS Collaboration *Topological cell clustering in the ATLAS calorimeters and its performance in LHC Run 1* Eur. Phys. J. C **77** (2017) 490 https://doi.org/10.1140/epjc/s10052-017-5004-5 56

[126] M. Cacciari, G. P. Salam, and G. Soyez *The anti-k_t jet clustering algorithm* JHEP **0804** (2008) 063 https://doi.org/10.1088/1126-6708/2008/04/063 56, 70

[127] The ATLAS Collaboration *Jet Trigger Public Results Run 2* https://twiki.cern.ch/twiki/bin/view/AtlasPublic/JetTriggerPublicResults 57

[128] The ATLAS Collaboration *Missing Energy Trigger Public Results Run 2* https://twiki.cern.ch/twiki/bin/view/AtlasPublic/MissingEtTriggerPublicResults 59

[129] S. Weinzierl *Introduction to Monte Carlo methods* NIKHEF-00-012 (2000) http://arxiv.org/abs/hep-ph/0006269 59

[130] J. C. Collins, D. E. Soper, and G. Sterman *Factorization of Hard Processes in QCD* Adv. Ser. Dir. High Energy Phys. **5** (1989) 1-91 https://doi.org/10.1142/9789814503266_0001 59

[131] A. Buckley *et al.* *General-purpose event generators for LHC physics* Phys. Rept. **504** (2011) 145-233 https://doi.org/10.1016/j.physrep.2011.03.005 59, 60, 61

[132] M. Dobbs and J. B. Hansen *The HepMC C++ Monte Carlo event record for High Energy Physics* Comput. Phys. Commun. **134** (2001) 41-46 https://doi.org/10.1016/S0010-4655(00)00189-2 60, 64

[133] V. N. Gribov and L. N. Lipatov *Deep inelastic e p scattering in perturbation theory* Sov. J. Nucl. Phys. **15** (1972) 438-450 http://inspirehep.net/record/73449 60

[134] G. Altarelli and G. Parisi *Asymptotic Freedom in Parton Language* Nucl. Phys. B **126** (1977) 298-318 https://doi.org/10.1016/0550-3213(77)90384-4

[135] Y. L. Dokshitser *Calculation of structure functions of deep-inelastic scattering and e^+e^- annihilation by perturbation theory in quantum chromodynamics* Sov. Phys. JETP **46** (1977) 641 http://inspirehep.net/record/126153 60

[136] R. D. Ball *et al.* *Parton distributions with LHC data* Nucl. Phys. B **867** (2013) 244-289 https://doi.org/10.1016/j.nuclphysb.2012.10.003 60, 82

[137] H. L. Lai *et al.* *New parton distributions for collider physics* Phys. Rev. D **82** (2010) 074024 https://journals.aps.org/prd/abstract/10.1103/PhysRevD.82.074024 85

[138] A. D. Martin, W. J. Stirling, R. S. Thorne, and G. Watt *Parton distributions for the LHC* Eur. Phys. J. C **63** (2009) 189-285 https://doi.org/10.1140/epjc/s10052-009-1072-5 60

[139] T. Kinoshita *Mass Singularities of Feynman Amplitudes* Journal of Mathematical Physics **3** (1962) 650
https://doi.org/10.1063/1.1724268 61

[140] T. D. Lee and M. Nauenberg *Degenerate Systems and Mass Singularities* Phys. Rev. **133** (1964) B1549
https://doi.org/10.1103/PhysRev.133.B1549 61

[141] V. V. Sudakov *Vertex parts at very high-energies in quantum electrodynamics* Zh. Eksp. Teor. Fiz. **30** (1956) 87-95
http://inspirehep.net/record/9137/ 61

[142] M. L. Mangano, M. Moretti, F. Piccinini, and M. Treccani *Matching matrix elements and shower evolution for top-pair production in hadronic collisions* JHEP **0701** (2007) 013
https://doi.org/10.1088/1126-6708/2007/01/013 62

[143] S. Catani, F. Krauss, B. R. Webber, and R. Kuhn *QCD Matrix Elements + Parton Showers* JHEP **0111** (2001) 063
https://doi.org/10.1088/1126-6708/2001/11/063 62

[144] S. Höche, F. Krauss, N. Lavesson, L. Lönnblad, and M. Mangano *Matching Parton Showers and Matrix Elements* HERA and the LHC: A Workshop on the Implications of HERA for LHC Physics: CERN - DESY Workshop (2004)
https://doi.org/10.5170/CERN-2005-014.288 62

[145] B. Andersson, G. Gustafson, G. Ingelman, and T. Sjöstrand *Parton fragmentation and string dynamics* Phys. Rept. **97** (1983) 31-145
https://doi.org/10.1016/0370-1573(83)90080-7 63

[146] T. Sjöstrand *Jet fragmentation of multiparton configurations in a string framework* Nucl. Phys. B **248** (1984) 469-502
https://doi.org/10.1016/0550-3213(84)90607-2 63

[147] B. R. Webber *A QCD model for jet fragmentation including soft gluon interference* Nucl. Phys. B **238** (1984) 492-528
https://doi.org/10.1016/0550-3213(84)90333-X 63

[148] G. Marchesini and B. R. Webber *Monte Carlo simulation of general hard processes with coherent QCD radiation* Nucl. Phys. B **310** (1988) 461-526
https://doi.org/10.1016/0550-3213(88)90089-2 63

[149] D. Amati and G. Veneziano *Preconfinement as a property of perturbative QCD* Phys. Lett. B **83** (1979) 87-92
https://doi.org/10.1016/0370-2693(79)90896-7 63

[150] Y. Kulchitsky on behalf of the ATLAS Collaboration *Measurement of the underlying-event properties with the ATLAS detector* ATL-PHYS-PROC-2016-098
http://arxiv.org/abs/arXiv:1608.04954 63

[151] T. Sjöstrand and M. van Zijl *A multiple-interaction model for the event structure in hadron collisions* Phys. Rev. D **36** (1987) 2019 https://doi.org/10.1103/PhysRevD.36.2019 63

[152] G. Corcella *et al. HERWIG 6.5: an event generator for Hadron Emission Reactions With Interfering Gluons (including supersymmetric processes)* JHEP **0101** (2001) 010 https://doi.org/10.1088/1126-6708/2001/01/010 63

[153] J. M. Butterworth, J. R. Forshaw, and M. H. Seymour *Multiparton interactions in photoproduction at HERA* Z. Phys. C **72** (1996) 637-646 https://doi.org/10.1007/s002880050286 63

[154] T. Gleisberg, S. Hoeche, F. Krauss, M. Schonherr, S. Schumann, F. Siegert, and J. Winter *Event generation with SHERPA 1.1* JHEP **0902** (2009) 007 https://doi.org/10.1088/1126-6708/2009/02/007 63, 85

[155] T. Sjöstrand, S. Mrenna, and P. Skands *A Brief Introduction to PYTHIA 8.1* Comput. Phys. Commun. **178** (2008) 852-867 https://doi.org/10.1016/j.cpc.2008.01.036 64, 82

[156] T. Sjöstrand and P. Skands *Transverse-Momentum-Ordered Showers and Interleaved Multiple Interactions* Eur. Phys. J. **39** (2005) 129-154 https://doi.org/10.1140/epjc/s2004-02084-y 64

[157] M. Bahr *et al. Herwig++ Physics and Manual* Eur. Phys. J. C **58** (2008) 639-707 https://doi.org/10.1140/epjc/s10052-008-0798-9 64

[158] J. Alwall *et al. The automated computation of tree-level and next-to-leading order differential cross sections, and their matching to parton shower simulations* JHEP **1407** (2014) 079 https://doi.org/10.1007/JHEP07(2014)079 64, 82

[159] S. Alioli, P. Nason, C. Oleari, and E. Re *A general framework for implementing NLO calculations in shower Monte Carlo programs: the POWHEG BOX* JHEP **1006** (2010) 043 https://doi.org/10.1007/JHEP06(2010)043 64, 85

[160] The ATLAS Collaboration *The ATLAS Simulation Infrastructure* Eur. Phys. J. C **70** (2010) 823-874 https://doi.org/10.1140/epjc/s10052-010-1429-9 64

[161] S. Agostinelli et al. *Geant4 - a simulation toolkit* Nucl. Instrum. Meth. **506** (2003) 250-303 https://doi.org/10.1016/S0168-9002(03)01368-8 64

[162] The ATLAS Collaboration *The simulation principle and performance of the ATLAS fast calorimeter simulation FastCaloSim* ATL-PHYS-PUB-2010-013 (2010) https://cds.cern.ch/record/1300517 64

[163] T. Cornelissen et al. *The new ATLAS track reconstruction (NEWT)* J. Phys. Conf. Ser. **119** (2008) 032014
https://doi.org/10.1088/1742-6596/119/3/032014 64

[164] A. Rosenfeld and J. L. Pfaltz *Sequential Operations in Digital Picture Processing* JACM **13** (1966) 471-494
https://doi.org/10.1145/321356.321357 64

[165] R. Frühwirth *Application of Kalman filtering to track and vertex fitting* Nucl. Instrum. **262** (1987) 444-450
https://doi.org/10.1016/0168-9002(87)90887-4 65

[166] The ATLAS Collaboration *Performance of the ATLAS Track Reconstruction Algorithms in Dense Environments in LHC Run 2* Eur. Phys. J. C **77** (2017) 673
https://doi.org/10.1140/epjc/s10052-017-5225-7 65

[167] ATLAS Colaboration *A neural network clustering algorithm for the ATLAS silicon pixel detector* JINST **9** (2014) P09009
https://doi.org/10.1088/1748-0221/9/09/P09009 65

[168] Maaike Limper *Track and vertex reconstruction in the ATLAS inner detector* NIKHEV Library (2009)
https://www.nikhef.nl/pub/services/biblio/theses_pdf/thesis_M_Limper.pdf 65

[169] The ATLAS Collaboration *Reconstruction of primary vertices at the ATLAS experiment in Run 1 proton-proton collisions the LHC* Eur. Phys. J. C **77** (2017) 332
https://doi.org/10.1140/epjc/s10052-017-4887-5 66

[170] The ATLAS Collaboration *Electron efficiency measurements with the ATLAS detector using the 2015 LHC proton-proton collision data* ATLAS-CONF-2016-024 (2016)
http://cdsweb.cern.ch/record/2157687 67, 68

[171] The ATLAS Collaboration *Improved electron reconstruction in ATLAS using the Gaussian Sum Filter-based model for bremsstrahlung* ATLAS-CONF-2012-047 (2012)
http://cdsweb.cern.ch/record/1449796 67

[172] The ATLAS Collaboration *Muon reconstruction performance of the ATLAS detector in proton-proton collision data at* $\sqrt{s} = 13$ *TeV* Eur. Phys. J. C **76** (2016) 292
https://doi.org/10.1140/epjc/s10052-016-4120-y 69

[173] D. Krohn, J. Thaler, and L-T. Wang. *Jets with Variable R* JHEP **0906** (2009) 059
https://doi.org/10.1088/1126-6708/2009/06/059 71

[174] The ATLAS Collaboration *Jet energy scale measurements and their systematic uncertainties in proton-proton collisions at $\sqrt{s}$ = 13 TeV with the ATLAS detector* Phys. Rev. D **96** (2017) 072002
https://doi.org/10.1103/PhysRevD.96.072002 71, 73, 127

[175] M. Cacciari, G. P. Salam, and G. Soyez *The Catchment Area of Jets* JHEP **0804** (2008) 005
https://doi.org/10.1088/1126-6708/2008/04/005 71

[176] M. Cacciari and G. P. Salam *Pileup subtraction using jet areas* Phys. Lett. B **659** (2008) 119-126
https://doi.org/10.1016/j.physletb.2007.09.077 71

[177] The ATLAS Collaboration *Data-Quality Requirements and Event Cleaning for Jets and Missing Transverse Energy Reconstruction with the ATLAS Detector in Proton-Proton Collisions at a Center-of-Mass Energy of $\sqrt{7}$ TeV* ATLAS-CONF-2010-038 (2010)
http://cdsweb.cern.ch/record/1277678/ 72

[178] The ATLAS Collaboration *Performance of pile-up mitigation techniques for jets in pp collisions at $\sqrt{s}$ = 13 TeV using the ATLAS detector* Eur. Phys. J. C **76** (2016) 581
https://doi.org/10.1140/epjc/s10052-016-4395-z 72

[179] The ATLAS Collaboration *Reconstruction of hadronic decay products of tau leptons with the ATLAS experiment* Eur. Phys. J. C **76** (2016) 295
https://doi.org/10.1140/epjc/s10052-016-4110-0 73

[180] The ATLAS Collaboration *Optimisation of the ATLAS b-tagging performance for the 2016 LHC Run* ATL-PHYS-PUB-2016-012 (2016)
https://cds.cern.ch/record/2160731 74

[181] The ATLAS Collaboration *Secondary vertex finding for jet flavour identification with the ATLAS detector* ATL-PHYS-PUB-2017-011 (2017)
https://cds.cern.ch/record/2270366 74, 148

[182] The ATLAS Collaboration *Search for the Decay of the Higgs Boson to Charm Quarks with the ATLAS Experiment* Phys. Rev. Lett. **120** (211802) 2018
https://doi.org/10.1103/PhysRevLett.120.211802 75

[183] The ATLAS Collaboration *Optimisation of the ATLAS b-tagging performance for the 2016 LHC Run* ATL-PHYS-PUB-2016-012 (2016)
https://atlas.web.cern.ch/Atlas/GROUPS/PHYSICS/PUBNOTES/ATL-PHYS-PUB-2016-012/ 75

[184] G. Piacquadio and C. Weiser *A new inclusive secondary vertex algorithm for b-jet tagging in ATLAS* J. Phys. **119** (2008) 032032
http://stacks.iop.org/1742-6596/119/i=3/a=032032 75

[185] The ATLAS Collaboration *Publications of the ATLAS Collaboration - Jet EtMiss group*
https://twiki.cern.ch/twiki/bin/view/AtlasPublic/JetEtMissPublications 76

[186] The ATLAS Collaboration *Performance of missing transverse momentum reconstruction with the ATLAS detector using proton-proton collisions at* $\sqrt{s} =$ 13 *TeV* Eur. Phys. J. C **78** (2018) 903
https://doi.org/10.1140/epjc/s10052-018-6288-9 76

[187] The ATLAS Collaboration *Search for Scalar Charm Quark Pair Production in pp Collisions at* $\sqrt{s} = 8$ *TeV with the ATLAS Detector* Phys. Rev. Lett. **114** (2015) 161801
https://doi.org/10.1103/PhysRevLett.114.161801 79, 80

[188] The ATLAS Collaboration *Search for pair-produced third-generation squarks decaying via charm quarks or in compressed supersymmetric scenarios in pp collisions at* $\sqrt{s} = 8$ *TeV with the ATLAS detector* Phys. Rev. D **90** (2014) 052008
https://doi.org/10.1103/PhysRevD.90.052008 79, 80

[189] The ATLAS Collaboration *Search for new phenomena in final states with an energetic jet and large missing transverse momentum in pp collisions at* $\sqrt{s} = 8$ *TeV with the ATLAS detector* Eur. Phys. J. C **75** (2015) 299
https://doi.org/10.1140/epjc/s10052-015-3517-3 79

[190] The CMS Collaboration *Searches for third-generation squark production in fully hadronic final states in proton-proton collisions at* $\sqrt{s} = 13$ *TeV* JHEP **1506** (2015) 116
https://doi.org/10.1007/JHEP06(2015)116 79

[191] CDF Collaboration *Search for scalar top quark production in pp collisions at* $\sqrt{s} =$*1.96 TeV* JHEP **2012** (2012) 158
https://doi.org/10.1007/JHEP10(2012)158 80

[192] D0 Collaboration *Search for scalar top quarks in the acoplanar charm jets and missing transverse energy final state in pp collisions at* $\sqrt{s} =$*1.96 TeV* Phys. Lett. B. **665** (2008) 1-8
https://doi.org/10.1016/j.physletb.2008.05.037 80

[193] M. Baak, G.J. Besjes, D. Côte, A. Koutsman, J. Lorenz, and D. Short *HistFitter software framework for statistical data analysis* Eur. Phys. J. C **75** (2015) 153
https://doi.org/10.1140/epjc/s10052-015-3327-7 81, 130

[194] The ATLAS Collaboration *Summary of ATLAS Pythia 8 tunes* ATL-PHYS-PUB-2012-003
https://cds.cern.ch/record/1474107 82

[195] L. Lönnblad and S. Pretsel *Merging Multi-leg NLO Matrix Elements with Parton Showers* JHEP **1303** (2013) 166
https://doi.org/10.1007/JHEP03(2013)166 82

[196] W. Beenakker, M. Krämer, T. Plehn, M. Spira, and P. M. Zerwas *Stop production at hadron colliders* Nucl. Phys. B **515** (1998) 3-14
https://doi.org/10.1016/S0550-3213(98)00014-5 83

[197] W. Beenakker, S. Brensing, M. Krämer, A. Kulesza, E. Laenen, and I. Niessen *Supersymmetric top and bottom squark production at hadron colliders* JHEP **1008** (2010) 098
https://doi.org/10.1007/JHEP08(2010)098

[198] W. Beenakker *et al. Squark and Gluino Hadroproduction* Int. J. Mod. Phys. A **26** (2011) 2637-2664
https://doi.org/10.1142/S0217751X11053560 83

[199] The D0 Collaboration *D0 top public web pages*
https://www-d0.fnal.gov/Run2Physics/top/top_public_web_pages/top_feynman_diag
84

[200] T. Gleisberg and S. Hoeche *Comix, a new matrix element generator* JHEP **0812** (2008) 039
https://doi.org/10.1088/1126-6708/2008/12/039 85

[201] F. Cascioli, P. Maierhofer, and S. Pozzorini *Scattering Amplitudes with Open Loops* Phys. Rev. Lett. **108** (2012) 111601
https://doi.org/10.1103/PhysRevLett.108.111601 85

[202] S. Hoeche, F. Krauss, M. Schonherr, and F. Siegert *QCD matrix elements + parton showers: The NLO case* JHEP **1304** (2013) 027
https://doi.org/10.1007/JHEP04(2013)027 85

[203] NNPDF Collaboration *Parton distributions for the LHC Run II* JHEP **1504** (2015) 040
https://doi.org/10.1007/JHEP04(2015)040 85

[204] T. Sjöstrand, S. Mrenna, and P. Skands *PYTHIA 6.4 physics and manual* JHEP **2006** (2006)
http://iopscience.iop.org/article/10.1088/1126-6708/2006/05/026/meta 85

[205] P. Skands *Tuning Monte Carlo Generators: The Perugia Tunes* Phys. Rev. D **82** (2010) 074018
https://doi.org/10.1103/PhysRevD.82.074018 85

[206] The ATLAS Collaboration *Simulation of top quark production for the ATLAS experiment at* $\sqrt{s} = 13$ *TeV* ATL-PHYS-PUB-2016-004 (2016)
https://cds.cern.ch/record/2120417 86

[207] The ATLAS Collaboration *Calibration of light-flavour jet b-tagging rates on ATLAS proton-proton collision data at* $\sqrt{s} = 13$ *TeV* ATLAS-CONF-2018-006 (2018)
https://cds.cern.ch/record/2314418 90

[208] The ATLAS Collaboration *Calibration of b-tagging using dileptonic top pair events in a combinatorial likelihood approach with the ATLAS experiment* ATLAS-CONF-2014-004 (2014)
http://cdsweb.cern.ch/record/1664335 90

[209] The ATLAS Collaboration *Measurement of b-tagging Efficiency of c-jets in $t\bar{t}$ Events Using a Likelihood Approach with the ATLAS Detector* ATLAS-CONF-2018-001 (2018)
https://cds.cern.ch/record/2306649 91

[210] OPAL Collaboration *A Measurement of the rate of charm production in W decays* Phys. Lett. B **490** (2000) 71-86
https://doi.org/10.1016/S0370-2693(00)00971-0 91

[211] J. Erdmann *et al. A likelihood-based reconstruction algorithm for top-quark pairs and the KLFitter framework* Nucl. Instrum. Meth. **748** (2014) 18-25
https://doi.org/10.1016/j.nima.2014.02.029 91

[212] The ATLAS Collaboration *Search for squarks and gluinos using final states with jets and missing transverse momentum with the ATLAS detector in $\sqrt{s} =$ 7 TeV proton-proton collisions* Phys. Lett. B **701** (2011) 186-203
https://doi.org/10.1016/j.physletb.2011.05.061 120

[213] B. Nachman and C. G. Lester *Significance Variables* Phys. Rev. D **88** (2013) 075013
https://doi.org/10.1103/PhysRevD.88.075013 120

[214] The ATLAS Collaboration *Jet energy resolution in proton-proton collisions at $\sqrt{s} = 7$ TeV recorded in 2010 with the ATLAS detector* Eur. Phys. J. C **73** (2013) 2306
https://doi.org/10.1140/epjc/s10052-013-2306-0 127

[215] The ATLAS Collaboration *Improved luminosity determination in pp collisions at $\sqrt{s} = 7$ TeV using the ATLAS detector at the LHC* Eur. Phys. J. C **73** (2013) 2518
https://doi.org/10.1140/epjc/s10052-013-2518-3 127

[216] L. A. Harland-Lang, A. D. Martin, P. Motylinski, and R. S. Thorne *Parton distributions in the LHC era: MMHT 2014 PDFs* Eur. Phys. J. C **75** (2015) 204
https://doi.org/10.1140/epjc/s10052-015-3397-6 128

[217] S. Dulat *et al. New parton distribution functions from a global analysis of quantum chromodynamics* Phys. Rev. D **93** (2016) 033006
https://doi.org/10.1103/PhysRevD.93.033006 128

[218] A. Buckley *et al. LHAPDF6: parton density access in the LHC precision era* Eur. Phys. J. C **75** (2015) 132
https://link.springer.com/article/10.1140/epjc/s10052-015-3318-8 128

[219] P. Nason *A New method for combining NLO QCD with shower Monte Carlo algorithms* JHEP **11** (2004) 040
https://doi.org/10.1088/1126-6708/2004/11/040 128

[220] S. Gieseke, C. Rohr, and A. Siodmok *Colour reconnections in Herwig++* Eur. Phys. J. C **72** (2012) 2225
https://doi.org/10.1140/epjc/s10052-012-2225-5 128

[221] The ATLAS Collaboration *Measurement of the cross-section for W boson production in association with b-jets in pp collisions at* $\sqrt{s} = 7$ *TeV with the ATLAS detector* JHEP **1306** (2013) 084
https://doi.org/10.1007/JHEP06(2013)084 128

[222] K. Cranmer, G. Lewis, L. Moneta, A. Shibata, and W. Verkerke *HistFactory: A tool for creating statistical models for use with RooFit and RooStats* CERN-OPEN-2012-016
https://cds.cern.ch/record/1456844 130

[223] G. Cowan, K. Cranmer, E. Gross, and O. Vitells *Asymptotic formulae for likelihood-based tests of new physics* Eur. Phys. J. C **71** (2011) 1554
https://doi.org/10.1140/epjc/s10052-013-2501-z 131

[224] L. Moneta, K. Cranmer, G. Schott, and W. Verkerke *The RooStats Project* PoS ACAT (2010) 057
https://doi.org/10.22323/1.093.0057 131

[225] A. L. Read *Presentation of search results: the CLs technique* J. Phys. G **28** (2002) 10
https://iopscience.iop.org/article/10.1088/0954-3899/28/10/313/meta 131

[226] The ATLAS Collaboration *Search for dark matter and other new phenomena in events with an energetic jet and large missing transverse momentum using the ATLAS detector* JHEP **1801** (2018) 126
https://doi.org/10.1007/JHEP01(2018)126 136, 140

[227] The CMS Collaboration *Search for the pair production of third-generation squarks with two-body decays to a bottom or charm quark and a neutralino in protonâĂŞproton collisions at* $\sqrt{s} = 13$ *TeV* Phys. Lett. B **778** (2018) 263-291
https://doi.org/10.1016/j.physletb.2018.01.012 141

[228] The ATLAS Collaboration *Search for supersymmetry in events with b-tagged jets and missing transverse momentum in pp collisions at* $\sqrt{s} = 13$ *TeV with the ATLAS detector* JHEP **11** (2017) 195
https://doi.org/10.1007/JHEP11(2017)195 142, 143, 163

[229] The ATLAS Collaboration *Search for direct top squark pair production in final states with two leptons in* $\sqrt{s} = 13$ *TeV pp collisions with the ATLAS detector* Eur. Phys. J. C **77** (2017) 898
https://link.springer.com/article/10.1140/epjc/s10052-017-5445-x 142, 143

[230] The CMS Collaboration *Measurement of* $B\bar{B}$ *Angular Correlations based on Secondary Vertex Reconstruction at* $\sqrt{s} = 7$ *TeV* JHEP **1103** (2011) 136
https://doi.org/10.1007/JHEP03(2011)136 144

[231] The CMS Collaboration *Search for direct production of supersymmetric partners of the top quark in the all-jets final state in proton-proton collisions at* $\sqrt{s} = 13$ *TeV* JHEP **1710** (2017) 005
https://doi.org/10.1007/JHEP10(2017)005 144

[232] M. Aleksa *et al.* *Results of the ATLAS solenoid magnetic field map* J. Phys. Conf. Ser. **110** (2008) 092018
https://iopscience.iop.org/article/10.1088/1742-6596/110/9/092018 148

[233] The ATLAS Collaboration *Ring-shaped Calorimetry Information for a Neural Egamma Identification with ATLAS Detector* J. Phys. Conf. Ser. **762** (2016) 012049
https://doi.org/10.1088/1742-6596/762/1/012049 168

[234] The ATLAS Collaboration *Electron efficiency measurements with the ATLAS detector using 2012 LHC proton-proton collision data* Eur. Phys. J. C **77** (2017) 195
https://doi.org/10.1140/epjc/s10052-017-4756-2 172